

***In-Operando* Water Visualization in Polymer  
Electrolyte Membrane Fuel Cells: Effects of Selected  
Operating Conditions on the Distribution of Liquid  
Water**

by

**John Alexander Haines MacDonald**

B.Sc. (Environmental Engineering), Florida Gulf Coast University, 2020

Thesis Submitted in Partial Fulfillment of the  
Requirements for the Degree of  
Master of Applied Science

in the  
School of Sustainable Energy Engineering  
Faculty of Applied Sciences

© John Alexander Haines MacDonald 2024

SIMON FRASER UNIVERSITY

Spring 2024

Copyright in this work is held by the author. Please ensure that any reproduction or re-use is done in accordance with the relevant national copyright legislation.

## Declaration of Committee

**Name:** John Alexander Haines MacDonald

**Degree:** Master of Applied Science (Sustainable Energy Engineering)

**Title:** *In-Operando* Water Visualization in Polymer Electrolyte Membrane Fuel Cells: Effects of Selected Operating Conditions on the Distribution of Liquid Water

**Committee:**

**Chair: Mahda Jahromi**  
Lecturer, Sustainable Energy Engineering

**Erik Kjeang**  
Supervisor  
Professor, Mechatronic Systems Engineering

**Gordon McTaggart-Cowan**  
Committee Member  
Associate Professor, Sustainable Energy Engineering

**Colin Copeland**  
Examiner  
Associate Professor, Sustainable Energy Engineering

## Abstract

Effective water management is required to enable polymer electrolyte membrane fuel cells (PEMFCs) to operate efficiently, particularly at the high current densities needed to make them relevant for transportation and stationary applications. This study was conducted to evaluate the effects of selected operating conditions on the performance of PEMFCs, as well as their influence on the distribution of liquid water within specific fuel cell components. The investigation included assessments of the impact of operating temperature, oxidant concentration gas delivery rates, relative humidity of influent gases, and current density on fuel cell (FC) performance and water distribution. Miniaturized PEMFCs were constructed, and their performance was assessed using three main electrochemical diagnostic tools, including polarization curve measurements, cyclic voltammetry, and electrochemical impedance spectroscopy. Liquid water distribution and volume were determined *in-operando* using X-ray computed tomography-based procedures and associated image processing methods. The results of this study indicated that the performance of PEMFCs can be substantially affected by varying operational conditions, including test station setup, influent gas temperature and flow rates, oxidant concentration (*i.e.*, air vs O<sub>2</sub> at varying concentrations), with the best performance observed at 70°C, high influent gas flow rates, and high oxygen concentrations. Water distribution within the membrane electrode assembly was influenced by current density, operating temperature, influent gas flow rates, and oxidant type. Information on the distribution of liquid water was useful for explaining differences in FC performance under various operating conditions (*e.g.*, 40°C compared to 70°C). The results of this work provide useful information for optimizing the performance of PEMFCs and enhancing their uses in target applications.

**Keywords:** Polymer electrolyte membrane fuel cell; performance; liquid water distribution; operating conditions; X-ray computed tomography; water management

## **Dedication**

This study is dedicated to my professors and mentors who assisted in my academic journey and inspired me to work on sustainable energy issues and concerns.

## Acknowledgements

It would be difficult to explicitly identify all of the individuals who contributed to this work. Nevertheless, I would like to take this opportunity to thank those people who made substantial contributions over the past three years. First, I would like to thank Prof. Erik Kjeang for his inspiration, support, encouragement, and mentoring during my Master's program. I would also like to thank Prof. Gordon McTaggart-Cowan for his timely insights and contributions to my work, particularly during the preparation of this document. I particularly appreciate the technical input, training and invaluable discussions provided by Mr. Frank Orfino. The comments and suggestions from my Examiner, Dr. Colin Copeland, were also very helpful. I want acknowledge Dr. Mahda Jahromi for his efforts as the Chair during my defence. As a collaborative project between Simon Fraser University (SFU) and Ballard Power Systems, the insights of the oversight team (*i.e.*, provided during biweekly and quarterly meetings) were particularly valuable; this team included Monica Dutta, Esmaeil Alvar, Alan Young and Shanna Knights. I also want to thank my SFU colleagues for their support and encouragement, including Dr. Jonathan Halter, Dr. Fabusuyi Akindele Aroge, Yixuan Chen, Nitish Kumar, Amin Bahrami and Dr. Yanuar Philip Wijaya. Four co-op students also made valuable contributions to this investigation, including Colin Buchko, Samarth Gupta, Olivia Lowe, and Dennis Huang. The staff at 4D Labs provided invaluable assistance during the precise cutting of the materials needed to construct the miniaturized FCs. Furthermore, I would like to thank our funding agencies, including SFU, Natural Sciences and Engineering Research Council (NSERC) of Canada, Ballard Power Systems, Canada Foundation for Innovation (CFI), British Columbia Knowledge Development Fund (BCKDF), and Canada Research Chairs (CRC). Finally, I would like to recognize my parents, who have supported my academic endeavours from the beginning.

# Table of Contents

|   |          |
|---|----------|
| Declaration of Committee .....  | ii       |
| Abstract .....  | iii      |
| Dedication .....  | iv       |
| Acknowledgements .....  | v        |
| Table of Contents .....   | vi       |
| List of Tables .....  | ix       |
| List of Figures .....   | x        |
| List of Acronyms .....  | xv       |
| <b>Chapter 1. Introduction .....</b>  | <b>1</b> |
| 1.1. Motivation .....   | 1        |
| 1.2. Problem Statement and Research Objectives .....                        | 6        |
| <b>Chapter 2. Polymer Electrolyte Membrane Fuel Cell Fundamentals .....</b> | <b>8</b> |
| 2.1. Structure and Function of PEMFCs .....                                 | 8        |
| 2.2. PEMFC Components .....   | 10       |
| 2.2.1. Polymer Electrolyte Membrane .....                                   | 10       |
| 2.2.2. Catalyst Layers .....  | 11       |
| 2.2.3. Gas Diffusion Layers .....   | 12       |
| 2.2.4. Flow Field Plates .....  | 13       |
| 2.3. Thermodynamics of PEMFCs .....   | 14       |
| 2.4. Voltage Losses .....   | 16       |
| 2.5. Current and Potential Applications of PEMFCs .....                     | 18       |
| 2.5.1. Portable Applications of PEMFCs .....                                | 19       |
| 2.5.2. Stationary Applications of PEMFCs .....                              | 19       |
| 2.5.3. Transportation Applications of PEMFCs .....                          | 20       |
| 2.6. Advantages and Limitations of PEMFCs .....                             | 22       |
| 2.7. Factors Affecting the Performance and Durability of PEMFCs .....       | 23       |
| 2.8. Water Management in PEMFCs .....                                       | 25       |
| 2.8.1. Water Production .....   | 25       |
| 2.8.2. Membrane Water Transport Mechanisms .....                            | 26       |
| 2.8.2.1. Electro-Osmotic Drag .....   | 27       |
| 2.8.2.2. Back Diffusion .....   | 28       |
| 2.8.2.3. Thermo-Osmotic Drag .....  | 28       |
| 2.8.2.4. Hydraulic Permeation .....   | 28       |
| 2.8.3. Water Transport Within Fuel Cell Components .....                    | 29       |
| 2.8.4. Effects of Desiccation and Flooding on Fuel Cell Performance .....   | 30       |
| 2.8.4.1. Effects of Water Imbalances in the Anode Region .....              | 30       |
| 2.8.4.2. Effects of Water Imbalances in the Cathode Region .....            | 31       |
| 2.8.5. Strategies for Optimizing Fuel Cell Water Management .....           | 33       |
| 2.9. Methods for Visualizing Liquid Water in PEMFCs .....                   | 36       |
| 2.9.1. Direct Visualization .....   | 37       |
| 2.9.2. Neutron Imaging .....  | 37       |

|                   |  |           |
|-------------------|--|-----------|
| 2.9.3.            | Nuclear Magnetic Resonance Imaging .....   | 38        |
| 2.9.4.            | X-ray Computed Tomography .....  | 38        |
| 2.10.             | Critical Research Needs .....  | 39        |
| 2.11.             | Focus of Current Research Project.....   | 41        |
| <b>Chapter 3.</b> | <b>Experimental Methods .....</b>  | <b>42</b> |
| 3.1.              | Preparation of Fuel Cell Materials and Components .....  | 42        |
| 3.2.              | Assembly of Fuel Cell Small-Scale Fixture .....  | 45        |
| 3.3.              | Conditioning of Fuel Cell.....   | 46        |
| 3.4.              | Fuel Cell Operation and Testing .....  | 48        |
| 3.5.              | Diagnostic Testing .....   | 49        |
| 3.6.              | X-ray Computed Tomography.....   | 52        |
| 3.7.              | XCT Image Processing.....  | 55        |
| 3.8.              | Application of One-Dimensional Model.....  | 61        |
| 3.9.              | Optimization of Fuel Cell Test Station and Comparison of High and Low Flow Rates of Gases.....   | 62        |
| 3.10.             | Evaluation of the Effect of Temperature Variation on the Performance of PEMFCs .....   | 63        |
| 3.11.             | Evaluation of the Effect of Varying Relative Humidities on Cell Performance and Liquid Water Distribution at Various Temperatures..... | 65        |
| 3.12.             | Evaluation of the Effect of Current Density on the Distribution of Liquid Water Within the Gas Diffusion Layer .....                   | 66        |
| <b>Chapter 4.</b> | <b>Results and Discussion.....</b>   | <b>70</b> |
| 4.1.              | Optimization of Fuel Cell Test Station and Comparison of High and Low Flow Rates of Gases.....   | 71        |
| 4.2.              | Evaluation of the Effects of Temperature Variation on the Performance of PEMFCs.....   | 74        |
| 4.2.1.            | Application of Scribner Setup .....  | 74        |
| 4.2.2.            | Application of <i>In-Operando</i> Setup .....  | 77        |
| 4.3.              | Evaluation of the Effect of Varying Relative Humidities on Cell Performance and Liquid Water Distribution at Various Temperatures..... | 82        |
| 4.3.1.            | Experimental Results .....   | 82        |
| 4.3.2.            | Model Results .....  | 88        |
| 4.3.2.1.          | Channel Region .....   | 88        |
| 4.3.2.2.          | Lands Region .....   | 92        |
| 4.4.              | Evaluation of the Effects of Current Density on the Distribution of Liquid Water Within the Gas Diffusion Layer .....                  | 96        |
| 4.4.1.            | Influence of Current Density at 40°C .....   | 98        |
| 4.4.1.1.          | High flow rate analysis .....  | 103       |
| 4.4.1.2.          | Oxygen variation .....   | 105       |
| 4.4.1.3.          | High current density .....   | 109       |
| 4.4.2.            | Influence of Current Density at 50°C .....   | 112       |
| 4.4.2.1.          | Oxygen Variation.....  | 115       |
| 4.4.2.2.          | High Current Density.....  | 117       |
| 4.4.3.            | Influence of Current Density at 60°C .....   | 120       |

|   |   |            |
|---|---|------------|
| 4.4.3.1.  | Oxygen Variation.....   | 123        |
| 4.4.3.2.  | High Current Density.....   | 125        |
| 4.4.4.  | Influence of Current Density at 70°C .....  | 128        |
| 4.4.4.1.  | Oxygen Variation.....   | 131        |
| 4.4.4.2.  | High Current Density.....   | 133        |
| 4.4.5.  | Discussion of the Effect of Current Density on the Distribution of Liquid Water Within the Gas Diffusion Layer at Various Temperatures..... | 135        |
| 4.5.  | Comparison of Model Predictions and Experimental results at Various Current Densities and Temperatures.....                                 | 137        |
| <b>Chapter 5. Uncertainty Analysis.....</b>                     |   | <b>143</b> |
| 5.1.  | Uncertainty Associated with Differences in MEAs Between Trials .....  | 143        |
| 5.2.  | Uncertainty Associated with Segmentation of Liquid Water within the GDL .....   | 144        |
| 5.3.  | Uncertainty Associated with Resistance in the Load Wires during <i>In-operando</i> Setup.....   | 145        |
| 5.4.  | Uncertainty Associated with Electrical Connections Between the Load Wires and the Graphite Plates.....                                      | 146        |
| 5.5.  | Uncertainty Associated with the Application of Long Gas Lines from the Scribner to the XCT Machine during <i>In-operando</i> Testing.....   | 146        |
| 5.6.  | Reproducibility of Liquid Water Quantification.....   | 147        |
| <b>Chapter 6. Summary, Conclusions and Recommendations.....</b> |   | <b>149</b> |
| 6.1.  | Summary.....  | 149        |
| 6.2.  | Conclusions.....  | 151        |
| 6.3.  | Recommendations.....  | 153        |
| <b>Chapter 7. References Cited.....</b>                         |   | <b>155</b> |

## List of Tables

|           |  |    |
|-----------|--|----|
| Table 1.  | Laser micromachining tool cutting parameters. ....   | 44 |
| Table 2.  | MEA component dimensions. ....   | 44 |
| Table 3.  | Listing of diagnostic operational parameters used in the low-flow rate trials. ....  | 49 |
| Table 4.  | Listing of diagnostic operational parameters used in the high-flow rate trials. ....   | 49 |
| Table 5.  | XCT parameters used for the <i>In-situ</i> investigations. ....  | 54 |
| Table 6.  | XCT parameters used for the <i>In-operando</i> investigations. ....  | 54 |
| Table 7.  | Operational conditions used in the Fuel Cell Test Station Optimization and Comparison Experiment. ....                                       | 63 |
| Table 8.  | Operational conditions for the direct Scribner tests conducted during the effect of temperature on fuel cell performance investigation. .... | 64 |
| Table 9.  | Operational conditions for the in-operando tests conducted during the effect of temperature on fuel cell performance investigation. ....     | 64 |
| Table 10. | Influent gas conditions used during the RH variation trials. ....  | 65 |
| Table 11. | Operational conditions for the trials conducted at 40°C to evaluate the effect of current density on water volume in the GDL. ....           | 67 |
| Table 12. | Operational conditions for the trials conducted at 50°C to evaluate the effect of current density on water volume in the GDL. ....           | 68 |
| Table 13. | Operational conditions for the trials conducted at 60°C to evaluate the effect of current density on water volume in the GDL. ....           | 68 |
| Table 14. | Operational conditions for the trials conducted at 70°C to evaluate the effect of current density on water volume in the GDL. ....           | 69 |

## List of Figures

|            |  |    |
|------------|--|----|
| Figure 1.  | Schematic representation of a PEMFC, showing the components of the MEA and the flow plates (Reproduced with permission from White <i>et al.</i> 2019).....   | 9  |
| Figure 2.  | Schematic diagram showing the functionality of a PEMFC (Reproduced with permission from Halter 2019).....  | 10 |
| Figure 3.  | Schematic representation of a catalyst layer of a PEMFC, as located between the microporous layer (MPL) and the Nafion membrane, showing the platinum (Pt) particles supported on a carbon structural element (Reproduced with permission from Chen 2020).....                 | 12 |
| Figure 4.  | XCT slice of a GDL ( <i>i.e.</i> , Avcarb); the carbon fibers are shown in light grey.....   | 13 |
| Figure 5.  | Example designs of flow fields commonly used in PEMFCs (Reproduced with permission from Chen 2020).....  | 14 |
| Figure 6.  | Example polarization curve for a PEMFC, showing the three regions of potential voltage losses (Adapted from Agaesse 2016).....   | 17 |
| Figure 7.  | Mechanisms of water transport in PEM fuel cell membranes (Adapted from Ijaodola <i>et al.</i> 2019).....   | 27 |
| Figure 8.  | Polarization curves showing the impacts of cathode flooding on the performance of PEMFCs (Adapted from Li <i>et al.</i> 2008).....   | 33 |
| Figure 9.  | Schematic representation of miniaturized PEMFC that identifies all of the components including: (a) a 3D view of the cell components; (b) a plan view of the key components; and, (c) a cross-sectional view of the apparatus (Reproduced with permission from Chen 2020)..... | 43 |
| Figure 10. | Schematic diagram of representative vacuum plates used to assemble an MEA (Reproduced with permission from Chen 2020).....   | 45 |
| Figure 11. | Three-dimensional schematic diagram of the SSF components (Reproduced with permission from Chen 2020).....   | 46 |
| Figure 12. | Setup of Scribner 850C fuel cell testing system.....   | 47 |
| Figure 13. | Example cyclic voltammogram.....   | 51 |
| Figure 14. | Theoretical Nyquist plot (Reproduced with permission from Chen 2020).....  | 52 |
| Figure 15. | Schematic diagram of the procedure for segmenting liquid water starting from a wet and dry image set (Reproduced with permission from Aroge 2023).....   | 56 |
| Figure 16. | Example image slice from a dry image set.....  | 58 |
| Figure 17. | Example image slice from a wet image set.....  | 59 |
| Figure 18. | Example image slice from a subtraction image set generated by subtracting the wet image stack from the dry image stack.....  | 59 |
| Figure 19. | Example image slice from a segmented image set.....  | 60 |
| Figure 20. | Comparison of the performance of PEMFC operated on the G20 test station, the Scribner test station operated at low gas flow rates, and the Scribner test station operated at high flow rates.....  | 72 |

|            |   |    |
|------------|---|----|
| Figure 21. | Polarization curves generated for a PEMFC operated at temperatures ranging from: (a) 30 to 70°C; and, (b) 70 to 90°C. ....  | 75 |
| Figure 22. | High frequency resistance derived from EIS measurement vs. operating temperature of a PEMFC. ....   | 76 |
| Figure 23. | Polarization curves generated for a PEMFC operated at temperatures ranging from: (a) 30 to 70°C; and, (b) 70 to 90°C, under <i>in-operando</i> conditions.....                        | 78 |
| Figure 24. | Resistance corrected polarization curves generated for a PEMFC operated at temperatures ranging from: (a) 30 to 70°C; and, (b) 70 to 90°C, under in-operando conditions. ....         | 80 |
| Figure 25. | Polarization curves generated for a PEMFC operated at 70°C and RHs ranging from 25% to 100%.....  | 83 |
| Figure 26. | Polarization curves generated for a PEMFC operated at 60°C and RHs ranging from 25% to 100%.....  | 83 |
| Figure 27. | Polarization curves generated for a PEMFC operated at 50°C and RHs ranging from 25% to 100%.....  | 84 |
| Figure 28. | Polarization curves generated for a PEMFC operated at 40°C and RHs ranging from 50% to 100%.....  | 85 |
| Figure 29. | Polarization curves generated for a PEMFC operated at 100% RH and temperatures ranging from 40°C to 70°C.....   | 86 |
| Figure 30. | Polarization curves generated for a PEMFC operated at 75% RH and temperatures ranging from 40°C to 70°C.....  | 86 |
| Figure 31. | Polarization curves generated for a PEMFC operated at 50% RH and temperatures ranging from 40°C to 70°C.....  | 87 |
| Figure 32. | Polarization curves generated for a PEMFC operated at 25% RH and temperatures ranging from 50°C to 70°C.....  | 88 |
| Figure 33. | RH variation map for under the channels displaying a wet, dry or in transition from wet to dry GDL at fifteen separate operational conditions. ....                                   | 90 |
| Figure 34. | Transition region map for under the channels displaying wet or dry conditions within the GDL at four different current densities at two identified transition regions conditions..... | 90 |
| Figure 35. | Plot displaying the ratio of water vapor pressure to saturation vapor pressure under the channels at 60°C and 100% RH for four different current densities.....                       | 91 |
| Figure 36. | Plot displaying the ratio of water vapor pressure to saturation vapor pressure under the channels at 40°C and 75% RH for four different current densities.....                        | 92 |
| Figure 37. | RH variation map for under the lands displaying a wet, dry or in transition from wet to dry GDL at fifteen separate operational conditions.....                                       | 93 |
| Figure 38. | Transition region map for under the lands displaying wet or dry conditions within the GDL at 40°C and 75% RH for four different current densities. ....                               | 93 |
| Figure 39. | Plot displaying the ratio of water vapor pressure to saturation vapor pressure under the lands at 40°C and 75% RH for four different current densities.....                           | 94 |

|            |   |     |
|------------|---|-----|
| Figure 40. | Example image slice from a segmented image set, which was located at approximately 70 $\mu\text{m}$ from the CL. ....                                     | 97  |
| Figure 41. | Example image slice from a segmented image set, which was located at approximately 110 $\mu\text{m}$ from the CL. ....                                    | 98  |
| Figure 42. | Overall water volume profile of the cathode GDL substrate of a fuel cell operated at 40°C at four separate current densities.....                         | 99  |
| Figure 43. | Water volume profile of the cathode GDL substrate under the lands of a fuel cell operated at 40°C at four separate current densities.....                 | 99  |
| Figure 44. | Water volume profile of the cathode GDL substrate under the channels of a fuel cell operated at 40°C at four separate current densities.....              | 100 |
| Figure 45. | Representative curve of the relationship between temperature and water saturation vapour pressure (data obtained from Engineering ToolBox 2023).....      | 102 |
| Figure 46. | Overall water volume profile of the GDL substrate of a fuel cell operated at 40°C with high flow rates at four separate current densities. ....           | 104 |
| Figure 47. | Water volume profile of the GDL substrate under the lands of a fuel cell operated at 40°C with high flow rates at four separate current densities. ....   | 104 |
| Figure 48. | Water volume profile of the GDL substrate under the channels of a fuel cell operated at 40°C with high flow rates at four separate current densities..... | 105 |
| Figure 49. | Direct Scribner polarization curves generated under air, 60% O <sub>2</sub> and 100% O <sub>2</sub> .....   | 106 |
| Figure 50. | <i>In-operando</i> polarization curves generated under air, 60% O <sub>2</sub> and 100% O <sub>2</sub> .....  | 106 |
| Figure 51. | Overall water volume profile of the GDL substrate of a fuel cell operated at 40°C at three separate oxygen concentrations. ....                           | 107 |
| Figure 52. | Water volume profile of the GDL substrate under the lands of a fuel cell operated at 40°C at three separate oxygen concentrations. ....                   | 107 |
| Figure 53. | Water volume profile of the GDL substrate under the channels of a fuel cell operated at 40°C at three separate oxygen concentrations.....                 | 108 |
| Figure 54. | Overall water volume profile of the GDL substrate of a fuel cell operated at 40°C at three selected high current densities. ....                          | 110 |
| Figure 55. | Water volume profile of the GDL substrate under the lands of a fuel cell operated at 40°C at three selected high current densities.....                   | 110 |
| Figure 56. | Water volume profile of the GDL substrate under the channels of a fuel cell operated at 40°C at three selected high current densities. ....               | 111 |
| Figure 57. | Overall water volume profile of the GDL substrate of a fuel cell operated at 50°C at six separate current densities. ....                                 | 112 |
| Figure 58. | Water volume profile of the GDL substrate under the lands of a fuel cell operated at 50°C at six separate current densities. ....                         | 114 |
| Figure 59. | Water volume profile of the GDL substrate under the channels of a fuel cell operated at 50°C at six separate current densities. ....                      | 115 |

|            |   |     |
|------------|---|-----|
| Figure 60. | Overall water volume profile of the GDL substrate of a fuel cell operated at 50°C at three separate oxygen concentrations. ....                                 | 116 |
| Figure 61. | Water volume profile of the GDL substrate under the lands of a fuel cell operated at 50°C at three separate oxygen concentrations. ....                         | 117 |
| Figure 62. | Water volume profile of the GDL substrate under the channels of a fuel cell operated at 50°C at three separate oxygen concentrations. ....                      | 117 |
| Figure 63. | Overall water volume profile of the GDL substrate of a fuel cell operated at 50°C at selected high current densities and oxygen concentrations. ....            | 118 |
| Figure 64. | Water volume profile of the GDL substrate under the lands of a fuel cell operated at 50°C at selected high current densities and oxygen concentrations. ....    | 119 |
| Figure 65. | Water volume profile of the GDL substrate under the channels of a fuel cell operated at 50°C at selected high current densities and oxygen concentrations. .... | 119 |
| Figure 66. | Overall water volume profile of the GDL substrate of a fuel cell operated at 60°C at five separate current densities. ....                                      | 121 |
| Figure 67. | Water volume profile of the GDL substrate under the lands of a fuel cell operated at 60°C at five separate current densities. ....                              | 122 |
| Figure 68. | Water volume profile of the GDL substrate under the channels of a fuel cell operated at 60°C at five separate current densities. ....                           | 123 |
| Figure 69. | Overall water volume profile of the GDL substrate of a fuel cell operated at 60°C at three separate oxygen concentrations. ....                                 | 123 |
| Figure 70. | Water volume profile of the GDL substrate under the lands of a fuel cell operated at 60°C at three separate oxygen concentrations. ....                         | 124 |
| Figure 71. | Water volume profile of the GDL substrate under the channels of a fuel cell operated at 60°C at three separate oxygen concentrations. ....                      | 125 |
| Figure 72. | Overall water volume profile of the GDL substrate of a fuel cell operated at 60°C at three selected high current densities. ....                                | 126 |
| Figure 73. | Water volume profile of the GDL substrate under the lands of a fuel cell operated at 60°C at three selected high current densities. ....                        | 126 |
| Figure 74. | Water volume profile of the GDL substrate under the channels of a fuel cell operated at 60°C at three selected high current densities. ....                     | 127 |
| Figure 75. | Overall water volume profile of the GDL substrate of a fuel cell operated at 70°C at five separate current densities. ....                                      | 129 |
| Figure 76. | Water volume profile of the GDL substrate under the lands of a fuel cell operated at 70°C at five separate current densities. ....                              | 130 |
| Figure 77. | Water volume profile of the GDL substrate under the channels of a fuel cell operated at 70°C at five separate current densities. ....                           | 131 |
| Figure 78. | Overall water volume profile of the GDL substrate of a fuel cell operated at 70°C at three separate oxygen concentrations. ....                                 | 132 |
| Figure 79. | Water volume profile of the GDL substrate under the lands of a fuel cell operated at 70°C at three separate oxygen concentrations. ....                         | 133 |
| Figure 80. | Water volume profile of the GDL substrate under the channels of a fuel cell operated at 70°C at three separate oxygen concentrations. ....                      | 133 |

|            |  |     |
|------------|--|-----|
| Figure 81. | Overall water volume profile of the GDL substrate of a fuel cell operated at 70°C at three selected high current densities. ....                     | 134 |
| Figure 82. | Water volume profile of the GDL substrate under the lands of a fuel cell operated at 70°C at three selected high current densities.....              | 135 |
| Figure 83. | Water volume profile of the GDL substrate under the channels of a fuel cell operated at 70°C at three selected high current densities. ....          | 135 |
| Figure 84. | Model map for under the channels displaying a wet or dry GDL at various current densities and temperatures. ....                                     | 139 |
| Figure 85. | Model map for under the lands displaying a wet or dry GDL at various current densities and temperatures. ....  | 140 |
| Figure 86. | Experimental map for under the channels displaying a wet or dry GDL at various current densities and temperatures.....                               | 140 |
| Figure 87. | Experimental map for under the lands displaying a wet or dry GDL at various current densities and temperatures.....                                  | 141 |
| Figure 88. | Plot displaying the ratio of water vapor pressure to saturation vapor pressure under the channels at 60°C for five different current densities. .... | 141 |

## List of Acronyms

|                     |   |
|---------------------|---|
| 2D                  | Two dimensional                               |
| 3D                  | Three dimensional                             |
| ACL                 | Anode catalyst layer                          |
| BOL                 | Beginning of life                             |
| CAD                 | Computer-aided design                         |
| CCL                 | Cathode catalyst layer                        |
| CCM                 | Catalyst-coated membrane                      |
| CH <sub>4</sub>     | Methane                                       |
| CHP                 | Combined heating and power                    |
| CL                  | Catalyst layer                                |
| CO <sub>2</sub>     | Carbon dioxide                                |
| CV                  | Cyclic voltammetry                            |
| DOE                 | United States Department of Energy            |
| E°                  | Cell potential                                |
| E <sub>th</sub>     | Theoretical electrical potential              |
| E <sub>Thermo</sub> | Theoretical maximum potential                 |
| ECSA                | Electrochemical surface area                  |
| EIS                 | Electrochemical impedance spectroscopy        |
| EPA                 | United States Environmental Protection Agency |
| EV                  | Electric vehicle                              |
| F                   | Faraday's constant                            |
| FC                  | Fuel cell                                     |
| FCV                 | Fuel cell vehicle                             |
| FP                  | Flow plate                                    |
| ΔG                  | Gibbs free energy                             |
| GDL                 | Gas diffusion layer                           |
| GHG                 | Greenhouse gas                                |
| GTCO <sub>2e</sub>  | Gigatonnes of equivalent carbon dioxide       |
| ΔH                  | Hydrogen higher heating value                 |
| HTEC                | Hydrogen Technology and Energy Corporation    |
| H <sub>3</sub> O    | Hydronium ion                                 |
| HFR                 | High frequency resistance                     |

|            |  |
|------------|--|
| HOR        | Hydrogen oxidation reaction            |
| MEA        | Membrane electrode assembly            |
| MPL        | Microporous layer                      |
| $n_a$      | Activation losses                      |
| $n_{mass}$ | Mass transport losses                  |
| $n_{ohm}$  | Ohmic losses                           |
| $N_2O$     | Nitrous oxide                          |
| $O_2$      | Oxygen                                 |
| OCV        | Open circuit voltage                   |
| ORR        | Oxygen reduction reaction              |
| P          | Pressure                               |
| PED        | Personal electronic device             |
| PEM        | Polymer electrolyte membrane           |
| PEMFC      | Polymer electrolyte membrane fuel cell |
| PFSA       | Perfluorosulfonic acid                 |
| PTFE       | Polytetrafluoroethylene (Teflon)       |
| RH         | Relative humidity                      |
| R          | Universal gas constant                 |
| $R_\Omega$ | Internal resistance                    |
| SSF        | Small-scale fixture                    |
| $SO_3$     | Sulfur trioxide                        |
| T          | Temperature                            |
| TM         | Trademark                              |
| $\omega$   | Frequency                              |
| XCT        | X-ray computed tomography              |
| X-ray      | X-ray radiation                        |
| $Z_m$      | Imaginary impedance                    |
| $Z_{Re}$   | Real impedance                         |

# Chapter 1. Introduction

One of the main objectives of this study was to enhance our understanding the influence of operating conditions on the formation, distribution, and abundance (*i.e.*, volume) of liquid water within the membrane electrode assembly (MEA) of operating polymer electrolyte membrane fuel cell (PEMFC). In this chapter, the motivation for conducting this work and the purpose of the study are described. In addition, a problem statement is presented that guided the design of the investigation. Collectively, this information is intended to provide the reader with a basic understanding of the purpose of this research and the approach that was used to conduct it.

## 1.1. Motivation

Climate change is broadly considered to be one of the greatest threats to the environment and human wellbeing worldwide (Xu *et al.* 2020; Zhao *et al.* 2022). Such changes in the global climate are largely associated with releases of greenhouse gases (GHGs) into the atmosphere (Lamb *et al.* 2021). According to Holechek *et al.* (2022), fossil fuels accounted for about 83.1% of the world's primary energy consumption in 2021. By comparison, nuclear energy and renewable energy sources (including hydroelectric power, wind power, and solar power sources), collectively accounted for 16.9% of the global energy production, respectively (Holechek *et al.* 2022). Of these cleaner energy sources, nuclear facilities accounted for 4.3% of the total global energy production, while hydroelectric systems and other renewable energy sources accounted for 6.9% and 5.7% of the total energy generation, respectively (British Petroleum 2022). Hence, non-carbon-based energy sources still account for only a fraction of the total energy production worldwide (Holechek *et al.* 2022; Rapier 2020).

The burning of fossil fuels, which is widely regarded as the principal source of GHG releases to the atmosphere (Holechek *et al.* 2022), is having a significant negative impact on the environment. While carbon dioxide (CO<sub>2</sub>), methane (CH<sub>4</sub>), and nitrous oxide (N<sub>2</sub>O) are the principal GHGs that are emitted during the burning coal, natural gas, and oil, fluorinated gases (such as hydrofluorocarbons, perfluorocarbons, sulfur hexafluoride, and nitrogen trifluoride) are also released and contribute significantly to total GHG emissions (Sovacool *et al.* 2021). According to the Environmental Protection

Agency (EPA 2020; 2022), carbon emissions associated with the use of fossil fuels increased drastically during the period from 1900 to 2014, with total worldwide emissions of carbon estimated at approximately 10,000 million metric tons in 2014. The United Nations Environment Programme (2022) estimated that total global GHG emissions (which includes emissions of CO<sub>2</sub> and other GHGs) were about 53 GTCO<sub>2</sub>e (gigatons of carbon dioxide equivalents) in 2021, with roughly 27% of this total originating from the transportation sector of the economy. Similarly, the Environmental Protection Agency reported that the transportation industry is responsible for about 28% of total fossil fuel consumption and associated GHG emissions in the United States (USEPA 2018). Hence, there is an immediate need to reduce emissions of greenhouse gases (GHGs) into the atmosphere, if we, as a society, are to mitigate the effects of human activities on the global climate (Holechek *et al.* 2022).

Many actions are needed to foster the transition from fossil fuels to renewable energy sources. While effective mitigations are needed within all sectors of the economy, the transportation and stationary power sectors represent particularly high priorities for action because they collectively account for about 52% of total fossil fuel consumption worldwide (USEPA 2018; 2020). Renewable energy (such as hydroelectric power, solar power, and wind power) can be utilized in both sectors; however, energy storage is an ongoing challenge that needs to be effectively addressed if we, as a society, are to optimize the benefits associated with renewable power production (*i.e.*, because renewable energy is not always produced when and where it is most needed). Advancements in battery technologies (*e.g.*, Li-ion batteries, solid-state batteries, etc.) are helping to address this challenge in light automotive and stationary energy applications. However, it is becoming increasingly apparent that battery-based storage may not be the most applicable approach for other applications within these sectors of the economy. More specifically, alternative energy storage options, such as hydrogen, may be more attractive in certain circumstances (*e.g.*, heavy trucking, rail transport, marine transport, aviation, meeting peak power requirements by stationary power facilities, etc.). In such applications, hydrogen fuel cells can provide a means of converting stored energy into electricity when and where it is needed.

The fuel cell industry is gaining momentum worldwide, primarily due to the increasingly urgent need for zero-emission transportation systems across all sectors of the economy (Wang *et al.* 2020). Polymer electrolyte membrane (PEM) fuel cells have

high power density outputs, have scalable architecture, operate at low temperatures, and have zero greenhouse gas emissions associated with their operation, all of which make them ideal for transportation applications. Hence, hydrogen fuel cell technologies represent an important element of a global strategy for energy sustainability. However, a number of improvements are needed if PEMFCs are to realize their full potential in the transportation sector. Importantly, improvements to PEMFC technologies are needed to reduce construction and operation costs, to improve durability, and to optimize performance, if they are to effectively compete with internal combustion engine-powered and battery-powered vehicles (Schmittinger and Vahidi 2008). Such needed improvements can be classified into four general categories, including improvements to PEMFC design and construction, improvements to FC systems, improvements to fuel cell vehicles (FCVs), and improvements to FC infrastructure.

As PEMFCs operate on hydrogen fuel and an oxidant (air or oxygen), it is essential that the design of the gas flow panels, cooling channels, and bipolar plates be optimized to facilitate the efficient delivery of gases and effective removal of water and waste heat (Tsushima and Hirai 2011). In addition to meeting the need for efficient gas distribution, design improvements need to focus on identification of materials that provide high thermal and electrical conductivities, consider the need for component hydrophobicity, are amenable to high-volume manufacturing, and achieve long-term cost targets (*i.e.*, <\$30/ kW; Wang *et al.* 2020). Improvements in the design of diffusion media (*i.e.*, gas diffusion layer-GDL and micro-porous layer-MPL) are also needed to enhance reactant transport, water and heat removal, membrane electrode assembly (MEA) support, and catalyst layer (CL) protection (Rahman *et al.* 2016). As GDLs are subject to degradation over long operation periods, refinements are needed to prevent losses of polytetrafluoroethylene (PTFE) and fiber breakdown associated with freeze-thaw cycles (Wang *et al.* 2011). Refinements to the CLs are also needed to reduce the costs associated with this component of PEMFCs, which could include finding effective replacements for platinum or reducing loadings of platinum in the CL (Wang *et al.* 2011; Osmieri and Meyer 2022). For PEMFCs, the major challenge is to further the development of membranes that exhibit high ionic conductivity, prevent electron transport, minimize cross-over of hydrogen and oxygen gases, and reduce production costs (Schmittinger and Vahidi 2008). Such improvements in FC design and in construction methods and materials will help to reduce the costs, increase durability, and

enhance performance of PEMFCs, thereby making them more competitive with internal combustion engines (Wang *et al.* 2020).

Fuel cell systems and FCVs also need to be improved to achieve durability, performance, and accessibility objectives (Schmittinger and Vahidi 2008). For example, automotive FC systems must be able to withstand changing load cycles (start-stop cycling), in addition to swings in temperature from below freezing to greater than 30°C (Li *et al.* 2021). Refinements to the design of these systems also need to ensure that degradation is minimized over extended periods of use (Mench 2008; Sinigaglia *et al.* 2017, Ahmadi and Kjeang 2017). Furthermore, automotive fuel cells must be able to achieve very high-power densities (Jiao *et al.* 2021). Although significant improvements have been made to increase power densities in fuel cells, further optimization is still required before they can be more fully integrated into the transportation sector of the economy (Wang *et al.* 2020).

The need for enhanced fuel cell performance is not the only challenge that is currently limiting the broader application of this technology. While hydrogen is considered a promising energy carrier, there are several limitations associated with its production, storage, and distribution including:

- The primary methods of hydrogen production are through steam methane reforming, coal gasification, and electrolysis. Steam methane reforming and coal gasification rely on fossil fuels, which contribute to greenhouse gas emissions and are non-renewable (USDOE 2023). Electrolysis, which uses electricity to split water into hydrogen and oxygen, requires a significant amount of energy, often sourced from fossil fuels (USDOE 2023). Expanding the production of hydrogen through renewable energy sources is essential to mitigate these concerns (Tashie-Lewis and Nnabuife 2021);
- The cost of hydrogen production is relatively high compared to other fuels. The expense is primarily due to the energy-intensive processes involved in its production. Additionally, the development of infrastructure for hydrogen production and distribution adds to the overall costs associated with the use of this fuel (Nazir *et al.* 2020);
- Hydrogen gas has a low volumetric energy density (*i.e.*, compared to liquid fuels), meaning a large volume of hydrogen is required to store a significant amount of

- energy (USDOE 2023). Hence, it presents challenges for practical storage and transportation (Tashie-Lewis and Nnabuife 2021). Compressing hydrogen gas requires high-pressure containers, which can be costly and pose safety concerns (Nazir *et al.* 2020). Alternatively, storing hydrogen in liquid form requires extremely low temperatures, making it challenging and energy-intensive (Nazir *et al.* 2020);
- Establishing a comprehensive hydrogen distribution infrastructure is a significant challenge. Existing pipelines and storage facilities are primarily designed for natural gas and they may not be compatible with hydrogen due to its unique properties (Litvinenko *et al.* 2020). In addition, there are few retail distribution facilities in Canada, which makes refueling a significant challenge for consumers. Retrofitting or building new infrastructure for hydrogen distribution would require significant investments by both the public and private sectors (Litvinenko *et al.* 2020);
  - Hydrogen is highly flammable and has a wide flammability range in air (*i.e.*, the range of concentrations capable of producing a flash of fire; USDOE 2023). Safety measures and precautions must be in place for its storage, handling, and transportation to prevent accidents (Nazir *et al.* 2020). Addressing safety concerns is crucial to gain public acceptance and confidence in hydrogen technologies; and,
  - Hydrogen molecules are small and can escape through materials that are impermeable to other gases USDOE 2023; Nazir *et al.* 2020). This characteristic poses challenges for containment and leads to potential hydrogen leakage during storage and distribution, which can contribute to safety hazards and energy loss (Tashie-Lewis and Nnabuife 2021).

Addressing these challenges is crucial for the widespread adoption and integration of hydrogen as a clean energy alternative, both in Canada and worldwide. Researchers and engineers are actively working to overcome the existing limitations associated with the application of PEMFCs through the development of technological advancements and innovations. Operation of fuel cells at higher power densities represents a very promising approach to achieving cost reductions and reducing the overall footprint of PEMFCs (Wang *et al.* 2020). Enhancing power density would support the use of smaller, less expensive fuel cell stacks for specific applications. However, higher rates of water production tend to offset the benefits of high-power density operation by reducing the performance of the PEMFCs. Hence, formation and

accumulation liquid water represents a limiting factor for operating PEM fuel cells at high current densities (*i.e.*, there is a need to avoid flooding to maintain the power output of PEMFCs). Accordingly, there is a need to identify operating conditions that optimize power output, while minimizing the formation and accumulation of liquid water in PEMFCs (Wang *et al.* 2020).

The research described in this document was conducted to support the further development of PEMFC technology. More specifically, this study was undertaken to identify operating conditions that can be used optimize the performance of PEMFCs. As accumulation of liquid water in MEA can impair fuel cell performance (Okonkwo and Otor 2021), acquisition of data and information on the influence of operating conditions on liquid water production, distribution, and abundance can lead to innovations that improve the performance of PEM fuel cells. A detailed review of the scientific literature on PEMFC structure and operation, existing applications, benefits and limitations, factors influencing performance, and priority research needs is presented in Chapter 2 to provide additional rationale for the research conducted in the current investigation.

## **1.2. Problem Statement and Research Objectives**

Large-scale commercialization of fuel cell technology in the transportation sector is currently limited by the need for improvements in the efficiency of individual PEMFCs, in the size and capacity of FC systems, in the design of FC vehicles, and in the infrastructure needed to refuel such vehicles (Wang *et al.* 2020). Expansion of the use of this technology in stationary power facilities requires improvements in the performance and longevity of PEMFCs and FC systems. For both of these applications of PEMFCs, there is a need to identify the factors that are limiting fuel cell performance and to develop solutions that support further innovation of fuel cell technology.

Information from numerous studies indicated that the performance of FCs can be influenced by various factors related to their design and operation (Park and Li 2006; Zhang *et al.* 2007; Belkhiri *et al.* 2011; Sun *et al.* 2015; Kawase *et al.* 2016; Raman *et al.* 2017). For any FC design, operating conditions (*e.g.*, cell temperature, fuel type, oxidant type, gas temperature, gas delivery rates, etc.) can substantially influence performance (Belkhiri *et al.* 2011; Sun *et al.* 2015; Eller *et al.* 2017). Accordingly, a primary goal of this study is to evaluate the influence of selected operating conditions on the

performance of PEMFCs. Because flooding has been frequently identified as a limiting factor on fuel cell performance, evaluation of the distribution of liquid water within the membrane electrode assembly (MEA) as a function of selected operating conditions was also identified as a research objective (*i.e.*, by applying X-ray computed tomography and associated image processing techniques). Accordingly, this research is intended to complement recent work on liquid water movement through the GDLs and within the flow channels of the fuel cell (White *et al.* 2017; 2019; Chen 2020). In this way, this project is expected to contribute to a better understanding of water balance within fuel cells and, hence, improve the management of liquid water in PEMFCs. Specific research objectives that were identified for this project include:

- Evaluate the effects of temperature, RH, oxygen concentration, flow rate and current density on fuel cell performance;
- Evaluate the distribution of liquid water within the MEA at various temperatures, current densities, flow rates and oxygen concentrations; and,
- Determine how the liquid water distribution within the MEA impacts the performance of the fuel cell.

## Chapter 2. Polymer Electrolyte Membrane Fuel Cell Fundamentals

Fuel cells are electrochemical devices that convert chemical energy into electrical energy and heat. A PEMFCs is one type of fuel cell that is comprised of anodic and cathodic regions and a proton-conducting polymer membrane electrolyte. PEMFCs utilize hydrogen as the fuel, oxygen as the oxidant, and are designed to operate at relatively low temperatures (*i.e.*, less than 100° C; O'Hayre *et al.* 2016). PEMFCs have high power densities and low emissions, which makes them suitable for numerous applications (Agyekum *et al.* 2022). This section provides a brief overview of the structure and function of PEMFCs, a discussion of the thermodynamics of PEMFCs, a description of the sources of voltage losses in PEMFCs, a listing of the advantages and limitations of PEMFCs, a description of the factors influencing PEMFC performance, and a discussion of water management issues and strategies. The results of this literature review were used to identify critical research needs related to PEMFCs and to inform the design of a research program that could address a subset of the research needs identified.

### 2.1. Structure and Function of PEMFCs

PEMFCs convert the chemical potential energy contained in hydrogen molecules directly into electrical energy (Barbir 2006). PEMFCs function through the use of a membrane electrode assembly (MEA), which is sandwiched between two flow plates (FPs; *i.e.*, also known as bipolar plates). The MEA is typically comprised of anode and cathode catalyst layers (*i.e.*, ACL and CCL), two gas diffusion layers (GDL), and a polymer electrolyte membrane (PEM) that is located between the anode and cathode components; Barbir 2006; Figure 1).

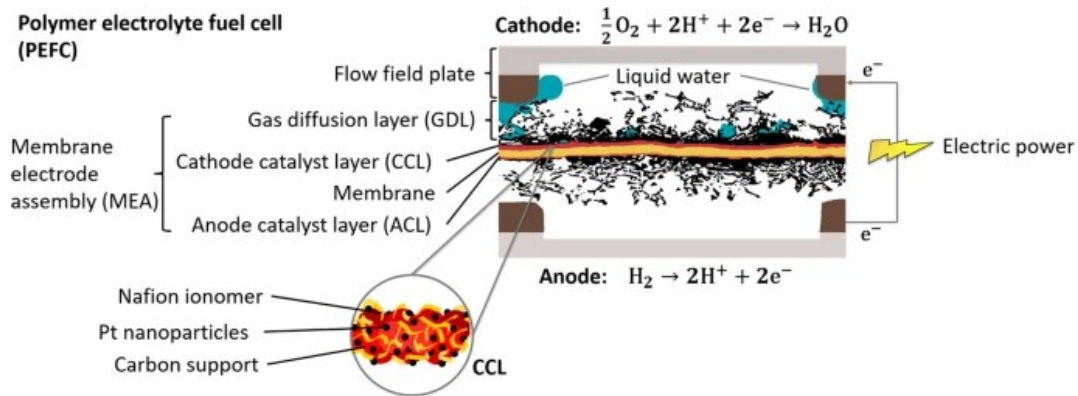


**Figure 1. Schematic representation of a PEMFC, showing the components of the MEA and the flow plates (Reproduced with permission from White *et al.* 2019).**

As shown in Figure 2, hydrogen and oxygen (or ambient air) are the only inputs required to support the operation of PEMFCs. The hydrogen gas is delivered, via the flow field, to the anode side of the fuel cell. Upon delivery, the hydrogen diffuses through the GDL and undergoes a hydrogen-oxidation reaction (HOR) at the anode CL, which produces protons and electrons (Mench 2008). The electrons generated by breaking down the hydrogen fuel pass from the anode to the cathode through an external electrical circuit, thereby generating electricity that can be used to do work (*e.g.*, power an electric motor; O’Hayre *et al.* 2016). The protons are conducted through the PEM to the cathode, where they react with the electrons and the oxygen (*i.e.*, which is delivered to cathode side of the cell) through an oxygen reduction reaction (ORR) to produce water and heat (Wang *et al.* 2011). The anode, cathode, and overall chemical reactions that take place in an operational PEMFC are displayed in Equations 1, 2, 3, respectively (Barbir 2006).

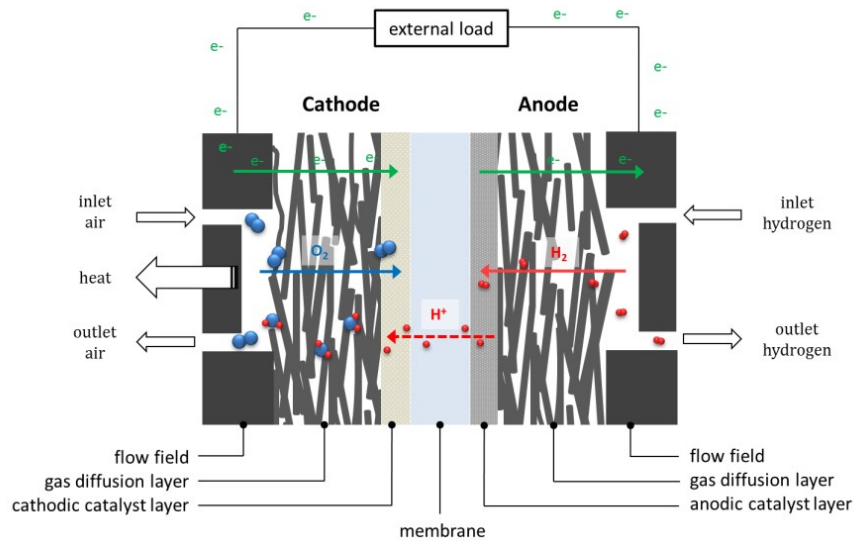
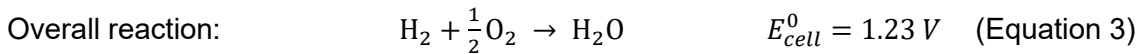
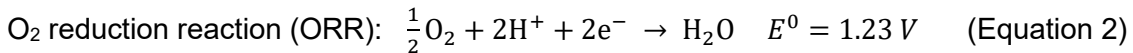


**Figure 2. Schematic diagram showing the functionality of a PEMFC (Reproduced with permission from Halter 2019).**



The outputs of these electrochemical reactions are electricity, heat, and water, which makes PEMFCs efficient and clean sources of electricity.

## 2.2. PEMFC Components

As indicated previously, PEMFCs are comprised of four main components. These include a polymer electrolyte membrane, catalyst layers, gas diffusion layers, and flow plates (Barbir 2006). Each of these components are briefly described in the following sections.

### 2.2.1. Polymer Electrolyte Membrane

The polymer electrolyte membrane plays a key role in the operation of PEMFCs. PEMs are very thin membranes (*i.e.*, typically on the order of 10  $\mu\text{m}$ ) that function to enable proton transport from the anode to the cathode, while simultaneously restricting

passage of electrons and gases through the membrane (O'Hayre *et al.* 2016). Typically, the membrane is composed of a polytetrafluoroethylene (PTFE) backbone with a sulfonic acid side chain, which promotes proton transport. Consequently, the membrane is composed of two very different sub-structures. The first sub-structure is the sulfonic acid side chain, which is hydrophilic and ionically conductive (O'Hayre *et al.* 2016). The second sub-structure is the PTFE group, which is hydrophobic and not ionically conductive (O'Hayre *et al.* 2016). The PTFE group is essential because it provides chemical stability and durability (Barbir 2006).

PEMs are usually hydrated during operation, which promotes the formation of  $\text{H}_3\text{O}^+$ - $\text{SO}_3^-$  groups to enable proton movement through the membrane (Mench 2008). The motion of protons in this state is dominated by Grotthuss mechanism (which is also known as proton jumping), which allows for the transport of protons along a connected pathway within the ionomer structure (Klose 2020). Hydration is important because the perfluorinated ionomer is almost completely non-conductive under dry conditions. When dehydrated, the sulfonic acid cluster becomes isolated and the protons are transported instead by physical means, which is referred to as the vehicular mechanism (Mench 2008). This transport mechanism tends to be inefficient; hence, PEMFC efficiency tends to be substantially reduced under dry conditions. For this reason, humidified reactant gases are commonly delivered to improve membrane hydration.

### **2.2.2. Catalyst Layers**

The catalyst layers are located on both sides of the PEM and facilitate the HOR and ORR reactions (Wang *et al.* 2020). The catalyst layers of PEMFCs are typically composed of high-surface-area carbon particles, usually with nanometer-sized particles of platinum dispersed on it (Mench 2008). This structural design supports high platinum dispersion onto the carbon particles, while providing high electrical conductivity of electrons. Functionally, the carbon provides structural integrity and conducts the electrons towards the flow plates, the platinum catalyzes the HOR and ORR reactions, and the pores in the carbon matrix facilitate gas and water transport. Surrounding the catalyst particles are perfluorosulfonic acid (PFSA) ionomers, which function to conduct protons to the catalyst layer active sites (Barbir 2006; Figure 3). Typically, catalyst layers have a thickness in the range of 5 – 30  $\mu\text{m}$  and can often be coated on either side of the PEM to form a catalyst-coated membrane (CCM; O'Hayre *et al.* 2016). The

cathode catalyst loadings range from around 0.1 – 0.5 mg Pt/cm<sup>2</sup>, with the anode platinum loadings often being much lower because the HOR tends to be much faster than the ORR (O’Hayre *et al.* 2016). Due to the costs of platinum in the production of these catalyst layers, significant research is currently focused on developing FCs with reduced cathode platinum loadings and testing alternative catalysts for use in PEMFCs (Mench 2008; Müller-Hülstede *et al.* 2022a; 2022b).

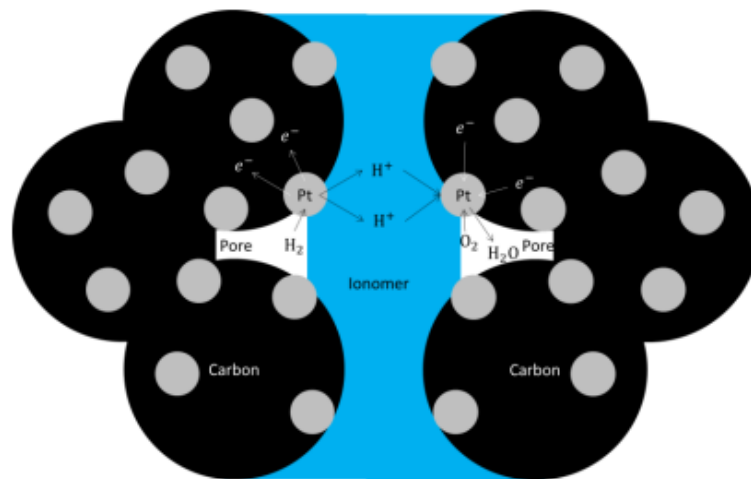


**Figure 3.** Schematic representation of a catalyst layer of a PEMFC, as located between the microporous layer (MPL) and the Nafion membrane, showing the platinum (Pt) particles supported on a carbon structural element (Reproduced with permission from Chen 2020).

### 2.2.3. Gas Diffusion Layers

The GDLs are sandwiched between the CL and the flow field on both sides of a PEMFC (*i.e.*, the anode and the cathode). The GDLs are key FC components that facilitate the delivery of reactant gases to the catalyst layers and the removal of water from the cell, while being electrically and thermally conductive (Barbir 2006). The GDLs also provide structural stability for the electrochemically active components of the MEA (Mench 2008; Figure 4). Typically, GDLs are comprised of a sheet of carbon fibre that is partially coated with polytetrafluoroethylene (PTFE), which acts as a hydrophobic treatment to prevent water accumulation (O’Hayre *et al.* 2016). The porosity of GDLs is typically quite high when uncompressed and ranges between 70-90%; pore sizes typically range between 10 and 80  $\mu\text{m}$  (Peinador *et al.* 2022). Many GDLs feature an

additional highly hydrophobic and electrically-conductive microporous layer (MPL) at the interface between the catalyst layer and GDL. This layer is coated with PTFE and gives the GDL much smaller pore sizes closer to the catalyst layer, which helps in water management and improves electrical conduction through reduced contact resistance between the catalyst layer and GDL (Barbir 2006; Mench 2008).

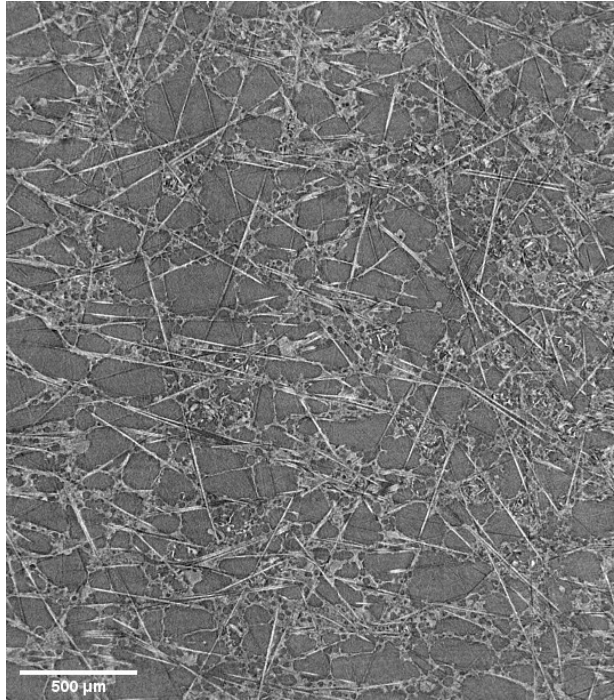


**Figure 4.** XCT slice of a GDL (*i.e.*, Avcarb); the carbon fibers are shown in light grey.

#### **2.2.4. Flow Field Plates**

The flow field plates are positioned on both the anode and the cathode side of a PEMFC and are commonly made of metal, carbon, or various composite materials. The surface of the FPs contains flow fields to allow for the transport of hydrogen gas on the anode side of the FC and oxygen gas (or air) on the cathode side of the FC (Barbir 2006). The FPs also act to connect the external electrical circuit to the MEA and to transport water out of the cell (Mench 2008). In addition, the flow plates function as thermal conductors, which is important for dissipating the heat produced during FC operation. Figure 5 provides examples of the designs that are commonly used in PEMFCs (Iranzo *et al.* 2010; Marappan *et al.* 2020).

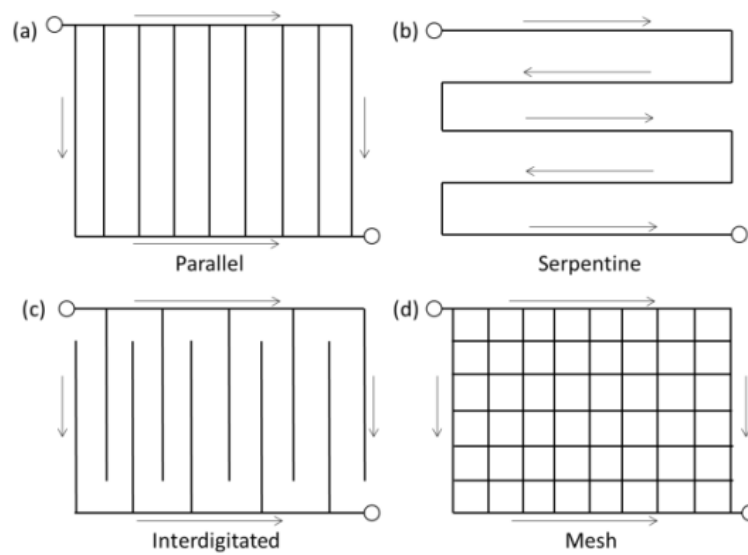


**Figure 5. Example designs of flow fields commonly used in PEMFCs (Reproduced with permission from Chen 2020).**

### 2.3. Thermodynamics of PEMFCs

Thermodynamics is the study of the relationships between work, heat, and other forms of energy. PEMFCs convert the chemical energy of hydrogen gas into electrical energy through a series of electrochemical reactions. Thermodynamic analysis of these reactions is important for assessing FC performance and providing information relevant to their optimization (Miansari *et al.* 2009).

The theoretical thermal potential of a PEM fuel cell  $E_{th}$  is 1.48 V. This can be calculated using the enthalpy of the reactants and products (equation below). In equation 4,  $\Delta H$  is the change in enthalpy (kJ/mol),  $F$  is the Faradays constant (C/mol), and  $n$  is the number of electrons transferred (Mench 2008).

$$E_{th} = -\frac{\Delta H}{nF} \quad (\text{Equation 4})$$

Fuel cells are energy conversion devices; therefore, the laws of thermodynamics are key to understanding the conversion of chemical energy into electrical energy. Under thermodynamically-reversible conditions, the theoretical maximum cell potential that can be achieved is a function of the Gibbs free energy ( $\Delta G$ , O'Hayre *et al.* 2016). Assuming that all of the Gibbs free energy can be converted to electrical energy, the

maximum theoretical efficiency of a fuel cell can be calculated as the ratio between the Gibbs free energy and the hydrogen higher heating value enthalpy of reaction ( $\Delta H$ ; Barbir 2006). More specifically, the reversible cell potential for the overall fuel cell reaction can be calculated to be 1.23 V using equation 5 below (Mench 2008):

$$E^o = -\frac{\Delta G}{nF} \quad (\text{Equation 5})$$

Using this equation, the theoretical maximum potential that can be generated under specific conditions can be determined. For example,  $E^o$  at 25°C and standard atmospheric pressure to be 1.23 V. As both  $\Delta G$  (237.34 J/mol) and  $\Delta H$  (286.02 J/mol) are known, the theoretical maximum efficiency of a PEMFC can be calculated to be 83% using equation 6 (O'Hayre *et.al.* 2016):

$$\epsilon_{thermo} = \frac{\Delta G}{\Delta H} \quad (\text{Equation 6})$$

While this simplified calculation is useful for estimating fuel cell efficiency, it is important to note that reversible voltage is a function of the temperature and pressure of the reactants and products (Mench 2008). The Nernst equation (Equation 7) provides a basis for calculating the maximum possible open-circuit voltage of a fuel cell (*i.e.*, at zero cell current):

$$E(T, P) = E^o - \frac{RT}{nF} \ln \frac{\prod a_{products}^{v_i}}{\prod a_{reactants}^{v_i}} \quad (\text{Equation 7})$$

Where:

T is temperature (K);

P is pressure (atm);

$E^o$  is reversible cell potential (V);

n is the number of electrons transferred;

F is Faraday's constant (96,485 C/mol);

R is the universal gas constant (8.314 J/mol\*K);

$a_{products}$  is the thermodynamic activity coefficient of the products;

$a_{reactants}$  is the thermodynamic activity coefficient of the reactants.

$v_i$  is the stoichiometric factor of the products or reactants;

It is important to note that the actual potential of a fuel cell is always lower than the theoretical maximum voltage due to irreversible losses that occur due to the kinetics of the electrochemical reactions, internal electrical and ionic resistance, reactant mass transport limitations, and other factors (Barbir 2006). The various sources of voltage losses are discussed in the following section of this document.

## 2.4. Voltage Losses

As discussed previously, the theoretical maximum voltage that can be generated by a fuel cell is 1.23 V (Barbir 2006). However, during operation, fuel cells suffer from irreversible potential losses known as overpotential or polarization. These losses can be divided into four major categories, including, open circuit voltage losses ( $n_{OCV}$ ), activation losses ( $n_{act}$ ), ohmic losses ( $n_{ohmic}$ ), and mass transport losses ( $n_{mass}$ ) (Mench 2008). Cell voltage losses can be calculated using Equation 8 below:

$$E = E^o - n_{OCV} - n_{act} - n_{ohmic} - n_{mass} \quad (\text{Equation 8})$$

The relationship between the current density and the voltage generated by a PEMFC can be illustrated in a polarization curve. Figure 6 shows an example polarization curve displaying each of the loss regions.

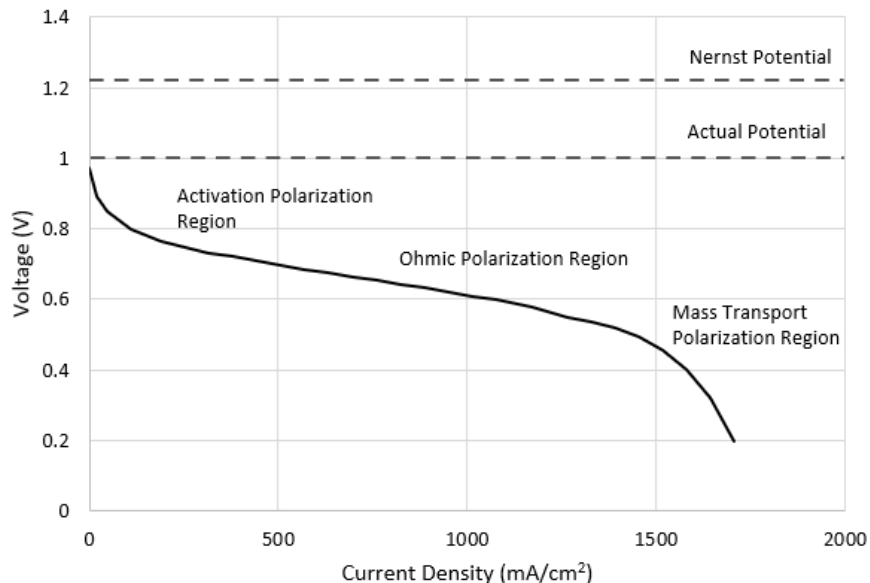


**Figure 6. Example polarization curve for a PEMFC, showing the three regions of potential voltage losses (Adapted from Agaesse 2016).**

The polarization curve can be divided into four major loss regions, including mixed potential, activation, ohmic, and mass transport. The measured open circuit voltage (OCV) of a PEMFC usually ranges between 0.9 V and 1 V, which deviates from the expected value of 1.23 V calculated using the Nernst equation. This departure is mainly due to reactant crossover through the membrane electrolyte and subsequent mixed-potential reactions (Mench 2008). Activation polarization or activation overpotential typically dominates at low current densities, with voltage losses largely associated with reductions in the rate of the ORR. The voltage losses in this region are associated with overcoming the activation energy of the electrochemical reactions on the platinum surfaces within the CL (Mench 2008). This loss region depends on a complex three-phase interface where influent gas, catalyst surface and ionomer must all make contact. Thus, activation polarization losses are influenced by a number of factors including, but not limited to, reaction mechanisms, catalyst layer efficiency, operating parameters, impurities and reactant species concentration (Mench 2008). The ohmic region losses result from the electrical and ionic resistances of individual components within the fuel cell. For example, components such as the PEM, GDL, and flow plates can reduce the conduction of electrons and protons by adding resistances to the system (Mench 2008). Due to the sensitivity of the proton exchange membrane to humidity, this region can often contribute significant ohmic losses. Therefore, it is important to

properly humidify the membrane during operation. The final loss region is the mass transport region. The voltage losses in this region typically occur at higher current densities and are dominated by the limitations on the reactant gases ability to reach the catalyst layer (Mench 2008). This phenomenon typically takes place on the cathode side of the cell (*i.e.*, where water production occurs) due, in part, to the lower diffusion coefficient of oxygen gas (as compared to hydrogen gas). The presence of liquid water can also block the pathways for gases to pass through to the CL. Hence, accumulation of liquid water can result in significant performance losses in PEMFCs.

The approximate efficiency of a fuel cell that is operational and producing electrical power can be calculated. This can be done by dividing the operating voltage by the thermodynamic voltage (Equation 9; Harrison *et al.* 2010).

$$\text{Voltage efficiency} = \frac{\text{Operating voltage}}{\text{Thermodynamic voltage}} \quad (\text{Equation 9})$$

## 2.5. Current and Potential Applications of PEMFCs

The uses of PEMFCs fall into three main categories, including portable applications, stationary applications, and transportation applications (Wang *et al.* 2020). Each of these applications have unique requirements that dictate the design and operations of FC systems. For example, FCs for portable applications typically need to deliver power outputs of <0.1 kW (Mench 2008). By comparison, FCs for stationary power and transportation applications need to produce up to 50-250 kW and on the order of 100 kW of power, respectively (Mench 2008; Wang *et al.* 2020). Such power requirements dictate the type of FC required, the type of fuel used, the size of the system (*i.e.*, stack size), and the performance specifications. Meeting such unique requirements for performance, durability, and costs will be essential for support the widespread commercialization of FC technology across the various sectors of the economy.

### **2.5.1. Portable Applications of PEMFCs**

The energy demand for portable electronic devices (PEDs), such as laptops, tablets, cell phones and military devices, has grown rapidly in recent years. Various types of batteries have been developed to store and deliver power for PEDs; however, in some cases, battery technology may not be able to deliver the energy densities needed for long term operation of these devices (Wang *et al.* 2020). Accordingly, micro-PEMFCs are starting to play a larger role in this market sector, accounting for about two-thirds of the portable FC market in 2009 (Wang *et al.* (2011). More recently, Wang *et al.* (2020) reported that total portable FC shipments had quadrupled between 2008 and 2014 (*i.e.*, from 5,000 units to more than 21,000 units). Wang *et al.* (2020) also indicated that the commercialization of FCs for military applications has continued to expand in recent years. In particular, the demand is growing for FCs that deliver 30 – 165 W of continuous power for portable power for military applications (Wang *et al.* 2020). Hence, there appears to be an ongoing role for PEMFCs in the PED and military applications markets. Nevertheless, it is unlikely that PEMFCs will play more than a niche role as power sources for portable devices.

### **2.5.2. Stationary Applications of PEMFCs**

Currently, most of the world's electrical power is largely supplied by large, centralized power stations that operate on various fossil fuels (*e.g.*, natural gas, coal, and/or diesel fuel). While such facilities have a number of advantages (*e.g.*, efficiency, low cost, etc.), they have certain disadvantages that increase the attractiveness of alternative energy sources for stationary power applications. While emissions of GHGs represents the single largest disadvantage of these systems, other factors (*e.g.*, losses of power during transmission, inability to fully utilize waste heat, etc.) need to be considered in power acquisition decisions. One way to address these disadvantages is through transitioning to decentralized power distribution systems (Wang *et al.* 2020). To address this need, combined heating and power (CHP) solutions are being developed using FC technology. For example, Wang *et al.* (2011) reported that fuel cells can be used for residential power supplies, with PEMFCs particularly useful for meeting peak power demands in this application (*i.e.*, the demand for power in the early morning and evening periods of the day). By being located closer to the end users of the power, it may be possible to reduce transmission losses for PEMFC-based stationary power

supplies. In addition, the waste heat generated from fuel cells can be used for household heating applications (Wang *et al.* 2011). Furthermore, electrical energy generated from PEMFCs has the potential to act as back-up power for banks and telecommunication companies, as power interruptions have significant costs associated with them. However, some work remains to be done to meet the U.S. Department of Energy durability target of 60,000 hours (*i.e.*, operating lifetimes were in the 12,000 – 70,000-hour range in 2015; Wang *et al.* 2020). In addition, the capital costs of these systems still need to be brought down to meet the U.S. Department of Energy target of US \$1,500/kW (*i.e.*, equipment costs were typically in the US \$2,300 - \$2,800/kW in 2015; Wang *et al.* 2020).

The use of PEMFCs in stationary applications has expanded rapidly in recent years. For example, Ballard Power Systems recently announced that construction of the Renewable Power Plant commenced in French Guiana in 2021. This power plant is considered to be the world's first multi-megawatt hydrogen power plant. The project will include a solar park, short-term battery storage, long-term hydrogen storage, and two 1.5 MW PEMFC systems. The power plant will provide 100% renewable power to the equivalent of 10,000 households at a lower cost than a diesel power plant, without emitting any greenhouse gases, fine particulates, noise, or fumes during operation (Ballard 2021). This type of project, which integrates clean energy sources with hydrogen fuel cell technology, has the potential to replace diesel power plants in many locations that can generate renewable energy (*i.e.*, the system can deliver power when it is needed by users by utilizing hydrogen as a means of storing the renewable energy until it is required).

### **2.5.3. Transportation Applications of PEMFCs**

While PEMFCs can be used in portable and stationary applications, the transportation industry may represent a principal use of this technology (*i.e.*, use in fuel cell vehicles; FCVs). Importantly, the high-power densities of these FCs make them attractive alternatives to internal combustion engines for cars and light trucks (Whiston *et al.* 2019; Wang *et al.* 2020). To date, Ford, Honda, Nissan, Toyota, Hyundai, Volkswagen, and Kia have all developed light-duty vehicles that operate using fuel cell technology (Wang *et al.* 2020). The FC systems that power these FCVs typically generate maximum power output within the 57 to 114 kW range (Wang *et al.* 2020). The

FC system in the 2017 Toyota Mirai, for example, generates a power density of 3.1 kW/L (Wang *et al.* 2020). Importantly, these vehicles can now achieve effective ranges of 400 to 685 km (Wang *et al.* 2020). Although there are currently only about 5,000 FCVs in the United States, Japan is expected to have 800,000 FCVs by 2030 (Wang *et al.* 2020).

To guide the further development of PEMFCs for transportation applications, the U.S. Department of Energy (USDOE 2020b) developed the technical targets for hydrogen-based FC systems. For example, long-term targets for durability, cost, and power density for passenger cars have been set at 8,000 hours, \$30/kW, and 850 W/L, respectively (USDOE 2020b). By comparison, USDOE (2020a) reported that, as of 2020, the targets for durability, power density, peak energy efficiency, and costs are still outstanding issues that need to be resolved by the light-duty FCV industry, with durability and cost likely to be the primary focus areas for further development of FCs for this application. Fuel cells developed for heavy-duty applications in the transportation sector will also need to meet or exceed the corresponding durability, cost and power density targets (USDOE 2020b).

One of the challenges associated with commercialization of light-duty fuel cell vehicles is associated with refueling. Various countries are responding to this challenge by constructing and operating hydrogen filling stations. For example, there are currently only seven publicly-accessible hydrogen filling stations in Canada, with four of these located in the lower mainland region of British Columbia, one on Vancouver Island, one in the vicinity of Toronto, and one in Quebec City (HTEC 2023). By comparison, the United States had a total of 89 hydrogen fueling stations in 2022, with most (*i.e.*, 70) of these located in California (H2 Energy News 2023). China, Japan, South Korea and Germany continue to be the world leaders in the development of FCV refueling infrastructure, with 250, 161, 141, and 93 stations currently in operation, respectively (FuelCellsWorks 2020; Wang *et al.* 2020; Statista 2022). Hence, there is a need to further develop hydrogen refueling infrastructure, if the goal is to promote the sales of FCVs in Canada and abroad.

Commercialization of FC technology is progressing more quickly for fleets of vehicles that are used on-site or return to a fixed location each day. More specifically, buses, forklifts, delivery trucks, and light rail systems represent ideal applications for FC technology. For example, Ballard Power Systems has partnered with five companies

worldwide to provide fuel cell stacks, modules, and systems (e.g., the FCveloCity motive module) to power municipal transit and other buses, including Canada's own New Flyer Industries. According to Ballard (2020), these zero-emission systems typically deliver on the order of 70 - 150 kW of power, have effective ranges of about 450 km, can provide over 30,000 hours of service, and refuel in about 10 minutes. Daimler-Chrysler introduced its first fuel cell buses in 1997; since then, the company has continued to refine the technology and produce buses for fleets across the globe (Wang *et al.* 2011). Use of fuel cell buses for public transport is now supported by several government-funded programs, including the US National Fuel Cell Bus Program and Europe's Fuel Cell and Hydrogen Joint Technology Initiative (Wang *et al.* 2020). By far, China is the world leader in the development of FC bus fleets, with more than 4,700 vehicles currently in service (Mao *et al.* 2023).

Progress is also being made on the development of FC systems that can be used in other transportation applications. For example, Ballard Power Systems (Ballard 2020) recently began marketing PEMFC-based power systems to the heavy trucking, shipping, and rail industries. Fuel cell technology is also being tested in the aviation industry (Wang *et al.* 2020). These developments demonstrate that fuel cell technology is beginning to enter the mainstream of the transportation sector. Nevertheless, there are a number of substantial obstacles that need to be addressed before FC technology can gain broad acceptance, with many of these challenges limiting the broader commercialization of FC systems for cars and light trucks.

## **2.6. Advantages and Limitations of PEMFCs**

Various authors have suggested that PEM fuel cell technology represents a sustainable solution to the ongoing need of the transportation sector for reliable energy sources (Mench 2008; Wang *et al.* 2011; Wang *et al.* 2020). Hence, transitioning towards the use of FCs is likely to help reduce emissions of GHGs since transportation-related activities account for the largest share of the fossil fuels that are currently being consumed in the United States (USEPA 2020). Some of the advantages of PEMFCs, relative to other technologies, are that they provide continuous power supplies with high energy density and high operating efficiencies (O'Hayre *et al.* 2016). In addition, PEMFC systems are compact, easy and safe to handle, have fast start-up times, and have low maintenance requirements (Mench 2008). Furthermore, hydrogen-powered

vehicles have relatively long ranges and can be rapidly refueled (*i.e.*, minutes vs. hours for EVs), which can reduce range anxiety. Most importantly, they provide zero emission power sources that are useful in a variety of transportation-based applications.

In addition to their many advantages, there are also a number of disadvantages of PEMFCs that are limiting their widespread commercialization. More explicitly, PEMFC systems are expensive to manufacture due to the cost of their component parts, such as Nafion™ and platinum (Mench 2008; O'Hayre *et al.* 2016). In addition, PEMFCs can be adversely affected by faulty conditions (*e.g.*, flooding, dehydration, starvation, and poisoning) that influence their durability and performance (Sorrentino *et al.* 2020). Furthermore, the lack of infrastructure and the cost of pure hydrogen fuel currently make the widespread use of PEMFCs impractical (Wang *et al.* 2020). Overcoming these challenges requires a detailed understanding of the underlying problems and development of solutions that effectively address them.

## **2.7. Factors Affecting the Performance and Durability of PEMFCs**

There are a number of factors that can influence the durability and performance of PEMFCs. These factors can be classified into two categories, including reversible degradation processes and irreversible degradation processes. Reversible degradation of PEMFCs can be corrected without causing adverse effects on the long-term performance or durability of PEMFCs. Examples of reversible degradation processes include diffusion media chemical intrusion (*i.e.*, contamination of media by airborne impurities), flooding/desiccation, reactant starvation, voltage reversal, and contaminant influx (Singh *et al.* 2022; Schmittinger and Vahidi 2008). In contrast, irreversible degradation processes can cause failure of PEMFCs during longer-term operation. These processes can include diffusion media plastic deformation, catalyst layer cracking/delamination, electrolyte loss, platinum dissolution/migration, and ionic impurity contamination (Singh *et al.* 2022; Schmittinger and Vahidi 2008). Some of the faulty conditions, degradation mechanisms, and associated effects on PEMFCs are briefly discussed below. This information is provided to support the identification of the improvements that are needed for more broadly commercializing this technology and of the research activities needed to support such advancements.

Condensation and accumulation of liquid water at the cathode side of the FC, a process known as flooding, can alter both the performance and durability of PEMFCs. Flooding commonly occurs in the cathode due to the constant production of water in the oxygen reduction reaction (Shen *et al.* 2020). Flooding is important because the accumulation of liquid water impedes the flow of oxidant to and within the cathode and can restrict fuel flow if it occurs in the anode (Sorrentino *et al.* 2020). In both cases, water accumulation reduces the electrochemical surface area (ECSA) of the electrodes and decreases PEMFC performance (*e.g.*, as measured by voltage output; Shen *et al.* 2020). In addition to affecting the hydrogen oxidation reaction, long-term operation of PEMFCs under flooded conditions can result in dissolution of platinum in the catalyst layer and corrosion of the carbon surfaces in the FC, which further impairs FC performance by increasing electrical resistance and/or decreasing the mechanical strength of the catalyst layer (Sorrentino *et al.* 2020).

Dehydration is also an issue that can influence the performance of PEMFCs. More specifically, desiccation of the MEA leads to low proton conductivity in the Nafion™ (Sorrentino *et al.* 2020). Membrane thinning, mechanical strength reduction, and/or perforation are commonly associated with prolonged dehydration, all of which tend to increase ohmic resistance in the membrane and in the catalyst layers (Sorrentino *et al.* 2020). In addition, membrane failure can lead to increased gas crossover and associated loss in performance (Zhao *et al.* 2020).

Reactant starvation is typically caused by factors operating outside the PEMFC, often involving malfunction of the fuel and/or oxidant delivery system (Shen *et al.* 2020). Such changes in the delivery of gases to the FC can decrease the rate of the hydrogen reduction reaction, increase the rate of platinum dissolution, and/or enhance corrosion of the carbon-bases fixtures (Sorrentino *et al.* 2020). In turn, these degradation mechanisms can lead to reductions in the ECSA, increases in electronic resistance, and/or lowering of the mechanical strength of the catalyst layer (Sorrentino *et al.* 2020). All of these problems lead to reduced performance and compromised durability (Shen *et al.* 2020).

Introduction of impurities into the FC system is commonly referred to as poisoning. Impurities, such as carbon monoxide (CO) or hydrogen sulphide (*i.e.*, if natural gas is used as a fuel source), tend to adsorb onto sites in the catalyst layer

and/or accumulate in the Nafion™ membrane (Shabani *et al.* 2019). These degradation mechanisms can lead to reductions in proton conductivity and decreases in the ECSA (Sorrentino *et al.* 2020). Although long-term exposure to CO does not affect the durability of the FC, performance losses are commonly observed in association with this type of poisoning (Shabani *et al.* 2019). However, long-term exposure to ammonia, H<sub>2</sub>S, metals, or salts can permanently decrease the hydrophobicity of the GDL, which can lead to increased water retention times and decreased mass transport of oxygen (Sorrentino *et al.* 2020). These alterations can impair FC performance and durability.

## **2.8. Water Management in PEMFCs**

Effective water management is essential for optimizing the performance of PEMFCs under a variety of conditions (Wang *et al.* 2020). This section provides an overview of the recent literature on water management in PEMFCs. Accordingly, the factors that result in water production in PEMFCs are identified. Similarly, the mechanisms that transport water within and from PEMFCs are described. In addition, the impacts associated with suboptimal water management in the PEMFCs are discussed, along with the methods for identifying water-related reductions in PEMFC efficiency. Finally, the measures that have been used to address water management issues are identified and evaluated. As such, this literature review is intended to provide the background information needed to support the design of a research program for evaluating the influence of operating conditions on PEMFC performance, as influenced by the accumulation and distribution of liquid water.

### **2.8.1. Water Production**

In PEMFCs, water is primarily produced as a result of the oxygen-reduction reaction that occurs in the cathode region (*i.e.*, as described in Equation 2). Production of liquid water can influence the performance of a PEMFC when the rate of water production exceeds the rate of water removal (O'Rourke *et al.* 2009). Such accumulation of water within the cell becomes problematic when the pores within the GDL become filled, resulting in restriction of the transport of reactants to the CL and to the active sites of the catalyst (Ijaodola *et al.* 2019). In addition, liquid water can accumulate within the flow field channels, thereby impeding the flow of reactant gases

(Asif *et al.* 2019). Once excess water starts to accumulate in the cathode region, water can move by diffusion to the anode region of the fuel cell (Irango and Boillat 2014). Hence, excess water production can result in flooding on both sides of the membrane, which can substantially impair fuel cell performance (Zhang *et al.* 2008; Chen *et al.* 2019).

While flooding represents an important problem that needs to be avoided, maintaining adequate quantities of water is also essential to maintain FC performance. Wolfgang and Ardalan (2008) reported that membrane dehydration can occur when water removal rates exceed water production rates. Such dehydration of the membrane can reduce ionic conductivity, which reduces reaction rates, decreases FC efficiency, and increases voltage losses (Ijaodola *et al.* 2019). Therefore, effective water management requires balancing of two operational objectives, including maintenance of adequate membrane hydration and prevention of flooding within the fuel cell (Hasson *et al.* 2009).

## **2.8.2. Membrane Water Transport Mechanisms**

Effectively managing the quantity and distribution of liquid water is critical for maintaining and enhancing the performance of PEMFCs. There are two main sources of water in a PEMFC, including delivery of humidified gases to enhance the proton conductivity of the membrane and production of water at the cathode as a result of the ORR. Development of effective water management strategies necessitates an understanding of the mechanisms through which water is transported in a PEMFC. This section briefly describes the major water transport mechanisms that operate in fuel cell membranes, including: i) electro-osmotic drag; ii) back diffusion; iii) thermo-osmotic drag; and, iv) hydraulic permeation (Figure 7).

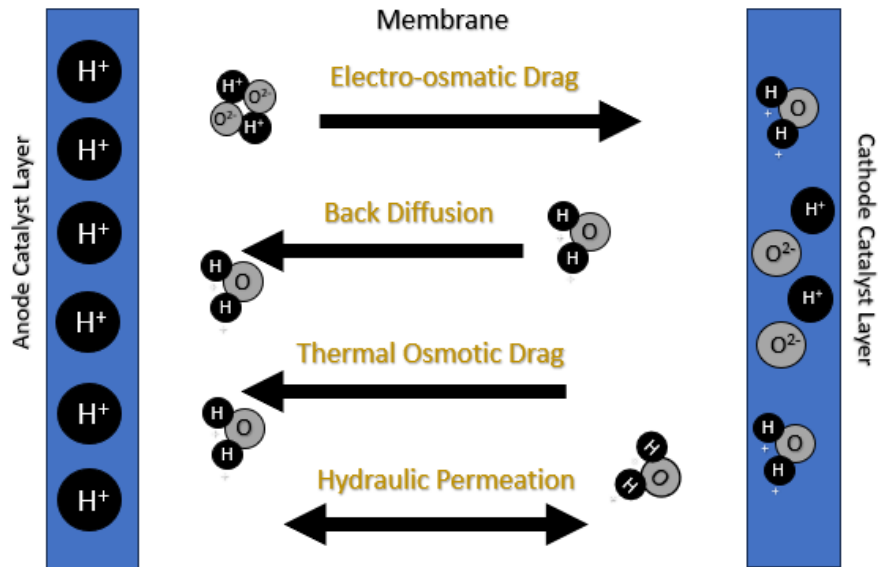


**Figure 7. Mechanisms of water transport in PEM fuel cell membranes (Adapted from Ijaodola *et al.* 2019).**

### 2.8.2.1. *Electro-Osmotic Drag*

Electro-osmotic drag (EOD) occurs as a result of the movement of protons through the membrane of the fuel cell. This transport mechanism exists because water is a polar molecule that has a high potential to become associated with the positively-charged protons that are produced at the anode CL. While various investigators have reported that water is dragged across the membrane by the protons (*e.g.*, Zhou *et al.* 2015; Zawadzinski *et al.* 1999; Berning 2011), more recent studies have concluded that the transport of liquid water in the PEM occurs primarily by diffusion (Berning 2020; *i.e.*, provided that the EOD coefficient is constant, where  $n_d$  is expressed as the number of moles of water that is associated with one mole of protons; Park and Canton 2008). Hence, EOD may not be a significant water transport mechanism inside the membrane. Nevertheless, EOD is likely an important mechanism for transporting water from the CL to the membrane in the anode region of the fuel cell and for transporting water from the membrane to the CL on the cathode region of the fuel cell (Berning 2020). Investigators have also reported that EOD coefficients are dependent on the water content of the Nafion membrane and temperature (Park and Canton 2008; Xu *et al.* 2017). Although this mechanism of water transport in fuel cells appears to be incompletely understood, it has been identified as one of the main water transport mechanisms in PEMFCs (Ijaodola *et al.* 2019).

#### **2.8.2.2. Back Diffusion**

Back diffusion is also an important water transport mechanism in PEMFCs. This transport process results in the movement of water molecules from the cathode electrode towards the anode region of the fuel cell (Ijaodola *et al.* 2019). Back diffusion occurs when excess water accumulates within the cathode region of the fuel cell. This condition enables liquid water to diffuse back towards the anode region along concentration gradients within the cell (Springer *et al.* 1991; Kong *et al.* 2017). While concentration gradients appear to be an important factor controlling back diffusion, membrane thickness and pressure gradients through the membrane were also identified as contributing factors (Zhao *et al.* 2011).

#### **2.8.2.3. Thermo-Osmotic Drag**

Thermo-osmotic drag is a water transport mechanism that occurs as a result of temperature differences across the membrane in PEMFCs (Ijaodola *et al.* 2019). Although this process has not been well characterized in fuel cells, there is evidence that water tends to flow from the cold regions of the cell towards warmer regions (Cespedes *et al.* 2016). As the ORR is exothermic, fuel cell operation can result in a temperature gradient within the cell. When the cathode region becomes warmer than the anode region, thermo-osmotic drag can enhance the movement of water through the anode region and across the membrane (Cespedes *et al.* 2016). It is possible that this process also occurs within the cathode region, as cooler conditions typically exist within the flow channels. Zaffou *et al.* (2006) reported that this transport mechanism is likely to be most important during the start-up and shut-down phases of fuel cell operation. However, it may also be important during operation of the fuel cell at high current densities, when the ORR increases the temperature of the cathode region of the fuel cell. This transport mechanism could lead to accumulation of liquid water within the cathode region, potentially leading to flooding if excess water is not efficiently removed from the fuel cell.

#### **2.8.2.4. Hydraulic Permeation**

While it is likely less important than other water transport mechanisms, hydraulic permeation may be important under certain circumstances. Hydraulic permeation occurs due to the presence of a pressure gradient between the anode and cathode regions of a fuel cell (Ijaodola *et al.* 2019). By this process, water transport can occur due to capillary pressure differential or gas-phase pressure differential (Ijaodola *et al.*

2019). This process can potentially improve fuel cell performance when the hydrogen is delivered to the cell at a lower pressure than the oxygen, resulting in the net movement of water away from the cathode and towards the anode (Belkiri *et al.* 2015; Tamayol and Bahrami 2011). However, this mechanism yields positive benefits on fuel cell performance only if the membrane has the mechanical strength to withstand the pressure differential (Soler *et al.* 2003; Adachi *et al.* 2010).

### **2.8.3. Water Transport Within Fuel Cell Components**

PEMFCs can be operated over a broad range of conditions. These different operational conditions can have a significant impact on the state and behavior of the water that occurs within the fuel cell. In a fuel cell, water occurs primarily in the liquid, and/or vapor phases. However, it can occur as a solid under freeze start conditions or can be absorbed in the ionomer phase (Liu and Weber 2022). The transport mechanisms that take place within the components of the MEA depend on the phase of water that is present. In this section, the water transport mechanisms within the CL and GDL are explained.

Water transport within the CL can occur in vapor or liquid form (Dai *et al.* 2009; Mularczyk 2021). The state and movement of water are determined by the water vapor partial pressure. In the vapor phase, water transport is dominated by Knudsen diffusion (Dai *et al.* 2009). In contrast, if water condenses within the CL, it is instead transported through the pores by capillary pressure (Dai *et al.* 2009). The capillary pressure in the CL pores is determined by the pore size and the substrate wetting properties (Dai *et al.* 2009). Within the MPL, water transport occurs by both molecular diffusion and Knudsen diffusion (Lu *et al.* 2015).

Due to the porous and tortuous nature of the GDL structure, transport of water within this FC component is primarily dominated by diffusion and convection for the vapour phase and by capillary flow for the liquid phase. In this context, convection refers to the bulk movement of a fluid as a result of a mechanical force and diffusion refers to the transport of a fluid due to a concentration gradient. Jiao and Li (2011) stated that, in PEMFCs, convective forces are dominated by pressure within the flow channel, which is influenced by reactant flow rates. The concentration gradient that governs diffusive transport results from the consumption/production of reactant/products at the CL and is

responsible for reactant delivery and water removal. Capillary transport generally occurs due to the buildup of liquid water within the pores of the GDL close to the CL, which creates a pressure gradient between the CL and flow channels (Jiao and Li. 2011; Jiao *et al.* 2021). Hence, the water moves from the high saturation region towards the low saturation region due to the differences in capillary pressure.

#### **2.8.4. Effects of Desiccation and Flooding on Fuel Cell Performance**

Information from numerous investigations indicates that effective water management is required to optimize the performance of PEMFCs. For example, Ijaodola *et al.* (2019) reported that Nafion membranes (which are commonly used in fuel cell) must be fully hydrated to maximize proton conductivity through the membrane. Operation of the fuel cell without sufficient hydration of the membrane can result in voltage losses (Taner 2015). Similarly, the presence of excess water (a condition referred to as flooding) can substantially impair fuel cell performance. The presence of excess liquid water in the anode or cathode regions results in filling of the pore spaces within these structures, thereby hindering gas transport within the GDL and covering the active sites within the CL (Song *et al.* 2005). Accumulation of liquid water in the flow fields can also restrict the movement of gases, resulting in mass transport voltage losses (Ibrahim *et al.* 2020). The consequences of such flooding events include uneven distribution of current, decreased cell performance, unstable operation, and rapid cell degradation (Shimpalee and Vanzee 2007). The effects of suboptimal water management on fuel cell performance were briefly described in Section 2.7. The following sections provide further information on the effects of water imbalances in various components of PEMFCs due to the importance of effective water management on fuel cell performance.

##### **2.8.4.1. Effects of Water Imbalances in the Anode Region**

At the catalyst layer of the anode, hydrogen gas is dissociated to produce protons and electrons (*i.e.*, through the hydrogen oxidation reaction; Babir 2006). The electrons are transported to the cathode region through an external circuit, while the protons are transported through the membrane of a PEMFC. Insufficient hydration of the PEM reduces the permeability of the membrane to protons, with such increases in ionic resistance associated with drying of the PEM resulting in impaired performance of

the fuel cell (Ijaodola *et al.* 2019). For example, Omasta *et al.* (2017; 2018) reported that cell voltages were decreased by even minor dry-out of the membrane. While such negative effects on performance were modest (*i.e.*, about 10% reduction in voltage) at lower current densities (*i.e.*, 1000 mA/cm<sup>2</sup>), more substantial impacts (*i.e.*, 40 to 65% reduction in voltage) were observed at higher current densities (*i.e.*, 3000 - 3400 mA/cm<sup>2</sup>; Omasta *et al.* 2017; 2018). Ogungbemi *et al.* (2019) reported that such effects can be, at least, partially mitigated by operating the cell under more acidic conditions and at higher temperatures. However, humidification of gases prior to delivery to the fuel cell (*i.e.*, delivery of gases at or near 100% relative humidity; RH) represents the most effective means of ensuring optimal conductivity of the PEM (Omasta *et al.* 2017; Ibrahim *et al.* 2020; Wang *et al.* 2020; Yan *et al.* 2006a; 2006b).

While dehydration represents one of the potential water management issues in the anode region of PEMFCs, flooding can also occur. Various investigators have reported that liquid water can flow from the cathode region to the anode region of PEMFCs through back diffusion (*e.g.*, Passogullari and Wang 2004; Xing *et al.* 2016). When back diffusion results in flooding within the anode region, the accumulation of excess liquid water typically results in fluctuations and reductions in cell voltage (Lee and Bae 2012). Such effects on PEMFC performance are likely associated with reduced fuel delivery rates, decreases in the rate of the hydrogen oxidation reaction (*i.e.*, due to covering of the catalyst active sites in the CL), and blockage of the channels (which further impairs the flow rates of gases (Song *et al.* 2005; Lee and Bae 2012; Zhang *et al.* 2007; 2013; Ogungbemi *et al.* 2019). Interestingly, transport of water vapour from the cathode region to the anode region of the fuel cell does not appear to negatively affect performance (as evaluated using polarization curves, transient ohmic resistance, and cell voltage; Zhang *et al.* 2013). Overall, the results of these investigations demonstrate that liquid water flooding within the anode region can adversely affect fuel cell performance (Kim *et al.* 2014).

#### **2.8.4.2. Effects of Water Imbalances in the Cathode Region**

At the cathode region of a PEM fuel cell, oxygen is delivered via the flow channels, diffuses to the CCL, is reduced as a result of the ORR, and reacts with protons (that are transported through the membrane) and electrons to form water and produce heat (Babir 2006). While sufficient hydration is essential for proper functioning,

accumulation of excess water within the cathode region can negatively affect fuel cell performance. There are several mechanisms through which liquid water accumulation in the cathode region can impact the performance of PEMFCs. First, liquid water can cover the surface of the catalyst layer, thereby retarding the ORR rate (McCain *et al.* 2010). In addition, accumulation of liquid water within the open pores of the GDL can impair the delivery of oxygen to the CL, which can further reduce the delivery of oxidant and, thereby, reduce the rate of the ORR (Ibrahim *et al.* 2020). Furthermore, excess liquid water can block the flow channels of a PEMFC, which also reduces the delivery of oxygen to the GDL and CL (Ijaodola *et al.* 2019).

Flooding within the cathode region of PEMFCs is a serious issue that affects fuel cell performance and durability (Park *et al.* 2003). For example, Chin *et al.* (2019) reported that flooding hindered the transport of reactants from the flow channels to the CL, which adversely affected PEMFC performance. Importantly, Li *et al.* (2008) demonstrated that the extent of fuel cell performance impairment was dependent on the degree of flooding that occurred (Figure 8). Furthermore, operation of PEMFCs at high current densities was shown to increase the rate of liquid water formation and enhance the potential for flooding of the cathode region (Ibrahim *et al.* 2020). This is important because increasing current density is one of the strategies that has been identified for improving the utility of PEMFCs (Jiao and Li 2011). In addition to affecting PEMFC performance, flooding in the cathode region can cause long-term stability issues in the fuel cell. Notably, Wang *et al.* (2017) reporting that flooding of PEMFCs resulted in unstable operation and rapid cell degradation rates. Similarly, McCain *et al.* (2010) reported that flooding within the cathode region resulted in unstable voltages, unpredictable current, and impaired performance. Because the water that accumulates within the GDL may not be uniformly distributed, the delivery of reactants can be impaired in certain regions but not in others (Park *et al.* (2003). This situation can cause localized variations in current density, temperature, and water content within the GDL (Park *et al.* 2003).

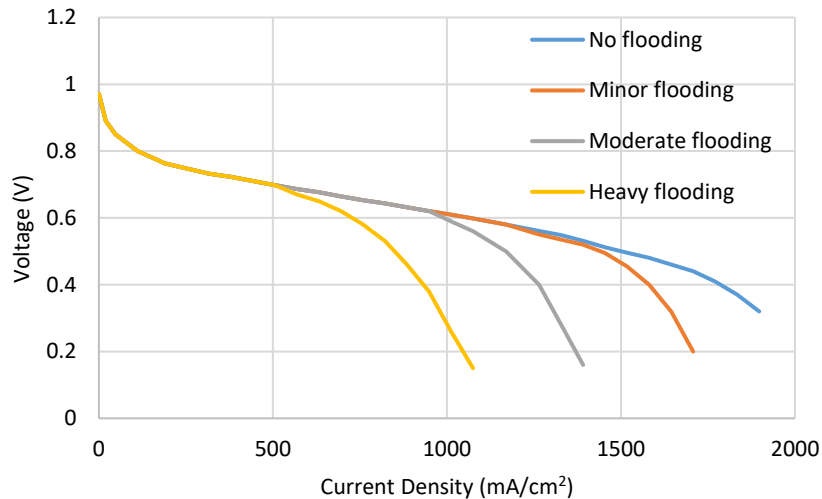


**Figure 8. Polarization curves showing the impacts of cathode flooding on the performance of PEMFCs (Adapted from Li *et al.* 2008).**

### 2.8.5. Strategies for Optimizing Fuel Cell Water Management

Water management is a crucial aspect of hydrogen fuel cell operation. Effective optimization strategies for water management in fuel cells are intended to maintain adequate hydration levels while avoiding flooding or drying out of the cell. Such optimization strategies can be classified into two main categories, including fuel cell design strategies; and, fuel cell operation strategies. Some of the key strategies that fall into each category are briefly described in this section.

Researchers have expended substantial effort in recent years to develop fuel cell components that help to improve water management in PEMFCs. Some of the strategies that have been evaluated include:

- **Improvement of the Design of Bipolar Plates:** The design of the bipolar plates can have a significant effect on water transport through the fuel cell, which in turn can reduce the potential for flooding. These plates can be engineered with channel designs and/or hydrophilic/hydrophobic coatings to facilitate the effective distribution and removal of water within the cell (Ijaodola *et al.* 2019; Ibrahim *et al.* 2020). Counterflow configurations can be employed in certain applications. In these configurations, the reactant gases flow in opposite directions. This setup enhances water management by promoting effective water transport and preventing excessive water accumulation (Qiao *et al.* 2020);

- Selection of Membrane Materials: The selection of the membrane material can affect water management. Proton exchange membranes (PEMs) with appropriate water uptake and transport properties can help maintain the necessary hydration levels without excessive water accumulation (Ogungbemi *et al.* 2019).
- Selection of Cathode Catalyst Materials that Enhance Water Transport: The choice of cathode catalyst materials can impact water management. More specifically, catalysts with appropriate hydrophobic/hydrophilic properties can aid in water removal from the cathode surface, which in turn minimizes flooding (Chi *et al.* 2018; Singh *et al.* 2022):
- Enhancement of the Hydrophobicity of the Gas Diffusion Layer: Modifying the hydrophobicity of the GDL can influence water distribution and water removal in PEMFCs. Optimizing the surface properties of the GDL can help control water transport, preventing flooding or drying. Enhancing hydrophobicity can be achieved through surface treatments, coatings, or selecting appropriate GDL materials (Chun *et al.* 2011; Omrani and Shabini 2017; Xu *et al.* 2022a; 2022b);
- Optimization of the Pore Size in the Gas Diffusion Layer: The pore structure of the GDL influences the transport of both water and gases. GDL materials that have small pore sizes tend to retain liquid water, while those with larger pores tend to facilitate gas diffusion and water removal (Xu *et al.* 2021; 2022a). Hence, water management can be improved by adjusting the pore size distribution by selecting appropriate GDL materials and ensuring that these materials are not over- or under-compressed (Li *et al.* 2021b; Xia *et al.* 2019; 2021);
- Development of Composite Gas Diffusion Layers: Developing composite GDL structures with different materials and properties can enhance water management. For example, combining hydrophobic and hydrophilic materials in specific regions of the GDL can create pathways for water removal while maintaining gas diffusion properties (Yang *et al.* 2017; Ijaodola *et al.* 2019);
- Modification of Microporous Layer Design: Improving the MPL's capability to transport water can aid in efficient water management. This can involve adjusting the thickness of the MPL, as thinner MPLs are likely to retain less liquid water. In addition, designing MPLs with optimized pore structures, including interconnected micropores that facilitate water movement from the catalyst layer to the GDL can enhance water transport. Furthermore, developing MPL materials with enhanced catalytic activity can improve the overall fuel cell performance and promote efficient

- water management. Finally, using hydrophobic MPL materials can minimize flooding and maintain effective gas diffusion pathways by repelling liquid water (Aoyama *et al.* 2018; Ijaodola *et al.* 2019; Okonkwo and Otor 2021); and/or,
- Application of Acoustic Vibration: Palan *et al.* (2006) employed vibro-acoustic methods to expedite the removal of water droplets from the flow field of PEMFCs. These authors reported that application of acoustic vibration to PEMFC stacks effectively removed water droplets of 2 mm radius using minimal energy (*i.e.*, 21 mW, at acoustic wave frequencies ranging from 20 to 120 Hz), thereby reducing water accumulation.

These improvements to the bipolar plates, GDL, and MPL are intended to optimize water distribution, prevent flooding or drying, and enhance the overall performance and durability of the hydrogen fuel cell. It is important to note that material selection, design considerations, and system-level integration are crucial aspects in implementing these improvements effectively.

Operational conditions play an important role in water management within PEMFCs. Hence, water management can be improved by employing various operational strategies, either singly or in combination. Some of the operational strategies that have been evaluated by fuel cell investigators include:

- Humidification of Influent Gases: Humidification is the process of adding moisture to the reactant gases before they enter the fuel cell (Ijaodola *et al.* 2019). This is crucial because the proton exchange membrane (PEM) in the fuel cell requires a certain level of hydration to function effectively (Jiao and Li 2011). Insufficient humidity can lead to membrane drying and reduced proton conductivity, affecting cell performance. Ozen *et al.* (2016) reported that humidification of both influent gases (hydrogen and oxygen/air) resulted in the substantial improvements in PEMFC performance (*i.e.*, relative to delivery of gases with lower humidification);
- Increase Flow Rates of Influent Gas to the Cathode: Controlling the airflow to the cathode side of the fuel cell helps regulate the water content within the cell. Sufficient airflow ensures efficient oxygen reduction and helps prevent excessive accumulation of water in PEMFCs (Amirinejad *et al.* 2006; Wahdame *et al.* 2006; Yan *et al.* 2006a; Manso *et al.* 2012; Omasta *et al.* 2017; 2018; Ijaodola *et al.* 2019; Zhou *et al.* 2022);

- Variation in Operating Temperature: Increasing cell temperatures above ambient levels can have a significant effect on the performance of PEMFCs by enhancing membrane permeability and expediting water transport through the CL and GDL (Yan *et al.* 2006a; Santarelli *et al.* 2007; Ozen *et al.* 2016; Ijaodola *et al.* 2019; Kato *et al.* 2020; Lochner *et al.* 2020; Trinh *et al.* 2022); and,
- Operation at High Current Density: Operation of PEMFCs at high current density can impact water management. More specifically, increasing current density can increase water production rates and lead to flooding unless measures are taken to enhance water removal rates (Eller *et al.* 2017; Zhao *et al.* 2021).

In addition to operational adjustments, fuel cell performance can be enhanced by applying various system controls and the results of modeling activities. More specifically, advanced control strategies can be employed to optimize water management in real-time. By continuously monitoring and adjusting parameters such as gas flows, humidification levels, and operating conditions, water management in fuel cells can be effectively regulated (Rahimian *et al.* 2017; Yang *et al.* 2020). System-level optimization techniques (*i.e.*, based on modelling results) can help determine the ideal gas flow rates and configurations to achieve optimal water management, while considering other performance parameters (Li *et al.* 2022; Yang *et al.* 2020).

## 2.9. Methods for Visualizing Liquid Water in PEMFCs

There are a variety of methods that have been used by investigators to evaluate the distribution and volume of liquid water in PEMFCs. Some of the methods that have been commonly used to study water management in PEMFCs include direct visualization, neutron imaging, nuclear magnetic resonance imaging, and X-ray imaging. Although other methods have been used (*e.g.*, electrochemical impedance spectroscopy, infrared thermograph) to infer the presence of liquid water in fuel cell components, this review is focused on the techniques that provide direct evidence of water production, transport, and/or accumulation.

### 2.9.1. Direct Visualization

Direct visualization methods involve using cameras or other optical techniques to directly observe liquid water in fuel cell components in two dimensions. Application of this technique necessitates the use of optical devices (e.g., high-speed cameras, microscopes, etc.) to observe the formation and/or movement of liquid water in PEMFCs. Application of this method typically involves construction of key fuel cell components (i.e., bipolar plates) from transparent or translucent material (Yang *et al.* 2004). However, some researchers have incorporated dyes or other indicators that make water visible (Ijaodola *et al.* 2019). These direct visualization techniques have been used to evaluate the formation, growth, and movement of water drops (Yang *et al.* 2004), to compare water formation in the flow fields for fuel cells with hydrophobic or hydrophilic GDL materials (Ge and Chao-Yang 2007), to assess reaction rates and cell performance at varying oxygen levels (Weng *et al.* 2006), to visualize water formation and transport in fuel cells with various GDL materials (Spernjak *et al.* 2007), and to determine the effect of air flow rate on temperature distribution in the fuel cell and water formation in the flow field channels (Aslam *et al.* 2019). Water droplet formation and flooding events have also been studied using direct visualization techniques (Hussaini and Wang 2009; Daino *et al.* 2011; Ous and Arcoumanis 2009). However, this technique cannot be used to observe water within the MEA.

### 2.9.2. Neutron Imaging

Neutron imaging is a non-destructive technique that has been used to evaluate the distribution and abundance of liquid water in PEMFCs in three dimensions. Neutrons interact strongly with light elements (e.g., hydrogen, lithium), but are only weakly absorbed by many metals. These characteristics enable neutrons to penetrate thick layers of metals and provide high sensitivity to light elements (Kardjilov *et al.* 2018). Ous and Arcoumanis (2009) reported that neutron imaging was an effective diagnostic tool for evaluating water management in PEMFCs because it is minimally invasive, it can be used for *in-situ* applications, and it provides localized data on various FC components. This technique is useful for evaluating the presence of liquid water because hydrogen-containing molecules, like water, scatter neutrons in a consistent manner, creating a fingerprint that is readily identified (Ijaodola *et al.* 2019). Neutron imaging has been used to study water content under various operating conditions

(Hickner *et al.* 2006), visualize water distribution in an operating PEMFC (Trabold *et al.* 2006), observe the accumulation of liquid water in the cathode region of a PEMFC (Owejan *et al.* 2006), and to optimize operational parameters to enhance FC performance (Kim *et al.* 2006; Boillat *et al.* 2008). Hence, this technique can be useful for investigations into water distribution and abundance in operating PEMFCs (Ijaodola *et al.* 2019). However, some of the limitations of this technique include the need for a consistent radioactive source of neutrons and the resolution may be lower than that for other imaging methods.

### **2.9.3. Nuclear Magnetic Resonance Imaging**

Nuclear magnetic resonance imaging (NMRI) is a technique that enables researchers to visualize water in opaque structures in three dimensions (Ijaodola *et al.* 2019). This technique works by passing an electric current through coiled wires to create a temporary magnetic field in a sample. A transmitter then sends radio waves through the sample, while a receiver collects the radio waves that emerge from the sample. A computer then uses these radio signals to make digital images of the scanned area of the sample (Britton 2017). NMRI is useful in PEMFC research because it is a non-invasive technique that investigators can use to visualize water in opaque structures, making it possible to determine the formation, transport, distribution, and volume of water in PEMFCs (Oukali *et al.* 2019). This technique has been used to evaluate water transport inside the membrane of a PEMFC (Bedet *et al.* 2008), assess the distribution of water in FCs operated with parallel and counter-current gas flow (Feindel *et al.* 2006), and three-dimensional water distribution in operating PEMFCs (Dunbar and Masel 2007). Hence, NMRI can provide useful information for managing water in PEMFCs. However, this technique has certain challenges which limit its applicability for fuel cell imaging, including its incompatibility with carbon-based materials and its restricted spatial and temporal resolution (Bazylak 2009).

### **2.9.4. X-ray Computed Tomography**

X-ray computed tomography is a non-invasive imaging technique that provides investigators with a means of visualizing MEA components in three dimensions with high resolution (White *et al.* 2016). X-ray imaging is based on the premise that the X-rays that pass through a material are attenuated at a rate that scales with that substance's

density (White *et al.* 2016). Hence, X-rays are strongly attenuated by heavy elements (such as platinum), while lighter elements (*e.g.*, hydrogen, helium) tend to have low attenuation of X-rays. Differential attenuation of x-rays by substances with different densities makes it possible to develop x-ray images that enable researchers to identify FC structures and the substances (such as water) contained therein (White *et al.* 2016). By generating multiple images during FC operation and comparing the images to the dry state, it is possible to determine how water content and distribution changes over time. Various investigators have used this technique to evaluate the influence of current density on water accumulation (Manke *et al.* 2007), water transport mechanisms (Markotter *et al.* 2012 Xu *et al.* 2021; Kato *et al.* 2022), temperature effects on water formation and distribution (Su *et al.* 2006)) and other phenomena (Mukaide *et al.* 2008; Lee *et al.* 2008; Kuhn *et al.* 2011; Kim *et al.* 2013). More information on this imaging technique is provided in Section 3.

## 2.10. Critical Research Needs

Two strategies have been identified to mitigate the various degradation issues that influence the performance of PEMFCs, including improvement of the FC components (*i.e.*, by developing more stable/resistant materials and by optimization of FC design); and, development of diagnostic tools for identifying and correcting faulty conditions during operations (Sorrentino *et al.* 2020; Goshtasbi and Ersal 2020). Significant applied research is required to overcome the existing durability and cost barriers associated with PEMFC technologies. PEMFCs are complex systems that have a number of elements and phenomena that need to be better understood and further improved. Some of the research that needs to be conducted to advance the design and manufacturing of FC components include:

- Evaluation of design alternatives and identification of more cost-effective materials for the various components of the MEA, including the electrolyte membrane, CLs and GDLs (*e.g.*, replacements for platinum as a catalyst; Lee *et al.* 2015; White *et al.* 2017; Singh *et al.* 2019; Solis *et al.* 2019; Alavijeh *et al.* 2019; Wang *et al.* 2020; Qi *et al.* 2020).
- Evaluation of the performance of MEAs with low platinum loading and better degradation resistance (Song *et al.* 2016; Jaouen *et al.* 2018; Salam *et al.* 2020);

- Evaluation of options for cost reduction and better corrosion resistance for the bipolar plates and gas flow channels (Song *et al.* 2019; Sauermoser *et al.* 2020); and,
- Development of approaches for large-scale production of FC components and stacks (Fowler *et al.* 2019; Whiston *et al.* 2019).

A continuing challenge for PEMFCs is water management (Ji and Wei 2009; Yan *et al.* 2006a; 2006b). This is an area that has been the focus of a great deal of research in recent years; however, significant issues still exist. The membrane in a PEMFC functions to transport protons from the anode to the cathode. Humidification of reactant gases is typically used to properly hydrate the membrane and enhance proton conductivity (Litster 2007). Substantial volumes of water are produced at the cathode due to oxygen reduction reactions (Rosli *et al.* 2009). This water can flood the pores of the CL and GDL, which restricts the transport of oxygen gas to the catalyst (Mortazavi 2019). Hence, performance of the FC is drastically impaired when excess water accumulates on the cathode side of the FC. Some of the research needs for improving PEMFC water management include:

- Evaluation of flooding of the CL and GDL of PEMFCs at high current densities and at varying operating temperatures. Such research should seek to identify conditions (e.g., levels of membrane humidification, current densities, operating temperature, etc.) that reduce water production at the cathode and maximize FC performance (Gao *et al.* 2009; velan Venkatesan *et al.* 2015; Gutru *et al.* 2020);
- Determination of the distribution of liquid water within the MEA of PEMFCs as a function of the design, operation, and degradation of the fuel cell;
- Determination of the behaviour of liquid water within the GDL and microporous layer (which is located between the GDL and CL) of PEMFCs (Eller *et al.* 2017). More specifically, there is a need to further understand the structures of these layers in order to improve water management of PEMFCs (Wang *et al.* 2020);
- Identification of strategies to expedite water removal from operating PEMFCs, such as adding serpentine channels to the cathode and supplying air flow rates high enough to force water out of the system (Litster 2007; Kandlikar 2008; Ashrafi and Shams 2017; Bao *et al.* 2019); and,

- Development and testing of PEMFCs that use self-humidification to eliminate the need for humidifying influent gases (Mirfarsi *et al.* 2020).

## **2.11. Focus of Current Research Project**

The current project is intended to address certain research needs that have been identified by investigators in this field. More specifically, this study was undertaken to establish correlations between operating conditions, performance, and liquid water distribution in the cathode GDL of PEMFCs. This research is intended to improve the fundamental understanding of water management at the cathode and establish which factors control the liquid water presence and flooding phenomena. In this study, a 3D *in-operando* X-ray imaging approach was used to determine the distribution of liquid water in PEMFC components.

The following sections of this document describe the methods that were used to address these research needs (Chapter 3). In addition, the results of experimental trials conducted to address these research needs are presented, along with a discussion of their significance for addressing some of the existing limitations of PEMFCs (Chapter 4). An assessment of the uncertainties associated with the experimental methods and results is presented in Chapter 5. Finally, conclusions and recommendations for further investigations are presented in Chapter 6 of this document.

## Chapter 3. Experimental Methods

This work was undertaken to evaluate the effect of operating conditions on the distribution of liquid water in the cathode GDL of PEMFCs. This study was intended to provide the data and information needed to test the following hypotheses:

1. Operational conditions affect the performance of PEMFCs. More specifically, the performance of PEMFCs will be influenced by cell temperature, gas delivery rates, oxidant concentration, and/or the relative humidity of influent gases;
2. The formation, distribution, and accumulation of liquid water is a key factor influencing the performance of PEMFCs. Varying operating conditions and current density will influence liquid water distribution and accumulation in predictable ways; and,
3. The performance of PEMFCs can be optimized by identifying operating conditions and current densities that minimize the potential for flooding by minimizing the rate of liquid water formation, maximizing the rate of liquid water removal, and/or altering the form of water in the PEMFC (*i.e.*, transforming liquid water to water vapour).

This section describes the materials and methods that were employed to generate the data and information needed to test these three hypotheses. The fuel cells used in this research were comprised of an anode flow-field plate, a membrane electrode assembly, and a cathode flow-field plate (Figure 1). As described previously, the MEA typically consists of five main elements, including an anode GDL, an ACL, a PEM, a CCL, and a cathode GDL (Figure 1). In this study, a miniaturized PEMFC system was used to support all investigations. The PEMFC system consisted of a small-scale fixture (SSF), an MEA, and graphite plates. Each of these components is described in the following sections.

### 3.1. Preparation of Fuel Cell Materials and Components

The membrane electrode assembly (MEA) used in these investigations consisted of a catalyst-coated membrane, two GDLs, two polyimide Kapton adhesive sheets, and a PTFE Teflon sheet (Figure 9; Chen 2020). The CCM for the selected MEA was composed of a PFSA ionomer membrane (Dupont Nafion NR211), coated with anode

and cathode catalyst layers with a 50:50 Pt/C ratio at 0.1 and 0.4 mg/cm<sup>2</sup> Pt loading, respectively (Chen 2020). The CCM was fabricated using a high-crack density half CCM. The anode catalyst layer was then applied to the membrane side of the half CCM through decal transfer. The anode and cathode GDLs utilized in the experiments were teflonated AvCarb, a non-woven carbon-paper coated with a microporous layer (MPL) on one side. During assembly, the MEA was sealed using a gasket comprised of a Kapton polyimide adhesive sheet and a PTFE (*i.e.*, Teflon) sheet on each side of the MEA. The adhesive Kapton sheets aid in preventing gas leaks during fuel cell operation, while the Teflon layers allow for optimization of the MEA thickness for the desired compression (*i.e.*, 20%).

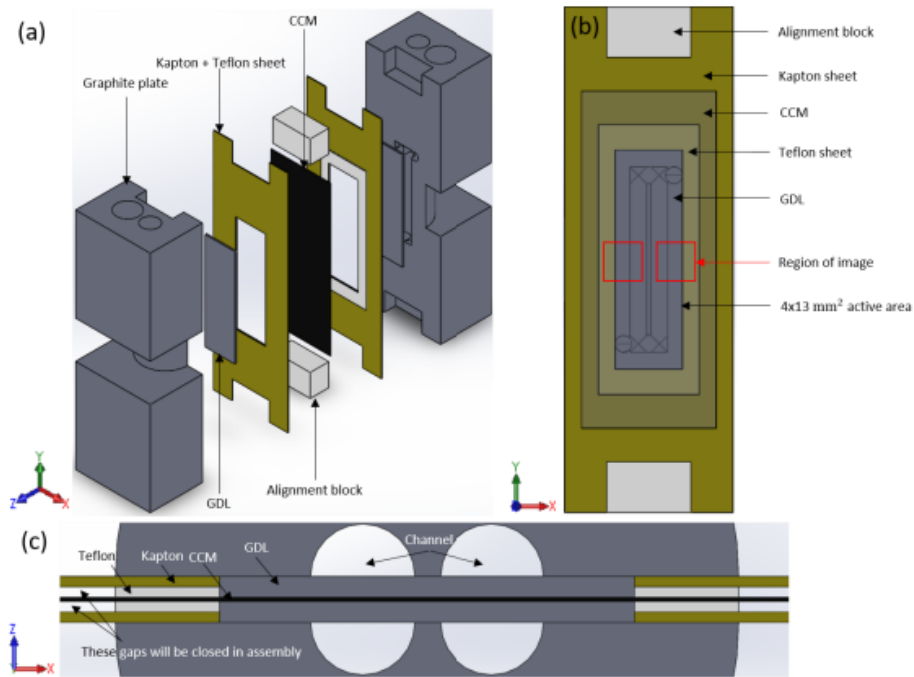


**Figure 9.** Schematic representation of miniaturized PEMFC that identifies all of the components including: (a) a 3D view of the cell components; (b) a plan view of the key components; and, (c) a cross-sectional view of the apparatus (Reproduced with permission from Chen 2020).

Prior to assembly of the MEA, the GDLs, CCM, and gasket were first cut to size using a high precision IPG-280 Photonics laser-micromachining tool. A listing of the parameters used to cut each material type is outlined in Table 1. Prior to cutting the materials, some preparation steps were taken. First, the gasket was prepared by applying the Kapton adhesive sheet to a 2-mil thickness Teflon sheet. Next, the ACL was applied to the half CCM by decal transfer at 150° C and 15 bar of pressure for 180

seconds. Finally, the GDLs and CCM were taped to glass slides to facilitate the cutting process (as per Chen 2020).

**Table 1. Laser micromachining tool cutting parameters.**

| Material                    | Beam Energy (mJ) | Frequency (Hz) | Pulse Rate ( $\mu\text{m}/\text{shot}$ ) | Passes | Attenuator (degree) | Beam Size ( $\mu\text{m} \times \mu\text{m}$ ) |
|-----------------------------|------------------|----------------|--|--------|---------------------|--|
| GDL                         | 4                | 950            | 0.4                                      | 2      | 80                  | 25 x 25  |
| CCM                         | 4                | 950            | 0.4                                      | 1      | 80                  | 25 x 25  |
| Kapton-Teflon (both)        | 4                | 950            | 0.4                                      | 2      | 80                  | 25 x 25  |
| Kapton-Teflon (Teflon only) | 4                | 950            | 1  | 2      | 80                  | 25 x 25  |

Using the laser cutter, the GDLs were cut to dimensions of 11.5 mm by 2.75 mm to give an active area of 0.316 cm<sup>2</sup>. The CCM was then cut to dimensions of 8 mm by 18 mm. For the Kapton/Teflon gasket material, two separate cuts were made. The first cut created an 11.5 mm by 2.75 mm inner window and the outer edges of the gasket. For this cut, both the Kapton and Teflon layers were penetrated through. For the second cut, a lower pulse rate was used that only penetrated the Teflon layer, leaving the Kapton adhesive sheet intact. This cut created a 6 mm by 16 mm window in the gasket material. A detailed list of the MEA component dimensions is provided in Table 2.

**Table 2. MEA component dimensions.**

| Material            | Kapton-Teflon (both; Inner cut) | Kapton-Teflon (both; outer cut) | Teflon (Inner) | Teflon (Outer) | GDL         | CCM    |
|---------------------|---------------------------------|---------------------------------|----------------|----------------|-------------|--------|
| Dimension (mm x mm) | 2.75 x 11.5                     | 10 x 30                         | 2.75 x 11.5    | 6 x 16         | 2.75 x 11.5 | 8 x 18 |

A step-wise approach was used to assemble the MEA that was facilitated using specifically-designed alignment vacuum plates (Figure 10). The first step was to peel off the outer Teflon layer of the gasket. Next, the gasket material with the newly exposed adhesive Kapton surface was placed onto one of the two vacuum plates with the Kapton adhesive facing up. The CCM was then placed on the adjacent vacuum plate and the two plates were clamped together with the vacuum enabled. Subsequently, the two

plates were pulled apart and the second piece of gasket material was placed onto the other vacuum plate. The two vacuum plates were then closed together for a second time to form a Kapton-CCM sub-assembly. The CCM had an area larger than the Kapton/Teflon gasket window to allow for proper sealing and to prevent gas crossover. Finally, the anode and cathode GDLs were placed on the window of the Kapton-CCM sub-assembly to form the MEA (Chen 2020).

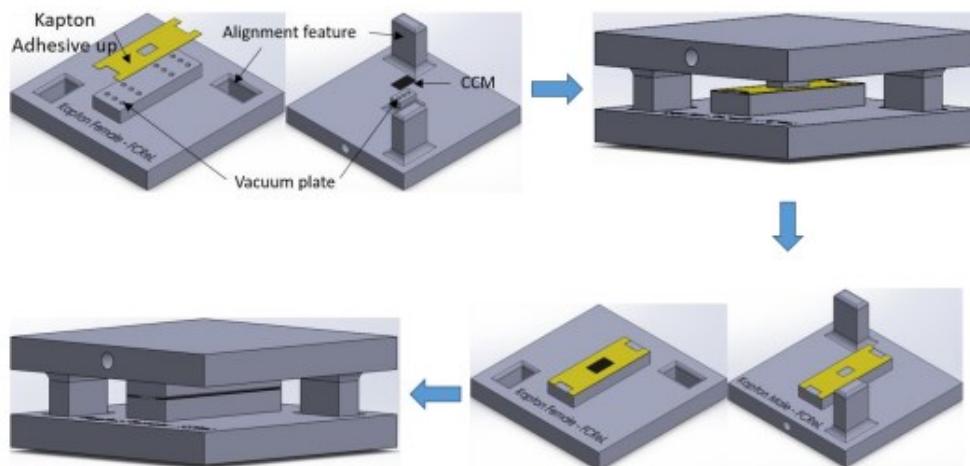


**Figure 10.** Schematic diagram of representative vacuum plates used to assemble an MEA (Reproduced with permission from Chen 2020).

### 3.2. Assembly of Fuel Cell Small-Scale Fixture

The MEA assembly was housed in a small-scale fixture (SSF), which was designed to allow for single cell operation within the XCT system. The SSF consisted of a top and bottom clamping portion (*i.e.*, that hold the graphite plates in place) and a base (Figure 11). The base of the SSF was designed to allow for attachment to the rotating stage within the XCT. The SSF was constructed by inputting the design specifications into a CAD program and using a 3-D plastic printer to generate the fixture. The MEA was compressed between two specially-designed two-channel (1 mm channel width, 0.25 mm land width) graphite plates (Figure 9). The MEA was compressed by tightening two metal hose clamps around the top and bottom clamping portions of the SSF, with

the MEA typically compressed to 3.0 in-lb (*i.e.*, using calibrated torque wrench) to achieve an overall GDL compression of about 20%.

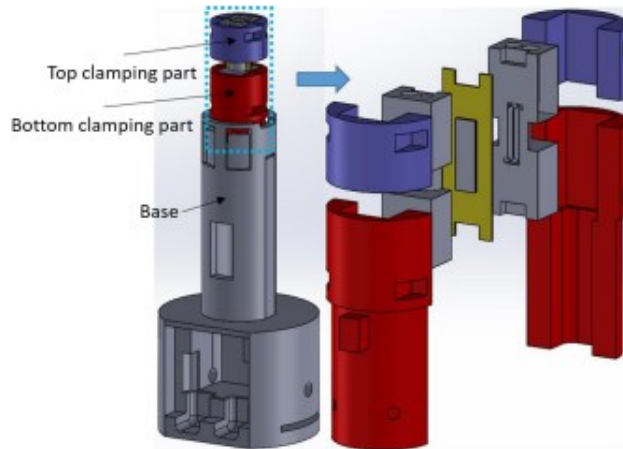


**Figure 11. Three-dimensional schematic diagram of the SSF components (Reproduced with permission from Chen 2020).**

### **3.3. Conditioning of Fuel Cell**

In these investigations, the miniaturized fuel cell was operated on the Scribner 850C Fuel Cell Test System. The fuel cell testing setup is shown in Figure 12. The main components in this setup included: influent gas lines; outlet gas lines; thermocouple; load cables; and, the SSF.

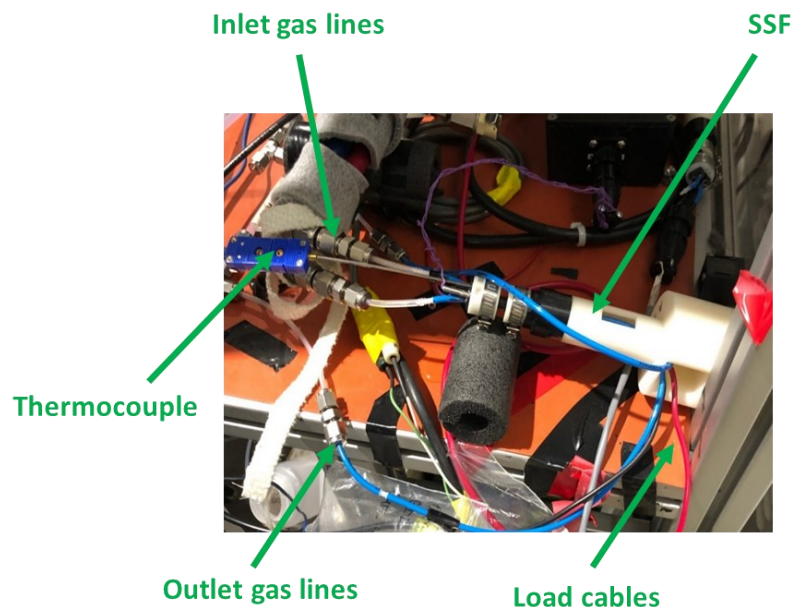


**Figure 12. Setup of Scribner 850C fuel cell testing system.**

Prior to experimental testing, the assembled fuel cell was first conditioned. The conditioning steps are usually undertaken to activate the electrodes in the fuel cell and, thereby, optimize performance during operation and/or testing (Yuan *et al.* 2012). In addition, conditioning transforms the platinum surface into a crystalline structure, which accelerates the HOR and ORR reactions (Kim *et al.* 2020).

The conditioning procedure consisted of three main steps, including: (i) five air starve cycles; (ii) 80 cycles of cyclic voltammetry (CV); and, (iii) a 20 h voltage hold at 0.5 V. For each step during conditioning, the cell temperature was set to 70°C, with a relative humidity of 100% (Chen 2020). The temperature of the fuel cell in this work was controlled by delivering heated gases into the system at atmospheric pressure, with a thermal-couple used to monitor cell temperature. Typically, the influent gas temperature was set 5°C higher than the desired cell temperature to allow for cooling in the lines prior to the gases reaching the cell. The air starves and 20 h hold were performed on the 850C Scribner Test Station, while the CV was conducted on a Autolab Potentiostat system. The air starves were performed by first flowing hydrogen and air at 0.2 and 0.5 L/min, respectively, to allow for a stable open-circuit voltage (OCV) to be reached (Chen 2020). Next, hydrogen and nitrogen were flowed, while drawing a current of 0.01 A, until the voltage dropped to 0.2 volts. At this point, the gases were switched back to hydrogen and air, and the current was set to zero. This procedure was repeated five

times. The air starvation step was conducted to convert platinum oxide to platinum through reduction reactions, which increases the active catalyst surface area.

The next step of conditioning was to apply 80 cycles of CV. Prior to CV, hydrogen and nitrogen were flowed at 0.2 L/min and 0.5 L/min, respectively, until the cell voltage dropped to 0.2 V. At this point, the fuel cell was connected to the CV cart. Cyclic voltammetry was conducted by flowing hydrogen and nitrogen at 0.2 and 0.5 L/min, respectively, and sweeping between 0.1 V and 1 V at a scan rate of 0.05 V/s (White *et al.* 2019). During this step, the platinum surface is reconstructed into a crystalline structure through cyclic oxidation and reduction reactions (Chen 2020).

As the final step of the conditioning process, a 20-hour voltage hold was conducted at a current value that corresponded to 0.5 V (typically around 900 mA/cm<sup>2</sup>). During the voltage hold, hydrogen and air were maintained at 0.2 and 0.5 L/min, respectively. The purpose of the steady-state operation was to condition the ionomer phase in the membrane and CLs, as well as to open up water channels in the ionomer phase (Chen 2020). The membrane ionomer becomes softer and fills the interfacial gaps between membrane and catalyst layer at high temperature and high RH (Chen 2020). To prevent degradation from high voltage and to produce water for humidification, the entire steady-state operation is conducted with current generation (Chen 2020).

### **3.4. Fuel Cell Operation and Testing**

For performance testing, the fuel cell was operated on the Scribner 850C fuel cell test station. The main components of the setup were identified in Section 3.3. For water visualization, the Scribner 850C test station was connected to the XCT to facilitate imaging during fuel cell operation. Both of these testing set-ups are further described in subsequent sections of this document.

### 3.5. Diagnostic Testing

Electrochemical diagnostics is a useful way to assess the performance of a fuel cell. In this work, beginning of life (BOL) diagnostics were used to determine the baseline performance of the cell following initial conditioning. The diagnostic techniques used in this study included polarization curve measurements, cyclic voltammetry (CV), and electrochemical impedance spectroscopy (EIS). The operational conditions used during the diagnostic testing were similar to those applied during initial conditioning (*i.e.*, 70°C cell temperature, RH of 100%, 0.2 L/min H<sub>2</sub>, and 0.5 L/min air). However, diagnostic testing was also conducted under higher flow rate conditions to achieve improved performance in some circumstances. Table 3 and 4 display the diagnostic operational parameters for the low flow rate and high flow rate conditions, respectively.

**Table 3. Listing of diagnostic operational parameters used in the low-flow rate trials.**

| Diagnostic Method  | Anode Gas      | Anode Flow Rate (L/min) | Cathode Gas | Cathode Flow Rate (L/min) | Cell Temperature (°C) | Relative Humidity (%) |
|--------------------|----------------|-------------------------|-------------|---------------------------|-----------------------|-----------------------|
| Polarization Curve | H <sub>2</sub> | 0.2                     | Air         | 0.5                       | 70                    | 100                   |
| CV                 | H <sub>2</sub> | 0.2                     | Air         | 0.5                       | 70                    | 100                   |
| EIS                | H <sub>2</sub> | 0.2                     | Air         | 0.5                       | 70                    | 100                   |

**Table 4. Listing of diagnostic operational parameters used in the high-flow rate trials.**

| Diagnostic Method  | Anode Gas      | Anode Flow Rate (L/min) | Cathode Gas | Cathode Flow Rate (L/min) | Cell Temperature (°C) | Relative Humidity (%) |
|--------------------|----------------|-------------------------|-------------|---------------------------|-----------------------|-----------------------|
| Polarization Curve | H <sub>2</sub> | 0.9                     | Air         | 1.2                       | 70                    | 100                   |
| CV                 | H <sub>2</sub> | 0.9                     | Air         | 1.2                       | 70                    | 100                   |
| EIS                | H <sub>2</sub> | 0.9                     | Air         | 1.2                       | 70                    | 100                   |

Polarization curve measurements were made using hydrogen and air as the respective anode and cathode reactant gases. The first measurement was recorded at an open circuit voltage, followed by increasing the current in steps and recording the resultant voltage. At each current step, the voltage was held for 20 s or until the voltage had stabilized. The measurements were taken until a voltage of 0.2 V was reached. In this work, three polarization curves were generated for each fuel cell and an average curve was calculated using the resultant data.

The second stage of diagnostic testing involved the use of CV. This technique is typically used to characterize fuel cell catalyst activity (O'Hayre *et al.* 2016). More specifically, cyclic voltammetry provides a useful tool for determining the electrochemically-active surface area (ECSA) of the catalyst on an electrode (Das *et al.* 2017). The ECSA of an electrocatalyst provides information on the number of electrochemically-active sites per gram of catalyst and, in so doing, facilitates comparison of various electrocatalytic materials (Das *et al.* 2017). An Autolab Potentiostat system was used to conduct the CV diagnostic testing. In this work, the voltage was swept from 0.05 V to 0.8 V, with a sweep rate of 50 mV/s (see Table 3 and 4 for operational conditions). The resultant data were then plotted to create a cyclic voltammogram, in which current was plotted as a function of voltage (Figure 13). The shape and size of the peaks on this plot provide useful information about reaction and diffusion rates in the system (O'Hayre *et al.* 2016).

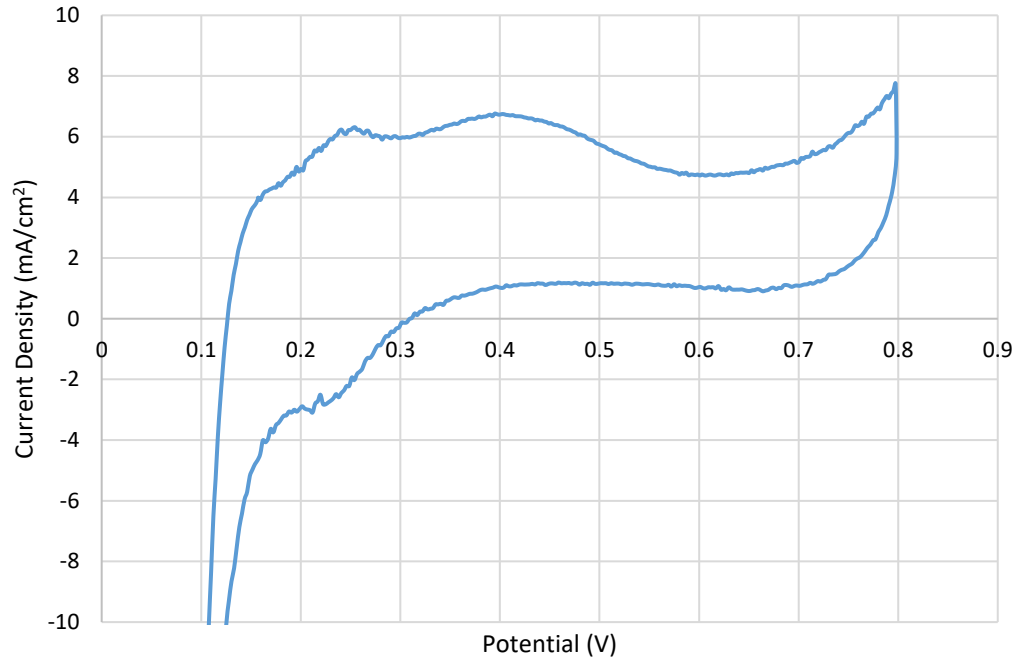


**Figure 13. Example cyclic voltammogram.**

The final stage of the diagnostic testing involved the use of EIS. Impedance is a measure of the ability of the fuel cell to impede the flow of electrical current and is a function of the resistance and reactance in a circuit (O'Hayre *et al.* 2016).

Electrochemical impedance spectroscopy provides a valuable diagnostic tool for evaluating the electrochemical behavior of the anode and cathode of operating fuel cells (Manohar *et al.* 2008). In addition, EIS can be used to infer the water content in the fuel cell by characterizing ohmic impedance, activation impedance, and concentration impedance, as these three impedances are linked to water management in fuel cells (Tongsh *et al.* 2021). Typically, dehydration of the PEM results in an increase in ohmic impedance (Kong *et al.* 2016). In addition, an increase in water content in the flow field results in increased concentration impedance, due to blockage of reactant pathways by liquid water (Kang *et al.* 2019). Furthermore, membrane dehydration or coverage of the three-phase interface with water can result in increased activation impedance (Tongsh *et al.* 2021).

In this study, EIS was conducted using a Gamry Interface 5000 Series potentiostat. The working and sense electrodes were connected to the cathode and the counter and reference electrodes were connected to the anode. A small amplitude

sinusoidal wave (*i.e.*, DC voltage of 0.45 V with a 10 mV perturbation) with varying frequency ( $\omega$ ; *i.e.*, 75 kHz to 0.1 Hz) was applied to measure impedance of the system (Chen 2020; see Table 3 and 4 for operational conditions). The EIS data were compiled and presented in Nyquist plots, which graph imaginary impedance ( $Z_{im}$ ) versus real impedance ( $Z_{Re}$ ). A theoretical Nyquist plot is shown in Figure 14 (Chen 2020; where  $R_{\Omega}$  is the internal resistance of the cell).

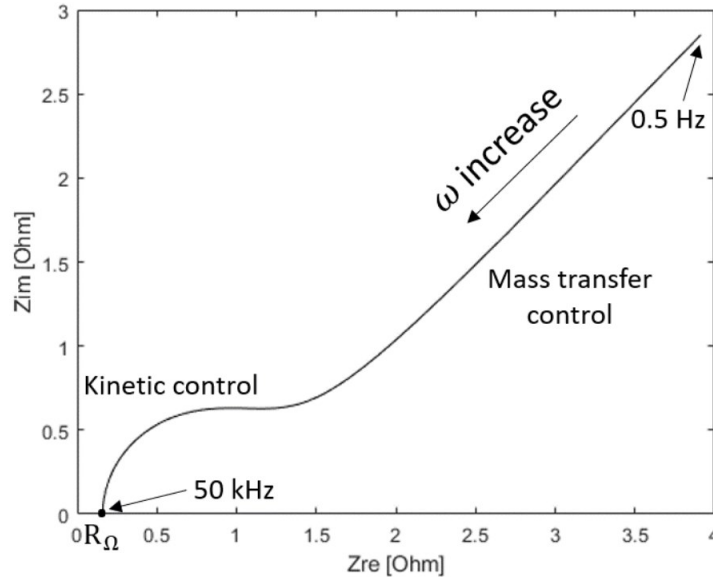


**Figure 14. Theoretical Nyquist plot (Reproduced with permission from Chen 2020).**

In this study, multiple FCs were used to investigate the impact of selected operational conditions on liquid water distribution within the cathode GDL. Several steps were taken to ensure the comparability of the FCs used in this investigation. First, care was taken to make sure that all FCs were constructed in a consistent manner. Second, the BOL diagnostic data were used to ensure that the performance of the various FCs was similar. Finally, the FCs used in this study achieved a BOL performance of 1 A/cm<sup>2</sup> at 0.6V and a peak current density of approximately 2 A/cm<sup>2</sup> at 0.2 V.

### 3.6. X-ray Computed Tomography

This work was undertaken to enhance our understanding of the liquid water distribution within the MEA of operating fuel cell, as a function of operating conditions and current density. This investigation was supported through the application of XCT

technology, which is a non-invasive 3D-imaging technique. This technology enables data acquisition of microstructural components within specific locations in the MEA.

A laboratory-based ZEISS Xradia 520 Versa micro-XCT system was used in this study. The XCT system consists of three main components, including an X-ray generating source, a four degree of freedom (X, Y, Z translation and Y rotation) platform (i.e., the rotating stage), and an X-ray detector. Following fuel cell conditioning and diagnostics, the cell was positioned on the rotating stage within the Versa micro-XCT system in preparation for testing. Electrical connections and gas lines were affixed to the staged SSF to allow for connection to the Scribner Fuel Cell Test Station while the PEMFC was housed in the XCT system. Temperature was controlled by delivering heated gases via the gas lines, with a thermocouple inserted into the graphite plate to monitor cell temperature. As described previously, two types of tests were conducted in this work, including *in-situ* and *in-operando* imaging. *In-situ* scans were primarily used as a proof of concept that liquid water could be visualized within the fuel cell using XCT techniques. By comparison, the *in-operando* scans were used to support data acquisition for this research project. Both testing methods are described in this section, with detailed specifications on the system set-up provided in Table 5 and 6.

The X-ray source and detector for both testing methods were set at a distance of approximately 28 mm and 30 mm from the sample center, respectively, with a 4X detector lens employed in all scans. This configuration provided a field of view (FOV) of about 2.6 mm by 3 mm, with a pixel resolution of about 1.61  $\mu\text{m}$ . This FOV covered both the channel and landing areas of the cell, which is important because previous investigations indicated that the distribution of liquid water differed for these two regions of the fuel cell (Eller *et al.* 2017; Kato *et al.* 2022). Additionally, a built-in X-ray filter LE#1 was selected to improve transmission of the beam. For each scan, a total of 801 (i.e., for *in-operando* scans; Table 6) or 1601 (i.e., for *in-situ* scans; Table 5) 2D radiographic projections were acquired over a 180° angle range with additional flip angle of 4°(-94° to +94°) of the rotating sample.

A step-wise approach was used to acquire *in-situ* XCT images. The first step was to acquire a wet scan of the operating fuel cell. This was done by first operating the cell at 70 °C, 750 mA/cm<sup>2</sup>, and 100% RH for at least one hour. The cell was then allowed to cool for 1 hour, after which an XCT scan was conducted. The second step

was to acquire a dry scan following fuel cell operation. This was achieved by flowing dry nitrogen for 45 minutes on both the anode and the cathode side of the cell to remove any water that had accumulated in the cell during operation. This was followed by conducting the second XCT scan. The XCT parameters used during the *in-situ* investigations are displayed in Table 5.

**Table 5. XCT parameters used for the *In-situ* investigations.**

| XCT Parameter          | Value |
|------------------------|-------|
| Exposure (sec)         | 5     |
| Projections            | 1601  |
| Voltage (kV)           | 80    |
| Power (W)              | 7     |
| Acquisition Time (hrs) | 3     |

A stepwise approach was also used to conduct *in-operando* XCT tests. The first step was to acquire an *in-operando* image set. This was done by scanning the cell while operating it under the desired conditions. This process was initiated by first operating the cell under chosen operational conditions (e.g., 500 mA/cm<sup>2</sup>, 70 °C, and 100% RH) for one hour to reach steady-state conditions. Following this step, XCT data acquisition was initiated. Once the first XCT scan was completed, the final step of the process was to acquire a dry image set as was done for the *in-situ* procedure. The XCT parameters used during the *in-operando* investigations are displayed in Table 6.

**Table 6. XCT parameters used for the *In-operando* investigations.**

| XCT Parameter  | Value |
|----------------|-------|
| Exposure (sec) | 4     |
| Projections    | 801   |
| Voltage (kV)   | 80    |
| Power (W)      | 7     |

### 3.7. XCT Image Processing

To obtain quantitative data from tomography data sets, segmentation of various components within the MEA was required. However, prior to segmentation some image processing steps were conducted. First, a tomography image set was generated for each XCT scan. These image sets were reconstructed using the ZEISS 3D reconstruction software and subsequently processed by open-source software (*i.e.*, Fiji ImageJ). The reconstruction process functions to mathematically combine the 2D projection images acquired from many angles during tomography image acquisition to create a 3D image volume (White *et al.* 2019). This software corrects for center shift, beam hardening, and rotation angle prior to the 3D reconstruction. Using the reconstructed image sets, quantitative data were gathered through segmentation of the various components within the MEA. Specifically, components such as the GDL fibers and liquid water were segmented to generate quantitative data on such variables as liquid water volume and liquid water saturation within the MPL and GDL.

The segmentation images created from the reconstructed 3D image volume were used to determine the distribution of liquid water within the various MEA components. Figure 15 displays a schematic representation of the steps followed to generate a segmentation image set. To accurately segment the liquid water within the GDL of a fuel cell, the dry reference image set was subtracted from the wet data set. This is essential to create enough contrast between the water and the surrounding air within the GDL. To effectively generate a subtraction image, the wet and dry data sets were first aligned with each other. A number of key steps were preformed to manually align the image stacks, including (White *et al.* 2019):

- i) Coordinate greyscale values;
- ii) Crop the image sets;
- iii) Perform tilt correction;
- iv) Perform rotation correction; and,
- v) Perform Z-shift correction.

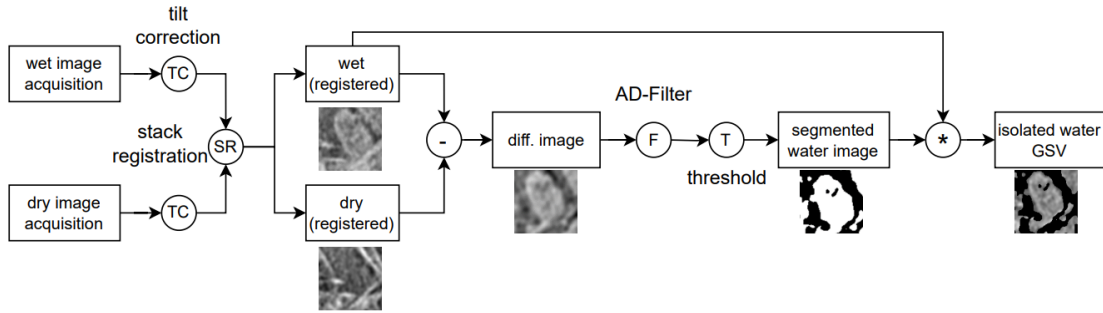


**Figure 15. Schematic diagram of the procedure for segmenting liquid water starting from a wet and dry image set (Reproduced with permission from Aroge 2023).**

The first step in the image stack alignment process involved coordination of the greyscale values. To achieve this, a reconstruction setting for a standard image set was identified that could be copied for all subsequent image sets during the reconstruction process (i.e, exposure, number of projections, pixel size, greyscale value, etc). This allowed for the exact same image setting to be applied to each data set that was to be compared. During this step, only the center shift and rotation settings were changed between image sets. It is important to note that it was essential to have the byte scaling parameter matched between the image sets to ensure consistent greyscale values (White *et al.* 2017; White 2019; White *et al.* 2019).

The next step involved cropping of the image sets. In this process, a region of interest was first selected and an appropriate rectangle size was determined. This rectangle was then used to crop all other subsequent image sets (White 2019; White *et al.* 2019).

The third step in the pre-segmentation process was to perform tilt correction on both the wet and dry image sets. This step corrects for movement of the regions of interest in the y-direction from the start slice to the end slice. To conduct this step, TranslateMacro\_.ijm was run and the instructions that appeared on the screen were followed. To check the effectiveness of the tilt correction, a re-slice from top to bottom was done. If the correction was completed appropriately, the lands should come in view evenly from top to bottom. If the lands did not come into view evenly, the tilt correction steps were repeated (White 2019).

The next step was to perform rotation correction for both the wet and dry image sets. This step corrects for movement of the regions of interest in the x-direction from the start slice to the end slice. From the through-plane view of the image stack on ImageJ, a center slice was selected. A straight line was then drawn from the left land to the right land, and the angle at which this line made was recorded. Finally, the rotation was applied by running Image>Transform>Rotate in the ImageJ software and rotating by the angle that was recorded. The effectiveness of the rotation was checked by reslicing the image set from top to bottom and checking that the lands come into view evenly when scrolling through the images. If the lands did not come into view evenly, the correction steps were repeated (White 2019).

The final step of the pre-segmentation process was to perform Z-shift correction. To complete this correction, the z-difference (*i.e.*, the offset in the through-plane direction) between the wet and dry image sets was first obtained. This was done by running the ZShiftCheck macro. Prior to running the macro, a slice from the dry stack with an identifiable feature that could also be seen in the wet image stack was selected. The image was then cropped to remove the black borders, duplicated and named “ref”. Next a slice in the wet image stack with the same identifiable feature was found, cropped to the same size as the dry image, duplicated and named “target”. The difference in slice number between the selected dry and wet image were then recorded (*e.g.*, slice 92 for dry and slice 99 for wet). The Z-shift macro was then run on the two images with the center slices filled in as the slice number identified for the wet image (*e.g.*, 99) and the range to check over as approximately plus or minus three. The macro then generated several subtraction images using the dry reference image and the range of wet images selected (*i.e.*, six subtraction images, if the range to check over was plus or minus three). Based on the generated subtraction images, an appropriate wet image was selected that matched the dry image most closely (*e.g.*, 97). The subtraction image selected had a black border around the outside, which indicated the amount in which the wet image stack needed to be shifted in the x and y direction to match the dry image stack. The values for x and y shift were determined using the measuring tool and applied to the wet image stack by going to Image>Transform>Translate and inputting the measured values. The final step was to align the z. This was done by saving the image stack with a different range of slices, as determined by the Z-shift Macro. For example, one could save the dry stack with slices ranging from 70 to 220 and the wet stack with

slices ranging from 75 to 225. After completion of all the listed steps, the images were ready for subtraction and segmentation (White 2019).

Following completion of the five pre-segmentation steps, a subtraction image set was generated for each XCT image set. This was conducted by subtracting the dry image stack from the wet image stack (see example of dry and wet images in Figure 16 and Figure 17, respectively). In ImageJ, the Process>Image Calculator was selected, and the macro was run in subtraction mode. Figure 18 displays an example image slice from a resultant subtraction image set. To enhance segmentation accuracy, a final filtering step was also conducted. In this work, a Gaussian Blur 3D filter with a 3 x 3 x 3 voxel despeckle function was applied to reduce noise (White 2019).

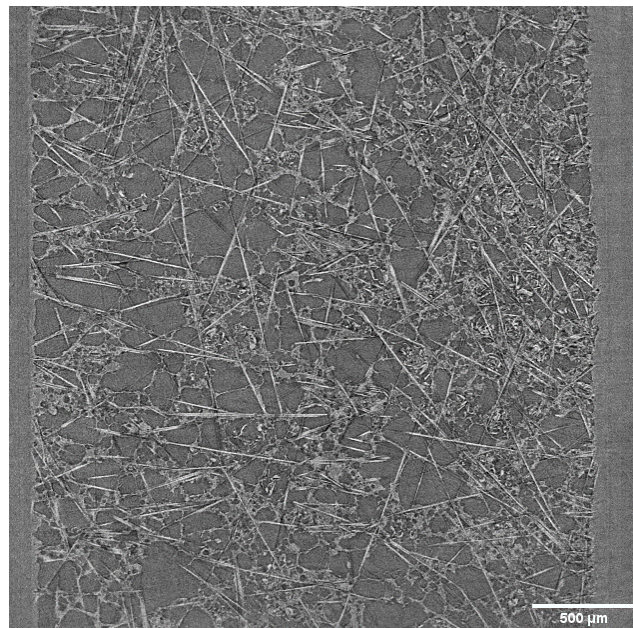


**Figure 16.** Example image slice from a dry image set.

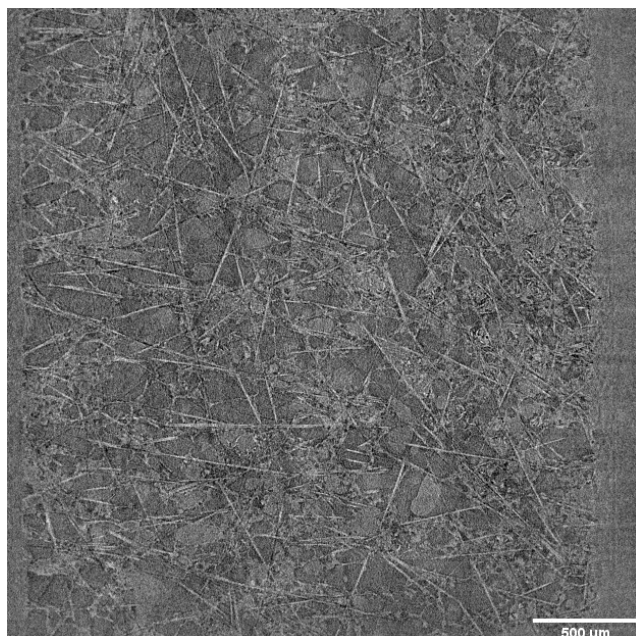


**Figure 17.** Example image slice from a wet image set.

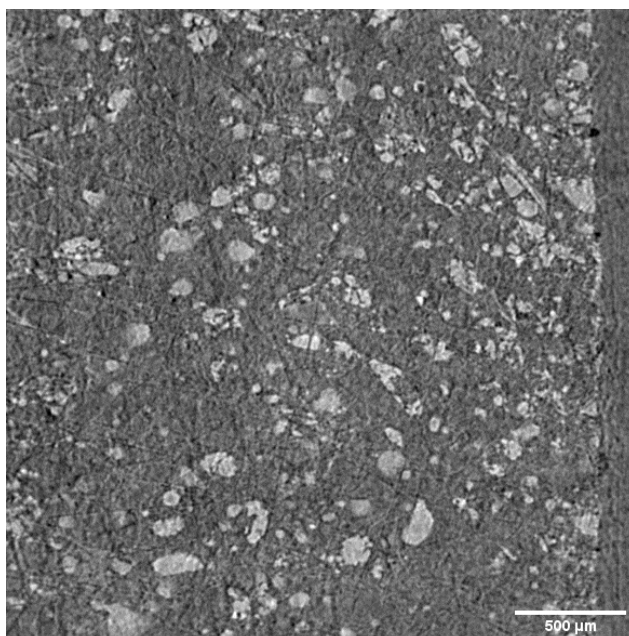


**Figure 18.** Example image slice from a subtraction image set generated by subtracting the wet image stack from the dry image stack.

Segmentation of liquid water within GDL/MPL regions was a primary focus of this study. Additionally, GDL fibers were also segmented to determine saturation within the GDL based on water volume and porosity. Segmentation was conducted using ImageJ. More specifically, greyscale thresholding was applied to the subtraction image set (*i.e.*,

Image > Adjust > Threshold). This method is generally effective for segmenting the liquid water within the GDL; however, some errors can arise in the MPL region due to resolution limits. Therefore, the difficult to resolve regions were often cropped out and not included in the quantification analysis process. Following the thresholding step, the segmented image set was filtered to remove noise due to imperfections in the subtraction or selection of the threshold value. An effective plugin for this step is called MorphoLibJ. This filtering was applied by first going to Plugins > MorphoLibJ > Filtering > Morphological Filters, then selecting white top hat from the drop-down menu, and assigning a value of one or two for X, Y and Z radius in voxels, depending on the amount of noise in the image set. The result obtained using this plugin was then subtracted from the initial segmented image. Additionally, if the segmented image appeared to have too much quantifiable water removed, a black top-hat filter was also applied. This was done in the same way as the white top-hat filter; however, black top hat was selected from the drop-down menu instead. The result obtained by applying this plugin was then added to the segmented image set. Figure 19 displays an example image slice of a fully segmented image set, with areas of white representing liquid water.

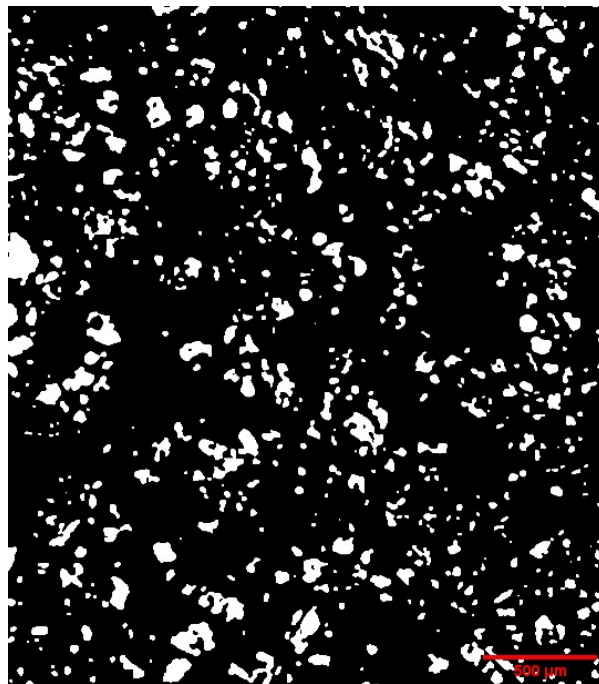


**Figure 19. Example image slice from a segmented image set.**

Following completion of all the segmentation steps, Plot Z-axis Profile was run to acquire quantifiable data from the image set. To run Plot Z-axis Profile, Image > Stacks

> Plot Z-axis Profile was selected. A graph was then generated. From this plot, a list was selected and the quantifiable data for the average amount of liquid water in each slice was copied and plotted into an excel spreadsheet to support generation of water volume vs thickness curves.

In the literature, the quantity of liquid water within the GDL is typically reported as percent saturation or water volume (Eller *et al.* 2017; Aroge 2023; Kato *et al.* 2022). In this study, the amount of liquid water was reported as water volume at specific locations within the GDL. This approach was selected because, at times, it is difficult to segment the GDL, which creates additional error in the percent saturation calculation. This issue was not relevant for the water volume calculations. Hence, water volume was considered to provide a more accurate estimate of liquid water distribution. For comparison, water volumes of 0.5, 1.5, and 2.5 nL roughly correspond to saturations of 7, 20, and 50 percent, respectively, when porosities were 0.55, 0.62, and 0.38, respectively.

### **3.8. Application of One-Dimensional Model**

Fuel cell performance is strongly affected by the presence of liquid water in the cathode GDL. In this study, a simple model (*i.e.*, one-dimensional) was used to predict the presence or absence of liquid water in the through-plane direction of a PEMFCs under a variety of operating conditions. The results of heat and water vapour transport modelling can provide useful information for explaining the results of experimental trials aimed at understanding the relationships between operating conditions, liquid water distribution, and fuel cell performance.

The model that was applied in this investigation was originally developed by Caulk and Baker (2010) and further refined by Olivia Lowe (SFU Undergraduate Co-op student). The model was designed to provide a tool for predicting heat and water vapour transport in a cathode diffusion medium. Accordingly, the model can be used to predict whether dry or wet conditions are likely to predominate in the cathode GDL under a variety of operating conditions (*i.e.*, using water vapour pressure and saturation vapour pressure to predict water condensation). Importantly, variables such as thermal conductivity and GDL diffusivity are key factors that influence the model results.

This work is not intended to evaluate the validity of the Caulk and Baker (2010) one-dimensional model or the refinements that were made subsequently by SFU personnel (Olivia Lowe). Rather, the goal was to apply the refined model to help explain the experimental results obtained in this study. Nevertheless, some of the key equations that are incorporated into the model are presented in equations 10, 11 and 12 below, to assist the reader in understanding the theoretical constructs of the model.

$$-k_j \frac{\partial T_j}{\partial x} = z_H (E - V_{cell}) i \quad (\text{Equation 10})$$

$$\frac{-D_{v,j}^{eff}}{RT_j} \frac{\partial p_{w,j}}{\partial x} = z_w \frac{i}{2F} \quad (\text{Equation 11})$$

$$p_{sat}(T)[Pa] = -2846.4 + 411.24T(^{\circ}C) - 10.554T(^{\circ}C)^2 + 0.16636T(^{\circ}C)^3 \quad (\text{Equation 12})$$

Equation 10 solves for the temperature  $T$  as a function of  $x$  distance from the CCL. Subscript  $j$  represents the index for land or channel region.  $k$  is the thermal conductivity,  $z_H$  is the fraction of reaction heat transported through the diffusion media to the cathode flow fields,  $E$  represents the lower heating value (1.25 V),  $V_{cell}$  is the cell potential, and  $i$  is the current density. Equation 11 solves for water vapour pressure as a function of distance  $x$  from the CCL. Where,  $D_{v,j}^{eff}$  is the effective water vapour diffusion coefficient in the GDL,  $z_w$  denotes the fraction of product water transported through the diffusion media to the cathode flow fields,  $R$  is the Universal gas constant, and  $F$  is the Faradays constant. Equation 12 solves for saturation vapour pressure at a given temperature.

### 3.9. Optimization of Fuel Cell Test Station and Comparison of High and Low Flow Rates of Gases

In this investigation, a miniaturized fuel cell was tested under three sets of conditions. The first test was conducted by directly connecting the cell to the Scribner test station. The station was operated at 70°C, 100% relative humidity, 0.2 L/min hydrogen and 0.5 L/min air, with an inlet gas temperature of 80°C. The second test was also performed by connecting the cell to the Scribner test station. The operating conditions for this test were the same as for test one; however, the influent gas flow rates were increased to 0.9 L/min hydrogen and 1.2 L/min air. The third and final test

was conducted using the Greenlight Innovation G20 test station. For this test, the cell was operated under the same conditions as test one; however, on the G20 station the dewpoint of the inlet gases was controlled. The dewpoint was set to 70°C to match the cell temperature. This dewpoint control differs from the Scribner station, which sets the dewpoint equal to the inlet gas temperature (*i.e.*, 80°C for both test one and test two). Table 7 displays the operational conditions used for each test. Under each operational setup, three polarization curves were generated and averaged for analysis. The results of this investigation are presented in section 4.1.

**Table 7. Operational conditions used in the Fuel Cell Test Station Optimization and Comparison Experiment.**

| Test Number | Anode Gas      | Anode Flow Rate (L/min) | Cathode Gas | Cathode Flow Rate (L/min) | Cell Temperature (°C) | Influent Gas Temperature (°C) | Relative Humidity (%) |
|-------------|----------------|-------------------------|-------------|---------------------------|-----------------------|-------------------------------|-----------------------|
| 1           | H <sub>2</sub> | 0.2                     | Air         | 0.5                       | 70                    | 80                            | 100                   |
| 2           | H <sub>2</sub> | 0.9                     | Air         | 1.2                       | 70                    | 80                            | 100                   |
| 3           | H <sub>2</sub> | 0.2                     | Air         | 0.5                       | 70                    | 80                            | 100                   |

### 3.10. Evaluation of the Effect of Temperature Variation on the Performance of PEMFCs

An investigation was conducted to evaluate the influence of operating temperature on the performance of a miniaturized fuel cell. In this study, two operational setups were used, including: direct connection of the cell to the Scribner test station; and, *in- operando* setup (*i.e.*, inside the XCT machine) (s. chapter 2b, Setups) to assess the effect of temperature on fuel cell performance. A total of six operating temperatures were evaluated in these trials (30°C, 50°C, 60°C, 70°C, 80°C, and 90°C). All of the tests were conducted at 0.9 L/min H<sub>2</sub> and 1.2 L/min Air, and 100% RH. The fuel cell temperature was controlled using heated gases, with the inlet gas temperature generally set 4 - 5°C higher than the desired cell temperature in the Direct Scribner set-up (*i.e.*, to compensate for the additional cooling within the gas tubes) and typically set 10 - 15°C higher than the desired cell temperature for the *in-operando* setup (*i.e.*, to allow for

greater cooling in the longer gas tubes). For each temperature tested, three polarization curves, EIS and CV were generated and used for diagnostic analysis. The polarization curve results were averaged and plotted with standard deviation error bars. A detailed description of the diagnostic methods used are presented in Section 3.5. Tables 8 and 9 display the operational conditions used for the direct Scribner setup and the *in-operando* setup, respectively.

**Table 8. Operational conditions for the direct Scribner tests conducted during the effect of temperature on fuel cell performance investigation.**

| Cell Temperature (°C) | Anode Gas      | Anode Flow Rate (L/min) | Cathode Gas | Cathode Flow Rate (L/min) | Influent Gas Temperature (°C) | Relative Humidity (%) |
|-----------------------|----------------|-------------------------|-------------|---------------------------|-------------------------------|-----------------------|
| 30                    | H <sub>2</sub> | 0.9                     | Air         | 1.2                       | 30                            | 100                   |
| 50                    | H <sub>2</sub> | 0.9                     | Air         | 1.2                       | 55                            | 100                   |
| 60                    | H <sub>2</sub> | 0.9                     | Air         | 1.2                       | 65                            | 100                   |
| 70                    | H <sub>2</sub> | 0.9                     | Air         | 1.2                       | 75                            | 100                   |
| 80                    | H <sub>2</sub> | 0.9                     | Air         | 1.2                       | 85                            | 100                   |
| 90                    | H <sub>2</sub> | 0.9                     | Air         | 1.2                       | 95                            | 100                   |

**Table 9. Operational conditions for the in-operando tests conducted during the effect of temperature on fuel cell performance investigation.**

| Cell Temperature (°C) | Anode Gas      | Anode Flow Rate (L/min) | Cathode Gas | Cathode Flow Rate (L/min) | Influent Gas Temperature (°C) | Relative Humidity (%) |
|-----------------------|----------------|-------------------------|-------------|---------------------------|-------------------------------|-----------------------|
| 30                    | H <sub>2</sub> | 0.9                     | Air         | 1.2                       | 30                            | 100                   |
| 50                    | H <sub>2</sub> | 0.9                     | Air         | 1.2                       | 60                            | 100                   |
| 60                    | H <sub>2</sub> | 0.9                     | Air         | 1.2                       | 75                            | 100                   |
| 70                    | H <sub>2</sub> | 0.9                     | Air         | 1.2                       | 85                            | 100                   |
| 80                    | H <sub>2</sub> | 0.9                     | Air         | 1.2                       | 90                            | 100                   |
| 90                    | H <sub>2</sub> | 0.9                     | Air         | 1.2                       | 98                            | 100                   |

### 3.11. Evaluation of the Effect of Varying Relative Humidities on Cell Performance and Liquid Water Distribution at Various Temperatures

This study component was undertaken to evaluate the influence of changes in relative humidity on the performance of a miniaturized PEMFC at selected temperatures. This investigation combined the use of both experimental data and results generated using a one-dimensional model. The Greenlight G20 fuel cell test station was used in the experimental work. The miniaturized fuel cell was operated at a total of four influent gas RHs (*i.e.*, 25%, 50%, 75% and 100%) and four temperatures (*i.e.*, 40°C, 50°C, 60°C and 70°C). Therefore, a total of sixteen unique operational conditions were tested. All of the tests were conducted with influent gas flow rates of 0.2 L/min H<sub>2</sub> and 0.5 L/min air. The influent gas temperature was set 15°C higher than the cell temperature to allow for cooling in the influent gas lines and to prevent condensation in the gas delivery tubes. For each unique condition, three polarization curves were generated and averaged to support diagnostic analysis similar to section 3.10 above. Table 10 summarizes the experimental procedure followed during this investigation.

**Table 10. Influent gas conditions used during the RH variation trials.**

| Cell Temp (°C) | RH (%) | Dewpoint (°C) | Gas Temperature (°C) |
|----------------|--------|---------------|----------------------|
| 40             | 0      | 0             | 55                   |
|                | 25     | 16.25         | 55                   |
|                | 50     | 27.6          | 55                   |
|                | 75     | 34.72         | 55                   |
|                | 100    | 40            | 55                   |
| 50             | 0      | 0             | 65                   |
|                | 25     | 24.62         | 65                   |
|                | 50     | 36.73         | 65                   |
|                | 75     | 44.34         | 65                   |
|                | 100    | 50            | 65                   |
| 60             | 0      | 0             | 75                   |
|                | 25     | 32.93         | 75                   |
|                | 50     | 45.83         | 75                   |
|                | 75     | 53.96         | 75                   |
|                | 100    | 60            | 75                   |
| 70             | 0      | 0             | 85                   |
|                | 25     | 41.2          | 85                   |
|                | 50     | 54.91         | 85                   |
|                | 75     | 63.55         | 85                   |

To provide additional context for the experimental results, a one-dimensional model was used to predict the effect of temperature and RH on the state of water present in a PEMFC. More specifically, the model was used to predict the effect of changes in RH on the state of water within the GDL substrate at various temperatures (Note: This model was developed by Olivia Lowe, Undergraduate Coop Student, SFU and was used with permission in this investigation). This model predicts whether wet or dry conditions (*i.e.*, the presence or absence of condensation) are likely to be present within the GDL, based on the difference between vapour pressure and saturation pressure. Importantly, variables such as thermal conductivity and GDL diffusivity are key factors that influence the model results. The model was run using the diagnostic data that was generated in Section 4.3.1. More specifically, the cell voltages at selected current densities were input into the model to generate predictions of wet or dry conditions in the fuel cell. The results of the model were used to generate plots of saturation vapor pressure and water vapor pressure vs distance from the CL for the regions under the lands and under the channel for each unique operating condition. Three types of graphs were generated to assist in the analysis and interpretation of the resultant data. First, a summary map was generated that predicts whether the GDL is likely to be wet, dry, or in transition from wet to dry. From this summary map, a transition region map was generated for the identified transition regions that forecasts the state of water at four different current densities (*i.e.*, 500, 750, 1000, and 1250 mA/cm<sup>2</sup>). The final type of plot displays the estimated ratio of water vapor pressure to saturation vapor pressure versus the distance from the CL for each selected condition that was run in the model. All three types of graphs were used to make predictions about the state of water in the fuel cell and to interpret the experimental results that were generated.

### **3.12. Evaluation of the Effect of Current Density on the Distribution of Liquid Water Within the Gas Diffusion Layer**

An investigation was conducted to evaluate the influence of current density on the distribution of liquid water within the GDL. In this investigation, tests were conducted

using the *in-operando* setup, with testing conducted at 40°C, 50°C, 60°C and 70°C and 100% relative humidity. Gases were delivered at a rate of 0.2 L/min for the fuel and 0.5 L/min for the oxidant. The XCT was operated at an exposure time of 4 seconds, 801 projections, a voltage of 80 kV, a power of 7 W and pixel size of 1.61  $\mu\text{m}$  (see section 3.6 for further details). For each selected temperature tested during this analysis, the data were broken down into three separate sections, including: low current density, high current density, and oxygen variation trials. Additionally, at 40°C, a varying flow rate analysis was conducted.

At 40 °C, current densities were initially tested between 500 mA/cm<sup>2</sup> and 1250 mA/cm<sup>2</sup> (*i.e.*, 500, 750, 1000, and 1250 mA/cm<sup>2</sup>) with air as the oxidant. For the varying oxygen concentration trials, the cell was operated at 1250 mA/cm<sup>2</sup> while flowing air, 60% O<sub>2</sub>, or 100% O<sub>2</sub>. During the high current density investigation, the cell was operated at 2000 mA/cm<sup>2</sup> and 3500 mA/cm<sup>2</sup> under 100% O<sub>2</sub> and at 1900 mA/cm<sup>2</sup> under air. Finally, for the varying flow rate investigation the cell was operated at 500, 750, 1000, or 1250 mA/cm<sup>2</sup> at flow rates of 0.9 L/min for H<sub>2</sub> and 1.2 L/min for air. The operational conditions for the 40 °C trials are summarized in Table 11.

**Table 11. Operational conditions for the trials conducted at 40°C to evaluate the effect of current density on water volume in the GDL.**

| Current Density (A/cm <sup>2</sup> ) | Oxygen Concentration (%) | Cell Temperature (°C) | Anode Gas      | Anode Flow Rate (L/min) | Cathode Gas    | Cathode Flow Rate (L/min) | Influent Gas Temperature (°C) | Relative Humidity (%) |
|--------------------------------------|--------------------------|-----------------------|----------------|-------------------------|----------------|---------------------------|-------------------------------|-----------------------|
| 500                                  | Air (21)                 | 40                    | H <sub>2</sub> | 0.2                     | O <sub>2</sub> | 0.5                       | 65                            | 100                   |
| 750                                  | Air (21)                 | 40                    | H <sub>2</sub> | 0.2                     | O <sub>2</sub> | 0.5                       | 65                            | 100                   |
| 1000                                 | Air (21)                 | 40                    | H <sub>2</sub> | 0.2                     | O <sub>2</sub> | 0.5                       | 65                            | 100                   |
| 1250                                 | Air (21)                 | 40                    | H <sub>2</sub> | 0.2                     | O <sub>2</sub> | 0.5                       | 65                            | 100                   |
| 1250                                 | 60                       | 40                    | H <sub>2</sub> | 0.2                     | O <sub>2</sub> | 0.5                       | 65                            | 100                   |
| 1250                                 | 100                      | 40                    | H <sub>2</sub> | 0.2                     | O <sub>2</sub> | 0.5                       | 65                            | 100                   |
| 1900                                 | Air (21)                 | 40                    | H <sub>2</sub> | 0.2                     | O <sub>2</sub> | 0.5                       | 65                            | 100                   |
| 2000                                 | 100                      | 40                    | H <sub>2</sub> | 0.2                     | O <sub>2</sub> | 0.5                       | 65                            | 100                   |
| 3500                                 | 100                      | 40                    | H <sub>2</sub> | 0.2                     | O <sub>2</sub> | 0.5                       | 65                            | 100                   |

At 50 °C, during the low current density investigation, the cell was run between 500 mA/cm<sup>2</sup> and 1700 mA/cm<sup>2</sup> (*i.e.*, 500, 750, 1000, 1250, 1500, or 1700 mA/cm<sup>2</sup>) with

air as the oxidant. For the varying oxygen concentration trials, the cell was operated at 1250 mA/cm<sup>2</sup> while flowing air, 60% O<sub>2</sub>, or 100% O<sub>2</sub>. Finally, during the high current density investigation, the cell was operated at 1700 mA/cm<sup>2</sup> or 2500 mA/cm<sup>2</sup> under 100% O<sub>2</sub> and at 1700 mA/cm<sup>2</sup> under air. The operational conditions for the 50 °C trials are summarized in Table 12.

**Table 12. Operational conditions for the trials conducted at 50°C to evaluate the effect of current density on water volume in the GDL.**

| Current Density (A/cm <sup>2</sup> ) | Oxygen Concentration (%) | Cell Temperature (°C) | Anode Gas      | Anode Flow Rate (L/min) | Cathode Gas    | Cathode Flow Rate (L/min) | Influent Gas Temperature (°C) | Relative Humidity (%) |
|--------------------------------------|--------------------------|-----------------------|----------------|-------------------------|----------------|---------------------------|-------------------------------|-----------------------|
| 500                                  | Air (21)                 | 50                    | H <sub>2</sub> | 0.2                     | O <sub>2</sub> | 0.5                       | 75                            | 100                   |
| 750                                  | Air (21)                 | 50                    | H <sub>2</sub> | 0.2                     | O <sub>2</sub> | 0.5                       | 75                            | 100                   |
| 1000                                 | Air (21)                 | 50                    | H <sub>2</sub> | 0.2                     | O <sub>2</sub> | 0.5                       | 75                            | 100                   |
| 1250                                 | Air (21)                 | 50                    | H <sub>2</sub> | 0.2                     | O <sub>2</sub> | 0.5                       | 75                            | 100                   |
| 1500                                 | Air (21)                 | 50                    | H <sub>2</sub> | 0.2                     | O <sub>2</sub> | 0.5                       | 75                            | 100                   |
| 1700                                 | Air (21)                 | 50                    | H <sub>2</sub> | 0.2                     | O <sub>2</sub> | 0.5                       | 75                            | 100                   |
| 1250                                 | 60                       | 50                    | H <sub>2</sub> | 0.2                     | O <sub>2</sub> | 0.5                       | 75                            | 100                   |
| 1250                                 | 100                      | 50                    | H <sub>2</sub> | 0.2                     | O <sub>2</sub> | 0.5                       | 75                            | 100                   |
| 1700                                 | 100                      | 50                    | H <sub>2</sub> | 0.2                     | O <sub>2</sub> | 0.5                       | 75                            | 100                   |
| 2500                                 | 100                      | 50                    | H <sub>2</sub> | 0.2                     | O <sub>2</sub> | 0.5                       | 75                            | 100                   |

At 60 °C, during the low current density investigation, the cell was run between 500 mA/cm<sup>2</sup> and 1700 mA/cm<sup>2</sup> (*i.e.*, 500, 750, 1000, 1250, or 1700 mA/cm<sup>2</sup>) with air as the oxidant. For the varying oxygen concentration trials, the cell was operated at 1250 mA/cm<sup>2</sup> while flowing air, 60% O<sub>2</sub>, or 100% O<sub>2</sub>. Finally, during the high current density investigation, the cell was operated at 1700 mA/cm<sup>2</sup> or 3000 mA/cm<sup>2</sup> under 100% O<sub>2</sub> and at 1700 mA/cm<sup>2</sup> under air. The operational conditions for the 60 °C trials are summarized in Table 13.

**Table 13. Operational conditions for the trials conducted at 60°C to evaluate the effect of current density on water volume in the GDL.**

| Current Density (A/cm <sup>2</sup> ) | Oxygen Concentration (%) | Cell Temperature (°C) | Anode Gas | Anode Flow Rate (L/min) | Cathode Gas | Cathode Flow Rate (L/min) | Influent Gas Temperature (°C) | Relative Humidity (%) |
|--------------------------------------|--------------------------|-----------------------|-----------|-------------------------|-------------|---------------------------|-------------------------------|-----------------------|
|--------------------------------------|--------------------------|-----------------------|-----------|-------------------------|-------------|---------------------------|-------------------------------|-----------------------|

|      |          |    |                |     |                |     |    |     |
|------|----------|----|----------------|-----|----------------|-----|----|-----|
| 500  | Air (21) | 60 | H <sub>2</sub> | 0.2 | O <sub>2</sub> | 0.5 | 85 | 100 |
| 750  | Air (21) | 60 | H <sub>2</sub> | 0.2 | O <sub>2</sub> | 0.5 | 85 | 100 |
| 1000 | Air (21) | 60 | H <sub>2</sub> | 0.2 | O <sub>2</sub> | 0.5 | 85 | 100 |
| 1250 | Air (21) | 60 | H <sub>2</sub> | 0.2 | O <sub>2</sub> | 0.5 | 85 | 100 |
| 1700 | Air (21) | 60 | H <sub>2</sub> | 0.2 | O <sub>2</sub> | 0.5 | 85 | 100 |
| 1250 | 60       | 60 | H <sub>2</sub> | 0.2 | O <sub>2</sub> | 0.5 | 85 | 100 |
| 1250 | 100      | 60 | H <sub>2</sub> | 0.2 | O <sub>2</sub> | 0.5 | 85 | 100 |
| 1700 | 100      | 60 | H <sub>2</sub> | 0.2 | O <sub>2</sub> | 0.5 | 85 | 100 |
| 3000 | 100      | 60 | H <sub>2</sub> | 0.2 | O <sub>2</sub> | 0.5 | 85 | 100 |

At 70 °C, during the low current density investigation, the cell was run between 500 mA/cm<sup>2</sup> and 1700 mA/cm<sup>2</sup> (*i.e.*, 500, 750, 1000, 1250, or 1500 mA/cm<sup>2</sup>) with air as the oxidant. For the varying oxygen concentration trials, the cell was operated at 1250 mA/cm<sup>2</sup> while flowing air, 60% O<sub>2</sub>, or 100% O<sub>2</sub>. Finally, during the high current density investigation, the cell was operated at 1500 mA/cm<sup>2</sup> or 2500 mA/cm<sup>2</sup> under 100% O<sub>2</sub> and at 1500 mA/cm<sup>2</sup> under air. The operational conditions for the 70 °C trials are summarized in Table 14.

**Table 14. Operational conditions for the trials conducted at 70°C to evaluate the effect of current density on water volume in the GDL.**

| Current Density (A/cm <sup>2</sup> ) | Oxygen Concentration (%) | Cell Temperature (°C) | Anode Gas      | Anode Flow Rate (L/min) | Cathode Gas    | Cathode Flow Rate (L/min) | Influent Gas Temperature (°C) | Relative Humidity (%) |
|--------------------------------------|--------------------------|-----------------------|----------------|-------------------------|----------------|---------------------------|-------------------------------|-----------------------|
| 500                                  | Air (21)                 | 70                    | H <sub>2</sub> | 0.2                     | O <sub>2</sub> | 0.5                       | 95                            | 100                   |
| 750                                  | Air (21)                 | 70                    | H <sub>2</sub> | 0.2                     | O <sub>2</sub> | 0.5                       | 95                            | 100                   |
| 1000                                 | Air (21)                 | 70                    | H <sub>2</sub> | 0.2                     | O <sub>2</sub> | 0.5                       | 95                            | 100                   |
| 1250                                 | Air (21)                 | 70                    | H <sub>2</sub> | 0.2                     | O <sub>2</sub> | 0.5                       | 95                            | 100                   |
| 1500                                 | Air (21)                 | 70                    | H <sub>2</sub> | 0.2                     | O <sub>2</sub> | 0.5                       | 95                            | 100                   |
| 1250                                 | 60                       | 70                    | H <sub>2</sub> | 0.2                     | O <sub>2</sub> | 0.5                       | 95                            | 100                   |
| 1250                                 | 100                      | 70                    | H <sub>2</sub> | 0.2                     | O <sub>2</sub> | 0.5                       | 95                            | 100                   |
| 1500                                 | 100                      | 70                    | H <sub>2</sub> | 0.2                     | O <sub>2</sub> | 0.5                       | 95                            | 100                   |
| 2500                                 | 100                      | 70                    | H <sub>2</sub> | 0.2                     | O <sub>2</sub> | 0.5                       | 95                            | 100                   |

## Chapter 4. Results and Discussion

It is critical to optimize the performance of PEM fuel cells, if this technology is to play a major role in the decarbonization of the transportation and other sectors of the economy. The performance of PEM fuel cells can be affected by a number of material properties and operating conditions. Material properties, including, membrane type, membrane thickness, membrane active area, electrochemically-active surface area, gas diffusion layer and microporous layer types, and other structural factors, can all influence cell performance (Salam *et al.* 2020). In addition, fuel cell performance can be altered by a variety of operating conditions, such as cell temperature, type of oxidant utilized (*i.e.*, air vs. oxygen), flow rate/pressure of hydrogen and oxidant, relative humidity of influent gases, and other factors (Yan *et al.* 2006a; Salam *et al.* 2020). Furthermore, the performance of PEM fuel cells can be impacted by accumulation of liquid water on the anode and/or cathode side of the cell and by various factors associated with fuel cell degradation (*e.g.*, accumulation of impurities, loss of catalyst, changes in membrane permeability, and others; Ji and Wei 2009).

In this study, the influence of selected operating conditions on fuel cell performance was evaluated. In addition, the accumulation and distribution of liquid water in operating PEM fuel cells was evaluated to determine how the presence of liquid water influences fuel cell performance under the selected operating conditions (Wang *et al.* 2011; White *et al.* 2019). The current study was designed to evaluate the importance of selected operating conditions on fuel cell performance, with a focus on varying cell temperatures. In addition, the impact of oxygen concentration on PEM fuel cell is presented. Finally, the influence of liquid water distribution in operating fuel cells was studied to explain the changes in fuel cell performance under various operating conditions.

## 4.1. Optimization of Fuel Cell Test Station and Comparison of High and Low Flow Rates of Gases

This section presents the results for an investigation that was designed to help better understand and optimize key fuel cell testing stations. More specifically, this investigation involved evaluating the performance of a fuel cell at two separate test stations including a Scribner 850C test station and a Greenlight G20 fuel cell test station. The performance of PEM fuel cells is typically evaluated by generating polarization curves under the conditions of interest in the experiment (See Introduction for a description of polarization curves and other diagnostic tools for assessing fuel cell performance). Polarization curves plot cell voltage against current density, which provides a basis for determining when performance is optimized and for identifying the sources of voltage losses in the system (*i.e.*, activation, ohmic, and/or mass transport losses). This study was conducted because the results of numerous trials indicated that cells tested using the Scribner test station had substantially lower performance compared to those tested using the G20 station. This performance reduction was especially evident during operation at high current densities.

The polarization curve results for this investigation are shown in Figure 20, where the polarization curves for the high flow rate Scribner (Test 2), G20 (Test 3), and lower flow rate Scribner (Test 1) tests are displayed on the graph in blue, orange, and grey, respectively. Looking at the results for test one, it can be observed that at higher current densities (*i.e.*, greater than 1.2 A/cm<sup>2</sup>) there are high fluctuations in voltages and a severe drop in performance with a maximum current density of 1.7 A/cm<sup>2</sup> observed at 0.2 volts. However, at lower current densities, the voltage fluctuations were minor. In comparison, the results of test two show a similar trend for current densities below 1.2 A/cm<sup>2</sup>. However, at current densities above 1.2 A/cm<sup>2</sup>, there was a significant increase in performance, with a maximum current density of 2.6 A/cm<sup>2</sup> observed at 0.2 volts. These observations are most likely explained by two main phenomena that result from higher influent gas flow rates. The first being the improved removal of condensed water within the influent gas lines and the second being enhanced water removal from the GDL.

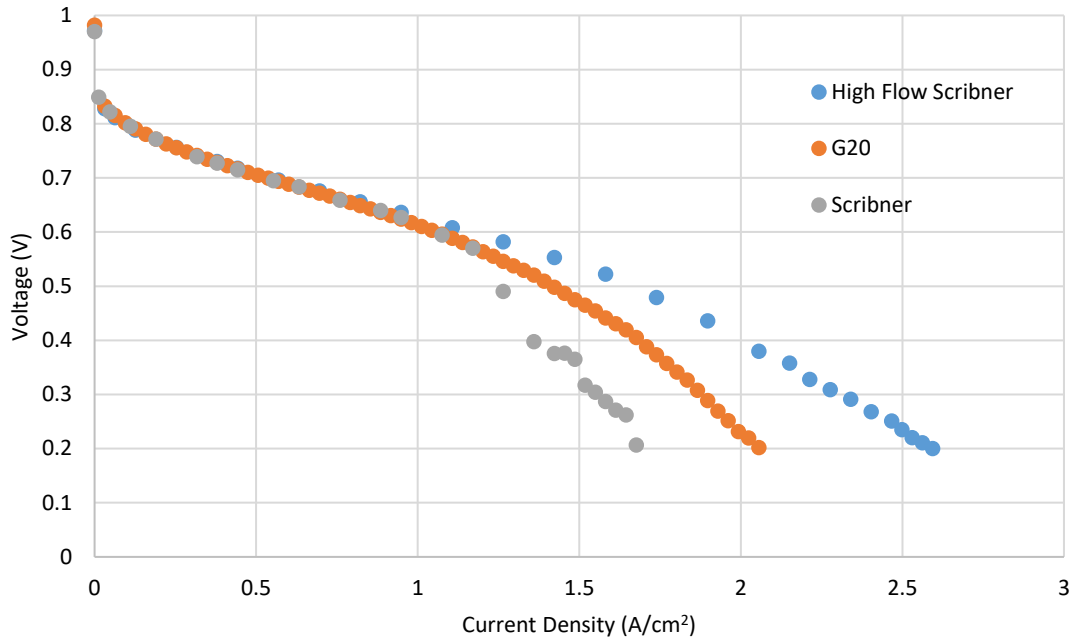


**Figure 20. Comparison of the performance of PEMFC operated on the G20 test station, the Scribner test station operated at low gas flow rates, and the Scribner test station operated at high flow rates.**

In both test one and test two, the influent gas temperature and dewpoint were set to 80°C (*i.e.*, RH was 100%) to achieve a cell temperature of 70°C. It was necessary to set the influent gas temperature higher than the target cell temperature because a portion of the influent gas lines is exposed to ambient air, which is much cooler (*i.e.*, about 30°C than the temperature of the fuel and oxidant). Cooling of the influent gases in the gas lines prior to delivery to the FC results in condensation within the influent gas lines. At high current densities, the demand for oxidant is high and, therefore, some of the excess water associated with this condensation can make its way into the MEA and have a substantial impact on the performance of the cell. This is likely due to water blocking some of the pores that would normally provide pathways for the oxidant to reach the catalyst layer. The higher flow rates used in test two help to improve the fuel cell performance by reducing gas residence time in the lines, transporting the condensed water within the influent gas lines through the cell and preventing the water from blocking the channel or entering the GDL (and thereby blocking pores). Additionally, this performance improvement can likely be explained by enhanced water removal from the edges of the GDL (*i.e.*, close to the flow channels) at higher flow rates. As a result of

this enhanced water removal, it is likely that water moves more quickly through the GDL and water accumulation is reduced.

Based on the polarization curve data generated for test three, it can be observed that the cell performance is similar to tests one and two for current densities below 1.2 A/cm<sup>2</sup>. However, at current densities above 1.2 A/cm<sup>2</sup>, the performance of the FC is different, as evidenced by a maximum current density of 2.1 A/cm<sup>2</sup> at 0.2 volts. At high current densities, the performance is improved when compared to the polarization curve data generated on the Scribner test station using 0.2 and 0.5 L/min hydrogen and air, respectively. This difference in performance can probably be attributed to the ability to control the dewpoint on the G20 test station. For test three, the influent gas dewpoint was set to 70°C to allow for cooling in the influent gas lines leading to the fuel cell. As a result, when the temperature of the influent gas cooled from 80°C to 70°C, there was little to no condensation occurring in the lines. This adjustment of the dew point prevented condensed water from entering the fuel cell and, thus, allowed for higher current densities to be reached.

When comparing test two and three data, it was observed that test two had better performance at higher current densities. Similar to what was discussed above, this phenomenon can most likely be explained by the enhanced water removal at higher flow rates (*i.e.*, 0.2 L/min hydrogen and 0.5 L/min air for test three vs. 0.9 L/min hydrogen and 1.2 L/min air for test two). This enhanced water removal prevented excessive water accumulation within the MEA (*i.e.*, that could have restricted the oxidant from reaching the catalyst layer) and, thereby, allowed higher current densities to be reached.

Based on the results of this investigation, it was determined that the miniaturized fuel cell had better performance under high flow rate conditions (*i.e.*, compared to low flow rate conditions). However, this research was undertaken to investigate water distribution through *in-operando* XCT experiments for a range of operating conditions. Under high flow rate conditions, the XCT results were similar across a range of current densities. Hence, this testing configuration made it difficult to evaluate the effects of current density on liquid water distribution within the cathode GDL. For this reason, low flow rates were used for the majority of the subsequent *in-operando* XCT experiments.

## 4.2. Evaluation of the Effects of Temperature Variation on the Performance of PEMFCs

This study was designed to evaluate the influence of operating temperature on the performance of a miniaturized PEM fuel cell (*i.e.*, active area of 0.316 cm<sup>2</sup>; 11.5 by 2.75 mm). All of the relevant information on the equipment and procedures used in these experiments is described in the Methods section of this document (*i.e.*, Section 3.9). Nevertheless, an overview of the testing methodology is provided as context for the results presented in this section. Briefly, two operational setups were used, including direct connection of the cell to the Scribner test station (*i.e.*, referred to as regular testing or regular setup); and, *in-operando* setup (*i.e.*, inside the XCT machine; referred to as XCT stage testing or XCT stage setup) to evaluate the effect of temperature on fuel cell performance. A total of six operating temperatures were evaluated in these trials (30°C, 50°C, 60°C, 70°C, 80°C, and 90°C). All of the tests were conducted at 0.9 L/min H<sub>2</sub> and 1.2 L/min Air, and 100% RH. The fuel cell temperature was controlled using heated gases, with the inlet gas temperature set 4 - 5°C higher than cell in the Direct Scribner set-up (*i.e.*, to compensate for the additional cooling within the gas tubes) and 10 - 15°C higher than cell for the *operando* setup (*i.e.*, to allow for greater cooling in the longer gas tubes).

### 4.2.1. Application of Scribner Setup

Polarization curves were generated by directly connecting the cell to the Scribner 850C Test Station, with the results of trials conducted at various temperatures shown in Figure 21(a) and (b). More specifically, Figure 21(a) displays polarization curves for operating temperatures ranging from 30°C to 70°C, while Figure 21(b) shows the polarization curves for operating temperatures ranging from 70°C to 90°C. The results presented in Figure 21(a) show that the best performance was achieved at 70°C, with performance decreasing at each of the temperatures tested below 70°C (*i.e.*, performance was lowest at 30°C). For example, cell voltage was 0.61 V at 70°C and 1000 mA/cm<sup>2</sup> and decreased to 0.54 V at 30°C and 1000 mA/cm<sup>2</sup> (Figure 21(a)). In addition, modest decreases in fuel cell performance were also observed at operating temperatures above 70°C (Figure 21(b)), with a voltage of 0.59 V observed at 1000 mA/cm<sup>2</sup> when operated at 90°C. Collectively, these results demonstrate that the cell tested in this study operated most efficiently at 70°C. However, the differences in

performance between 70°C and 80°C were negligible, suggesting that optimum performance is likely to be achieved at temperatures in this range.

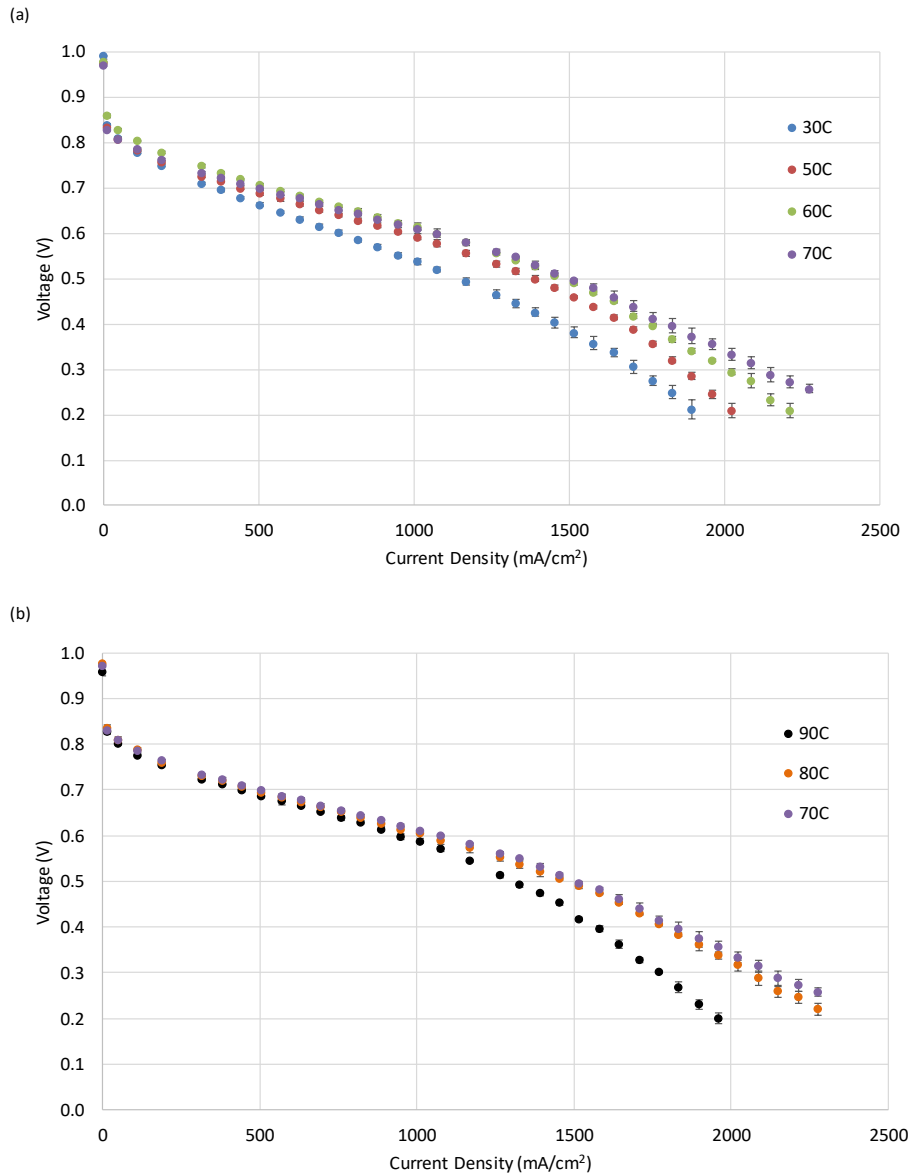


**Figure 21. Polarization curves generated for a PEMFC operated at temperatures ranging from: (a) 30 to 70°C; and, (b) 70 to 90°C.**

Electrochemical impedance spectroscopy (EIS) is a diagnostic tool for fuel cells that provides useful information for interpreting performance data. Importantly, EIS data can be used to estimate the high frequency resistance (HFR) of the cell, which closely relates to the ohmic resistance (impedance) of the membrane (*i.e.*, which is a function of the degree of humidification of the membrane). The HFR is determined from a Nyquist

plot by determining the internal resistance of the cell when capacitance is equal to zero (O'Hayre *et al.* 2016).

In order to further understand the influence of temperature on performance, EIS was measured at all operating temperatures between 30°C and 90°C. The HFR values for the fuel cell at each of the selected temperatures were derived from these measurements (Figure 22). These results demonstrate that the internal resistance in the fuel cell (*i.e.*, HFR) decreases with increasing operating temperature. This suggests that the decrease in performance that was observed at temperatures below 70°C can be attributed to an increasing ohmic resistance within the cell at lower operating temperatures (Belkhiri *et al.* 2011). Furthermore, at temperatures below 70°C, the electrochemical reaction rate of the fuel cell also decreases (Kawase *et al.* 2017). Hence, these two factors likely account for the majority of the performance losses at operating temperatures below 70°C. The differences in performance between operating temperatures were minor within the activation range (Figure 21(a) and (b)), suggesting that the activation losses are not driving the low-temperature performance losses in these trials.

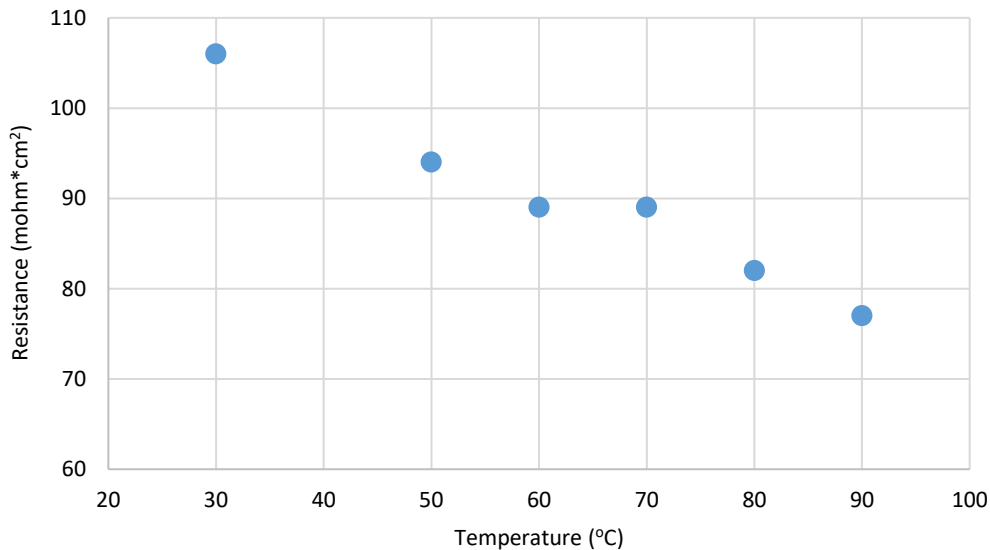


**Figure 22. High frequency resistance derived from EIS measurement vs. operating temperature of a PEMFC.**

Figure 21(b) shows that fuel cell performance was highest at 70°C and decreased at higher operating temperatures. However, since the HFR also decreased

with increasing temperatures above 70°C, it can be hypothesized that changes in membrane conductivity is not the primary factor influencing cell performance at higher operating temperatures. Upon closer inspection of the polarization curves shown in Figure 21(b), it appears that the differences in performance were minor within the activation and ohmic regions of the curves, with the main losses occurring within the mass transport region. This is especially evident from the data generated at 90°C, where a large reduction in voltage was observed at current densities greater than 1250 mA/cm<sup>2</sup>. However, the specific mechanisms that caused these voltage losses are not fully understood. One possible explanation for these results is that the temperature drop of the gases (*i.e.*, about 5°C) between their source (*i.e.*, Scribner Test Station) and the cell resulted in condensation within the gas tubes. At higher temperatures, more water is held in the vapor phase and, thus, more of the moisture in the influent gas condenses when the vapor cools during transport within the gas tubes. This condensed water could be blocking the channels and the pores in the GDL of the fuel cell, thereby restricting the delivery of oxidant to the catalyst layer on the cathode side of the cell.

#### 4.2.2. Application of *In-Operando* Setup

X-ray computed tomography-based techniques were used to study the influence of varying operating temperatures on the liquid water distribution within the GDL of operating fuel cells. To generate *in-operando* XCT images, the cell was situated within a ZEISS Xradia 520 Versa micro-XCT system. In order to operate the fuel cell within this system, long gas tubes and load wires were run from the Scribner to the XCT. The long gas tubes resulted in greater gas temperature losses between the Scribner and the cell (*i.e.*, due to the temperature difference between the influent gases and the ambient air); thus, it is likely that more liquid water condensation occurred in this setup (*i.e.*, compared to the direct Scribner setup). Additionally, the longer load wires likely created a higher ohmic resistance, which resulted in lower voltages compared to the Scribner setup. These two factors negatively impacted the performance of the fuel cell and, hence, an additional performance analysis was done for the tests conducted under *in-operando* conditions.

Figure 23(a) and (b) display the polarization curves generated for a fuel cell operating within the XCT machine. The temperatures evaluated ranged from 30°C to

90°C. Figure 23(a) displays the results for temperatures ranging from 30°C to 70°C, while Figure 23(b) shows the results for temperatures between 70°C and 90°C.

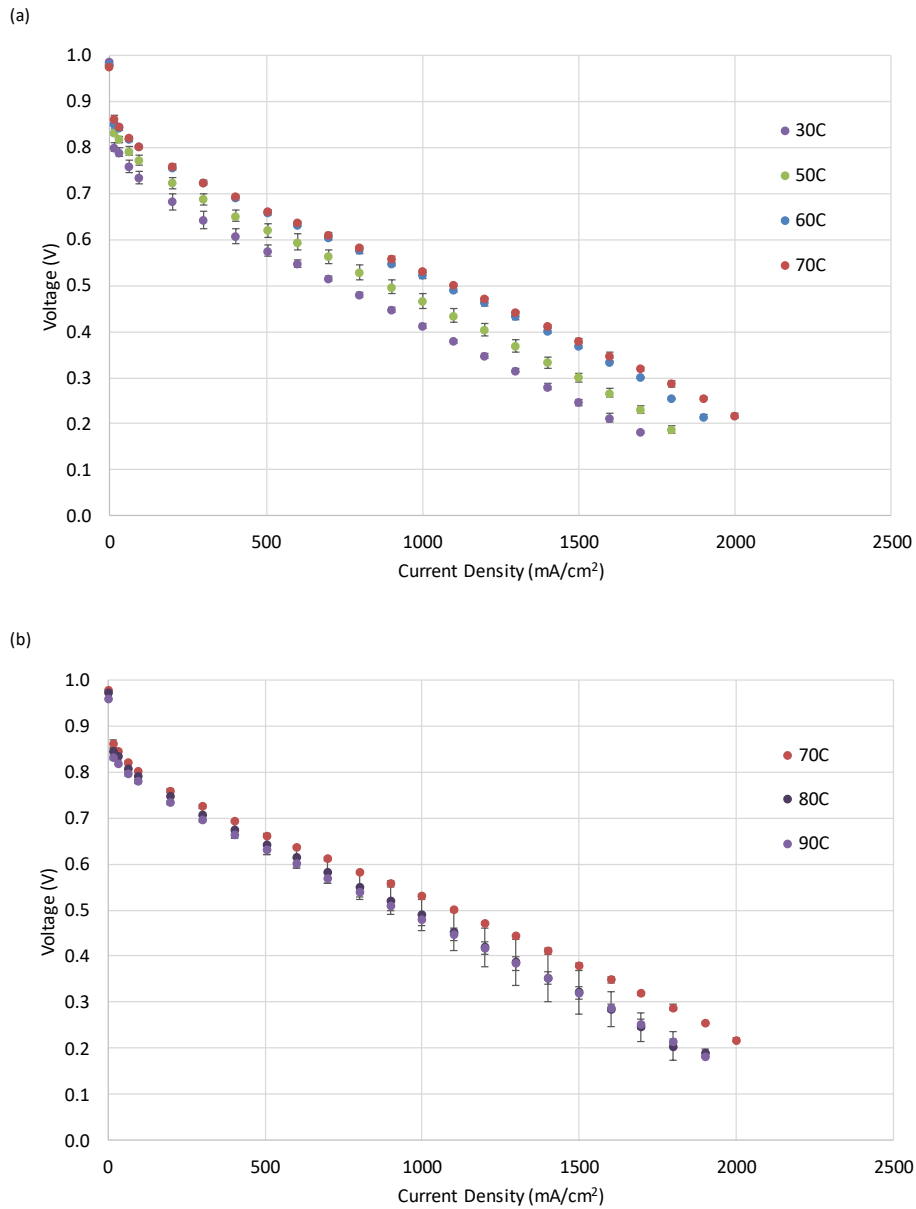


**Figure 23. Polarization curves generated for a PEMFC operated at temperatures ranging from: (a) 30 to 70°C; and, (b) 70 to 90°C, under *in-operando* conditions.**

The results of this analysis are consistent with the data shown in Figure 21(a) and (b), with the peak performance of the cell under *in-operando* conditions observed at 70°C. Decreasing fuel cell performance was observed at both temperatures lower and

higher than 70°C. As was the case for the Scribner setup, the reduced performance at lower temperatures can be explained by changes in the HFR, whereas those observed at higher temperatures are likely due to mass transport losses. Although the trends were similar for the tests conducted using the two setups, the overall performance was substantially lower for the *in-operando* tests. As discussed above, this reduced performance was likely due to additional water condensation due to cooling of the gases in the longer influent gas tubes and higher resistance associated with the longer load wires.

The purpose of these trials was to generate comparable data using the two test setups. However, the results showed that the performance of the fuel cell in the XCT setup was not directly comparable to those obtained using the direct Scribner approach. To make the data generated under the two setups more comparable, the polarization curves measured within the XCT were further studied in order to adjust for the voltage losses that occurred due to the higher resistance in the long load wires used in the latter setup.

Figure 24(a) and (b) display the *in-operando* polarization curves that have been corrected for the additional resistance in the longer load wires that run between the Scribner and the XCT system (See Chapter 3, Methods, for more information on the two setups). Based on the analysis conducted, the long load wires increased the overall resistance by approximately 0.23 ohm. Accordingly, the voltages measured during the *in-operando* tests were adjusted to account for the higher resistance. Figure 24(a) presents the results for temperatures ranging from 30°C to 70°C, while Figure 24(b) presents the results for temperatures ranging from 70°C to 90°C. As expected, the correction of the ohmic resistance led to a substantial improvement of the cell voltage. For example, at 70°C and 1 A/cm<sup>2</sup>, the voltage improved from 0.531 V to 0.605 V and at 2 A/cm<sup>2</sup>, the voltage increased from 0.218 V to 0.366 V. The correction for the resistance in the wires compensated for most of the differences in performance observed between the two setups. The remaining differences may be attributed to the additional condensation within the influent gas lines leading to the XCT (*i.e.*, which are longer than those used in the Scribner set-up and, hence, results in additional cooling of the influent gases).

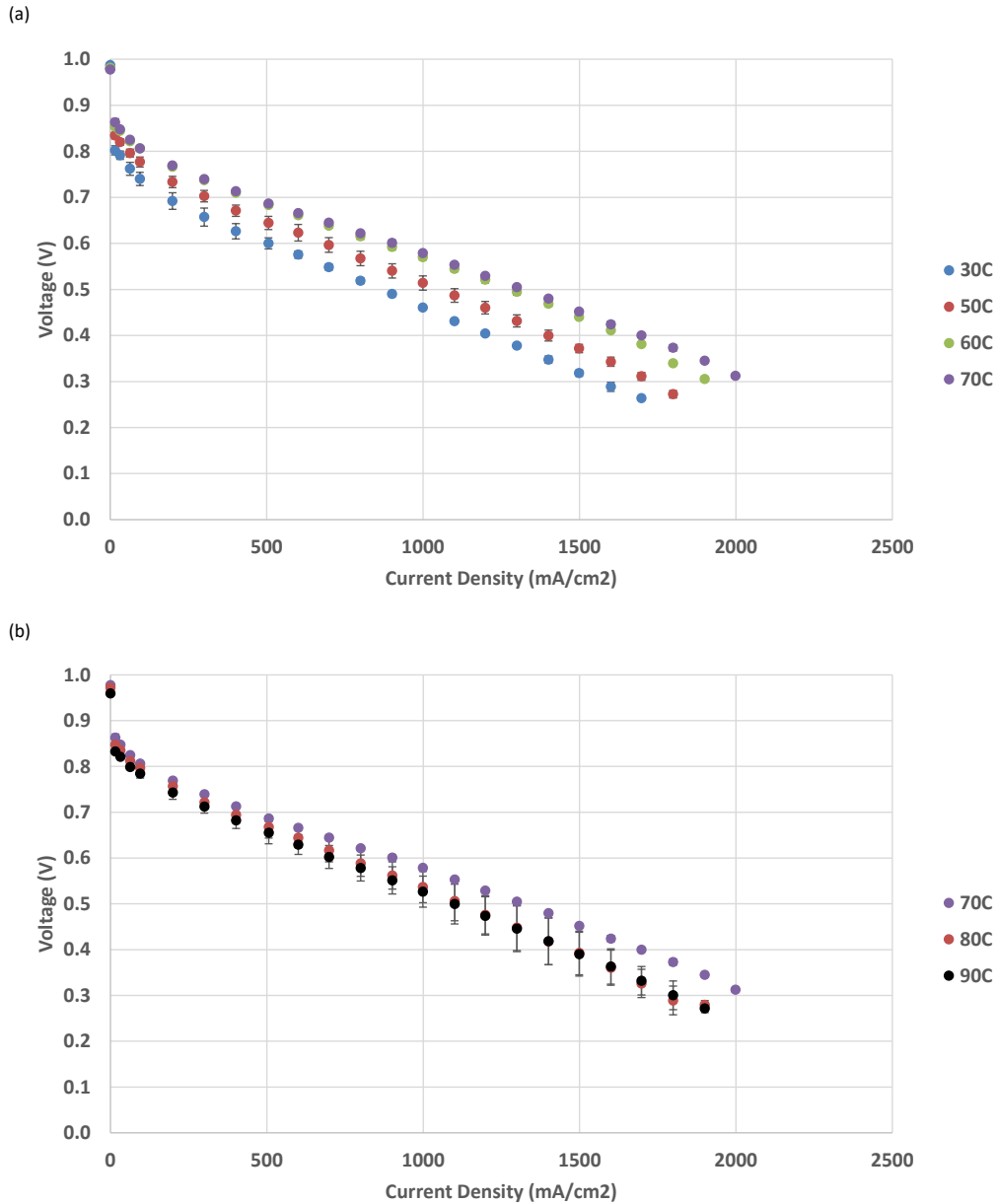


**Figure 24. Resistance corrected polarization curves generated for a PEMFC operated at temperatures ranging from: (a) 30 to 70°C; and, (b) 70 to 90°C, under in-operando conditions.**

In summary, the results of these experiments demonstrated that the Avcarb GDL used in the fuel cell operated most efficiently at 70°C. While few losses were observed within the activation region below this temperature, ohmic and activation losses resulted in lower voltages in the cell. At higher temperatures (*i.e.*, >70°C), mass transport losses were likely responsible for the lower performance that was observed. The performance

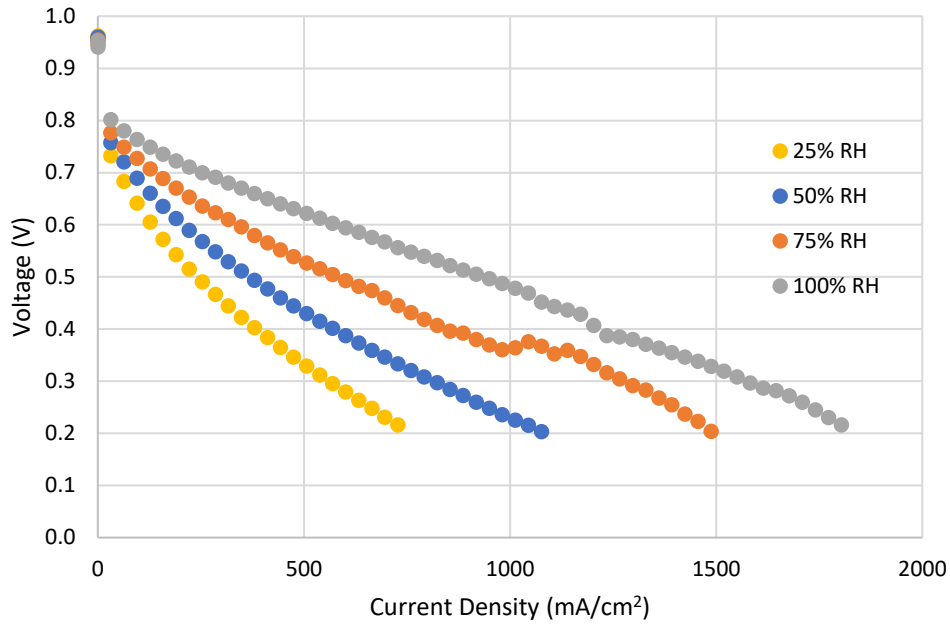
data generated under *in-operando* conditions showed that the cell was less efficient under these operating conditions. Based on the analysis conducted, it was concluded that these voltage losses were likely caused by the long load wires and long gas delivery tubes used for the XCT system. Most of the differences between the systems could be compensated for by applying a resistance correction to the resultant data. The residual differences observed between the results obtained for the two setups were likely due to additional mass transport losses associated with the long gas delivery tubes, leading to increased condensation of water vapour in the lines leading to the cell and/or in flow channels of the cell.

## 4.3. Evaluation of the Effect of Varying Relative Humidities on Cell Performance and Liquid Water Distribution at Various Temperatures

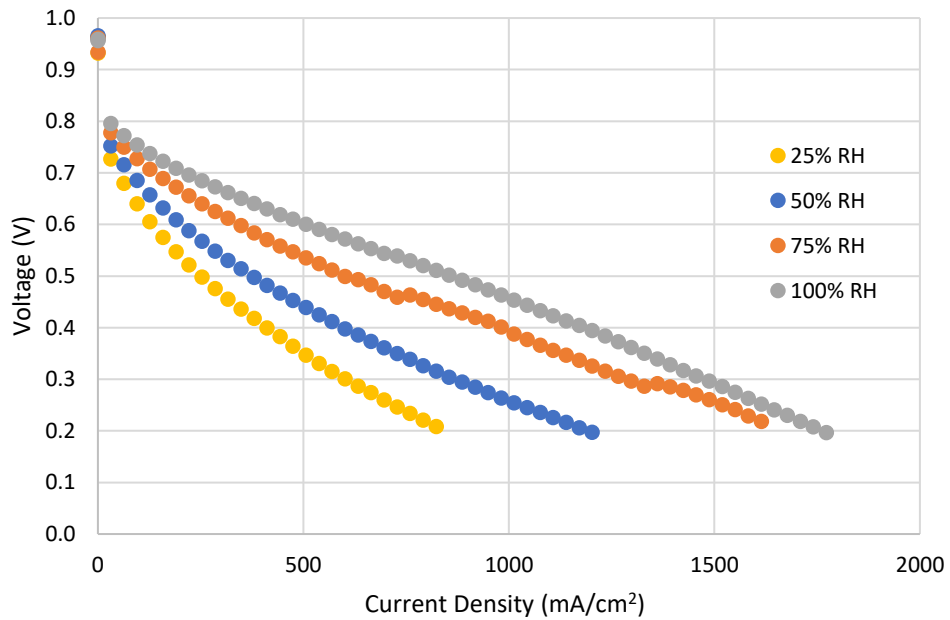
### 4.3.1. Experimental Results

This study was designed to evaluate the influence of changes in relative humidity on the performance of a miniaturized PEMFC at selected temperatures. The relevant information on the equipment and procedures used in these experiments is described in the Methods section of this document (*i.e.*, Section 3). Nevertheless, an overview of the testing methodology is provided as context for the results presented in this section. Briefly, a total of four influent gas RHs (25%, 50%, 75% and 100%) and four temperatures (40°C, 50°C, 60°C and 70°C) were tested on a Greenlight G20 station. At each unique operating condition (*e.g.*, 50% RH and 60°C,) three polarization curves were generated to support diagnostic analysis. The results of these trials are presented and discussed in this section.

Figure 25 displays polarization curves generated at 70°C with RHs ranging from 25% to 100%, while Figure 26 shows the polarization curves generated at 60°C with RHs ranging from 25% to 100%. The results presented in both Figure 25 and Figure 26 show that the best performance of the fuel cell was achieved at 100% RH, with performance decreasing at each of the RHs tested below 100% (*i.e.*, performance was lowest at 25% RH). Based on examination of the curves generated, it appears that the impaired performance at lower RHs is primarily due to voltage losses within the ohmic and activation regions. The increased ohmic resistance at lower RHs can be largely attributed to lower membrane hydration and associated reduced membrane permeability. In contrast, activation losses are potentially occurring due to poor platinum utilization at lower RHs (*i.e.*, the rates of the ORR and/or HOR are lower when RH is below 100%). At reduced RHs, lower ionomer hydration likely results in lower proton conductivity and, thus, fewer active sites being utilized within the catalyst layer (Jeon *et al.* 2010).



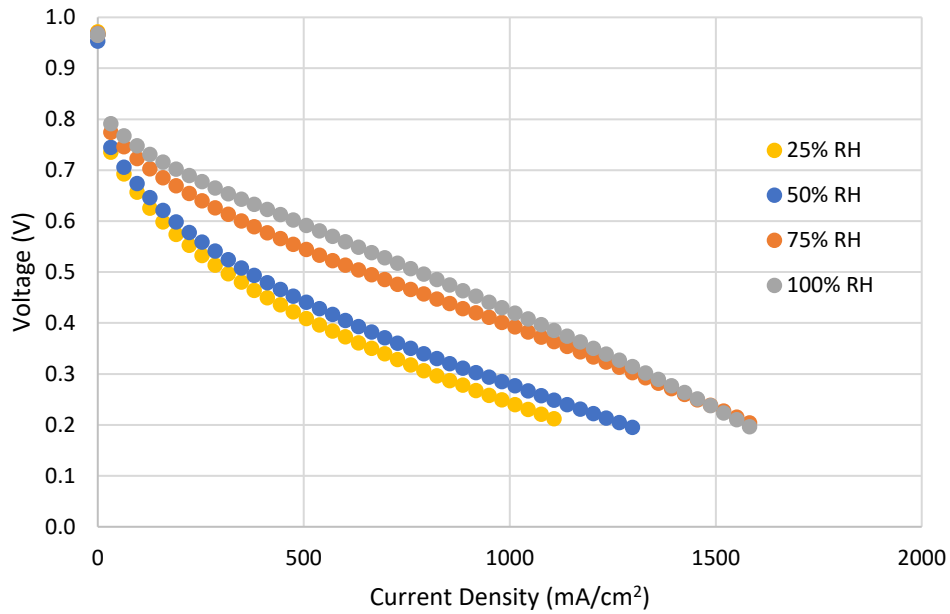
**Figure 25. Polarization curves generated for a PEMFC operated at 70°C and RHs ranging from 25% to 100%.**



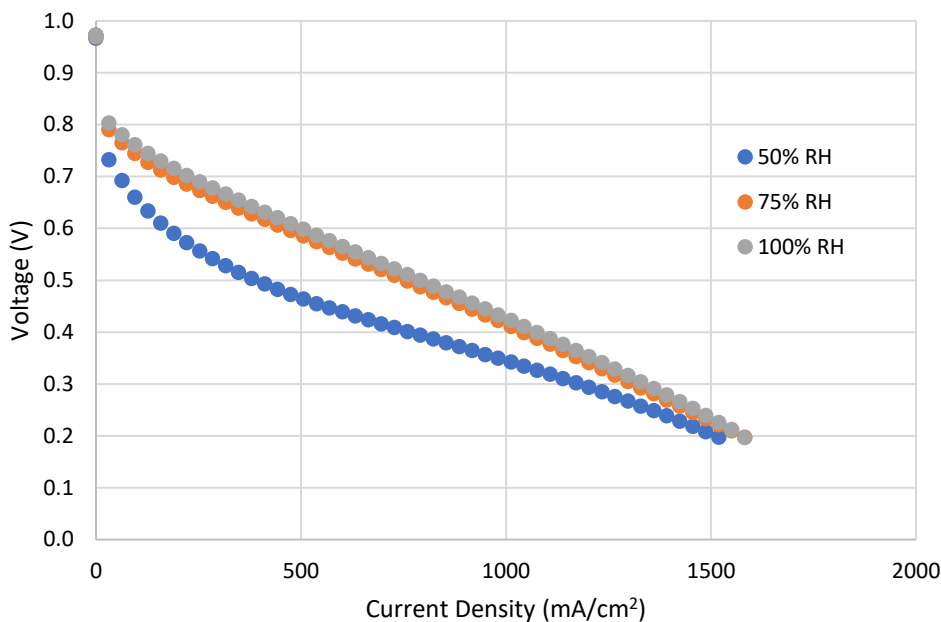
**Figure 26. Polarization curves generated for a PEMFC operated at 60°C and RHs ranging from 25% to 100%.**

Figure 27 and Figure 28 display polarization curves generated at 50°C and 40°C, which had RHs ranging from 25% to 100% and 50% to 100%, respectively. Similar to

what was observed at 60°C and 70°C, the highest performance was observed at 100% RH and performance decreased substantially with decreasing RH. However, at the lower operating temperatures (*i.e.*, 40°C and 50°C), activation losses appeared to be the dominant factor causing the performance reductions at lower RHs, with minimal to no differences in performance within the ohmic region over the range of RHs tested.

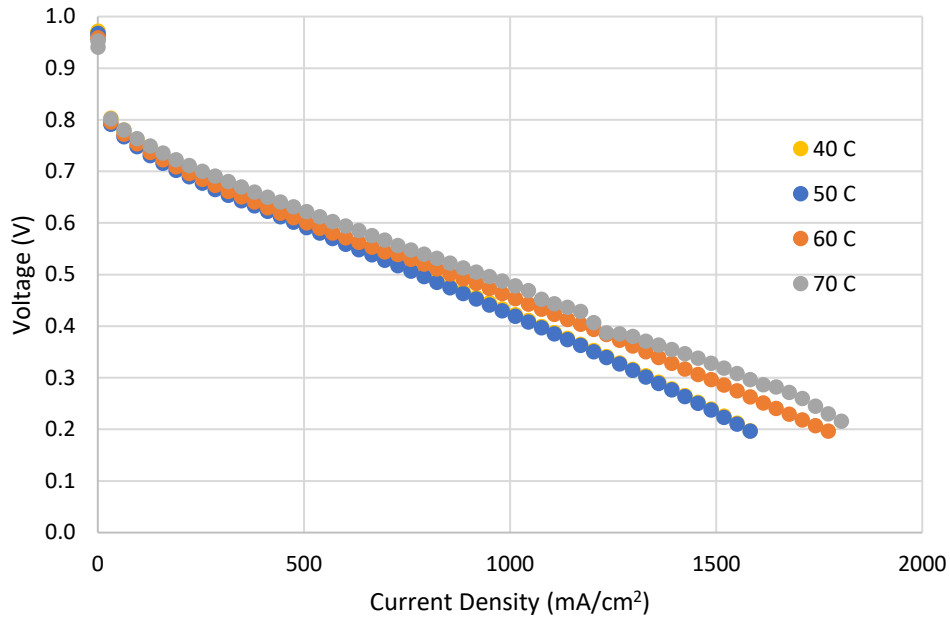


**Figure 27. Polarization curves generated for a PEMFC operated at 50°C and RHs ranging from 25% to 100%.**

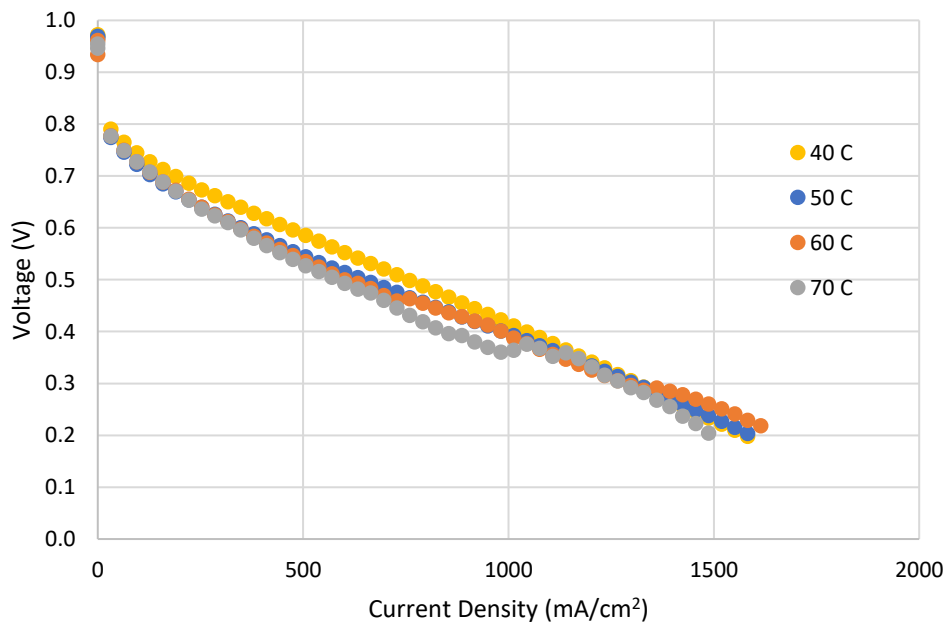


**Figure 28. Polarization curves generated for a PEMFC operated at 40°C and RHs ranging from 50% to 100%.**

Figure 29 and Figure 30 display polarization curves generated at 100% and 75% RH, respectively, for temperatures ranging from 40°C to 70°C. The results presented in Figure 29 show that the best performance was achieved at 70°C, while the lowest performance was achieved at 40°C. In addition, a trend of modestly decreasing performance with decreasing temperature was observed. The performance improvement at 70°C compared to 40°C can primarily be attributed to improved membrane hydration (*i.e.*, higher membrane conductivity) and increased reaction kinetics (*i.e.*, reduced activation losses; Ozen *et al.* 2016). Additionally, at 70°C, there appears to be reduced mass transport losses (*i.e.*, at higher current densities). Although similar trends were observed at 75% RH (Figure 30), the differences in performance were minimal at the four temperatures that were tested.



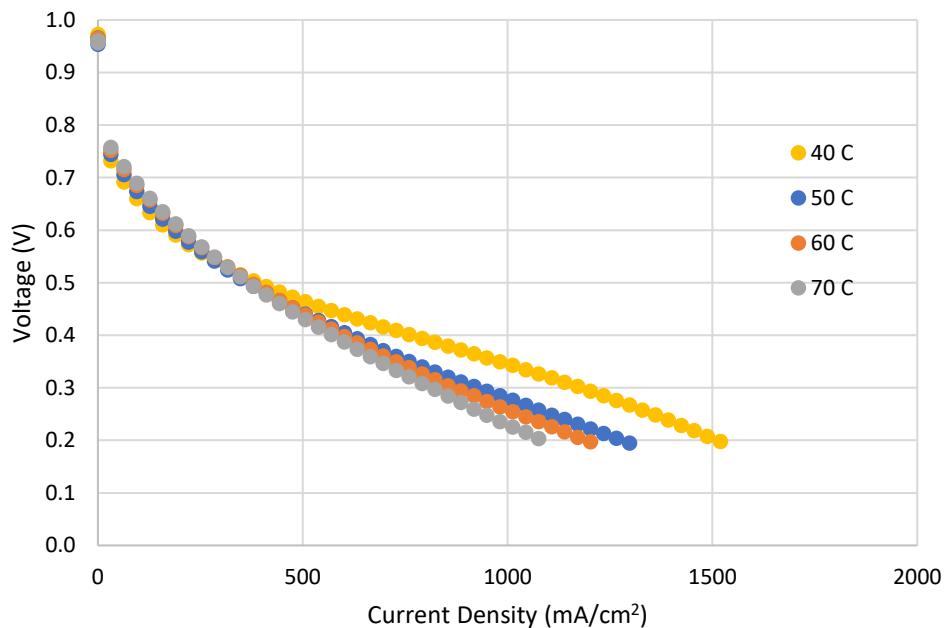
**Figure 29. Polarization curves generated for a PEMFC operated at 100% RH and temperatures ranging from 40°C to 70°C.**



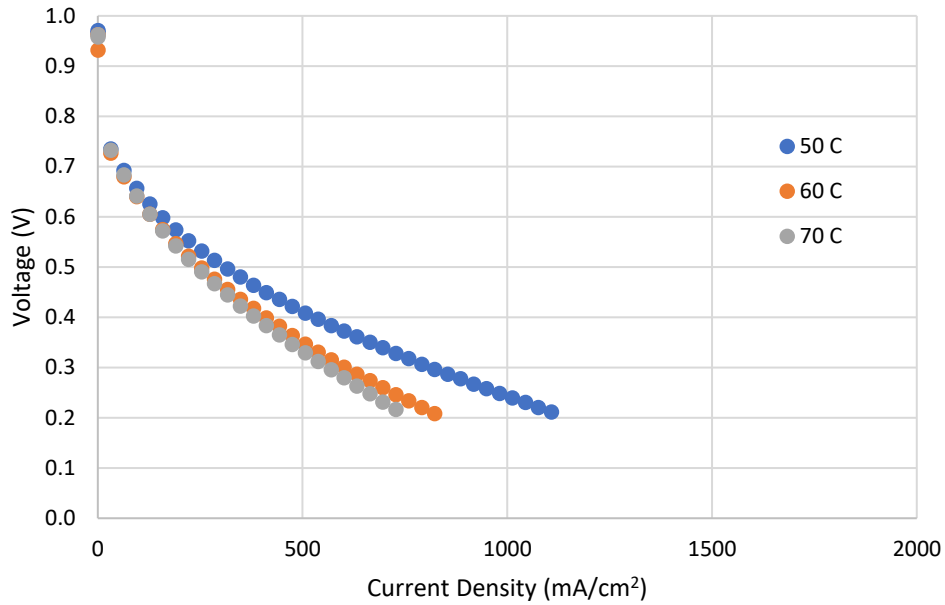
**Figure 30. Polarization curves generated for a PEMFC operated at 75% RH and temperatures ranging from 40°C to 70°C.**

Figure 31 and Figure 32 display polarization curves generated at 50% and 25% RH, for temperatures ranging from 40°C to 70°C and 50°C to 70°C, respectively. For the

results generated at both 50% and 25% RH, the highest performance was achieved at the lowest temperature tested (*i.e.*, 40°C at 50% RH and 50°C at 25% RH). These results differ from the trials conducted at 100% RH, where the highest performance was achieved at the highest temperature tested (*i.e.*, 70°C). Based on the results presented in Figure 31 and Figure 32, the primary voltage losses are occurring in the ohmic region. This indicates that at low RHs, greater membrane hydration can be achieved at lower temperatures potentially due to wetter conditions within the GDL/MPL region. More specifically, at the lower temperatures tested, the water produced in the fuel cell may aid ionomer and membrane hydration as the current density is increased.



**Figure 31. Polarization curves generated for a PEMFC operated at 50% RH and temperatures ranging from 40°C to 70°C.**



**Figure 32. Polarization curves generated for a PEMFC operated at 25% RH and temperatures ranging from 50°C to 70°C.**

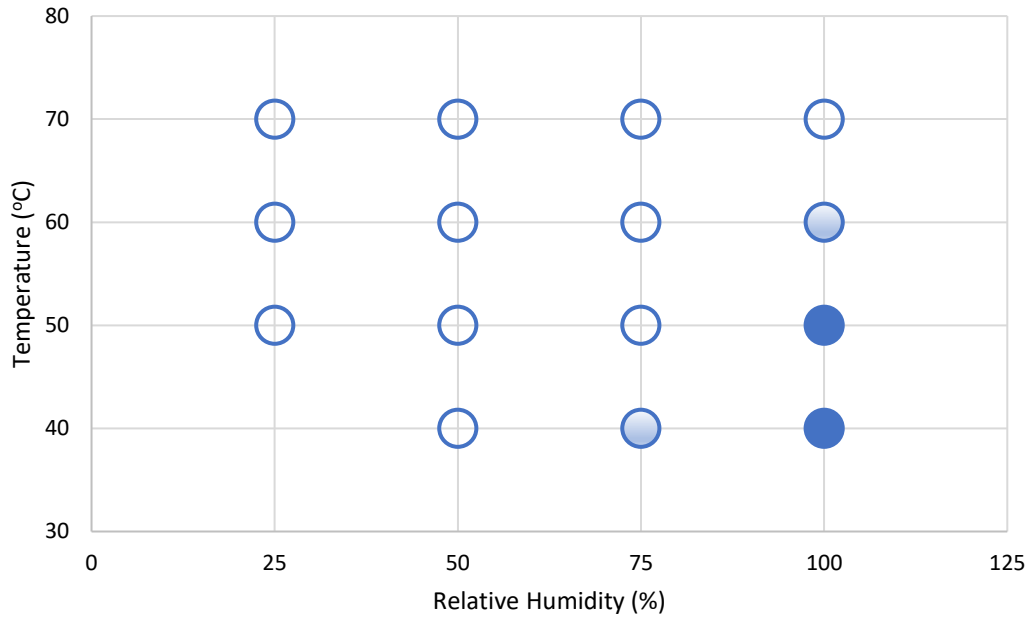
### 4.3.2. Model Results

A one-dimensional model (as described in Section 3.10) was used to conduct a series of trials to predict the effect of changes in RH on liquid water distribution within the GDL substrate at various temperatures. Three separate types of graphs were generated to assist in the analysis and interpretation of the resultant data. First, a summary map was generated that predicts whether the GDL is likely to be wet (*i.e.*, oversaturated; greater than 100% RH), dry (*i.e.*, vapour dominated; less than 100% RH) or in transition from wet to dry. From this summary map, a transition region map was generated for the identified transition regions that forecasts the state of water at four different current densities (*i.e.*, 500, 750, 1000, and 1250 mA/cm<sup>2</sup>). The final type of plot displays the estimated ratio of water vapor pressure to saturation vapor pressure versus the distance from the CL for each selected condition that was run in the model. These results are presented and discussed in the following sections.

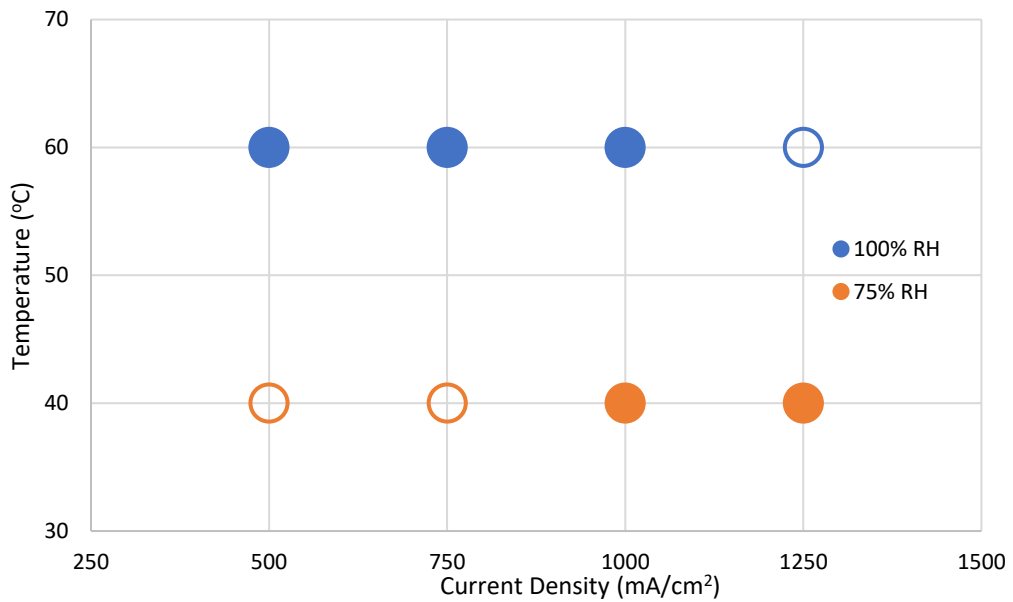
#### 4.3.2.1. Channel Region

Figure 33 provides a summary of the conditions within the GDL under the channels under fifteen different operational conditions, as predicted by the model. The

open circle indicates dry conditions, the filled circle indicates wet conditions, and the gradient circle indicates conditions that are transitioning between the wet and dry state. The map (Figure 33) shows that wet conditions are predicted within the GDL during operation at 40°C and 50°C with 100% RH, while a transition condition is predicted for 60°C with 100% RH and for 40°C with 75% RH. The GDL was predicted to be dry under all of the other operating conditions considered. Figure 34 presents a more detailed evaluation of conditions within the two identified transition regions under the channels, and displays the state of water at four different current densities. For the transition region at 60°C and 100% RH, the model predicts wet conditions at 500, 750 and 1000 mA/cm<sup>2</sup> and dry conditions at 1250 mA/cm<sup>2</sup>. These results could suggest that the dry conditions at 1250 mA/cm<sup>2</sup> are caused by increased heat production at the higher current density. This increased heat production is raising the saturation vapor pressure and, in turn, reducing condensation. For the transition region at 40°C and 75% RH the model predicts wet conditions at 1000 and 1250mA/cm<sup>2</sup> and dry conditions at 500 and 750 mA/cm<sup>2</sup>. These results could indicate that, at the lower current densities tested, there is insufficient water production at the CL to raise the water vapor pressure enough to reach a point of saturation.



**Figure 33.** RH variation map for under the channels displaying a wet, dry or in transition from wet to dry GDL at fifteen separate operational conditions.



**Figure 34.** Transition region map for under the channels displaying wet or dry conditions within the GDL at four different current densities at two identified transition regions conditions.

Figure 35 and Figure 36 display the ratio of water vapor pressure to saturation vapor pressure under the channels at 60°C and 100% RH and at 40°C and 75% RH, respectively, for four different current densities. The black dashed line indicates the boundary between wet and dry conditions. The values below one indicate that no condensation is likely to be occurring (*i.e.*, predominantly dry conditions are present); whereas values above one indicate that condensation is likely to be occurring (*i.e.*, predominantly wet conditions are present). As discussed above for 60°C and 100% RH, the model predicts wet conditions at 500, 750 and 1000 mA/cm<sup>2</sup> and dry conditions at 1250 mA/cm<sup>2</sup> (Figure 35). Similarly, at 40°C and 75% RH the model predicts wet conditions at 1000 and 1250 mA/cm<sup>2</sup> and dry conditions at 500 and 750 mA/cm<sup>2</sup> (Figure 36). However, based on the results presented in Figure 36, condensation is only occurring up to 15 and 40 μm from the CL at 1000 and 1250 mA/cm<sup>2</sup>, respectively. After these points, the ratio of water vapor pressure to saturation vapor pressure is too low to result in additional condensation. Instead, evaporation of liquid water is feasible and likely to occur further into the GDL substrate. It is important to note that all of the curves displayed in Figure 35 and Figure 36 are close to transition, *i.e.*, 100% RH, throughout the GDL, and local variations in liquid water presence are likely to occur.

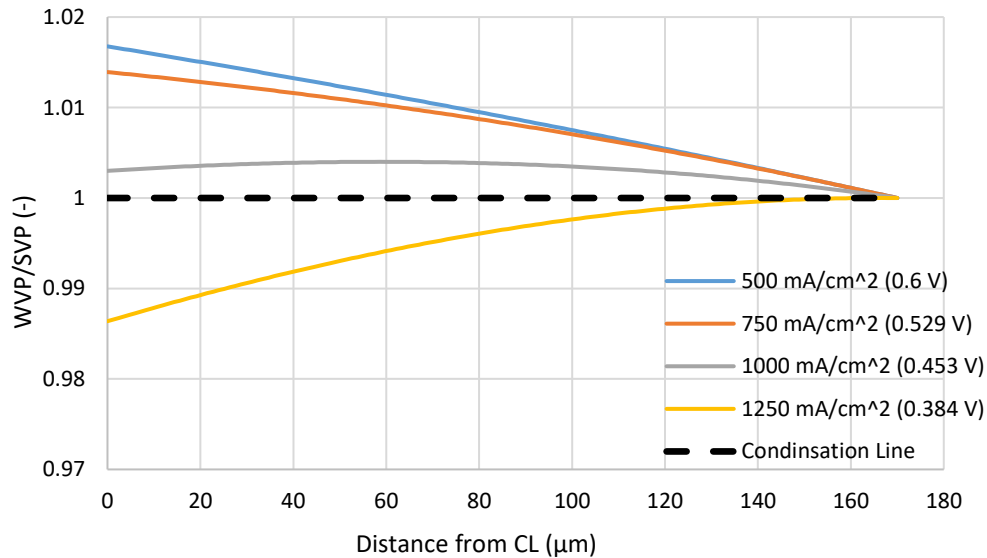


**Figure 35.** Plot displaying the ratio of water vapor pressure to saturation vapor pressure under the channels at 60°C and 100% RH for four different current densities.

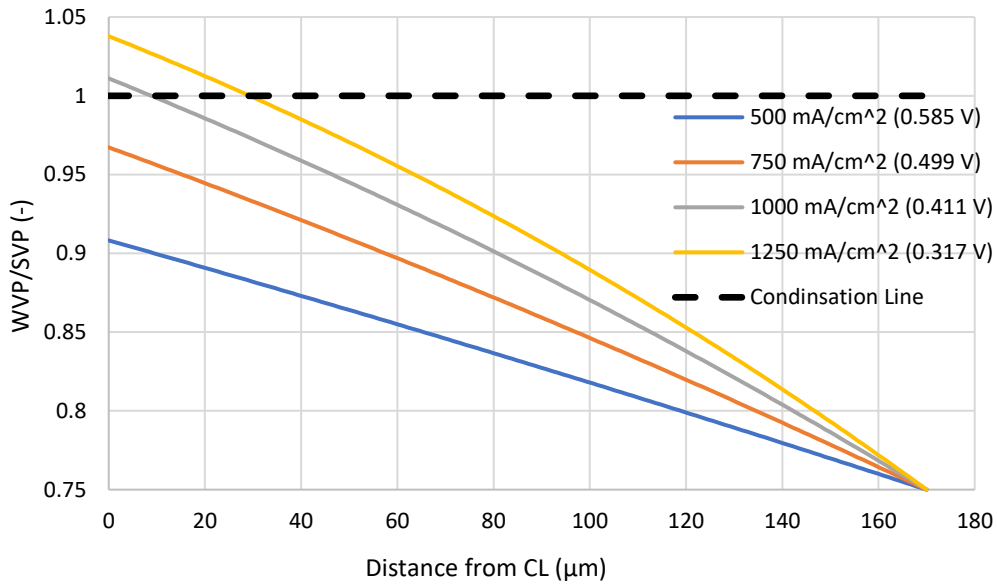


**Figure 36.** Plot displaying the ratio of water vapor pressure to saturation vapor pressure under the channels at 40°C and 75% RH for four different current densities.

#### 4.3.2.2. *Lands Region*

Figure 37 presents a summary of the conditions within the GDL under the lands at fifteen different operational conditions, as predicted by the model. The RH variation map shows that wet conditions are predicted within the GDL during operation at all temperatures with 100% RH, while a transition region is predicted at 40°C with 75% RH. All other conditions were predicted to be dry. Figure 38 presents predictions of the state of water for the transition region that occurred at 40°C with 75% RH at four different current densities. Under those operational conditions, the model predicted wet conditions at 750, 1000 and 1250 mA/cm<sup>2</sup> and dry conditions at 500 mA/cm<sup>2</sup>. Again, these results could suggest that the dry conditions predicted at the lower current density (*i.e.*, 500 mA/cm<sup>2</sup>) is resulting from insufficient water production to raise the water vapor pressure above the saturation vapor pressure within the GDL.

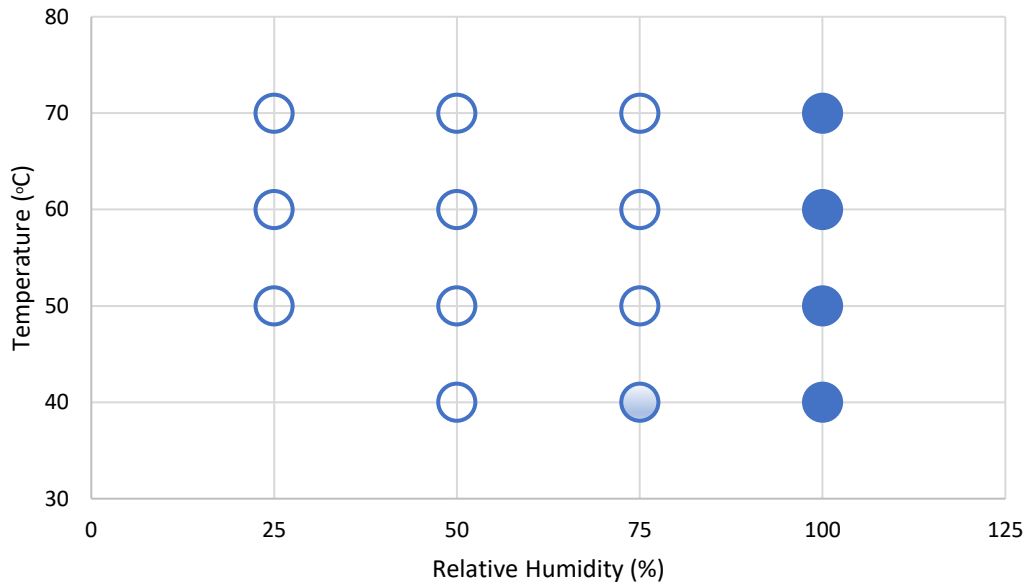


**Figure 37.** RH variation map for under the lands displaying a wet, dry or in transition from wet to dry GDL at fifteen separate operational conditions.

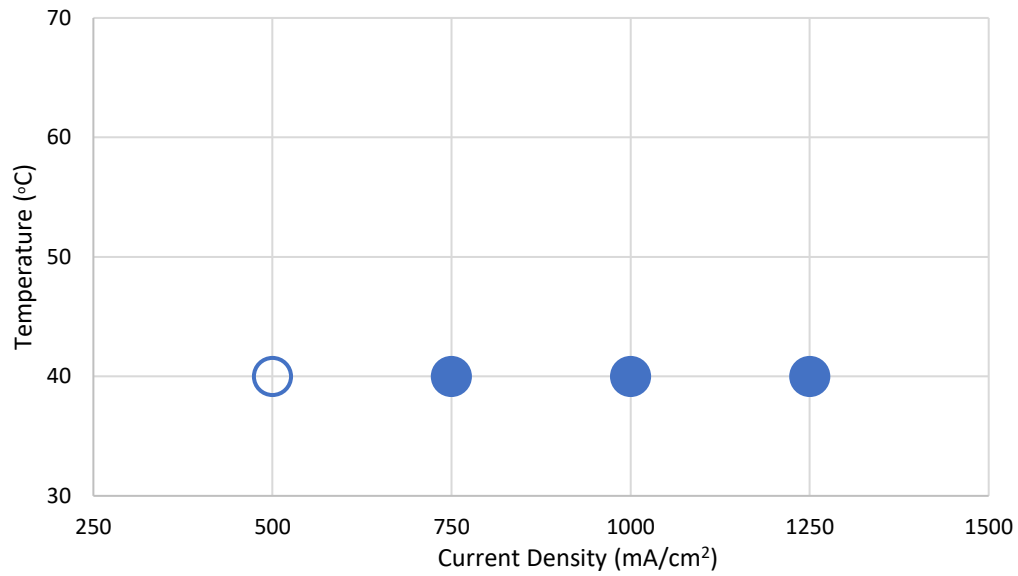


**Figure 38.** Transition region map for under the lands displaying wet or dry conditions within the GDL at 40°C and 75% RH for four different current densities.

Figure 39 presents the ratio of water vapor pressure to saturation vapor pressure under the lands at 40°C and 75% RH for four different current densities. Similar to

Figure 38 above, Figure 39 shows that, at 40°C and 75% RH, the model predicts wet conditions at 750, 1000 and 1250 mA/cm<sup>2</sup> and dry conditions at 500 mA/cm<sup>2</sup>. However, Figure 39 also indicates that condensation is only occurring up to 20, 40 and 60 μm from the CL, for 750, 1000 and 1250 mA/cm<sup>2</sup>, respectively. No additional condensation is predicted to occur after these points in the GDL, where evaporation of liquid water is more likely.

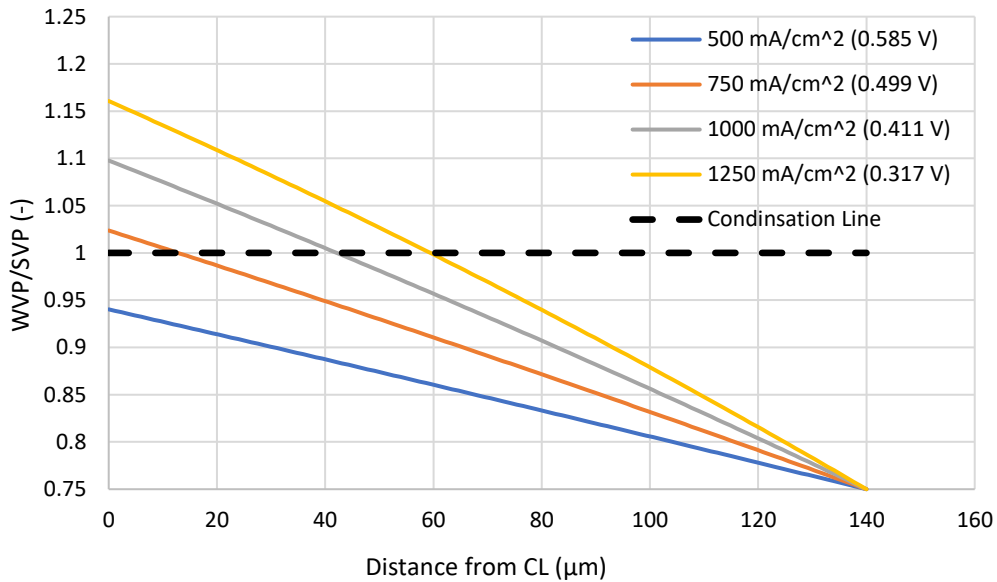


**Figure 39.** Plot displaying the ratio of water vapor pressure to saturation vapor pressure under the lands at 40°C and 75% RH for four different current densities.

In summary, the experimental data generated in the RH variation analysis in Section 4.3.1 were used to parameterize the predictive model. Therefore, it is reasonable to make comparisons between the model outputs and the experimental data. From the polarization curves presented in Figure 29, it is apparent that increased mass transport losses are likely occurring during fuel cell operation at 40°C and 50°C under 100% RH with current densities above 1 A/cm<sup>2</sup>. By comparison, the model predicts wet conditions under both the channel and land regions at these temperatures and RH (Figure 33 and Figure 37 respectively). These wetter conditions could be restricting oxygen diffusion to the CL, resulting in the observed increase in mass transport losses. Additionally, the model predicts dry conditions at the lower RHs tested (*i.e.*, 25, 50 and 75%). The polarization curves generated at all four temperatures (Figure 25 to Figure

28) show a decrease in performance with a decrease in RH, primarily due to increased activation and ohmic losses. These losses are indicative of low hydration and dryer conditions, which is predicted by the model at lower RHs. Therefore, it is concluded that the one-dimensional model applied in this investigation provides a reliable basis for predicting wet/dry/transition conditions in PEMFCs under a variety of operating conditions.

#### **4.4. Evaluation of the Effects of Current Density on the Distribution of Liquid Water Within the Gas Diffusion Layer**

There are many variables that can affect the performance of PEM fuel cells, such as temperature, pressure, gas flux, and various internal factors (Chen and Wu 2010). However, one of the main performance-modifying factors is water management within the fuel cell (Li *et al.* 2008). More specifically, maintaining an appropriate amount of water within the fuel cell is critical for reliable performance (Chen and Wu 2010). Too little water within the cell can lead to desiccation of the internal structures and impaired transport of protons. In contrast, too much water within the cell can lead to flooding and associated adverse effects on performance (Li *et al.* 2008). Hence, effective water management is essential for achieving optimal performance of PEM fuel cells.

This section presents the results of testing conducted to evaluate the influence of current density on the distribution of liquid water in an operating PEM fuel cell. The methods that were used in these experimental trials are described in Section 3.11 of this document. Therefore, only a brief overview of these methods are presented here. These tests were conducted using the *in-operando* setup of the Scribner test station, with testing conducted at 40°C, 50°C, 60°C and 70°C with 100% relative humidity. Gases were delivered at a rate of 0.2 L/min for H<sub>2</sub> and 0.5 L/min for Air/O<sub>2</sub>. The XCT was operated at an exposure time of 4 seconds, 801 projections, a voltage of 80 kV, a power of 7 W, and pixel size of 1.61 µm. All tests were conducted using an Avcarb GDL.

Water volume vs thickness curves provide effective tools for understanding the liquid water distribution within the GDL of operating fuel cells. In this study, XCT technology was utilized to generate images of the GDL during fuel cell operation. These images were processed and used to produce water volume profiles under varying operating conditions (*i.e.*, a range of current densities). Comparison of the resultant plots provides a means of identifying conditions that influence FC performance and, hence, relevant information for optimizing the management of liquid water within the fuel cell.

In this study, water volume was estimated within the GDL of the miniaturized fuel cell under a variety of operating conditions. This step in the water volume estimation process involved analysis of the segmented image set that was generated under each of the specific conditions that were tested. Using ImageJ, the number of white pixels (*i.e.*, number of pixels occupied by liquid water) was determined. This result was then multiplied by the volume occupied by one pixel (*i.e.*, 1.61  $\mu\text{m}$  length by 1.61  $\mu\text{m}$  width by 1.61  $\mu\text{m}$  height) to calculate the volume of water for that slice of the GDL. The volume that was determined for each slice of the GDL was then plotted against distance to generate the water volume vs. thickness plot. Two example image slices from a selected segmentation image set are shown in Figure 40 and Figure 41. Figure 40 represents a location approximately 70  $\mu\text{m}$  from the CL and Figure 41 represents a location close to the lands at approximately 110  $\mu\text{m}$  from the CL.

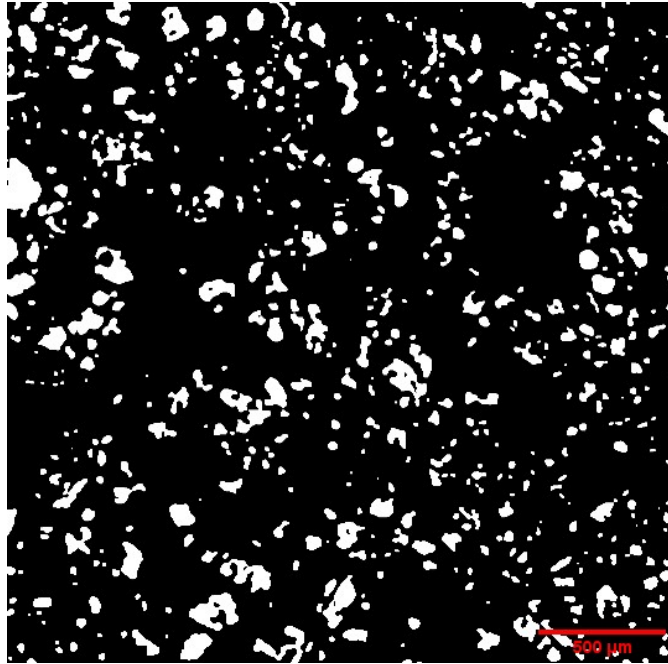


**Figure 40.** Example image slice from a segmented image set, which was located at approximately 70  $\mu\text{m}$  from the CL.

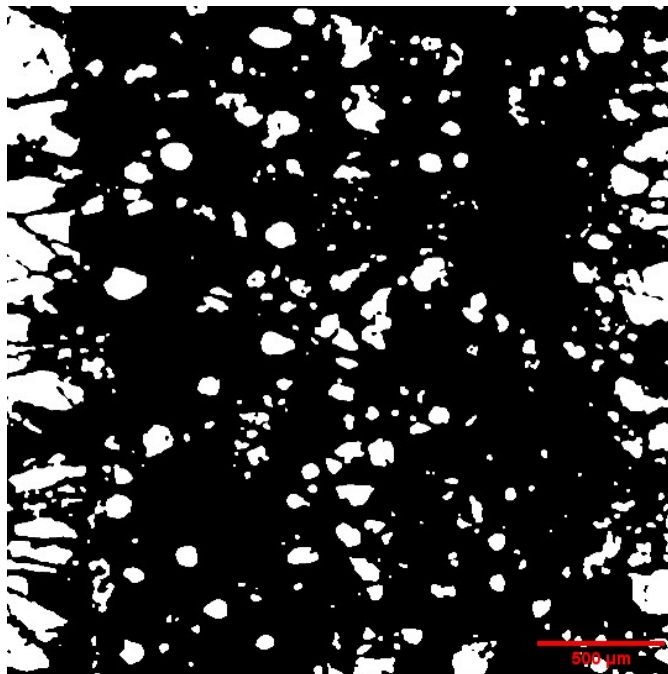


**Figure 41.** Example image slice from a segmented image set, which was located at approximately 110  $\mu\text{m}$  from the CL.

#### **4.4.1. Influence of Current Density at 40°C**

Figure 42 presents the overall water volume profile within the cathode GDL of a fuel cell operated at 40°C with current densities ranging from 500  $\text{mA}/\text{cm}^2$  to 1250  $\text{mA}/\text{cm}^2$ . The profile shows the water volume profile from a region close to the CCL (*i.e.*, where MPL/GDL pores become resolvable to a region proximal to the flow channel). The location on the curves where the volume peaks for the second time (*i.e.*, between 110  $\mu\text{m}$  and 130  $\mu\text{m}$ ) occurs at the GDL-lands interface. The location within the GDL where this point occurs varies somewhat for the different current densities tested, most likely due to differences in membrane swelling between the trials. The lands and channel profiles are presented in Figure 43 and Figure 44, respectively. These results are shown separately to determine if there are systematic differences in the levels of water volume between the two regions.

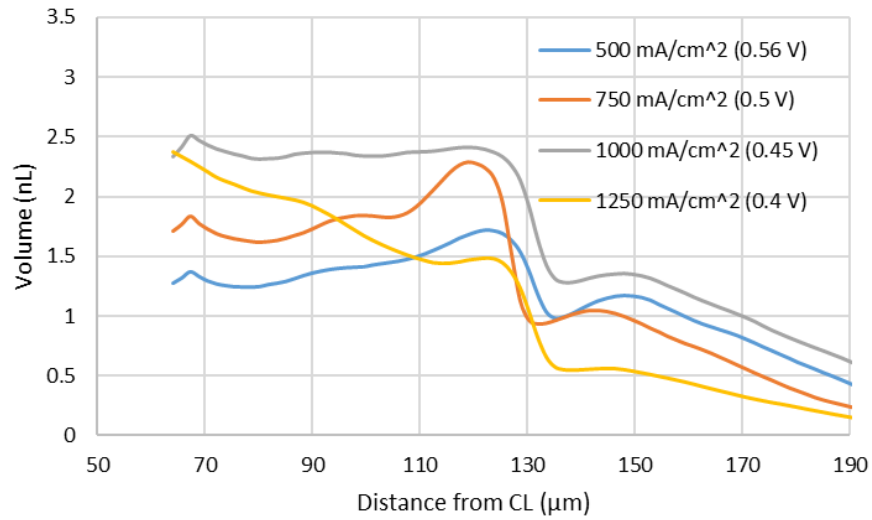


**Figure 42.** Overall water volume profile of the cathode GDL substrate of a fuel cell operated at 40°C at four separate current densities.

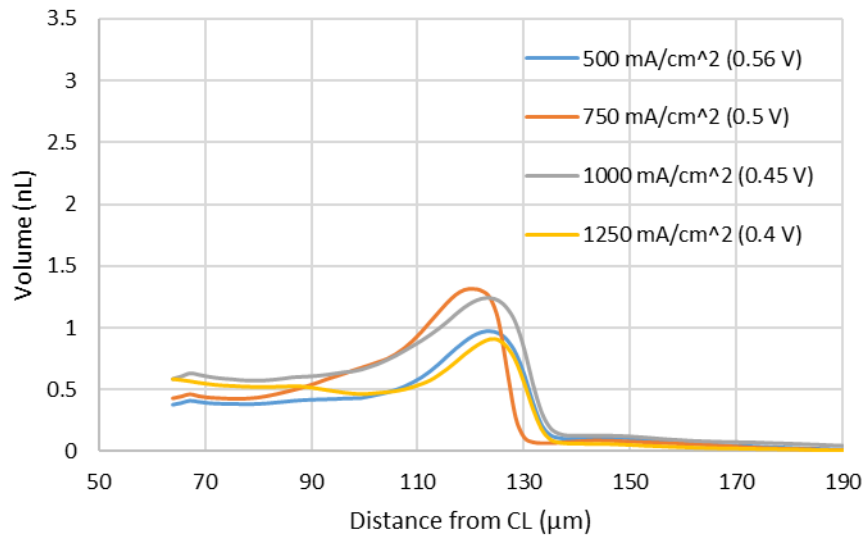


**Figure 43.** Water volume profile of the cathode GDL substrate under the lands of a fuel cell operated at 40°C at four separate current densities.

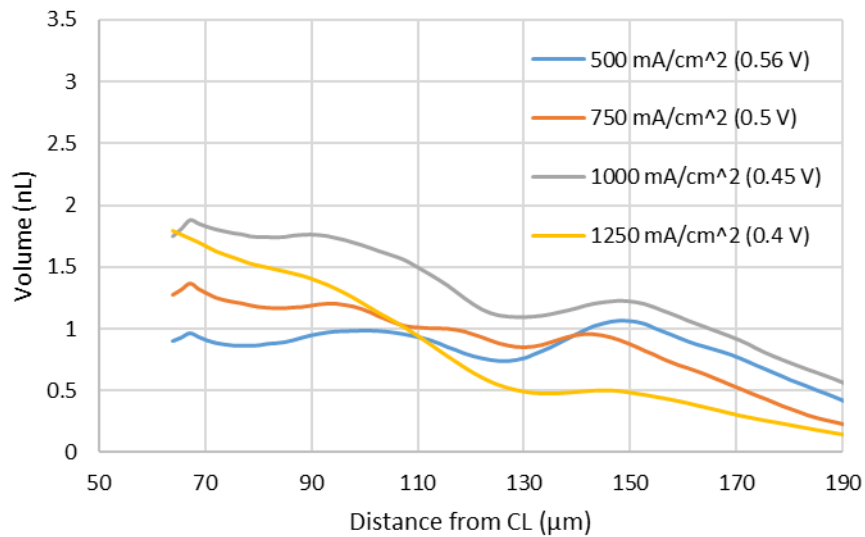


**Figure 44. Water volume profile of the cathode GDL substrate under the channels of a fuel cell operated at 40°C at four separate current densities.**

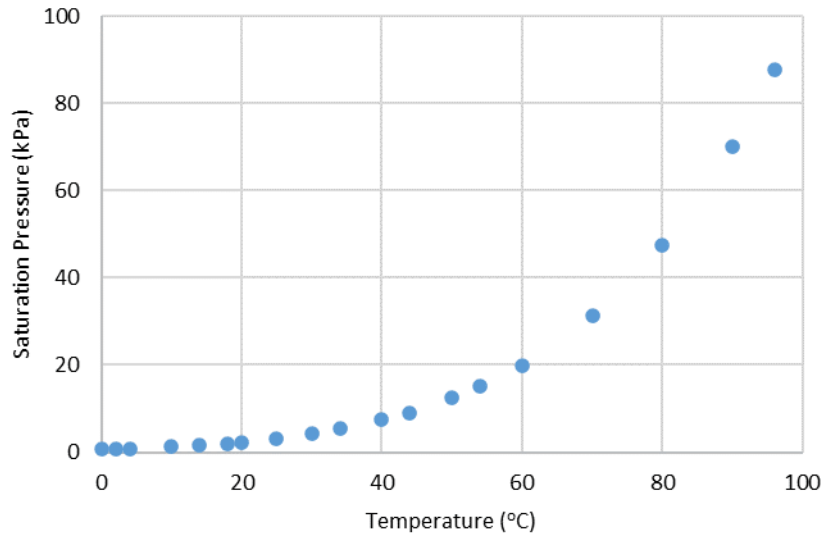
The results presented in Figure 42 show that liquid water volume tends to scale with current density between 500 mA/cm<sup>2</sup> and 1000 mA/cm<sup>2</sup>, with the highest water volumes occurring during operation of the fuel cell at 1000 mA/cm<sup>2</sup>. More specifically, the water volume increases with increasing current density between 500 mA/cm<sup>2</sup> and 1000 mA/cm<sup>2</sup>. However, lower water volumes were observed while operating the cell at 1250 mA/cm<sup>2</sup>. There is a general trend of increasing water volume with distance from the CL (*i.e.*, moving from left to right on the graph) for the tests conducted at 500 mA/cm<sup>2</sup> and 750 mA/cm<sup>2</sup>. In contrast, at 1000 mA/cm<sup>2</sup> and 1250 mA/cm<sup>2</sup>, the water volume trend is flat or decreasing. The slope of the water volume vs distance curve tends to increase when approaching the lands/GDL interface. This suggests that water vapor is leaving the CCL and condensing under the lands, most likely due to the region being cooler than the other regions of the GDL. This phenomenon has been observed in various other studies (*e.g.*, Eller *et al.* 2017; Kato *et al.* 2022). The cooler conditions tend to create an environment of lower saturation pressure. Additionally, the GDL-land interface appears to act as a barrier, which encourages liquid water clusters to accumulate and grow in size (Eller *et al.* 2017).

Differences in the observed water volume levels for the fuel cell operated at varying current densities provide important information for understanding processes that

are at work. More specifically, a substantial increase in water volume was observed during operation at  $1000 \text{ mA/cm}^2$  (compared to  $500 \text{ mA/cm}^2$ ). This observation can be explained by an increase in water production at the higher current density (Song *et al.* 2006; Muirhead 2017; Muirhead *et al.* 2018). However, the decrease in water volume between  $1000 \text{ mA/cm}^2$  and  $1250 \text{ mA/cm}^2$  must be explained by other phenomena. One possible explanation is that, at higher current densities, lower voltages result in more heat production at the CL. This increase in the temperature within the cell causes more water to exist in the vapor phase, thus reducing condensation and lowering the water volumes (Caulk and Baker 2010).

The results presented in Figure 43 show the through-plane liquid water volume under the lands for all four current densities tested. The water volume profile under the lands generally trends upwards from the CCL to the flow channels, peaking at the GDL/land interface (*i.e.*, at about  $120 \mu\text{m}$  from the CCL). Consistent with the explanation presented above, this pattern is indicative of water vapor condensing as it progresses closer to the cooler land/channel interface and/or liquid water being transported to the GDL/land interface and accumulating there due to higher compression. At the GDL/land interface, the highest water volume was observed for tests conducted at  $750 \text{ mA/cm}^2$  and  $1000 \text{ mA/cm}^2$ . In contrast, the lowest water volume was observed for tests conducted at  $500 \text{ mA/cm}^2$  and  $1250 \text{ mA/cm}^2$ . The differences in water volume between the current densities tested can generally be explained by changes in the rate of water production and the rate of heat production at different current densities. An increase in current density results in an increase in heat production (Askaripour 2019). Due to changes in the quantity of water and heat being produced, the vapor pressure and temperature within the fuel cell fluctuate. The balance between the amount of water produced at the catalyst layer and the temperature and, thus, the saturation vapor pressure within the cell, determines the phase of water that is transported through the GDL. The low water volume close to the lands at  $500 \text{ mA/cm}^2$  is mostly likely due to minimal water production at the lower current density tested. However, for  $1250 \text{ mA/cm}^2$ , the lower water volume is likely due to additional heat production at the catalyst layer, which raises the saturation pressure and allows for more water to exit the cell in the vapor phase (Figure 45). By comparison, the tests run at  $750 \text{ mA/cm}^2$  and  $1000 \text{ mA/cm}^2$  have approximately a ten percent increase in water volume

over 500 mA/cm<sup>2</sup> and 1250 mA/cm<sup>2</sup>. This is likely due to maintaining relatively low heat production within the fuel cell at these current densities.



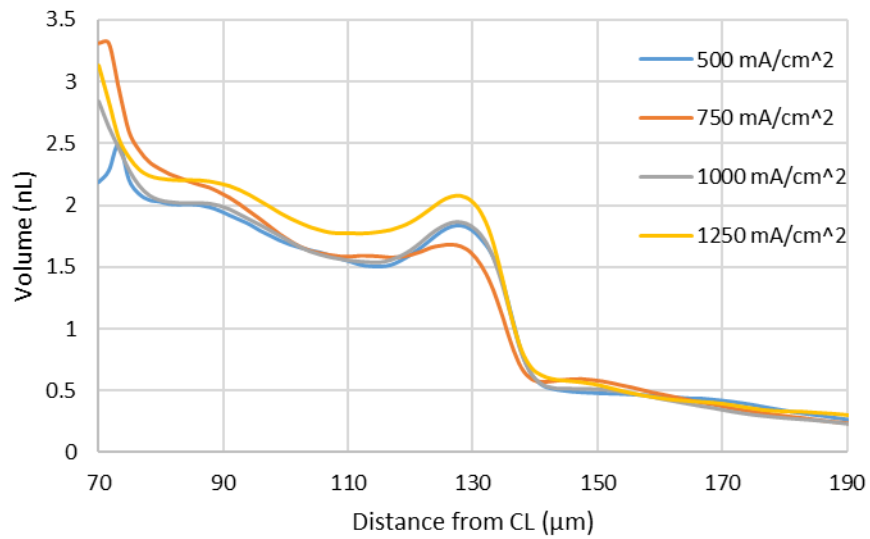
**Figure 45. Representitave curve of the relationship between temperature and water saturation vapour pressure (data obtained from Engineering ToolBox 2023).**

Figure 44 presents the water volume profile of the GDL substrate under the channels of a fuel cell operated at 40°C at four different current densities. The water volume profiles for the region under the channels had the opposite trend from what was observed under the lands. More specifically, a downward or flat trend in liquid water volume from the CCL to the flow channels was observed for each of the current densities tested. This suggests that under the channels water is condensing close to the CL and is being transported to the channels as a liquid through capillary pressure. The highest water volume under the channel was observed at 1000 mA/cm<sup>2</sup>, while the lowest water content was observed at 500 mA/cm<sup>2</sup>, except for at the GDL/land interface where 1250 mA/cm<sup>2</sup> had the lowest water volume. This decrease in water volume from the CL to the GDL-channel interface is most likely due to effective transport and removal of liquid water in the region. More specifically, as water progresses towards the flow channels, it is more efficiently removed due to convective forces from air in the flow channels. Hence, water volume levels near the flow field were low for all treatments. Such reductions in water volumes are important because they are associated with reductions in oxygen transport resistance and increases in cell performance (Baker *et al.*

2009; Caulk and Baker 2010; Baker and Caulk 2013). Overall, the results of these experiments show that changes in current density have a significant impact on the distribution of water within an operating fuel cell. Specifically, the balance between water production and heat production at the CL appears to be key factors influencing liquid water volume. Importantly, the increased heat production at highest current density tested was sufficient to compensate for enhanced water production, resulting in a reduction in the observed water volume.

#### **4.4.1.1. High flow rate analysis**

Based on polarization curve data that were generated during these trials, it was determined that increasing the influent gas flow rate improved the performance of an operating fuel cell (Figure 20). Therefore, an investigation was conducted to better understand the mechanisms that resulted in the performance improvements by evaluating how liquid water volume within the GDL was influenced by changes in influent gas flow rates. Figure 46 presents the overall water volume data that were generated by operating the cell at high flow rates (*i.e.*, 0.9 L/min of H<sub>2</sub> and 1.2 L/min of air) and at four current densities (*i.e.*, 500, 750, 1000, and 1250 mA/cm<sup>2</sup>). Figure 47 and Figure 48 provide ancillary information by displaying the water volume profiles that were observed within the GDL under the lands and under the channels, respectively. Based on the curves plotted on Figure 46, the water volume did not appear to scale with current density. Rather, all four current densities tested had comparable liquid water volumes from the CL to the flow channels. Additionally, there is a significant downwards trend of water volume when moving towards the flow channels. Furthermore, the magnitude of the drop in water volume for the high flow rate analysis is considerably larger than what was observed at lower flow rates (*i.e.*, 0.2 L/min H<sub>2</sub> and 0.5 L/min air). One explanation for these results is that the higher flow rates enhanced water removal from the GDL. More specifically, turbulent air flow within the flow channels may have expedited water removal from the GDL. As a result, it is likely that water was transported more quickly through the GDL, potentially taking similar pathways, and not accumulating as much near the GDL-channel interface.



**Figure 46.** Overall water volume profile of the GDL substrate of a fuel cell operated at 40°C with high flow rates at four separate current densities.

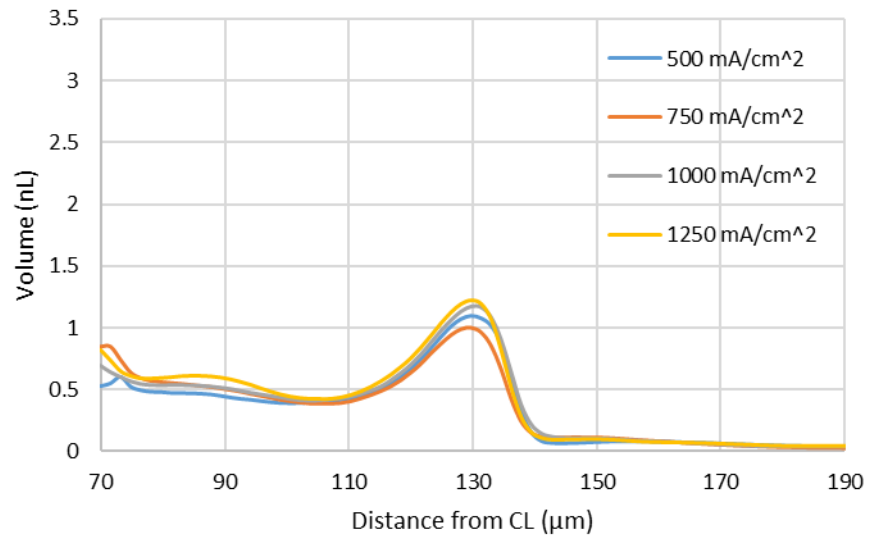


**Figure 47.** Water volume profile of the GDL substrate under the lands of a fuel cell operated at 40°C with high flow rates at four separate current densities.

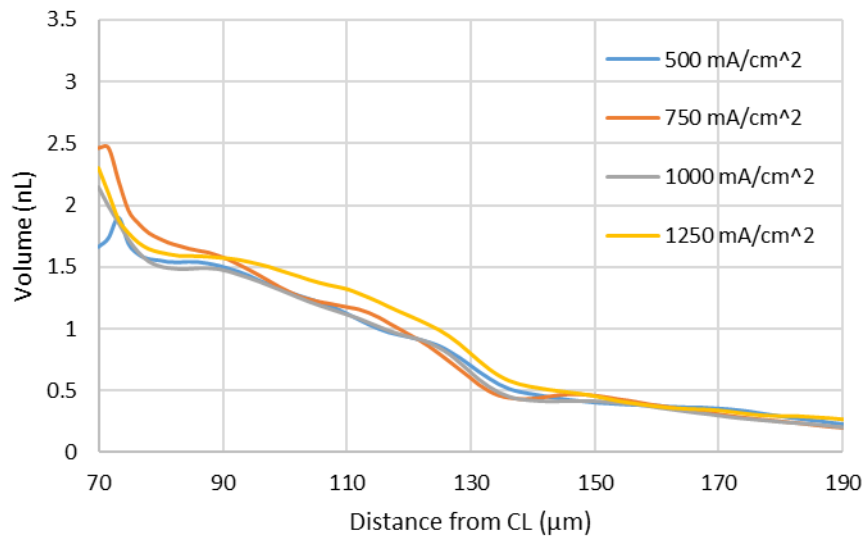


**Figure 48.** Water volume profile of the GDL substrate under the channels of a fuel cell operated at 40°C with high flow rates at four separate current densities.

The water volume under the land and channel regions (*i.e.*, Figure 47 and Figure 48, respectively) show a similar trend as the overall water volume results. In both cases, the liquid water volume does not appear to scale with current density. The water volume profiles trend upwards in the case of the land results. In contrast, there is a steep downward trend for the channel results. Like the results discussed above, the water volume levels are similar for all four current densities tested. Again, this is most likely due to the removal of condensed water within the inlet gas lines at the higher flow rates and/or expedited water removal from the GDL as a result of a higher pressure drop between the GDL and flow channels at the higher flow rate.

#### **4.4.1.2. Oxygen variation**

As stated above, the balance between water production and heat production at the CL appears to be a key factor influencing liquid water volume in the GDL. An oxygen variation experiment was conducted to help better understand this relationship. During this analysis, oxygen concentrations varied between 21% (*i.e.*, air) and 100%, while holding a constant current density (*i.e.*, 1250 mA/cm<sup>2</sup>). This experiment was designed to create conditions with varying heat production rates (*i.e.*, at different O<sub>2</sub> concentrations), while maintaining current density constant to facilitate a fixed water production rate. Figure 49 and Figure 50 show the polarization curves that were

generated at each of the three oxygen concentrations tested (*i.e.*, air, 60% and 100% oxygen) for both the direct Scribner and *in-operando* setups, respectively. The highest performance was observed at 100% oxygen, while the lowest occurred while operating the fuel cell under air. Figure 51, Figure 52 and Figure 53 display the overall, land and channel water volume profile results, respectively, for this analysis. Again, these results are shown separately to allow for differences to be identified between each region of the FC.

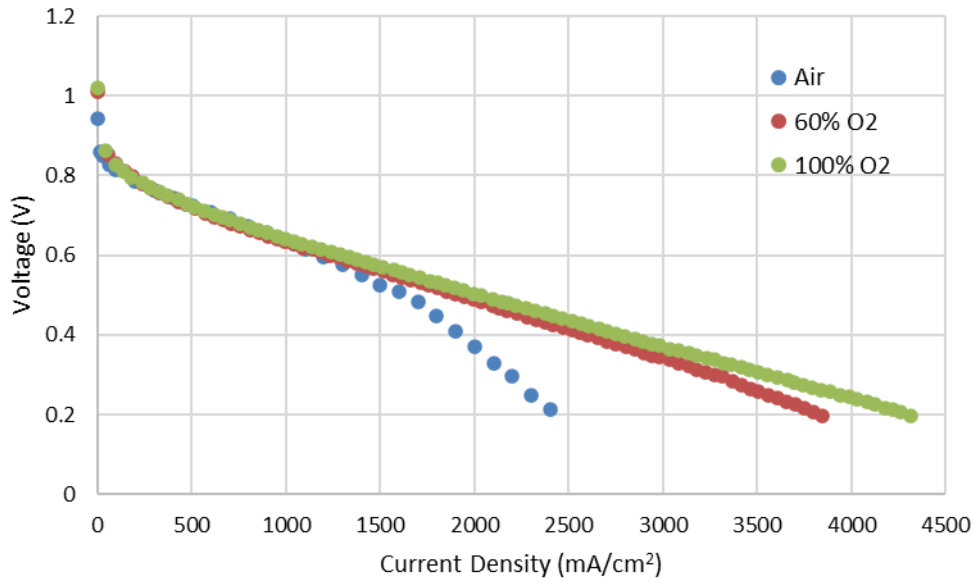


**Figure 49.** Direct Scribner polarization curves generated under air, 60% O<sub>2</sub> and 100% O<sub>2</sub>.

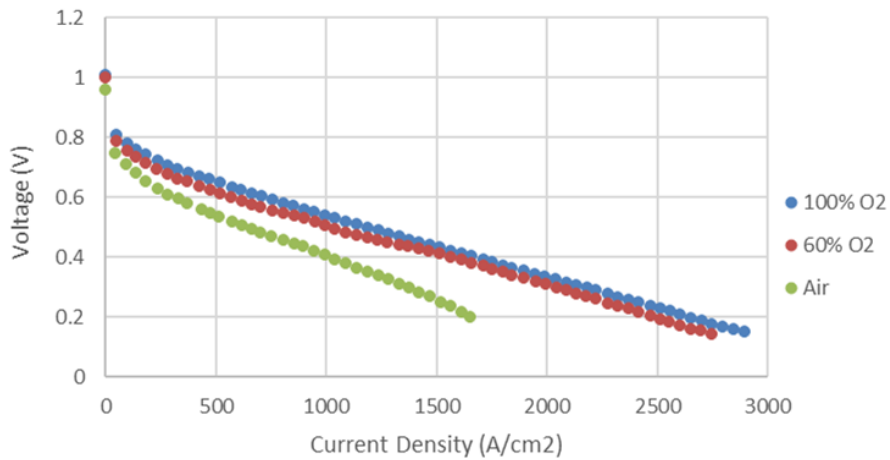


**Figure 50.** *In-operando* polarization curves generated under air, 60% O<sub>2</sub> and 100% O<sub>2</sub>.

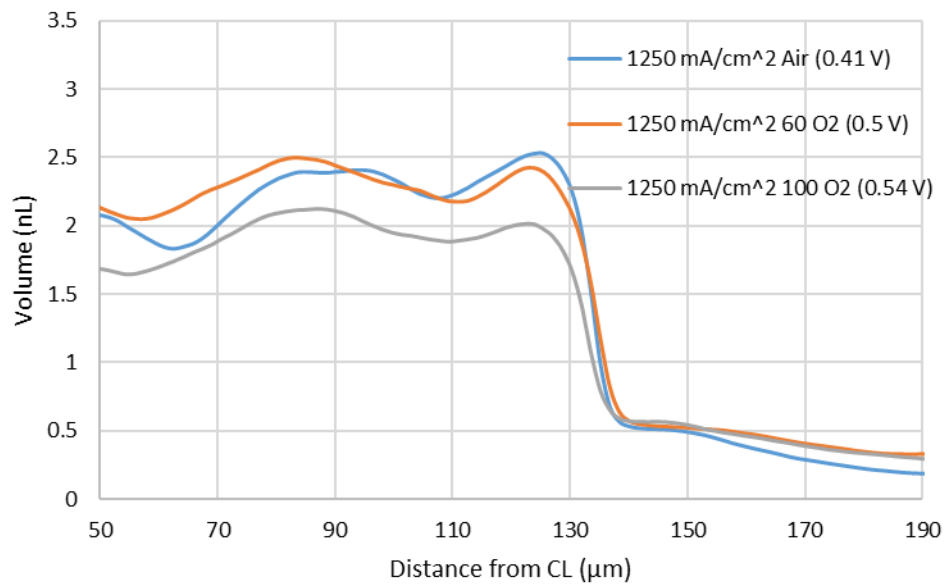


**Figure 51.** Overall water volume profile of the GDL substrate of a fuel cell operated at 40°C at three separate oxygen concentrations.

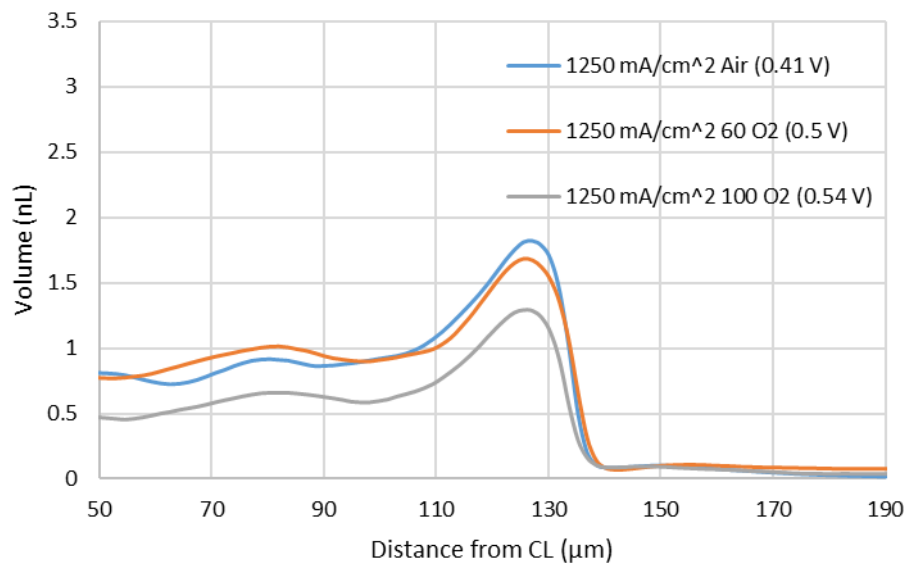


**Figure 52.** Water volume profile of the GDL substrate under the lands of a fuel cell operated at 40°C at three separate oxygen concentrations.

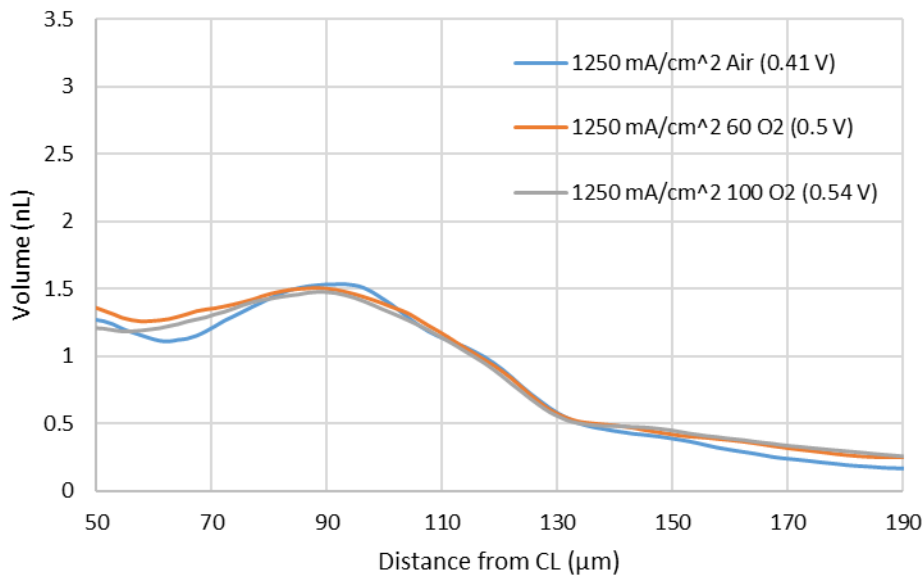


**Figure 53. Water volume profile of the GDL substrate under the channels of a fuel cell operated at 40°C at three separate oxygen concentrations.**

The results presented in Figure 51 show that the lowest water volume was observed for the test done under 100% oxygen, while the highest water volume occurred for tests done under air and 60% oxygen. These results have a reverse trend from what was expected. Where, the test done at 100% oxygen had the highest cell voltage with the lowest liquid water volume. The tests that were conducted under air and 60% oxygen had lower voltages with higher liquid water volume. The hypothesis was that at lower oxygen concentrations, lower voltages would result in more heat production and, thus, lower water volume values. However, the opposite was observed. One potential explanation for these results could be that the differences in voltage between the three trials were not large enough to have a significant impact on the liquid water volume. Based on the polarization curves shown in Figure 50, it appears that the difference in cell voltage between the air trial and the oxygen trials is greater as current density increases (e.g., at 1500 mA/cm<sup>2</sup> compared to 750 mA/cm<sup>2</sup>). Therefore, at higher current densities, larger voltage differences and, thus, larger variations in heat production at the CL may be observed. Another possible explanation for these results could be the differences in gas properties between air and oxygen. For example, the difference in water vapour diffusion in air vs oxygen could be impacting liquid water volume. However, based on the results that Schwertz and Brow (1951) published (diffusion

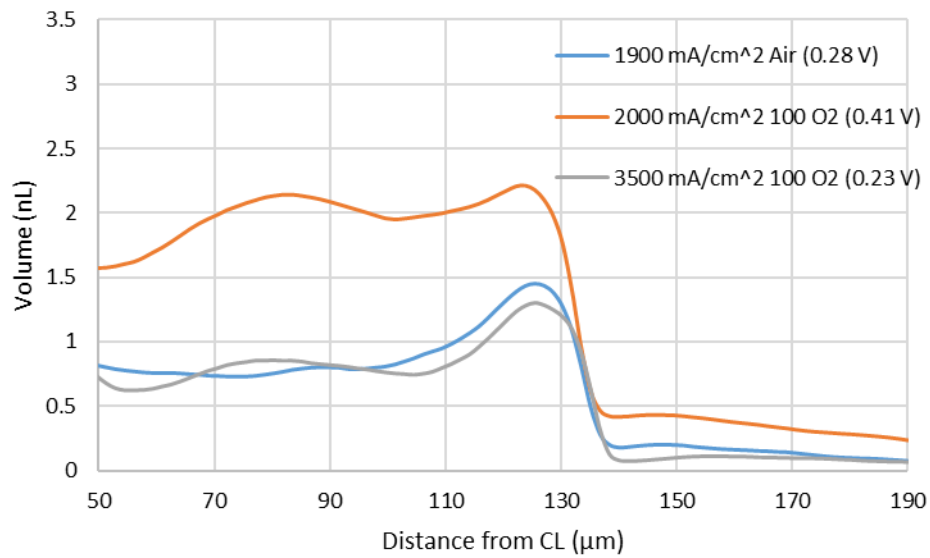
coefficient of water vapour in nitrogen 0.303 and 0.318 in oxygen at 55°C) it is unlikely that this factor is causing the trends in the curves presented in Figure 51.

The results presented in Figure 52 display the through-plane liquid water volume under the lands for all three oxygen concentrations tested. The water volume profile under the lands trended upwards from the CCL to the flow channels, typically peaking at the GDL/land interface. This is consistent with what was presented in Figure 43 above and is indicative of water vapor condensing as it progresses closer to the cooler land/channel interface. Similar to Figure 51, the liquid water volume was highest for the tests done with air and 60% oxygen, while the lowest volume was observed for the trial conducted using 100% oxygen. These results can potentially be explained by the minimal differences in cell voltage between the trials.

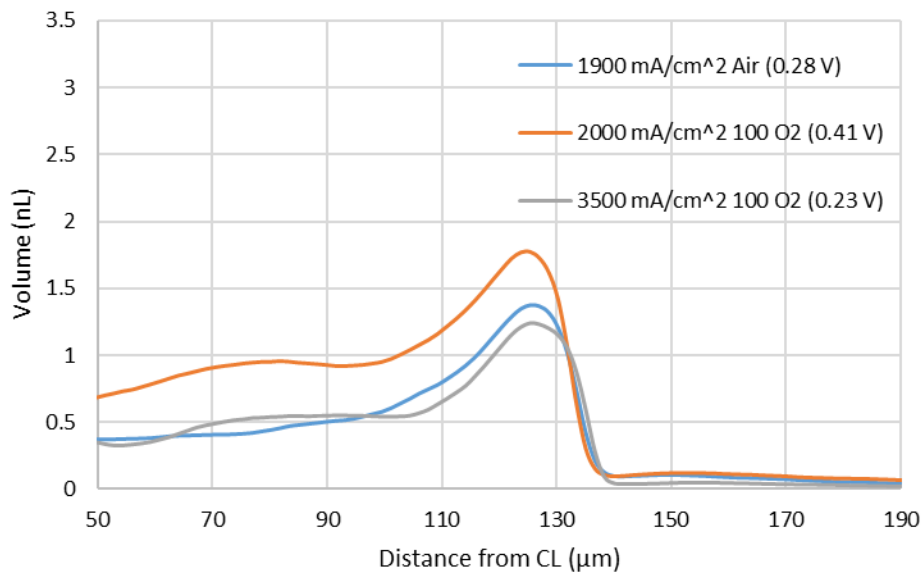
Figure 53 displays the liquid water volume profile under the channels for all three oxygen concentrations tested. These results are in contrast with what was observed in Figure 51 and Figure 52. More specifically, the water volume profiles generally overlapped for all of the three oxygen concentrations tested under the channels. This indicates a consistent under-the-channel liquid water presence and transport mechanism for all oxygen concentrations and their respective cell voltages in this case, and that the differences in water volume at different oxygen concentrations tested at 1250 mA/cm<sup>2</sup> and 40°C are most significant under the lands.

#### **4.4.1.3. High current density**

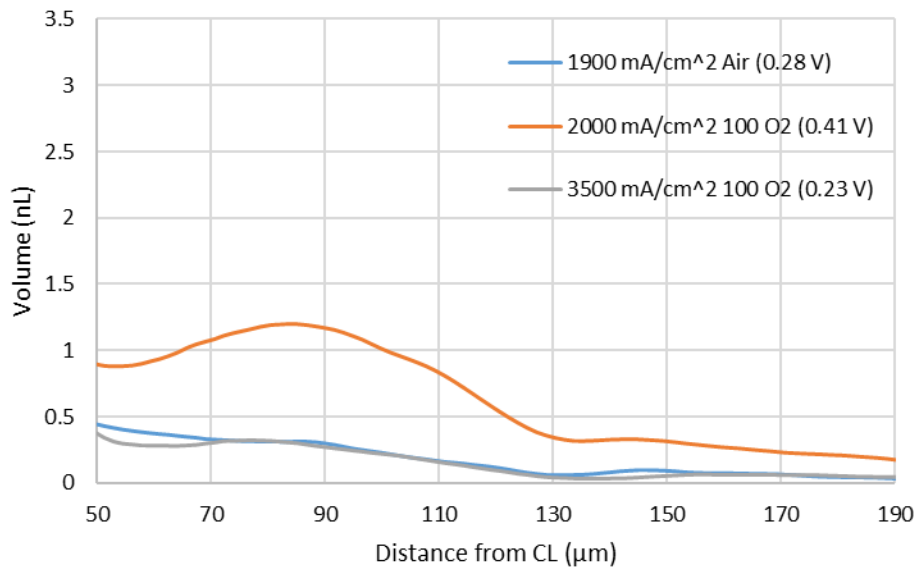
Operation of fuel cells at high current densities is essential for achieving cost reductions and lowering the overall footprint of PEMFCs. However, at high current densities water production is increased, which can result in flooding of the fuel cell and reduced performance. Therefore, a high current density analysis was conducted to investigate the impact of increased current densities on water distribution in an operating PEMFC. During this analysis, three high current densities were tested with one trial under air and two under 100% oxygen. The purpose of this analysis was to better understand the impact of high current densities and the corresponding lower voltages on liquid water distribution within the GDL. Figure 54, Figure 55 and Figure 56 display the overall, land and channel water volume profile results, respectively, for this analysis.



**Figure 54. Overall water volume profile of the GDL substrate of a fuel cell operated at 40°C at three selected high current densities.**



**Figure 55. Water volume profile of the GDL substrate under the lands of a fuel cell operated at 40°C at three selected high current densities.**



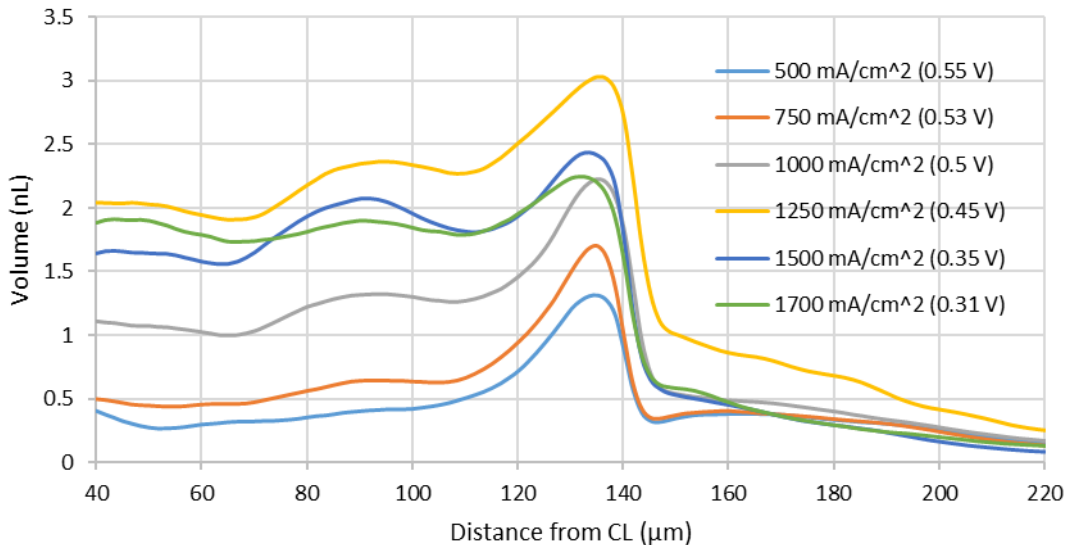
**Figure 56. Water volume profile of the GDL substrate under the channels of a fuel cell operated at 40°C at three selected high current densities.**

Figure 54 presents the overall water volume profile results for the three current densities tested. The highest water volume was observed for the trial conducted under 100% oxygen at 2000 mA/cm<sup>2</sup>. Lower water volume was observed for the tests done at 1900 mA/cm<sup>2</sup> using air and 3500 mA/cm<sup>2</sup> using 100% oxygen. In general, the water volume results appear to be dependent on cell voltage. More specifically, lower liquid water volume was observed in the trials with the lower voltages. For example, the trials done at 1900 mA/cm<sup>2</sup> using air and 3500 mA/cm<sup>2</sup> using 100% oxygen had the lowest voltages (*i.e.*, 280 mV and 230 mV, respectively) and had lower water volume than the trial that was conducted at 410 mV. This agrees with the hypothesis that at higher current densities, lower voltages result in more heat production at the CL. This causes more water to exist in the vapor phase due to the higher temperatures. As a result, at these two current densities (*i.e.*, 1900 mA/cm<sup>2</sup> using air and 3500 mA/cm<sup>2</sup> using 100% oxygen), it appears that water transport is primarily in the vapour phase. Figure 55 and Figure 56 display the water volume profile results for under the lands and channels, respectively. The results shown in Figure 55 exhibit a similar trend to the overall water volume results shown in Figure 54. However, an increase in water volume was observed under the lands in the region near the GDL/lands interface. Furthermore, the channel results shown in Figure 56 also display similar trends to those shown in Figure 54 (*i.e.*, the trials conducted at 280 mV and 230 mV have the lowest water volume).

Additionally, under the channels, it appears that a portion of the liquid water initially condenses close to the CL and is transported to the flow channels through capillary forces. However, most of the water is transported to the flow channels and out of the cell in the vapour phase.

#### 4.4.2. Influence of Current Density at 50°C

Figure 57 presents the overall water volume profile within the GDL of a fuel cell operated under air at 50°C with current densities ranging from 500 mA/cm<sup>2</sup> to 1700 mA/cm<sup>2</sup>. These results show that the volume of liquid water in the GDL tends to scale with current density, with the highest water volumes occurring during operation of the fuel cell at 1250 mA/cm<sup>2</sup> and lowest water volume observed while operating the cell at 500 mA/cm<sup>2</sup>. However, water volume tends to decrease at higher current densities (*i.e.*, 1500 and 1750 mA/cm<sup>2</sup>). When all six profiles (*i.e.*, 500, 750, 1000, 1250, 1500 and 1700 mA/cm<sup>2</sup>) are considered, there is a general trend of increasing liquid water volumes when approaching the land/GDL interface (*i.e.*, at approximately 140 μm from the CL). Similar to what was discussed in Section 4.4.1, this suggests that water vapor is leaving the CCL and condensing under the lands, most likely due to the region being cooler in temperature. Additionally, liquid water clusters tend to accumulate at the GDL-land interface due to an apparent barrier effect (Eller *et al.* 2017).



**Figure 57. Overall water volume profile of the GDL substrate of a fuel cell operated at 50°C at six separate current densities.**

A substantial increase in water volume was observed during operation at 1250 mA/cm<sup>2</sup> (compared to 500 mA/cm<sup>2</sup>). This result can be explained by an increase in water production at the higher current density (Song *et al.* 2006; Muirhead 2017; Muirhead *et al.* 2018). However, the decrease in water volume between 1250 mA/cm<sup>2</sup> and 1700 mA/cm<sup>2</sup> is likely occurring due to other phenomena. More specifically, this trend could be explained by additional heat production at the CL due to operation at higher current densities and lower voltages. This increase in the temperature within the cell could cause more water to exist in the vapor phase, thus reducing condensation and lowering the water volumes (Caulk and Baker 2010).

The results presented in Figure 58 display the through-plane liquid water volume under the lands at 50°C for all six current densities tested. The water volume profile under the lands trends upwards from the CCL to the flow channels, peaking at the GDL/land interface. Consistent with the explanation presented above and in Section 4.4.1, this pattern is indicative of water vapor condensing as it moves closer to the cooler land/channel interface. At the GDL/land interface, the highest water volume was observed for the test conducted at 1250 mA/cm<sup>2</sup>. In contrast, the lowest water volume was observed for the test conducted at 500 mA/cm<sup>2</sup>, which is similar to the overall water volume plot (Figure 57). Again, as stated in Section 4.4.1, the differences in water volume between the current densities tested can be generally explained by changes in the rate of water production and the rate of heat production at different current densities. An increase in current density results in an increase in heat production. Due to changes in the quantity of water and heat being produced, the vapor pressure and temperature within the fuel cell fluctuate. The balance between the amount of water produced at the catalyst layer and the temperature and, thus, the saturation vapor pressure within the cell, determines the phase of water that is transported through the GDL. The low water volume close to the lands at 500 mA/cm<sup>2</sup> is mostly likely due to minimal water production at the lower current density tested. However, the decrease in water volume from 1250 mA/cm<sup>2</sup> to 1700 mA/cm<sup>2</sup>, is likely due to additional heat production at the catalyst layer at the higher current density, which raises the saturation pressure and allows for more water to exit the cell in the vapor phase.

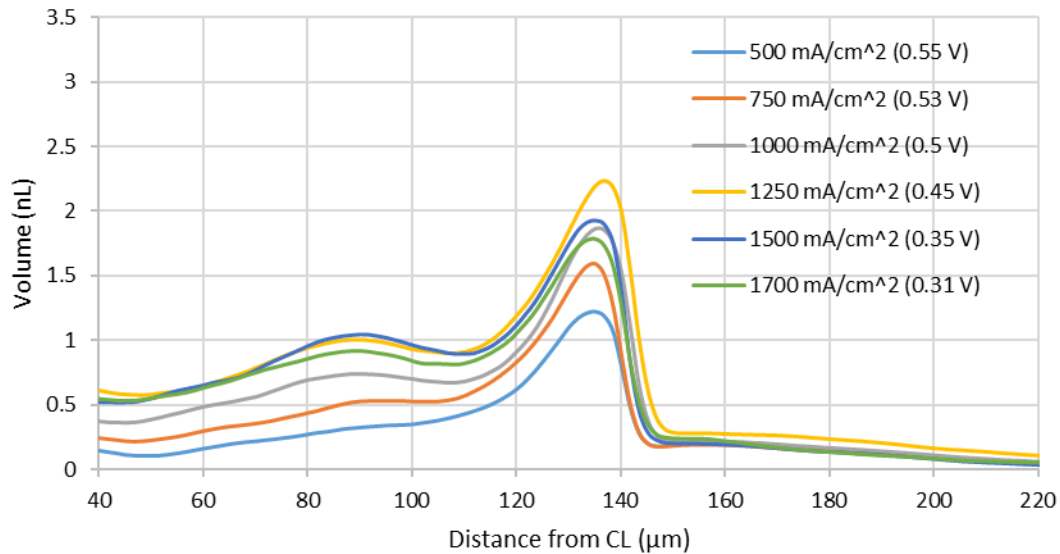


**Figure 58. Water volume profile of the GDL substrate under the lands of a fuel cell operated at 50°C at six separate current densities.**

Figure 59 presents the water volume profile of the GDL substrate under the channels of a fuel cell operated at 50°C at six different current densities. The water volume profiles for the region under the channels had a contrasting trend from what was observed under the lands. More specifically, a downward or constant slope of the relationship between liquid water volume and the distance from the CCL to the flow channels was observed for all six current densities tested. Similar to the overall results (Figure 57) and results for under the lands (Figure 58), the highest water volume under the channel was observed at 1250 mA/cm<sup>2</sup>, while the lowest water content was observed at 1700 mA/cm<sup>2</sup>. This decrease in water volume from the CL to the GDL-channel interface can most likely be explained by diffusive and capillary transport close to the CL and, more importantly, efficient water removal at the GDL-channel interface due to convective forces from air in the flow channels (Fan *et al.* 2018)

At 40°C and 50°C, similar trends in water volume were observed for both the channel and lands regions. More specifically, under the lands, a general increase in water volume was observed from the CL to the GDL-land interface for both temperatures. In contrast, under the channels, a general decrease in water volume from CL to GDL-channel interface was observed. Additionally, for both operational temperatures, water volume scaled with increasing current density up to a certain value,

where it then began to decrease. The transition point was at 1000 mA/cm<sup>2</sup> at 40°C, compared to 1250 mA/cm<sup>2</sup> at 50°C.

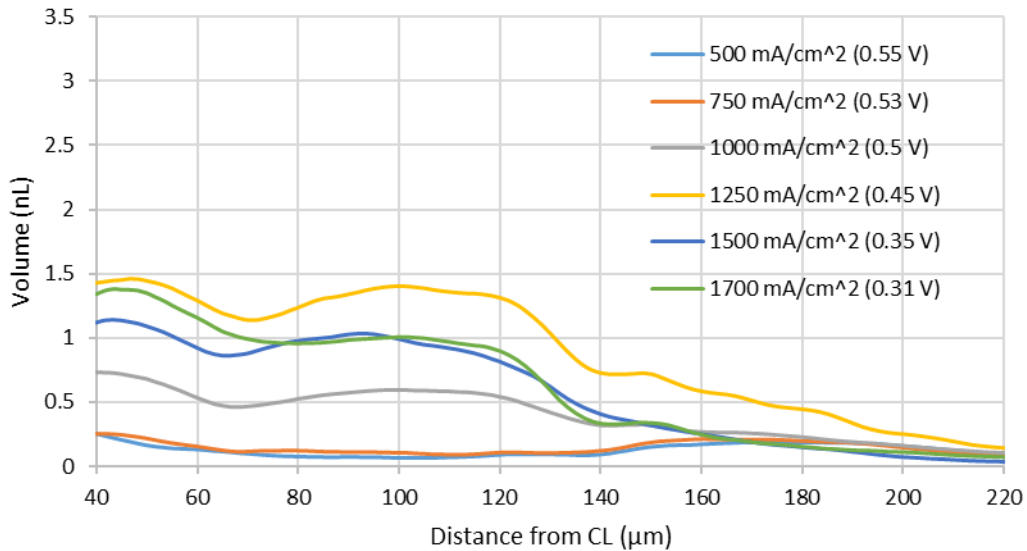


**Figure 59. Water volume profile of the GDL substrate under the channels of a fuel cell operated at 50°C at six separate current densities.**

#### 4.4.2.1. Oxygen Variation

The effect of oxygen concentration on water volume within the GDL of an operating PEMFC was also evaluated at 50°C. The results presented in Figure 60 show that the lowest water volume was observed for the test done under 11% oxygen. Among the treatments, the lowest water volume was observed for the test done under 100% oxygen while the highest water volume occurred for tests done under air (*i.e.*, 21% oxygen). Similar to what was discussed in Section 4.4.1, the oxygen concentration results between 21% and 100% show a reverse trend from what was expected. That is, the test done at 100% oxygen had the highest voltage with the lowest liquid water volume. By comparison, the tests conducted under air had lower voltages with higher liquid water volume. The results shown in Figure 60 exhibit similar trends to those observed for the 40°C trials; therefore, it was concluded that the differences in voltage among the various oxygen concentrations at 50°C were not great enough to significantly affect water volume. However, the trial conducted at 11% oxygen appeared to have a low enough voltage to impact the observed liquid water volume.

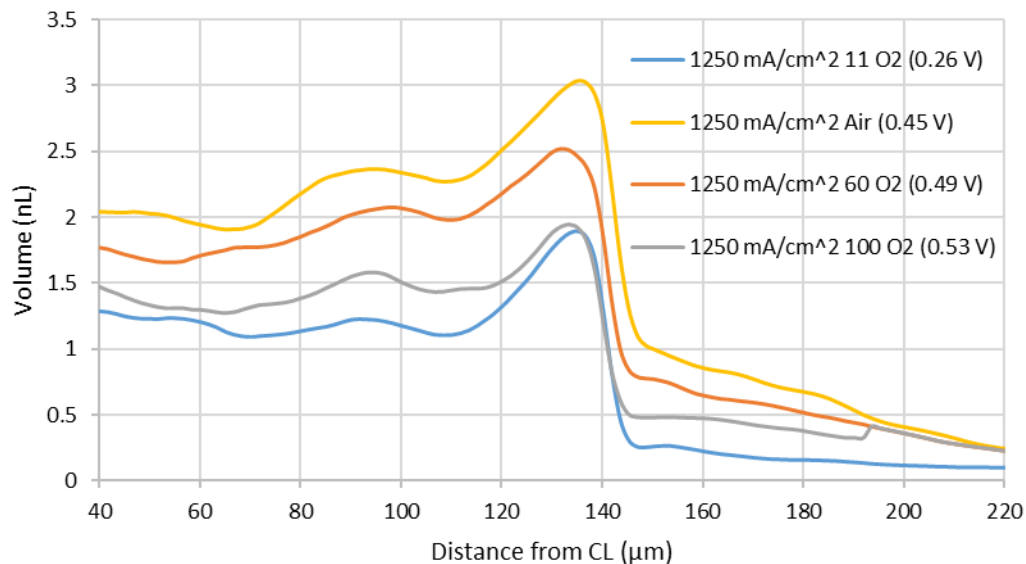


**Figure 60. Overall water volume profile of the GDL substrate of a fuel cell operated at 50°C at three separate oxygen concentrations.**

Figure 61 and Figure 62 display the through-plane liquid water volume under the lands and channels, respectively. The water volume profile under the lands generally trends upwards from the CCL to the flow channel, which contrasts with the channel region in which water volume trends downwards. For both Figure 61 and Figure 62, the liquid water volume was highest for the test done under air, while the lowest water volume was observed for the trial conducted using 11% oxygen. See Section 4.4.1 for a more detailed explanation of these trends.

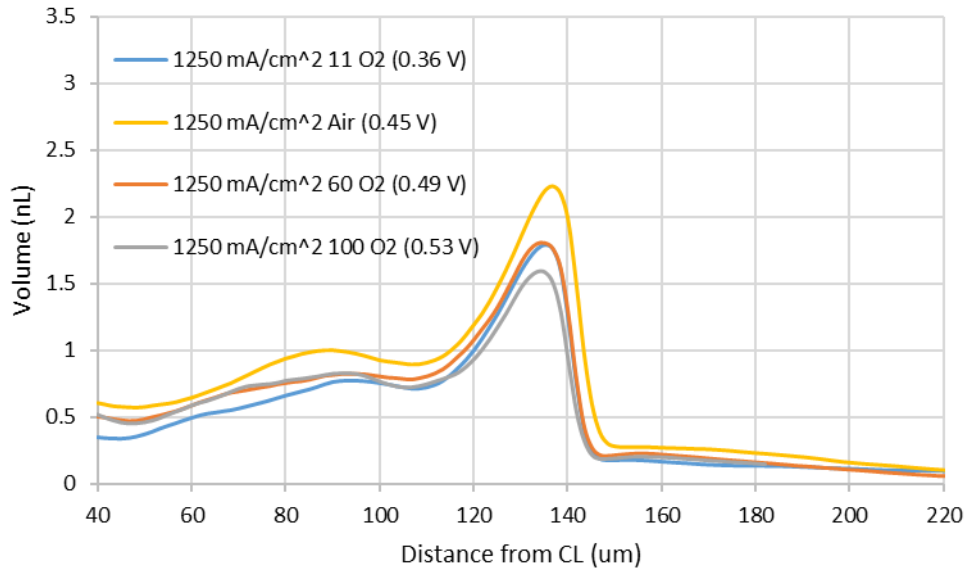


**Figure 61.** Water volume profile of the GDL substrate under the lands of a fuel cell operated at 50°C at three separate oxygen concentrations.

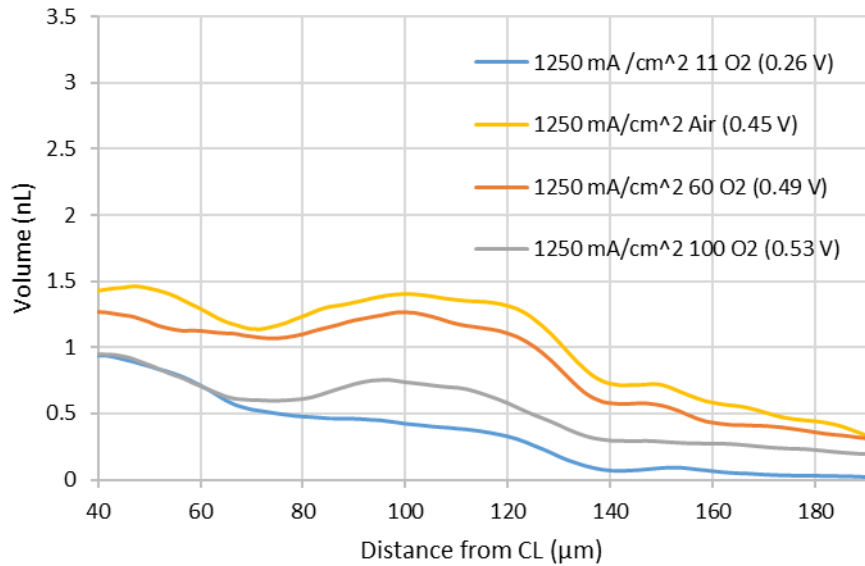
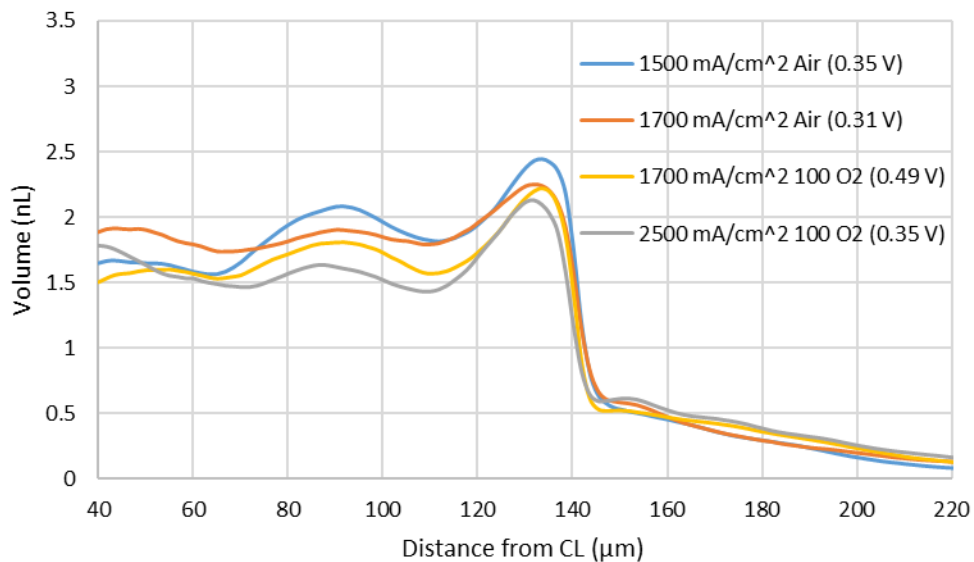


**Figure 62.** Water volume profile of the GDL substrate under the channels of a fuel cell operated at 50°C at three separate oxygen concentrations.

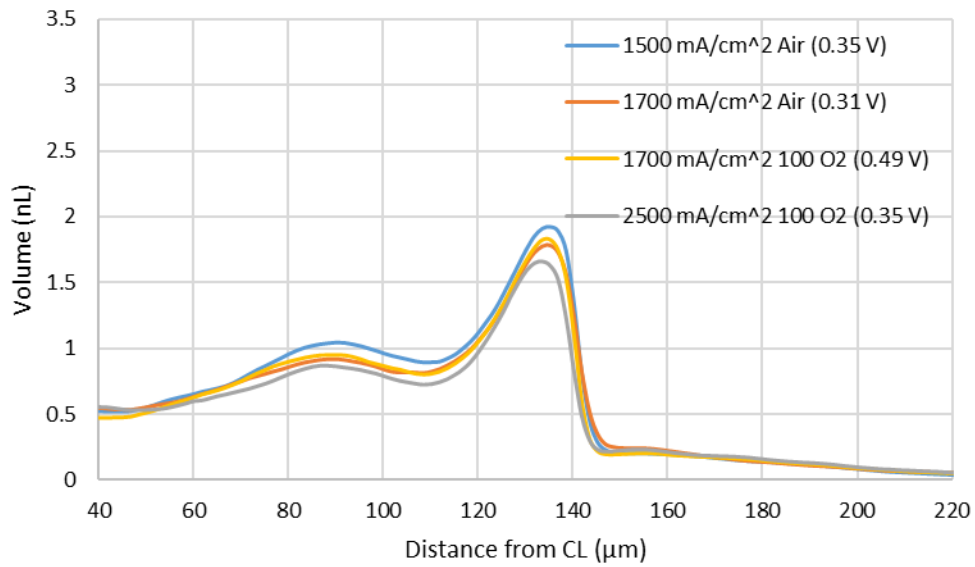
#### 4.4.2.2. High Current Density

Figure 63 presents the overall water volume profile results of a fuel cell operated at 50°C at three high current densities. The highest water volume was observed for the

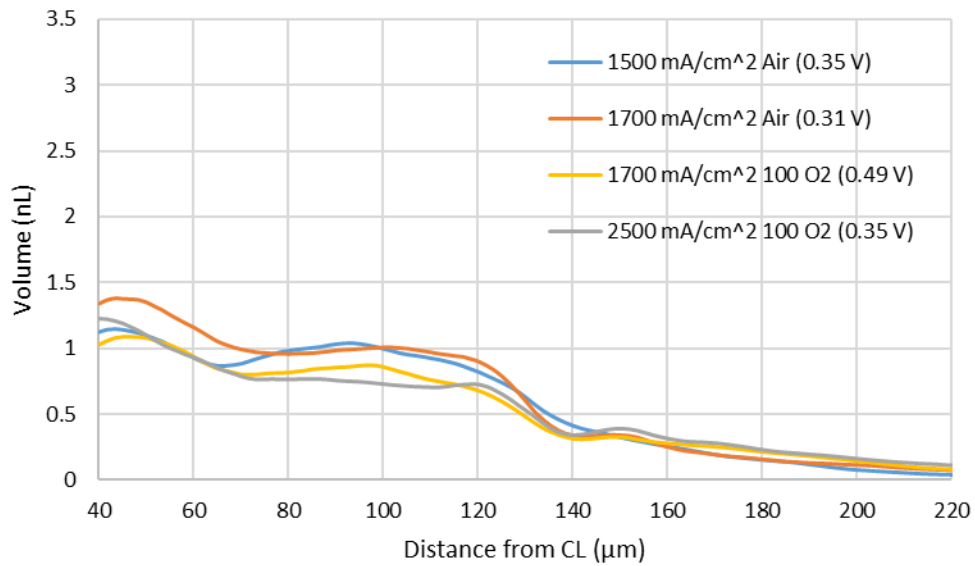
trial conducted under air at 1700 mA/cm<sup>2</sup>. The lowest water volume was observed for the test done at 2500 mA/cm<sup>2</sup> using 100% oxygen. In general, all three trials have similar water volume profiles throughout the GDL. Although the test conducted at 1700 mA/cm<sup>2</sup> under air had a slightly higher water volume compared to the other trials, the differences are not significant. No real trend can be identified with respect to changes in oxygen concentration under the conditions tested. One potential explanation for these results is the differences in voltages between the trials. More specifically, the 180 mV difference between 1700 mA/cm<sup>2</sup> under air compared to under 100% oxygen may not be large enough to see observable water volume differences. Figure 64 and Figure 65 display the water volume profile results for under the lands and channels respectively. These results show a similar trend to the overall water volume results shown in Figure 63.



**Figure 63. Overall water volume profile of the GDL substrate of a fuel cell operated at 50°C at selected high current densities and oxygen concentrations.**



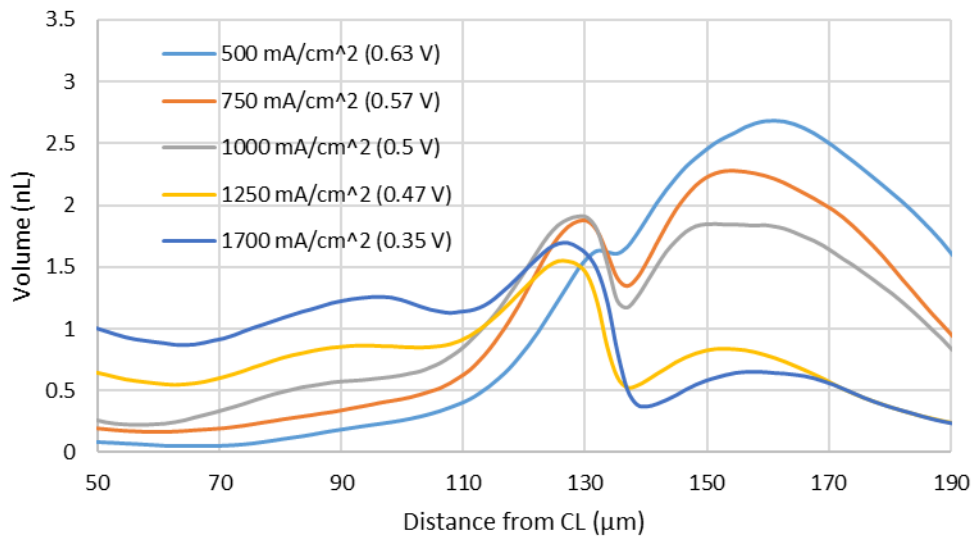
**Figure 64.** Water volume profile of the GDL substrate under the lands of a fuel cell operated at 50°C at selected high current densities and oxygen concentrations.



**Figure 65.** Water volume profile of the GDL substrate under the channels of a fuel cell operated at 50°C at selected high current densities and oxygen concentrations.

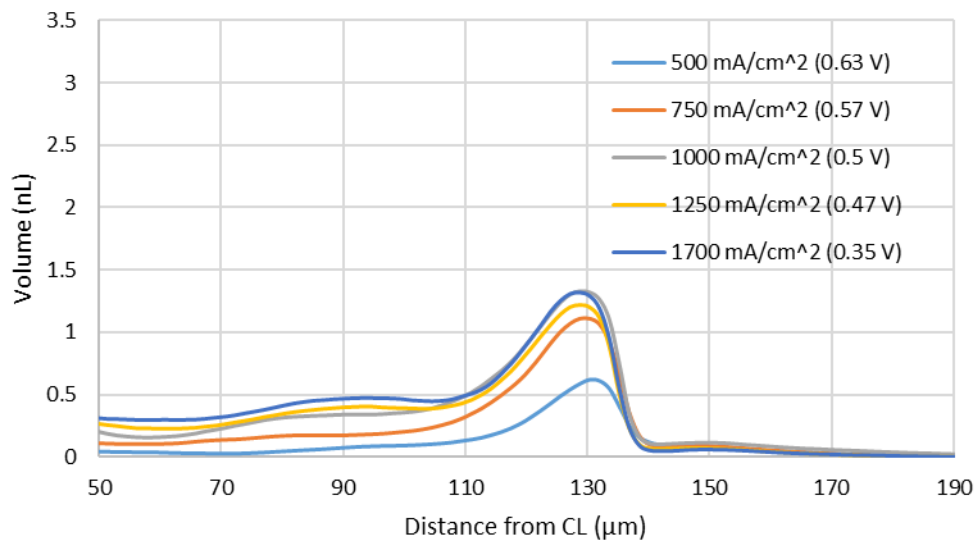
### 4.4.3. Influence of Current Density at 60°C

Figure 66 presents the overall water volume profile within the GDL of a fuel cell operated at 60°C with current densities ranging from 500 mA/cm<sup>2</sup> to 1700 mA/cm<sup>2</sup>. The results presented in Figure 66 show that, at a distance of 50 μm to 100 μm from the CL, the liquid water volume tended to scale with current density, with the highest water volumes occurring during operation at 1700 mA/cm<sup>2</sup> and lowest water volume observed while operating the cell at 500 mA/cm<sup>2</sup>. This trend of increasing water volume with increasing current density can be explained by an increase in water production at the higher current densities (Song *et al.* 2006; Muirhead 2017; Muirhead *et al.* 2018). However, the water volume closer to the flow channels (*i.e.*, approximately 130 μm from the CL) did not exhibit the same trend. At 130 μm from the CL, there was a spike in water volume within the GDL for 500, 750 and, 1000 mA/cm<sup>2</sup>. This increase in water volume appears to be due to increased condensation within the outer edge of the GDL substrate and flow channels. This increased condensation most likely resulted in a buildup of liquid water under the channels and, potentially, movement of some water backwards from the channel into the GDL. Based on the results that have been generated to date under many different operational conditions, this condensation appears to be atypical. However, it is important to note that the water volume within the edges of the GDL and in the channels appears to trend inversely with increasing current density. More specifically, the water volume appears to decrease with increasing current density. For all five current density profiles (*i.e.*, 500, 750, 1000, 1250, and 1700 mA/cm<sup>2</sup>), there is a general trend of increasing liquid water when approaching the land/GDL interface (*i.e.*, at approximately 130 μm from the CL). Similar to what was discussed in Section 4.4.1, this suggests that water vapor is leaving the CCL and condensing under the lands, most likely due to the region being cooler than the areas closer to the CL.



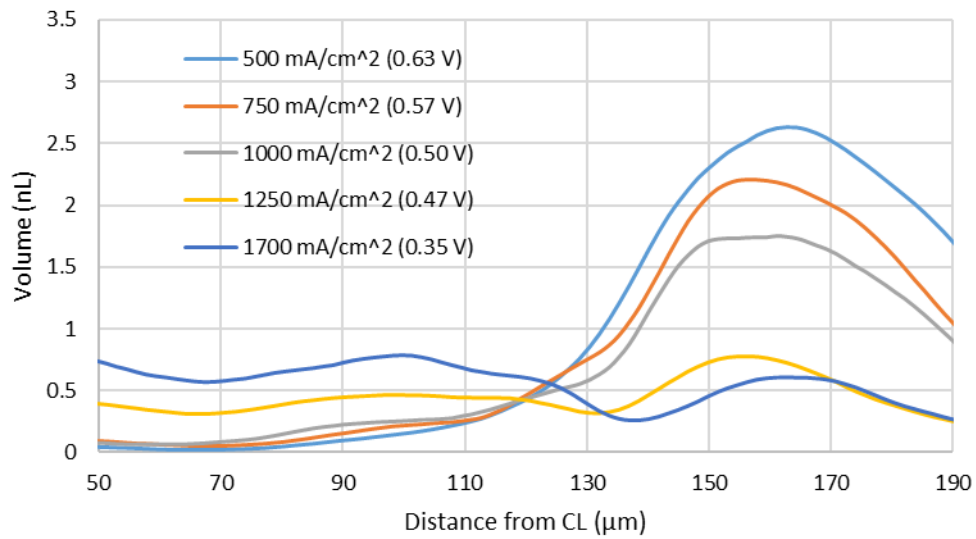
**Figure 66. Overall water volume profile of the GDL substrate of a fuel cell operated at 60°C at five separate current densities.**

The results presented in Figure 67 show the through-plane liquid water volume under the lands at 60°C for all five current densities tested. The water volume profile under the lands trends upwards from the CCL to the flow channels, peaking at the GDL/lands interface. Consistent with the explanation presented above and in Section 4.4.1. The highest water volume was observed at the GL/lands interface for the tests conducted at 1000 and 1700 mA/cm<sup>2</sup>. In contrast, the lowest water volume was observed for the test conducted at 500 mA/cm<sup>2</sup>. Generally, a trend of increasing water volume with increasing current density was observed. Again, as stated in Section 4.4.1, the differences in water volume between the various current densities tested can largely be explained by changes in the rate of water production at the different current densities tested. However, the trial conducted at 1000 mA/cm<sup>2</sup> does not follow the general trend; this can be explained by the increased condensation near the edge of the GDL and within the flow channel.



**Figure 67. Water volume profile of the GDL substrate under the lands of a fuel cell operated at 60°C at five separate current densities.**

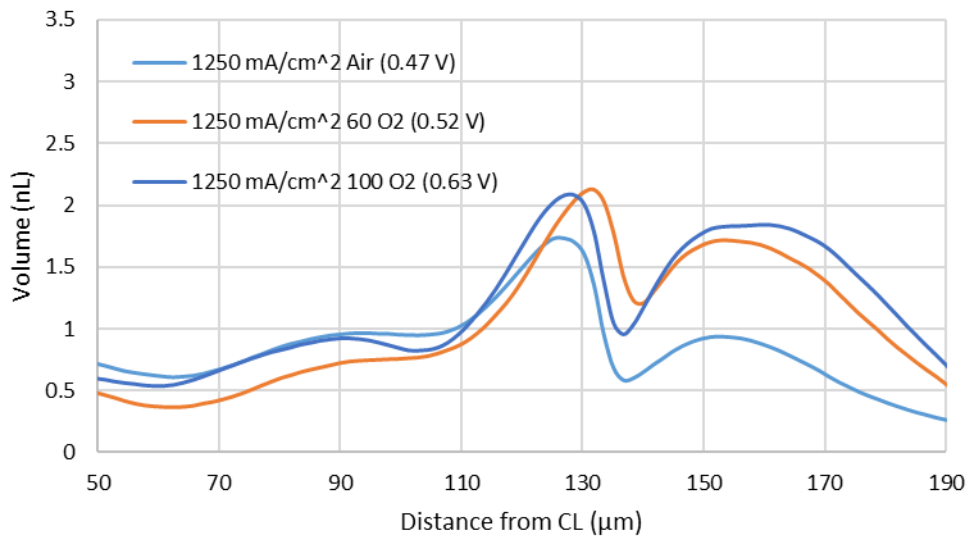
Figure 68 presents the water volume profile for the GDL substrate under the channels of a fuel cell operated at 60 °C at five different current densities. The water volume profiles for the region under the channels, from 50 μm to 100 μm from the CL had a relatively flat trend compared to the region under the lands (Figure 67). Similar to the overall results (Figure 66) and results for under the lands (Figure 67), the highest water volume under the channel was observed at 1700 mA/cm<sup>2</sup>, while the lowest water content was observed at 500 mA/cm<sup>2</sup>. However, similar to the overall results (Figure 66), at the GDL land interface (*i.e.*, approximately 130 μm from the CL) there was an increase in water volume for the tests conducted at 500, 750 and 1000 mA/cm<sup>2</sup>. This increase in water volume again is likely due to the increased condensation and thus buildup of liquid water within the channels.



**Figure 68.** Water volume profile of the GDL substrate under the channels of a fuel cell operated at 60°C at five separate current densities.

#### 4.4.3.1. Oxygen Variation

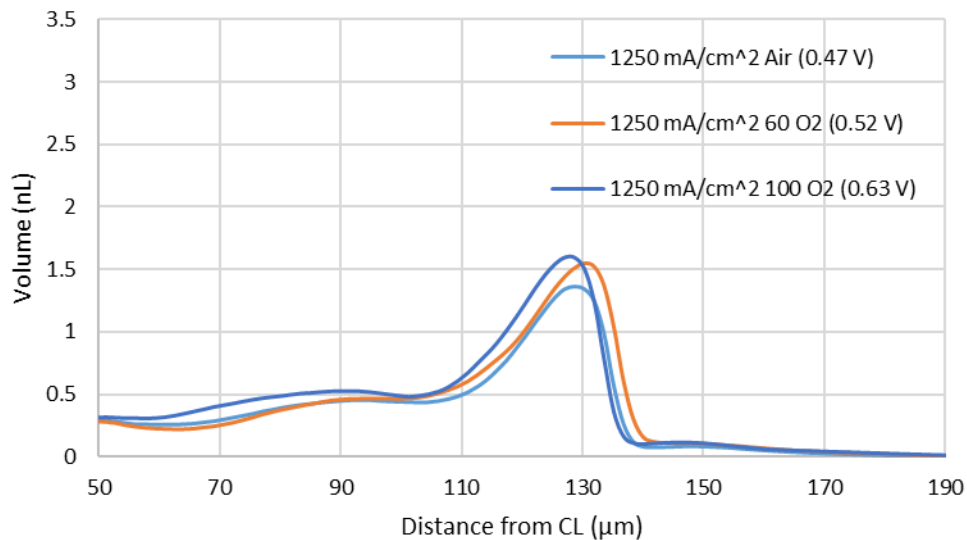
The results presented in Figure 69 show a similar water volume profile for all three oxygen concentrations tested at 60°C and 1250 mA/cm<sup>2</sup>, with only slight differences in the water volume at selected distances from the CL. However, there was no real trend in water volume with changes in oxygen concentration for these tests.



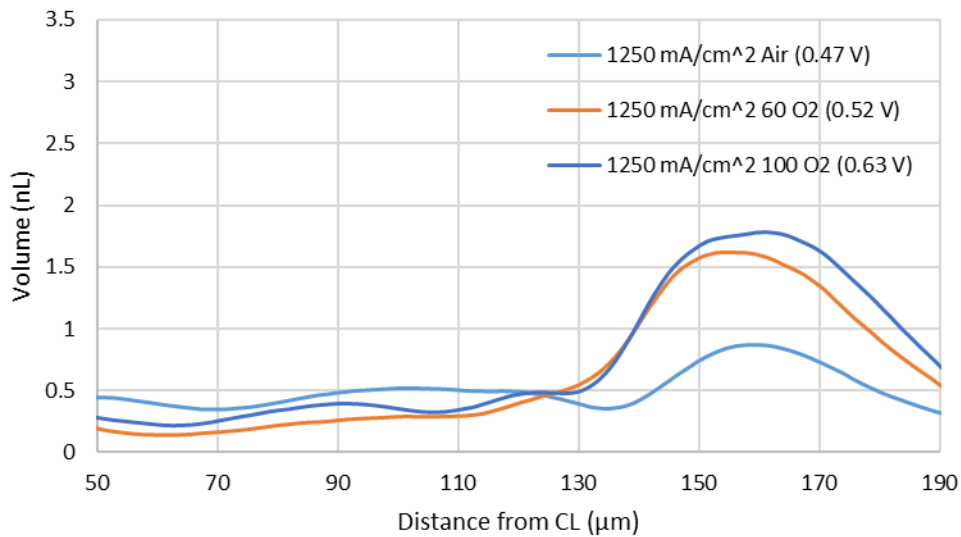
**Figure 69.** Overall water volume profile of the GDL substrate of a fuel cell operated at 60°C at three separate oxygen concentrations.

Figure 70 and Figure 71 display the through-plane liquid water volume under the lands and channels, respectively. The water volume profile under the lands generally trended upwards from the CCL to the flow channel. In comparison the channel region had a generally flat trend from the CCL to the flow channel, with a substantial increase in water volume under air and 60% oxygen due to the increased condensation, as explained above.

Similar trends in water volume were observed for both the channel and lands regions at 40°C and 50°C. More specifically, there was a trend of increasing water volume with decreasing oxygen concentration. However, at 60°C, this trend was no longer apparent, and the water volume was more or less the same at all three oxygen concentrations evaluated. Overall, the quantity of liquid water at 40°C and 50°C were similar, with reduced water volume observed at 60°C. This indicates that more water is present in the vapour phase for the 60°C trials.



**Figure 70. Water volume profile of the GDL substrate under the lands of a fuel cell operated at 60°C at three separate oxygen concentrations.**



**Figure 71. Water volume profile of the GDL substrate under the channels of a fuel cell operated at 60°C at three separate oxygen concentrations.**

#### **4.4.3.2. High Current Density**

Similar to the results at 40°C and 50°C discussed above, a high current density analysis was also conducted at 60°C. The purpose of this analysis was to better understand the impact of high current densities and thus lower voltages on liquid water distribution within the GDL. During this analysis, three high current densities were tested with one trial under air and two under 100% oxygen. Figure 72, Figure 73 and Figure 74 display the overall, land and channel water volume profile results, respectively, for this analysis.

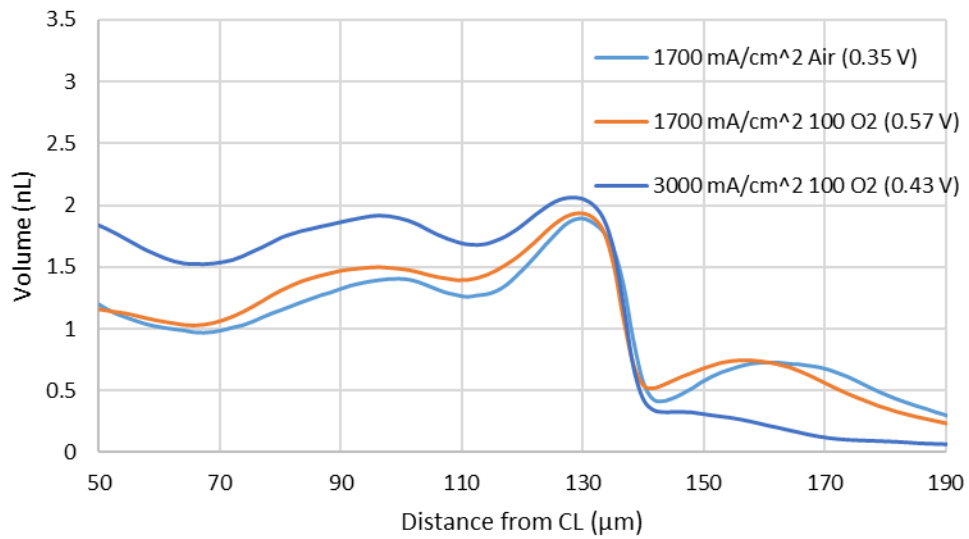


**Figure 72.** Overall water volume profile of the GDL substrate of a fuel cell operated at 60°C at three selected high current densities.

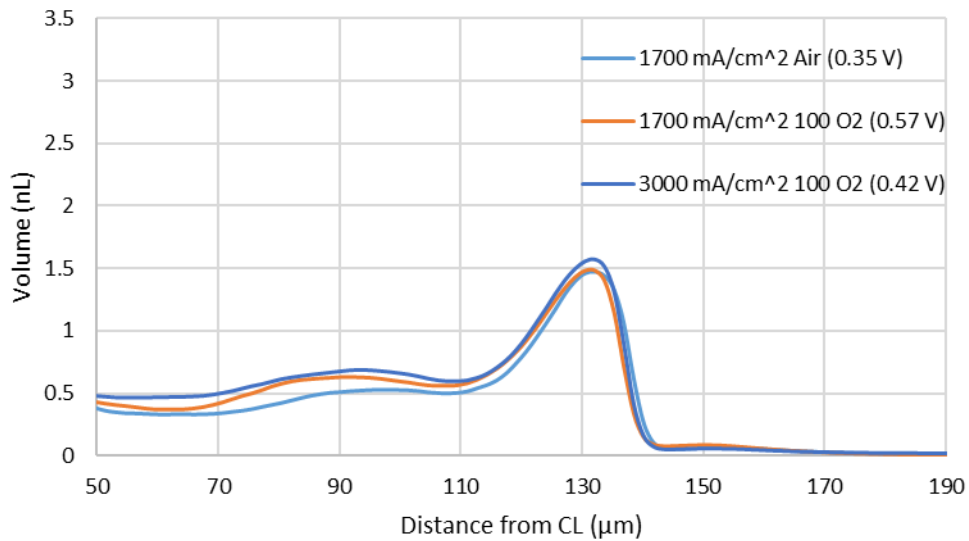


**Figure 73.** Water volume profile of the GDL substrate under the lands of a fuel cell operated at 60°C at three selected high current densities.

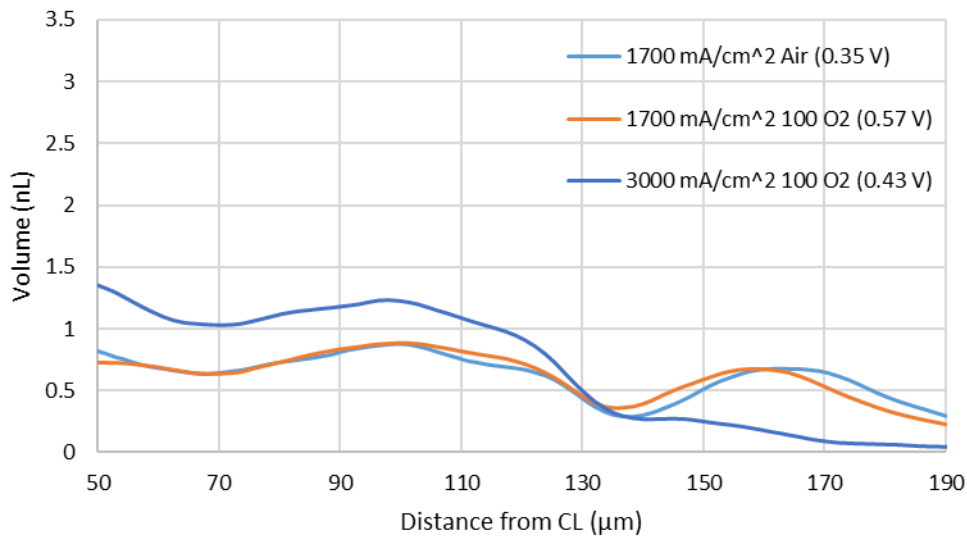


**Figure 74. Water volume profile of the GDL substrate under the channels of a fuel cell operated at 60°C at three selected high current densities.**

Figure 72 presents the overall water volume profile results for the three operational conditions tested. The highest water volume was observed for the trial conducted under 100% oxygen at 3000 mA/cm<sup>2</sup>. Lower water volumes were observed for the tests done at 1700 mA/cm<sup>2</sup> using air and 1700 mA/cm<sup>2</sup> using 100% oxygen. In general, the water volume appears to be dependent primarily on changes in current density and less on voltage. More specifically, the trials done at 1700 mA/cm<sup>2</sup> using air and 1700 mA/cm<sup>2</sup> using 100% oxygen had voltages of 0.35 V and 0.57 V, respectively; but had relatively similar water volume profiles. In comparison, the trial conducted at 3000 mA/cm<sup>2</sup> using 100% oxygen had an intermediate voltage of 0.43 V and had higher water volume through the GDL. This suggests that the differences in water production at the different current densities are having a substantial impact on the trends that were observed. Therefore, the higher water volume at 3000 mA/cm<sup>2</sup> under 100% oxygen is most likely due to greater water production at the higher current density.

Figure 73 displays the water volume profile results for under the lands for the three operational conditions tested. In contrast to the overall results, the results generated under the lands appear to have no distinct trend with changes in operational condition. Figure 74 displays the water volume profile results for under the channel region at the three operational conditions tested. These results show a similar trend to the overall water volume results shown in Figure 72, with the highest water volume

observed under 100% oxygen at 3000 mA/cm<sup>2</sup> and the lowest water volume at 1700 mA/cm<sup>2</sup> using air and 1700 mA/cm<sup>2</sup> using 100% oxygen. This suggests that the differences in water volume for the overall results are more substantially impacted by the water volume under the channel region than by the water volume under the lands.

Overall, water volumes were similar among the tests conducted at 40°C, 50°C and 60°C for the high current density investigation. However, there were some notable differences among the treatments. At 40°C, the water volume seemed to be primarily dependent on the operational voltage. More specifically, the lowest water volumes within the cathode GDL were observed at the lowest voltages tested. By comparison, the water volume within the GDL depended more on current density for the tests conducted at 60°C; that is, water volume scaled with increasing current density. The experimental work conducted at 50°C did not appear to be dependent on either current density or voltage, with similar water volume profiles observed for all high current densities tested. This could suggest that a transition region exists at about 50°C. Within this region, there seems to be a transition from voltage-dependent water volume to current density-dependent water volume when the fuel cell was operated at high current densities.

#### **4.4.4. Influence of Current Density at 70°C**

The overall water volume profiles within the GDL of a fuel cell operated at 70°C at current densities ranging from 500 mA/cm<sup>2</sup> to 1500 mA/cm<sup>2</sup> are presented in Figure 75. The results presented in Figure 75 show that the liquid water volume tends to scale with current densities within the range of 750 mA/cm<sup>2</sup> to 1500 mA/cm<sup>2</sup>, with the highest water volume occurring during operation at 1500 mA/cm<sup>2</sup> and lowest water volume observed at 750 mA/cm<sup>2</sup>. More specifically, the water volume tends to increase with increasing current density within this range. This trend of increasing water volume with increasing current density can be explained by an increase in water production at the higher current densities (Song *et al.* 2006; Muirhead 2017; Muirhead *et al.* 2018). However, at 500 mA/cm<sup>2</sup>, this trend was not evident, with the water volume at this current density being similar to results generated at 1250 mA/cm<sup>2</sup>. Based on interpretation of the data presented in Figure 75, this increase in water volume at 500 mA/cm<sup>2</sup> is likely due to increased condensation within the outer edges of the GDL and in flow channels. Similar to the results generated at 60°C, this increased condensation

likely resulted in a buildup of liquid water under the channels and lands. Additionally, liquid water may have moved backwards from the channel into the GDL.

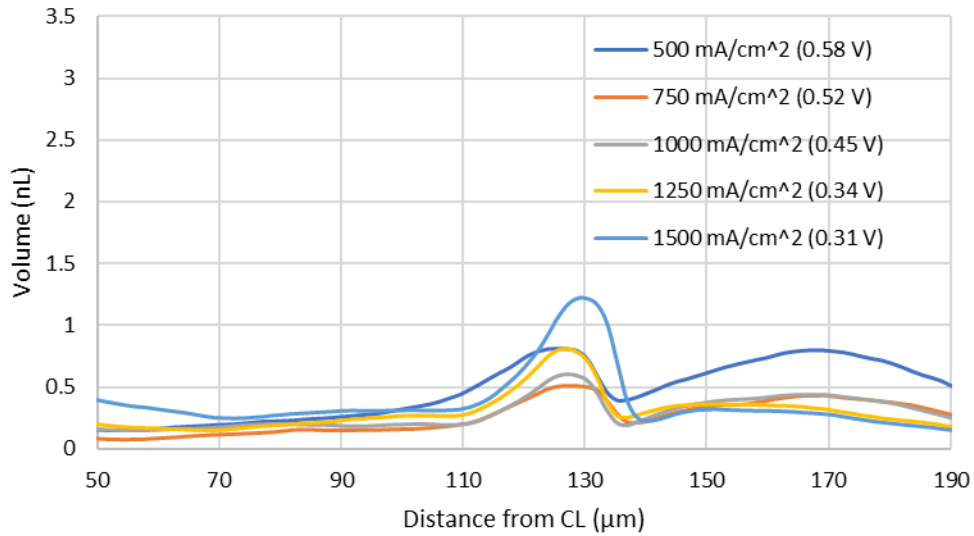


**Figure 75. Overall water volume profile of the GDL substrate of a fuel cell operated at 70°C at five separate current densities.**

The results presented in Figure 76 display the through-plane liquid water volumes under the lands at 70°C for all five current densities tested. The water volume profiles under the lands trend upwards from the CCL to the flow channels, peaking at the GDL/land interface. At this location, the highest water volume was observed for the test conducted at 1500 mA/cm<sup>2</sup>. In contrast, the lowest water volume was observed for the test conducted at 750 mA/cm<sup>2</sup>. Similar to the overall results, a trend of increasing water volume with increasing current density was observed. However, the test conducted at 500 mA/cm<sup>2</sup> did not appear to follow this trend, most likely due to increased condensation within the flow channels. Additionally, liquid water appears to be only located close to lands, with little to no liquid water accumulation within the GDL at 50 μm to 100 μm from the CL. This indicates that water produced at the CL is in the vapour phase and is only condensing as it approaches the cooler lands region. This is a trend that had been observed to some extent at each of the four temperatures tested. However, 70°C was the first temperature tested where vapour transport was likely the primary mode for all of the current densities tested.

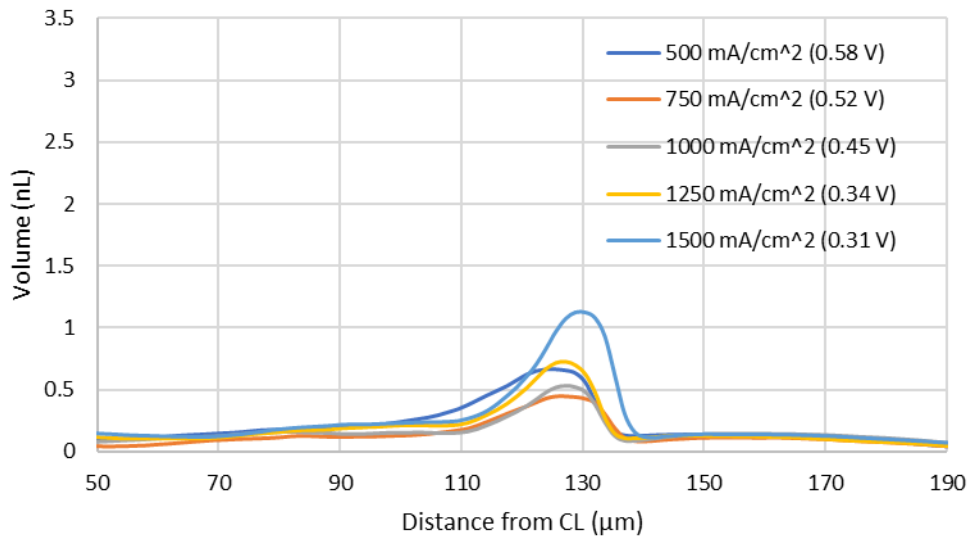


**Figure 76. Water volume profile of the GDL substrate under the lands of a fuel cell operated at 70°C at five separate current densities.**

Figure 77 presents the water volume profiles of the GDL substrate under the channels of a fuel cell operated at 70°C at five different current densities. For all five current densities, water was transported in the vapor phase from the CL to the flow channels. This suggests that the vapor pressure within the GDL was substantially lower than the saturation pressure. More specifically, at 70°C the saturation pressure is elevated and, thus, the air has more capacity to hold water vapor. Additionally, the thermal conductivity is lower under the channels when compared to the lands region. This results in higher temperatures within the GDL under the channels and contributes to a higher saturation vapour pressure.

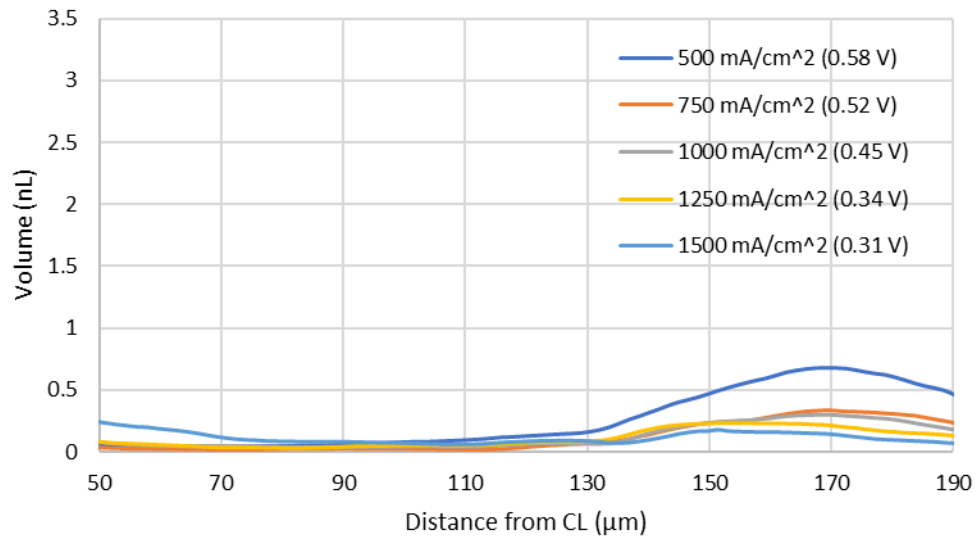


**Figure 77. Water volume profile of the GDL substrate under the channels of a fuel cell operated at 70°C at five separate current densities.**

#### **4.4.4.1. Oxygen Variation**

The results presented in Figure 78 for tests conducted at 70°C at 1250 mA/cm<sup>2</sup> show similar water volume profiles for all three oxygen concentrations tested, with slight differences in the water volume quantity at certain distances from the CL. However, there is no real trend in water volume with changes in oxygen concentration for these tests. Nevertheless, the water volume was significantly lower at all three oxygen concentrations tested when compared to the trials conducted at 40°C, 50°C and 60°C.

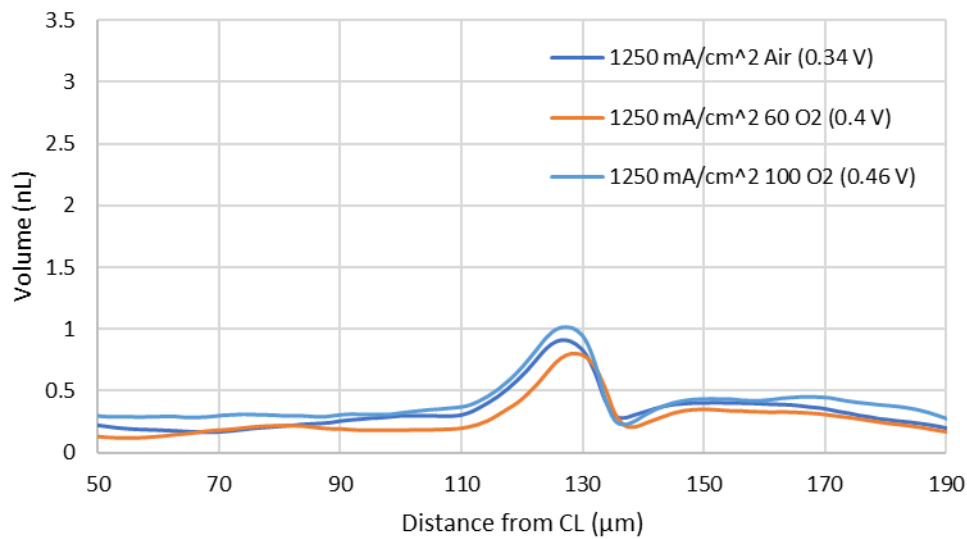


**Figure 78. Overall water volume profile of the GDL substrate of a fuel cell operated at 70°C at three separate oxygen concentrations.**

Figure 79 and Figure 80 display the through-plane liquid water volume under the lands and channels, respectively. The water volume profile under the lands generally trended upwards from the CCL to the flow channel. Similar to the overall results, the channel region had little or no liquid water present; hence, water was primarily transported in the vapor phase through the GDL. In general, there is no clear trend in water volume with changes in oxygen concentration for either the lands region or the channel region. Collectively, these results demonstrate that vapour-phase transport is dominating regardless of the oxygen concentration for the tests conducted at 70°C.

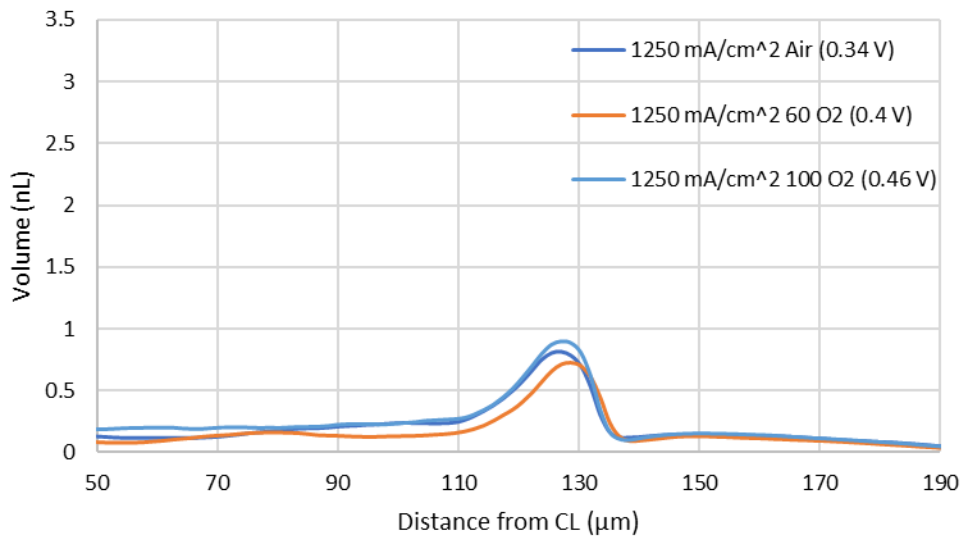


**Figure 79.** Water volume profile of the GDL substrate under the lands of a fuel cell operated at 70°C at three separate oxygen concentrations.

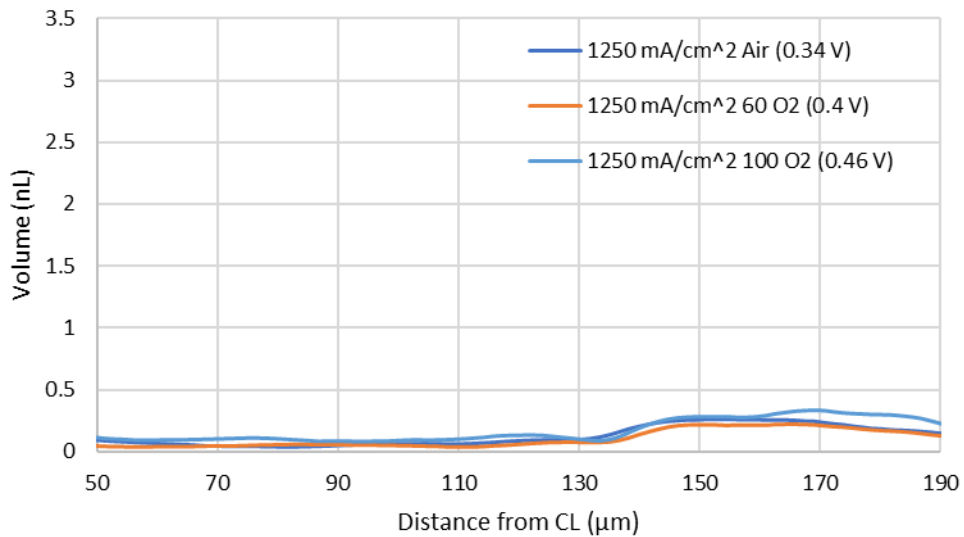


**Figure 80.** Water volume profile of the GDL substrate under the channels of a fuel cell operated at 70°C at three separate oxygen concentrations.

#### 4.4.4.2. High Current Density

Figure 81 presents the overall water volume profiles for the three operational conditions tested at high current densities. For the region between 50 μm and 110 μm from the CL, the highest water volume was observed for the trial conducted under 100% oxygen at 2500 mA/cm<sup>2</sup>. The lowest water volumes were observed for the tests done at

1500 mA/cm<sup>2</sup> using air and 1500 mA/cm<sup>2</sup> using 100% oxygen. However, when observing the water volume at the GDL/lands interface, the highest water volume occurred during operation at 1500 mA/cm<sup>2</sup> under air and the lowest water volume was observed at 1500 mA/cm<sup>2</sup> using 100% oxygen.

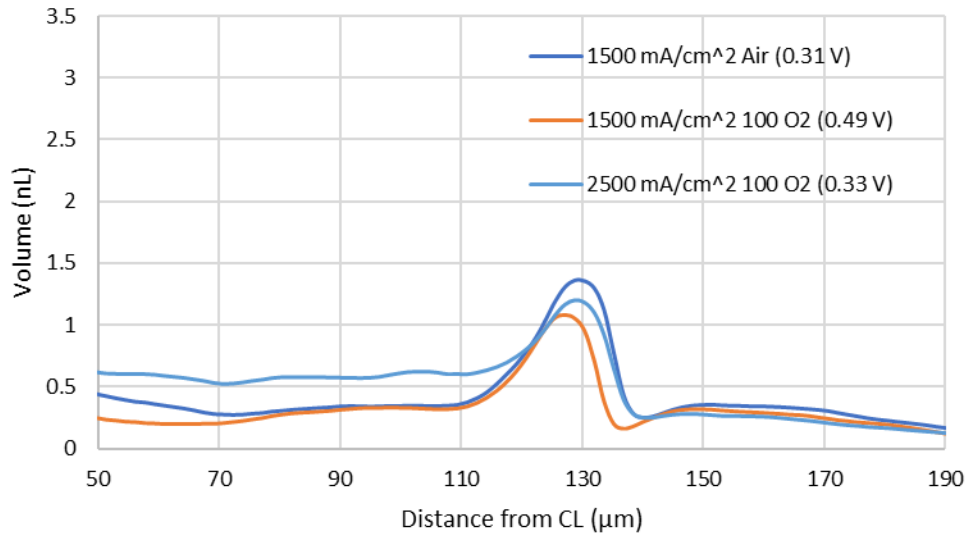


**Figure 81. Overall water volume profile of the GDL substrate of a fuel cell operated at 70°C at three selected high current densities.**

Figure 82 and Figure 83 display the water volume profile results for under the lands and channels, respectively. The results under the lands had a similar trend to the overall results, with the highest water volume at the GDL land interface occurring at 1500 mA/cm<sup>2</sup> using air and the lowest observed at 1500 mA/cm<sup>2</sup> using 100% oxygen. The channel results show very little liquid water within the GDL, which is consistent with the other tests conducted at 70°C. Although there were slight differences in the water volume profiles for the three operational conditions tested, the differences were minor. Hence, it is difficult to identify the factors causing the differences or to determine whether or not the differences indicate anything important. However, it appears that liquid water volume scales with increasing current density under the channels. More specifically, there is a slight increase in water volume for the test conducted at 2500 mA/cm<sup>2</sup> using 100% oxygen compared to the trials done at 1500 mA/cm<sup>2</sup>. This trend was also observed in the results obtained at 60°C.

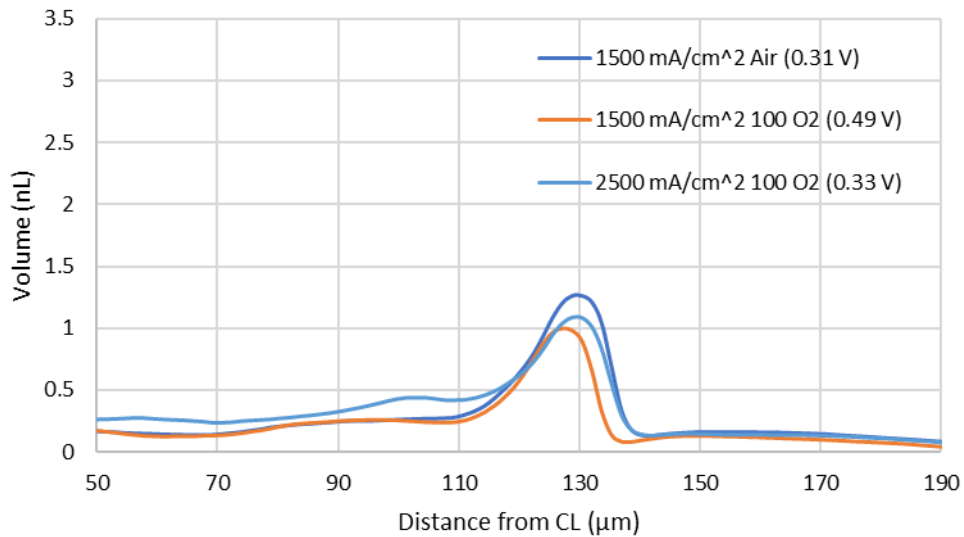


**Figure 82.** Water volume profile of the GDL substrate under the lands of a fuel cell operated at 70°C at three selected high current densities.

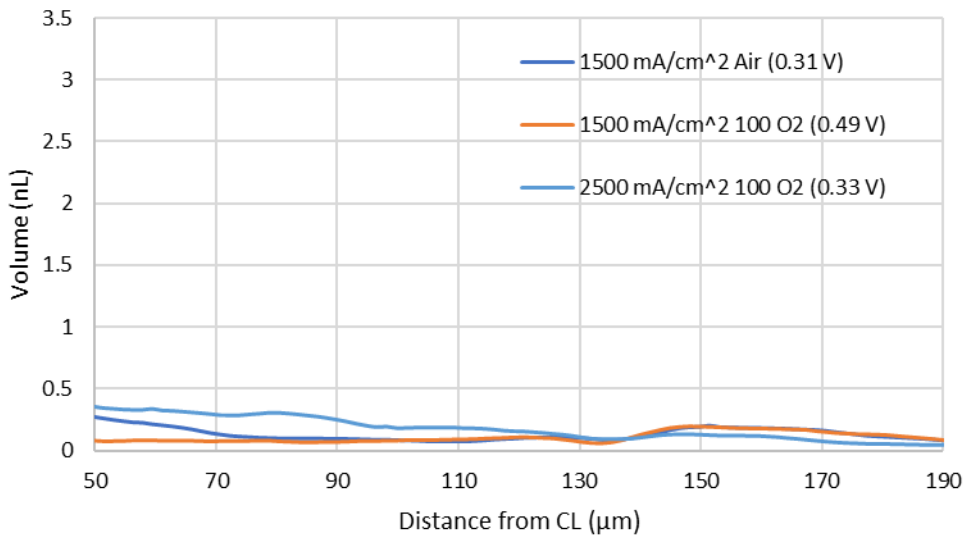


**Figure 83.** Water volume profile of the GDL substrate under the channels of a fuel cell operated at 70°C at three selected high current densities.

#### 4.4.5. Discussion of the Effect of Current Density on the Distribution of Liquid Water Within the Gas Diffusion Layer at Various Temperatures

It is important to be able to operate PEMFCs at high current densities to reduce the size and cost of this technology. However, operation at high current densities

implies increased water production and the potential for flooding of PEMFCs (Eller *et al.* 2017; Zhao *et al.* 2021). In this study, the effect of current density on the accumulation of liquid water in the GDL was evaluated at four operating temperatures (*i.e.*, 40°C, 50°C, 60°C, and 70°C). Each of these temperatures exhibited unique water volume trends for the range of current densities that were tested. The modes of water transport that predominated at each of the selected temperatures can be classified into three main categories: liquid and vapour transport, liquid transport dominated, and vapour transport dominated (Kato *et al.* 2022). In this analysis, the distribution of liquid water in the channel and land regions are discussed separately because they have different characteristics that can influence the water distribution within the GDL. Some of the more important characteristics of these two regions include thermal conductivity, electrical conductivity, temperature, effective diffusivity, and porosity.

Under the channel region the water volume was highest at 40°C and decreased with increasing temperature at all current densities. At 50°C and 60°C, the GDL was generally dry when the FC was operated at lower current densities (*i.e.*, 500 and 750 mA/cm<sup>2</sup>). At 70°C, low water volume was observed at all the current densities tested and the GDL was classified as generally dry. These results indicate that a transition region from generally wet to generally dry occurred at temperatures around 50°C to 60°C, depending on the current density. At lower temperatures (*i.e.*, 40°C and 50°C), water volume increased with increasing current density up to a certain threshold value, whereafter it began to decrease. At 40°C, for example, this threshold value was at 1000 mA/cm<sup>2</sup>; while the threshold was about 1250 mA/cm<sup>2</sup> at 50°C. However, at higher temperatures (*i.e.*, 60°C and 70°C), water volume increased with increasing current density for all current densities, with no threshold value observed for the range of current densities tested. At 40°C, the water volume was highest close to the CL and decreased closer to the flow channels. These results indicate that water is likely being transported as liquid and vapour concurrently. More specifically, water initially condensed near the CL and was transported through capillary pressure to the flow channel. Additionally, water may be condensing closer to the flow channels due to the presence of a temperature gradient (*i.e.*, warmer near the CL and cooler near the flow channels). Similar to the 40°C results, at 50°C and 60°C, water was transported concurrently as liquid and vapour at higher current densities. However, at lower current densities (*i.e.*, 500 and 750 mA/cm<sup>2</sup>) water seemed to be transported primarily in the vapour phase. At

70°C, water was primarily transported through the GDL in the vapour phase at all current densities. The changes in both the volume and phase of water between the different operational temperatures can be largely explained by changes in the saturation vapour pressure and the presence of a temperature gradient from the CL to GDL/channel interface (Kato *et al.* 2022). Saturation vapour pressure increases exponentially with increasing temperature (Kato *et al.* 2022). Additionally, due to the ORR, there tends to be a temperature gradient between the CL and the flow channels. Therefore, at the higher temperatures, the saturation vapour pressure increases and thus the liquid water volume tends to be lower. Furthermore, the increase in temperature at the CL due to the ORR further increases the saturation vapour pressure and contributes to the reduction in the liquid water content within the GDL.

Under the lands region, water volume was highest at 50°C and decreased at lower and higher temperatures. The reduction in water volume at temperatures above 50°C is similar to what was observed under the channel region. However, the reduction in water volume below 50°C was unique to the lands region. Additionally, liquid water was present under the lands at all of the temperatures and all of the current densities tested. At 40°C and 50°C, a portion of the water appears to condense close to the CL and is transported to the lands through capillary pressure. However, the bulk of the water was likely transported to the lands as vapour and condensed there due to a reduction in temperature and thus saturation vapour pressure. The same phenomenon was observed at 60°C for the higher current densities tested. However, for low current densities at 60°C and for all current densities at 70°C, water was transported through the GDL primarily in the vapour phase and only condensed near or at the GDL/lands interface.

#### **4.5. Comparison of Model Predictions and Experimental results at Various Current Densities and Temperatures**

In this study, the distribution of liquid water was evaluated in a miniaturized PEMFC under a variety of operating conditions. Incorporation of data from these experimental trials into the one-dimensional model yields predictions of the presence or absence of liquid water in the cathode GDL of an operating fuel cell. Comparison of such experimental results to the model predictions can improve our understanding of the

factors that influence water condensation and their effects on fuel cell performance. The following section of this document discusses these comparisons.

Model prediction maps for under both the channels and lands, displaying a wet or dry GDL at various current densities and temperatures, are shown in Figure 84 and Figure 85, respectively. Figure 86 and Figure 87 display the experimental results maps of wet or dry conditions for under the channel and lands, respectively, for the same operational conditions. Generally, when comparing the model prediction to the experimental results, there appears to be agreement for under the lands at all current densities and temperatures tested. More specifically, the experimental results and model predictions showed that the cathode GDL is wet under the lands for all the operational conditions tested (*i.e.*, temperatures ranging from 40°C to 70°C and current densities ranging from 500 mA/cm<sup>2</sup> to 1900 mA/cm<sup>2</sup>). Under the channels, the conditions were predicted to be wet during operation at 40°C, which was also observed during the experimental trials. Furthermore, at 70°C the model predicted dry conditions under the lands at all current densities (*i.e.*, 500 mA/cm<sup>2</sup> to 1500 mA/cm<sup>2</sup>), which again was observed during the experimental trials. At 50°C, the model predicted the GDL to be wet for all current densities test (*i.e.*, 500 mA/cm<sup>2</sup> and 1700 mA/cm<sup>2</sup>). However, the experimental results showed dry conditions at 500 mA/cm<sup>2</sup> and 750 mA/cm<sup>2</sup>, and wet conditions at 1000, 1250, 1500 and 1700 mA/cm<sup>2</sup>. For the trials conducted at 60°C, the model predicted wet conditions at 500, 750, 1000 and 1250 mA/cm<sup>2</sup>, and dry conditions for 1700 mA/cm<sup>2</sup>. In contrast, the experimental data showed dry conditions at 500, 750 and 1000 mA/cm<sup>2</sup> and wet conditions at 1250 mA/cm<sup>2</sup> and 1700 mA/cm<sup>2</sup>.

In general, the model does a reasonable job of predicting the presence or absence of liquid water within the cathode GDL. However, the model struggles to agree with the experimental results when in the transition region from undersaturated to oversaturated conditions (*i.e.*, 50°C and 60°C). More specifically, at 60°C the model predicts dry conditions at the highest current density tested (*i.e.*, 1700 mA/cm<sup>2</sup>) and wet conditions at the lower current densities (*i.e.*, 500, 750, 1000 and 1250 mA/cm<sup>2</sup>). Conversely, it can be observed that the experimental results are dry at the lower current densities (*i.e.*, 500, 750 and 1000 mA/cm<sup>2</sup>) and wet and the higher current densities (*i.e.*, 1250 mA/cm<sup>2</sup> and 1700 mA/cm<sup>2</sup>). This difference can likely be attributed to the relationship between water production and heat production. At the higher current densities, the model predicts that the additional heat production is sufficient to keep the

saturation vapour pressure above the water vapour pressure. However, during the experimental trials this was not the case and condensation occurred. Additionally, at the lower current densities, the model predicts that there is sufficient water production to raise the water vapour pressure above the saturation vapour pressure. In contrast, the experimental data showed, that the cathode GDL was dry under these operational conditions. Hence, there was likely insufficient water production at the lower current densities to cause condensation during the experimental trials. Its important to note that the experiments conducted within the transition region (*i.e.*, 50°C and 60°C) have a water vapour pressure to saturation vapour pressure ratio very close to one. More specifically at 60°C the ratio ranges from approximately 1.02 to 0.97 depending on the current density (Figure 88). This indicates that the RH is close to 100% and, therefore, it is very difficult to predict wet or dry condition for both the experimental and model results.

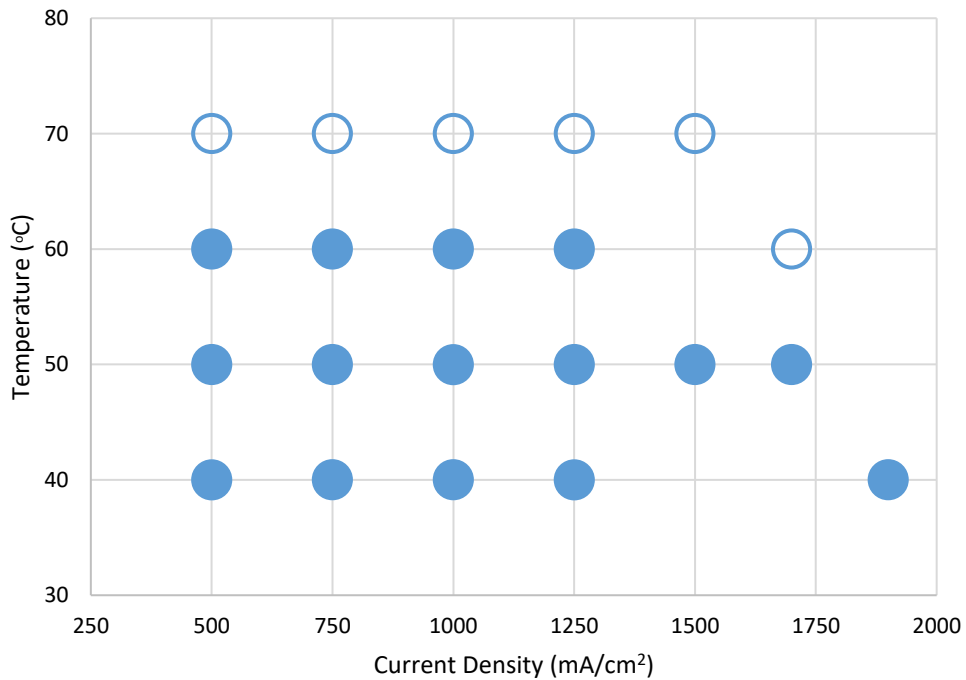


**Figure 84. Model map for under the channels displaying a wet or dry GDL at various current densities and temperatures.**

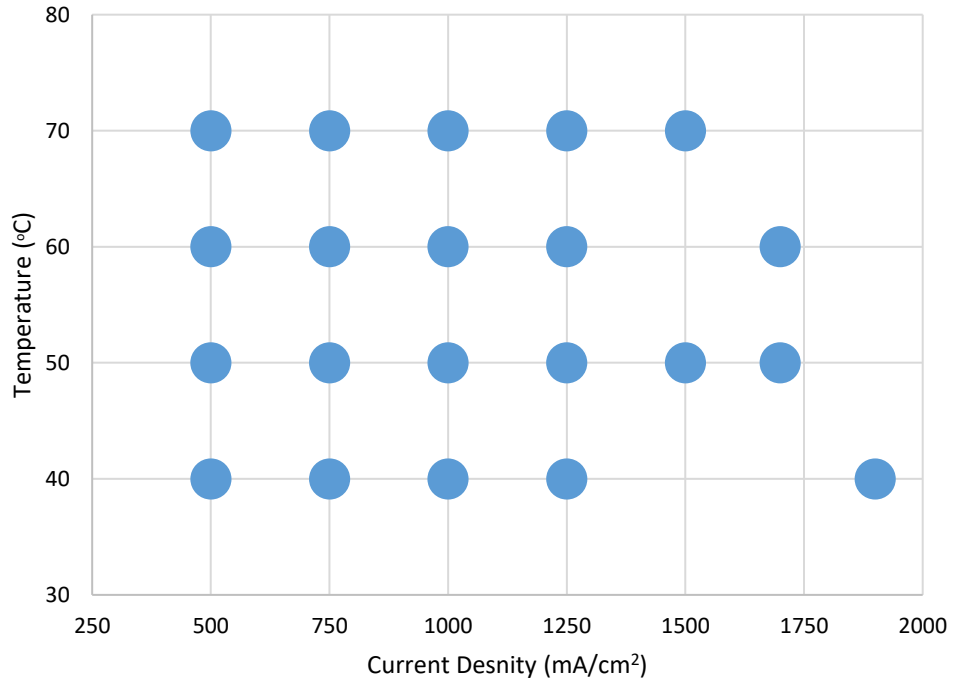


**Figure 85. Model map for under the lands displaying a wet or dry GDL at various current densities and temperatures.**

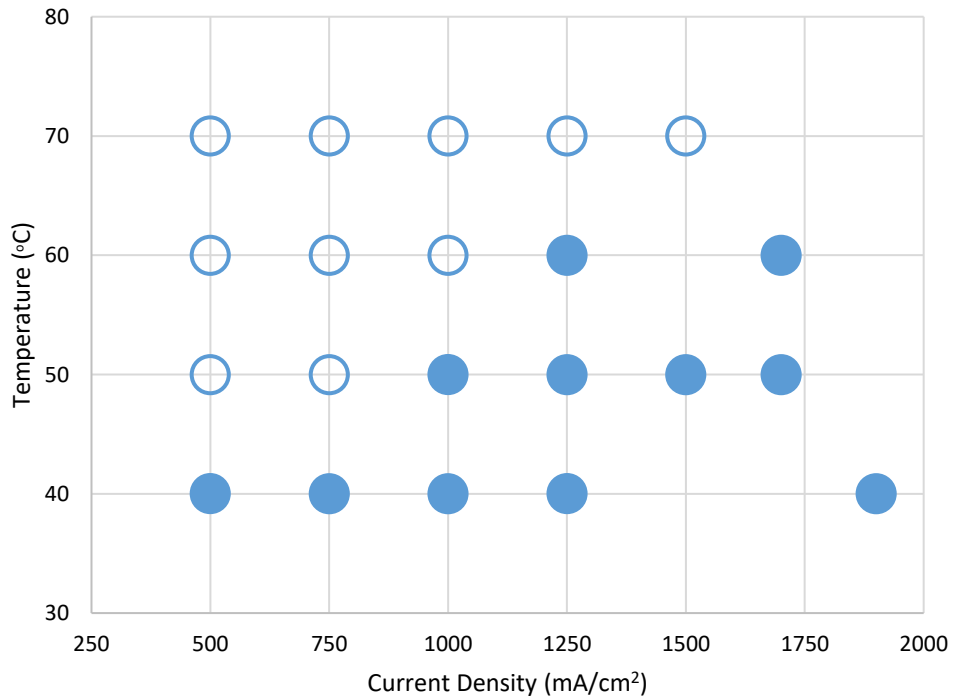


**Figure 86. Experimental map for under the channels displaying a wet or dry GDL at various current densities and temperatures.**

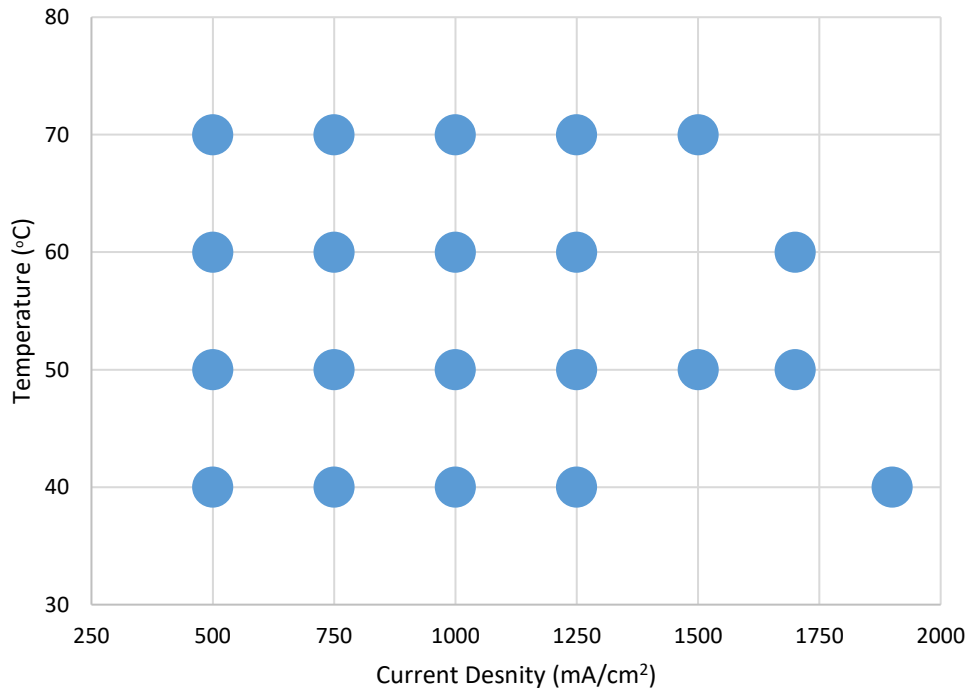


**Figure 87. Experimental map for under the lands displaying a wet or dry GDL at various current densities and temperatures.**

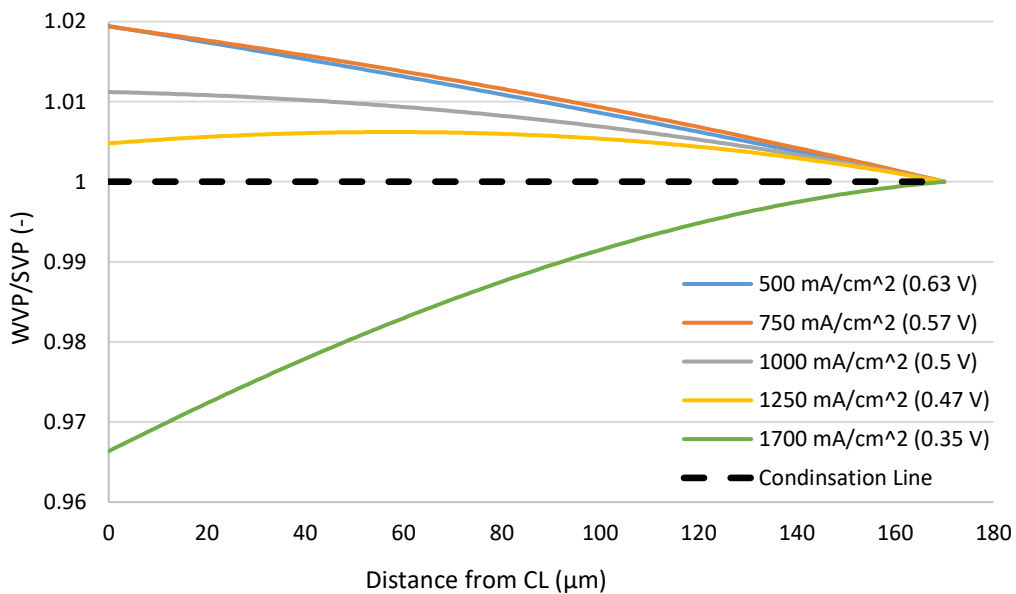


**Figure 88. Plot displaying the ratio of water vapor pressure to saturation vapor pressure under the channels at 60°C for five different current densities.**

The results of this study provide some important insights into the factors that influence the performance of PEMFCs. More specifically, comparisons between the performance data (*i.e.*, Polarization curves and EIS data) presented in section 4.2 and the water volume versus thickness plots presented in section 4.4, can help to expand knowledge related to mass transport losses in PEMFCs.

At low operating temperatures, the results of *in-operando* XCT testing showed that water had accumulated throughout portions of the GDL. The presence of liquid water likely resulted in mass transport losses when the cell was operated at higher current densities, which at least in part explains the impaired performance under these operating conditions. The experimental results also showed that there is a transition region within the 50°C to 60°C operating temperature range, wherein vapour transport was more prominent, specifically under the channels at lower current densities (*e.g.*, 500 mA/cm<sup>2</sup> and 750 mA/cm<sup>2</sup> at 50°C). Such changes in the state of the water present in the fuel cell may be sufficient to reduce mass transport losses and improve fuel cell performance. At 70°C, very little liquid water had condensed within the GDL for all current densities tested. As a result, mass transport losses were substantially reduced in the high current density regime and the fuel cell approached optimal performance. It is likely that supplemental heat production within the FC at the higher current densities and operating temperatures tested was sufficient to keep the water primarily in the vapour phase. Collectively, these results indicate that PEMFCs can be operated at high current densities under certain operational conditions to reduce the potential for flooding and therefore mass transport losses.

## Chapter 5. Uncertainty Analysis

This study was undertaken to evaluate the roles of various operational conditions on fuel cell performance and liquid water distribution. The investigation was conducted using materials and methods that were generally consistent with those that have been applied in other collaborative studies between SFU and Ballard Power Systems (*e.g.*, White 2019; White *et al.* 2016; 2017; 2019; Chen 2020; Aroge 2023) and at other fuel cell research laboratories (*e.g.*, Eller *et al.* 2017). While adherence to such methodologies helps to make the resultant data generally comparable to other data sets, there are still a number of uncertainties and/or errors that remain unresolved. These uncertainties were identified and qualitatively assessed to determine which ones were potentially of sufficient magnitude to alter the results of this investigation. Subsequently, approaches to mitigate these uncertainties were explicitly identified and implemented to minimize their impact on study outcomes. While quantitative analysis of residual uncertainty may have yielded further insights, it was mainly not pursued in this investigation.

### 5.1. Uncertainty Associated with Differences in MEAs Between Trials

It was not always possible to use the same MEA for a series of trials that were conducted to address the study objectives. In these cases, new MEAs were constructed and used to complete the experiment that was underway. However, MEAs are constructed by hand and, therefore, the new MEA may have differed from the original materials. More specifically, MEAs are constructed using pieces of GDL, CL and membrane materials. While every effort was taken to construct the MEAs using the same materials and by applying the same procedures, some differences may have existed. For example, various GDL materials could have slight differences in porosity, thickness, thermal conductivity and/or diffusivity. In addition, the CL materials could have slight differences in platinum loading, in addition to impurities on certain pieces of CL. Furthermore, assembled MEAs could have differential performance due to slight differences in assembly (*e.g.*, alignment of materials, compression, etc.). These differences can contribute to performance inconsistencies between MEAs. As a result, it can be difficult to compare results from trials conducted using different MEAs.

Due to the importance of preparing MEAs that are as similar as possible, the following mitigation strategies were used in this study. First, a stepwise approach was followed during the MEA and fuel cell assembly process to create consistency between different fuel cells. In addition, specifically designed vacuum plates were designed to assist in MEA assembly. Importantly, BOL diagnostics were conducted to gain information on the performance of the current fuel cell and support comparison to the original fuel cell. By assessing the magnitude of the differences in performance between cells, it is possible to determine if the subsequent experimental results are likely to be comparable. The results of this assessment showed that the various MEAs used in this study had consistent performance.

## **5.2. Uncertainty Associated with Segmentation of Liquid Water within the GDL**

The quality of XCT images, as well as the processing of these images to produce quantifiable data, can contribute to uncertainty in the results. Experience from numerous trials has shown that operation of the fuel cell at higher temperatures (*e.g.*,  $\geq 60^{\circ}\text{C}$ ) can result in image sets that are lower in quality (*i.e.*, relative to those produced when the FC is operated at lower temperatures). In addition, changes in operational conditions during *in-operando* XCT scans (*e.g.*, variation in current density or temperature) can impair image quality. Furthermore, movement of the fuel cell fixture during scans can result in degraded image quality. As the wet and dry image sets need to be virtually perfectly aligned to achieve proper subtraction, slight errors in alignment can result in poor subtraction and produce excess noise in the resultant image set. These and other operational and data processing issues can act alone or in combination to increase variability in the estimates of liquid water content within the GDL.

In addition to the uncertainty associated with the pre-segmentation steps, there are also uncertainties associated with the analysis of the subtraction data sets. More specifically, there are several sources of error in the thresholding step of the process, which are conducted to convert the greyscale image into a quantifiable binary image. Importantly, the magnitude of the uncertainty increases as image quality decreases. A sensitivity analysis was conducted to better understand the underlying variability in the segmentation process. This analysis involved evaluating subtracted images from a representative trial (*i.e.*,  $40^{\circ}\text{C}$  and 1000 mA, which was expected to have the highest

variability due to the high volume of liquid water present) and identifying low, moderate, and high grey-scale values during segmentation that provided acceptable quantification of liquid water volume. This range of grey-scale values reflects the range that would likely have been selected by analysts for the trials conducted in this study. The results of this analysis showed that, for the region within the GDL, the volume of water averaged 2.4 +/- 0.28 nL. Hence, variability in the selection of grey-scale values would typically result in estimates of water volume that were within about 12% of the "best" estimate value (i.e., that was calculated using the intermediate grey-scale value). Hence, image segmentation is considered to have a relatively limited impact on the water volume calculations.

A number of strategies were employed to mitigate the potential errors associated with the segmentation of liquid water within the GDL. First, the fuel cell was operated for one hour at a specific operational condition prior to initiating the XCT scans. This allows for equilibrium to be reached within the fuel cell, which results in less variation within the system during the trial and, hence, improved image quality. In addition, the SSF was specifically designed to enhance sample stability during XCT image scanning, which helps to improve image quality. Similarly, efforts were made to mount each sample in as close to the same way as possible to reduce variability between scans. Furthermore, a stepwise approach was carefully followed for each new data set during image subtraction and segmentation to help reduce alignment, subtraction, and segmentation errors. Finally, an overlay function was used in ImageJ to assist in making sure the volume and location of liquid water within the segmented data set reasonably matched the raw data. This final step in the image segmentation process ensured that the segmented data were comparable to the raw data that were generated in each trial. Although there may be residual uncertainties in the water volume estimates associated with the various trials, such uncertainties were not sufficient to alter the trends that were identified in this study.

### **5.3. Uncertainty Associated with Resistance in the Load Wires during *In-operando* Setup**

The long wires that connect Scribner test station to the XCT machine increase the internal resistance in the test system. Additionally, depending on how much the wires have been moved over time and how the fuel cell has been connected to the

wires, there can be variability in the resistance associated with the wires. This increased and variable resistance in the test system can result in changes in cell voltage, leading to incorrect measurements of the state of the fuel cell.

Several strategies were used to mitigate the effects of resistance variability associated with the long load wires. First, every effort was made to securely and consistently connect the fuel cell to the load wires during each trial to reduce variability in the voltage readings. Second, EIS measurements were periodically made following the experiments to determine the resistance within the wires on that specific day. This information provided a basis for resistance-correcting the resultant data prior to further data analysis.

#### **5.4. Uncertainty Associated with Electrical Connections Between the Load Wires and the Graphite Plates**

When assembling the SSF, load wires are inserted into connection ports within the graphite plates on the top and bottom. Over time these connections can become less secure and contribute to additional resistance within the system. This added resistance can result in voltage readings that do not accurately reflect the current state of the cell.

To minimize the voltage losses associated with these connections silver paste was added to the wires before inserting them into the graphite plates. This has proven to help maintain performance over time. Additionally, if the problem becomes too severe the graphite plates can be replaced. Comparison of BOL diagnostics to the current cell performance can help to identify the severity of the added resistance and whether the graphite plates need to be changed. This problem can sometimes be difficult to identify as the fuel cell also degrades over time, which results in reduced performance.

#### **5.5. Uncertainty Associated with the Application of Long Gas Lines from the Scribner to the XCT Machine during *In-operando* Testing**

Long gas lines are required to connect the Scribner and XCT machine during in-operando testing. Heat in the influent gas can be lost when travelling the long distance

in lines from the Scribner test station to the XCT machine. This temperature loss can contribute to condensation within the influent gas lines. Accumulation of liquid water within the gas lines and within the flow channels of the fuel cell can result in partial blockage of the pores near the GDL/channel interface, thereby contributing to mass transport losses. This becomes more of a problem at elevated temperatures due to the greater volume of water held in the air.

Two approaches were used to minimize the effects of water condensation in the influent gas delivery lines. First, heated tubes were used to help reduce the temperature loss in the lines. During each trial, these tubes were turned on and set to a temperature sufficient to reduce condensation within the lines. Second, higher flow rates were used in certain trials to reduce the accumulation of liquid water within the flow channels. However, this strategy was used only sparingly because higher flow rates can significantly alter the liquid water distribution within the GDL. In addition, higher gas delivery rates can result in degradation of XCT image quality.

## **5.6. Reproducibility of Liquid Water Quantification**

This study was conducted to quantify liquid water volume in the MEA of PEMFCs. The exploratory nature of this study resulted in the generation of data on liquid water volumes under many combinations of operating conditions. This section will discuss the reproducibility of the results of this investigation.

According to the National Academy of Sciences (2019), reproducibility (which assesses within-study variability) and replicability (which assesses between-study variability) are key factors that influence the level of confidence that can be placed in experimental results. Aroge (2023) conducted a reproducibility study that investigated differences in liquid water distribution under the channel and land regions between trials conducted using the same MEA under the same operating conditions. The results of this investigation showed that there were only slight differences in liquid water volume for the replicated trials, with the general through-plane trends in water distribution being similar. Additionally, Aroge (2023) investigated the reproducibility of results conducted using different MEAs under the same operating conditions. These results showed that there were some differences in the water volume estimates; however, the trends in water volume were consistent for the two MEAs tested (*i.e.*, decreasing liquid water volume

under the channel region in the through-plane direction away from the CCL and increasing liquid water volume under the lands in the through-plane direction away from the CCL).

Confidence in the water volume estimates generated in this study were enhanced by the fact that three investigators (*i.e.*, this study, Aroge 2023, and Halter *et al.* 2023) produced similar results based on experimental trials that were conducted independently for the same operating conditions. For example, Aroge (2023) investigated the water distribution under the channel for an Avcarb GDL at 50°C at current densities ranging from 250 mA/cm<sup>2</sup> to 1200 mA/cm<sup>2</sup>. The results showed decreasing water volume in the through-plane direction from the CCL towards the channels, which is consistent with the results of the current study. Furthermore, Halter *et al.* (2023) generated similar results under the same conditions.

## Chapter 6. Summary, Conclusions and Recommendations

### 6.1. Summary

Effective water management is required to enable PEMFCs to operate efficiently, particularly at the high current densities needed to make them relevant for various transportation and stationary applications. This study was conducted to evaluate the effects of selected operating conditions on the performance of PEMFCs, as well as their influence on the distribution of liquid water within specific fuel cell components.

The results of this study provide a number of important insights into the effects of selected operating conditions on liquid water distribution and on the electrochemical performance of PEMFCs. In this investigation, PEMFC performance was primarily assessed based on the relationships between current density and voltage under specified operating conditions, including various influent gas flow rates, cell temperatures, oxidant concentrations, and relative humidities. In addition, the effects of these operating variables and current density on the distribution of liquid water in the cathode GDL was evaluated under *in-operando* conditions using X-ray computed tomography. Collectively, the results of this study are intended to advance the development of PEMFC technology by identifying conditions that optimize PEMFC performance.

The experimental results presented in Chapter 4 showed that influent gas delivery rates can have a substantial impact on the performance of PEMFCs. More specifically, operation of a PEMFC (*i.e.*, on the Scribner Test Station;) at high influent gas flow rates (*i.e.*, 0.9 L/min H<sub>2</sub> and 1.2 L/min air) resulted in a substantial improvement in performance relative to lower influent gas flow rates (*i.e.*, 0.2 L/min H<sub>2</sub> and 0.5 L/min air). Improvements in performance were likely associated with better removal of condensed water from the influent gas lines and the cell flow channels. In addition, it is likely that high influent gas flow rates expedited removal of liquid water from those portions of the GDL located adjacent to the flow channels.

The results of these trials also exposed some of the limitations associated with operation of the FC on the Scribner Test Station during *in-operando* testing, including

the inability to regulate relative humidity (and dew point), the potential for water to condense in the long influent gas lines due to cooling of the gases by ambient air, and the higher resistance in the long load wires. While the inability to regulate relative humidity and the length of the influent gas lines are unresolved issues for investigations conducted using the Scribner Test Station, an approach to normalize the performance data to account for the high resistance in the load wires was developed and applied to make the results more comparable to those generated using direct Scribner connection and the G20 test station. This represents a relevant finding because it is important to ensure that results generated using the *in-operando* setup can be directly compared with those produced using direct Scribner connection and the G20.

Cell operating temperature was also identified as a key factor influencing PEMFC performance. More specifically, the best performance was observed at a temperature of 70°C, with poorer performance observed at higher and lower temperatures. At the lower temperatures (*i.e.*, 40°C, 50°C and 60°C) increased ohmic losses can be attributed to the performance reduction. However, at higher temperatures (*i.e.*, 80°C and 90°C) performance losses appeared to be a result of mass transport limitation.

Based on the results of the experimental trials conducted under a range of operating conditions, relative humidity was found to be an important factor influencing fuel cell performance. Regardless of the operating temperature considered, the best fuel cell performance was observed in the trials conducted at 100% RH. Performance scaled with RH at the lower RHs tested (*i.e.*, 25%, 50% and 75%), with the lowest performance observed at 25% RH. These reductions in fuel cell performance were primarily due to increased ohmic and activation losses, as a result of reduced membrane and ionomer conductivity. At 75% and 100% RH, an increase in temperature resulted in a slight increase in performance. The performance improvement at 70°C compared to 40°C can be attributed to improved membrane hydration and increased reaction kinetics. Additionally, there were reduced mass transport losses at 70°C. However, at lower RHs (*i.e.*, 25% and 50%), a decrease in operational temperature resulted in an increase in performance. These results indicate that at low RHs, greater membrane hydration can be achieved at lower temperatures potentially due to wetter conditions within the GDL/MPL region. More specifically, at the lower temperatures tested, the water produced in the fuel cell may aid ionomer and membrane hydration as the current

density is increased. In general, the model predictions were consistent with the experimental results generated in this study.

In this work, the effects of current density on the accumulation of liquid water in the cathode GDL was evaluated at four operating temperatures (*i.e.*, 40°C, 50°C, 60°C, and 70°C). It was found that the water volume trends and state of water within the GDL were highly dependent on both temperature and current density. The modes of water transport that predominated at each of the selected temperatures can be classified into three main categories: liquid and vapour transport, liquid transport dominated, and vapour transport dominated (Kato *et al.* 2022). The results of this study generally showed that water volume decreased under both the land and channel regions with increasing temperature. Under the channel region water initially condensed close to the CCL and was primarily transported in the liquid phase at lower temperatures. However, at elevated temperatures the majority of water was transported in the vapour phase with little to no condensation within the GDL. Under the land region water was transported concurrently as liquid and vapour at lower temperatures. Water initially condensed near the CCL and was transport through capillary pressure towards the lands and later condensed again when approaching the GDL/land interface. However, at higher temperatures water was primarily transported in the vapour phase and only condensed at the GDL/land interface. Current density was also a factor that influenced the liquid water dynamics within the fuel cell. More specifically, water volume generally increased with increasing current density at all four temperatures tested due to greater water production rate. However, at 40°C and 50°C water volume only increased up to 1250 mA/cm<sup>2</sup> and then began to decrease at higher current densities.

## 6.2. Conclusions

Based on the results that were obtained from the current investigation, it is possible to draw a number of conclusions regarding the effects of operational conditions on water accumulation and fuel cell performance, including:

1. Fuel cell performance tends to be enhanced when influent gases are delivered at higher rates. More specifically, at higher flow rates, the condensed water within the influent gas lines is more effectively moved through the cell preventing accumulation within the flow channels and the

GDL. Additionally, this performance improvement can likely be explained by enhanced water removal from the edges of the GDL at higher flow rates;

2. The performance of the miniaturized PEMFC was optimal at an operating temperature of 70°C using fully humidified gases (100% RH). At 70°C, reduced ohmic losses were observed when compared to the lower operational temperature tested. Additionally, at 70°C, mass transport losses were minimized as a result of vapour phase-dominated water transport;
3. Relative humidity is an important factor influencing fuel cell performance. More specifically, when RH increases from 25% to 100% at temperatures ranging from 40°C to 70°C, improved membrane and ionomer hydration was achieved. Additionally, at RHs around 100%, optimal fuel cell performance was reached at 70°C due to reduced ohmic, activation and mass transport losses. However, at lower RHs, better performance was achieved at lower temperatures due to a reduction in ohmic losses. The experimental results generated in the RH study were generally consistent with the model predictions;
4. The modes of water transport in PEMFCs are influenced by operational conditions. Importantly, temperature and current density are key conditions that impact the distribution and transport of water within the GDL of a fuel cell. At temperatures below 60°C, water is transported primarily in the liquid phase. At these lower temperatures (i.e., 40°C and 50°C), the saturation vapour pressure is reduced. As a result, less water can be held in the vapour phase and, thus, condensation is likely to occur. However, at temperatures above 60°C, water is transported primarily in the vapour phase from the CCL to the flow channels, with liquid water present only at the GDL-land interface. Again, this is related to the saturation vapour pressure at the tested operating temperature. At higher temperatures, the air within the GDL is able to hold more water in the vapour phase and thus less condensation is observed. Condensation is present when approaching the lands due to a reduction in temperature and, thus, saturation vapour pressure;

5. At temperatures that optimize fuel cell performance, accumulation of liquid water was minimized, even at the highest current densities tested. This indicates that fuel cells can be operated at high current densities without accumulating problematic levels of liquid water; and,
6. Supplemental benefits associated with operation of the PEMFC at 70°C are likely to include improved membrane conductivity, improved reaction kinetics, and improved ionomer hydration.

### 6.3. Recommendations

The results of this study provide important insights into the accumulation of liquid water in PEMFCs under various operating conditions. However, there are a number of questions that remain unanswered and would benefit from further investigations. Some of the recommendations that emerged from this study are listed below. For each of the tests recommended below, it would be useful to include sufficient replication to assess the variability in the results.

1. Conduct tests using different GDL types with variable thermal conductivities, thicknesses, and fiber structures. Such investigations could provide valuable information on GDLs that can limit excess water accumulation, while achieving good performance at high current densities;
2. Conduct *in-operando* tests at a wider range of temperatures, including room temperature and temperatures greater than 70°C (*i.e.*, 80°C and 90°C). This work would be intended to investigate the liquid water distribution at elevated temperatures. More specifically, this work should focus on determining if the water volume under the lands is reduced at operating temperatures above 70°C (*i.e.*, as was the trend when increasing temperature from 40°C to 70°C). Additionally, as discussed in Chapter 4, mass transport losses appear to be larger at 80°C and 90°C. Visualizing the water distribution under these conditions could help to expand knowledge in this area. However, improvements to the current XCT setup would be needed to conduct reliable scans at higher temperatures;
3. Conduct an analysis of the influence of varying oxygen concentrations on liquid water accumulation at higher current densities. This work would be intended to further evaluate the impact of heat generation at the CL on the liquid water

- distribution within the GDL. More specifically, conducting this type of analysis at higher current densities could increase the voltage differences between selected oxygen concentration trials and, thus, increase the differences in heat production. In doing so, greater water volume differences may be observed between trials;
4. Modify the *in-operando* setup to minimize the effects of the long gas delivery lines and long load wires. Such improvements would help to reduce condensation within the influent gas lines and reduce the resistance associated with the load wires;
  5. Validate the one-dimensional RH model through *in-operando* XCT testing under a variety of operating conditions. Improvements to the current *in-operando* XCT setup would be needed to test a range of RHs (*i.e.*, the current setup does not readily support testing at various RHs);
  6. Further develop the current one-dimensional model to include additional variables that influence the distribution and transport of water within PEMFCs. The goal of this work would be to enhance the ability of the model to predict liquid water distribution and volume within the fuel cell under a broad range of operational conditions; and,
  7. Evaluate the residual uncertainty associated with the liquid water volume quantification process. If warranted, further develop the current procedures for image segmentation and analysis to improve liquid water volume estimates.

## Chapter 7. References Cited

- Abd Rahman, S.N., Masdar, M.S., Rosli, M.I., Majlan, E.H., Husaini, T., Daud, W.R.W., Rejab, S.A.M. and Lye, C.C. (2016). Portable PEM fuel cell system: water and heat management. *J. Eng. Sci. Technol*, 11, 122-136.
- Adachi, M., Navessin, T., Xie, Z., Li, F. H., Tanaka, S., & Holdcroft, S. (2010). Thickness dependence of water permeation through proton exchange membranes. *Journal of Membrane Science*, 364(1-2), 183-193.
- Agaesse, T. (2016). *Simulations of one and two-phase flows in porous microstructures, from tomographic images of gas diffusion layers of proton exchange membrane fuel cells* (Doctoral dissertation).
- Agyekum, E. B., Ampah, J. D., Wilberforce, T., Afrane, S., & Nutakor, C. (2022). Research Progress, Trends, and Current State of Development on PEMFC-New Insights from a Bibliometric Analysis and Characteristics of Two Decades of Research Output. *Membranes*, 12(11), 1103.
- Ahmadi, P., & Kjeang, E. (2017). Realistic simulation of fuel economy and life cycle metrics for hydrogen fuel cell vehicles. *International Journal of Energy Research*, 41(5), 714-727.
- Alavijeh, A. S., Bhattacharya, S., Thomas, O., Chuy, C., Yang, Y., Zhang, H., & Kjeang, E. (2019). Effect of hygral swelling and shrinkage on mechanical durability of fuel cell membranes. *Journal of Power Sources* 427:207-214.
- Amirinejad, M., Rowshanzamir, S., & Eikani, M. H. (2006). Effects of operating parameters on performance of a proton exchange membrane fuel cell. *Journal of Power Sources*, 161(2), 872-875.
- Aoyama, Y., Tabe, Y., Nozaki, R., Suzuki, K., Chikahisa, T., & Tanuma, T. (2018). Analysis of water transport inside hydrophilic carbon fiber micro-porous layers with high-performance operation in PEFC. *Journal of the electrochemical society*, 165(7), F484.

Aroge, F. A. (2023). Investigations on liquid water distribution in polymer electrolyte fuel cells. PhD Thesis. School of Sustainable Energy Engineering. Simon Fraser University. Surrey, British Columbia.

Ashrafi, M., & Shams, M. (2017). The effects of flow-field orientation on water management in PEM fuel cells with serpentine channels. *Applied Energy* 208:1083-1096.

Asif, M. B., Fida, Z., Tufail, A., van de Merwe, J. P., Leusch, F. D., Pramanik, B. K., ... & Hai, F. I. (2019). Persulfate oxidation-assisted membrane distillation process for micropollutant degradation and membrane fouling control. *Separation and Purification Technology*, 222, 321-331.

Askaripour, H. (2019). Effect of operating conditions on the performance of a PEM fuel cell. *International Journal of Heat and Mass Transfer*, 144, 118705.

Aslam, R. M., Ingham, D. B., Ismail, M. S., Hughes, K. J., Ma, L., & Pourkashanian, M. (2019). Simultaneous thermal and visual imaging of liquid water of the PEM fuel cell flow channels. *Journal of the Energy Institute*, 92(2), 311-318.

Baker, D. R., Caulk, D. A., Neyerlin, K. C., & Murphy, M. W. (2009). Measurement of oxygen transport resistance in PEM fuel cells by limiting current methods. *Journal of The Electrochemical Society*, 156(9), B991.

Baker, D. R., & Caulk, D. A. (2013). Limiting current as a tool to study oxygen transport in PEM fuel cells. *ECS Transactions*, 50(2), 35.

Ballard Power Systems (Ballard). (2020). Advantages of fuel cell electric buses. Retrieved September 19, 2021, from <https://www.ballard.com/markets/transit-bus>

Ballard Power Systems (Ballard). (2021). Ballard & HDF Energy announce world's first multi-megawatt scale baseload hydrogen power plant. Retrieved February 20, 2022, from [Ballard & HDF Energy Announce World's First Multi-Megawatt Scale Baseload Hydrogen Power Plant](#)

Bao, Z., Niu, Z., & Jiao, K. (2019). Analysis of single-and two-phase flow characteristics of 3-D fine mesh flow field of proton exchange membrane fuel cells. *Journal of Power Sources* 438:226995.

Barbir, F. (2006). PEM fuel cells. In: N. Sammes (Ed.), *Fuel Cell Technology: Reaching Towards Commercialization* (pp. 27-51). Springer, London. [https://doi.org/10.1007/1-84628-207-1\\_2](https://doi.org/10.1007/1-84628-207-1_2)

Bazylak, A. (2009). Liquid water visualization in PEM fuel cells: A review. *International journal of hydrogen energy*, 34(9), 3845-3857.

Bedet, J., Maranzana, G., Leclerc, S., Lottin, O., Moyne, C., Stemmelen, D., ... & Canet, D. (2008). Magnetic resonance imaging of water distribution and production in a 6 cm<sup>2</sup> PEMFC under operation. *International Journal of Hydrogen Energy*, 33(12), 3146-3149.

Belkhiri, Z., Zeroual, M., Moussa, H. B., & Zitouni, B. (2011). Effect of temperature and water content on the performance of PEM fuel cell. *Journal of Renewable Energies*, 14(1), 121-130.

Belkhiri, Z., Moussa, H. B., Haddad, D., & Oulmi, K. (2015). Effect of permeability on the dynamic field in the PEM fuel cell. *International journal of hydrogen energy*, 40(39), 13789-13798.

Berning, T. (2011). On water transport in polymer electrolyte membranes during the passage of current. *International journal of hydrogen energy*, 36(15), 9341-9344.

Berning, T. (2020). On the Nature of Electro-Osmotic Drag. *Energies*, 13(18), 4726.

Boillat, P., Kramer, D., Seyfang, B. C., Frei, G., Lehmann, E., Scherer, G. G., ... & Shinohara, K. (2008). In situ observation of the water distribution across a PEFC using high resolution neutron radiography. *Electrochemistry Communications*, 10(4), 546-550.

British Petroleum. 2022. Statistical review of world energy: 2021. 70<sup>th</sup> Edition. Retrieved February 21, 2022, from [Full report – Statistical Review of World Energy 2021 \(bp.com\)](https://www.bp.com).

Britton, M. M. (2017). MRI of chemical reactions and processes. *Progress in nuclear magnetic resonance spectroscopy*, 101, 51-70.

- Caulk, D. A., & Baker, D. R. (2010). Heat and water transport in hydrophobic diffusion media of PEM fuel cells. *Journal of The Electrochemical Society*, 157(8), B1237.
- Cespedes, G., Asteazaran, M., & Castro Luna Berenguer, A. M. D. C. (2016). Effect of Water Content in the Gas Diffusion Layer of H<sub>2</sub>/O<sub>2</sub> PEM Fuel Cell. *Journal of Materials Science and Engineering A*, 6.
- Chen, H., Zhao, X., Zhang, T., & Pei, P. (2019). The reactant starvation of the proton exchange membrane fuel cells for vehicular applications: A review. *Energy conversion and management*, 182, 282-298.
- Chen, S. Z., & Wu, Y. H. (2008, September). Experimental investigation of gravity effect on water management in PEM fuel cell. In *2008 IEEE Vehicle Power and Propulsion Conference* (pp. 1-3). IEEE.
- Chen, Y. (2020). 4D in situ visualization of chemo-mechanical membrane degradation in fuel cells: Understanding and mitigating edge failures. MAS Thesis. School of Mechatronic Engineering. Faculty of Applied Sciences. Simon Fraser University. 108 pp.
- Chi, B., Hou, S., Liu, G., Deng, Y., Zeng, J., Song, H., ... & Ren, J. (2018). Tuning hydrophobic-hydrophilic balance of cathode catalyst layer to improve cell performance of proton exchange membrane fuel cell (PEMFC) by mixing polytetrafluoroethylene (PTFE). *Electrochimica Acta*, 277, 110-115.
- Chin, T. K., Liao, M. W., & Perng, T. P. (2019). Enabling higher electrochemical activity of Pt nanoparticles uniformly coated on cubic titanium oxynitride by vertical forced-flow atomic layer deposition. *Journal of Power Sources*, 434, 2267-16.
- Chugh, S., Chaudhari, C., Sonkar, K., Sharma, A., Kapur, G. S., & Ramakumar, S. S. V. (2020). Experimental and modelling studies of low temperature PEMFC performance. *international journal of hydrogen energy*, 45(15), 8866-8874.
- Chun, J. H., Park, K. T., Jo, D. H., Lee, J. Y., Kim, S. G., Park, S. H., ... & Kim, S. H. (2011). Development of a novel hydrophobic/hydrophilic double micro porous layer for use in a cathode gas diffusion layer in PEMFC. *International journal of hydrogen energy*, 36(14), 8422-8428.

- Dai, W., Wang, H., Yuan, X. Z., Martin, J. J., Yang, D., Qiao, J., & Ma, J. (2009). A review on water balance in the membrane electrode assembly of proton exchange membrane fuel cells. *International Journal of hydrogen energy*, 34(23), 9461-9478.
- Daino, M. M., Lu, Z., LaManna, J. M., Owejan, J. P., Trabold, T. A., & Kandlikar, S. G. (2011). Through-plane water transport visualization in a PEMFC by visible and infrared imaging. *Electrochemical and Solid-State Letters*, 14(6), B51.
- Daş, E., Gürsel, S. A., Şanlı, L. I., & Yurtcan, A. B. (2017). Thermodynamically controlled Pt deposition over graphene nanoplatelets: effect of Pt loading on PEM fuel cell performance. *International Journal of Hydrogen Energy*, 42(30), 19246-19256.
- Dunbar, Z., & Masel, R. I. (2007). Quantitative MRI study of water distribution during operation of a PEM fuel cell using Teflon® flow fields. *Journal of Power Sources*, 171(2), 678-687.
- Eller, J., Roth, J., Marone, F., Stampanoni, M., & Büchi, F. N. (2016). Operando properties of gas diffusion layers: saturation and liquid permeability. *Journal of The Electrochemical Society* 164(2):F115.
- Engineering ToolBox. (2023). Water – Saturation Pressure vs Temperature. Retrieved November 15, 2023, from [Water - Saturation Pressure vs. Temperature \(engineeringtoolbox.com\)](https://www.engineeringtoolbox.com/water-saturation-pressure-temperature_1028.html)
- Fan, L., Niu, Z., Zhang, G., & Jiao, K. (2018). Optimization design of the cathode flow channel for proton exchange membrane fuel cells. *Energy conversion and management*, 171, 1813-1821.
- Feindel, K. W., Bergens, S. H., & Wasylishen, R. E. (2006). Insights into the distribution of water in a self-humidifying H<sub>2</sub>/O<sub>2</sub> proton-exchange membrane fuel cell using 1H NMR microscopy. *Journal of the American Chemical Society*, 128(43), 14192-14199.
- Felseghi, R. A., Carcadea, E., Raboaca, M. S., Trufin, C. N., & Filote, C. (2019). Hydrogen fuel cell technology for the sustainable future of stationary applications. *Energies*, 12(23), 4593.

Fowler, D., Gurau, V., & Cox, D. (2019). Bridging the Gap between Automated Manufacturing of Fuel Cell Components and Robotic Assembly of Fuel Cell Stacks. *Energies* 12(19):3604.

Fuel Cell Store (FCS). 2023. Gas diffusion layer: Characteristics and modelling. Retrieved September 20, 2023, from <https://www.fuelcellstore.com/blog-section/gas-diffusion-layer-characteristics-and-modeling>

FuelCellsWorks. (2020). Germany once again had the highest increase in hydrogen refueling stations worldwide in 2018. Retrieved September 20, 2023, from [Germany Once Again Had The Highest Increase Of Hydrogen Refuelling Stations Worldwide In 2018 - FuelCellsWorks](#)

Gao, B., Steenhuis, T. S., Zevi, Y., Parlange, J. Y., Carter, R. N., & Trabold, T. A. (2009). Visualization of unstable water flow in a fuel cell gas diffusion layer. *Journal of Power Sources* 190(2):493-498.

Ge, S., & Wang, C. Y. (2007). Liquid water formation and transport in the PEFC anode. *Journal of the Electrochemical Society*, 154(10), B998.

Goshtasbi, A., & Ersal, T. (2020). Degradation-conscious control for enhanced lifetime of automotive polymer electrolyte membrane fuel cells. *Journal of Power Sources* 457:227996.

Greene, D. L., Ogden, J. M., & Lin, Z. (2020). Challenges in the designing, planning and deployment of hydrogen refueling infrastructure for fuel cell electric vehicles. *ETransportation*, 6, 100086.

Gu, X., Hou, Z., & Cai, J. (2021). Data-based flooding fault diagnosis of proton exchange membrane fuel cell systems using LSTM networks. *Energy and AI*, 4, 100056.

Gutru, R., Turtayeva, Z., Xu, F., Maranzana, G., Vigolo, B., & Desforges, A. (2020). A comprehensive review on water management strategies and developments in anion exchange membrane fuel cells. *International Journal of Hydrogen Energy*.

H2 Energy News. 2023. 130 new hydrogen filling stations created in 2022. Retrieved September 11, 2023, from <https://energynews.biz/130-new-hydrogen-filling-stations-created-in-2022/>

Halter, J., MacDonald, J. A., Aroge, F. A., Lowe, O. C., Orfino, F. P., Alvar, E. N., ... & Kjeang, E. (2023). The Role of Thermal Conductivity on Liquid Water Distribution in GDLs. In Electrochemical Society Meeting Abstracts 244 (No. 37, pp. 1786-1786). *The Electrochemical Society*.

Harrison, K. W., Remick, R., Hoskin, A., & Martin, G. D. (2010). *Hydrogen production: fundamentals and case study summaries*. NREL/CP-550-47302. National Renewable Energy Lab. (NREL). Golden, CO

Hassan, N. S. M., Daud, W. R. W., Sopian, K., & Sahari, J. (2009). Water management in a single cell proton exchange membrane fuel cells with a serpentine flow field. *Journal of Power Sources*, 193(1), 249-257.

Hickner, M. A., Siegel, N. P., Chen, K. S., McBrayer, D. N., Hussey, D. S., Jacobson, D. L., & Arif, M. (2006). Real-time imaging of liquid water in an operating proton exchange membrane fuel cell. *Journal of the Electrochemical Society*, 153(5), A902.

Holecchek, J. L., Geli, H. M., Sawalhah, M. N., & Valdez, R. (2022). A global assessment: can renewable energy replace fossil fuels by 2050?. *Sustainability*, 14(8), 4792.

Hussaini, I. S., & Wang, C. Y. (2009). Visualization and quantification of cathode channel flooding in PEM fuel cells. *Journal of Power Sources*, 187(2), 444-451.

Hydrogen Technology and Energy Corporation (HTEC). (2023). About hydrogen stations and fuel cell electric vehicles. Retrieved September 12, 2023, from [Stations and Distribution - HTEC](#)

Ibrahim, A., Hossain, O., Chaggar, J., Steinberger-Wilckens, R., & El-Kharouf, A. (2020). GO-nafion composite membrane development for enabling intermediate temperature operation of polymer electrolyte fuel cell. *International Journal of Hydrogen Energy*, 45(8), 5526-5534.

Ijaodola, O. S., El-Hassan, Z., Ogungbemi, E., Khatib, F. N., Wilberforce, T., Thompson, J., & Olabi, A. G. (2019). Energy efficiency improvements by investigating the water flooding management on proton exchange membrane fuel cell (PEMFC). *Energy*, 179, 246-267.

Iranzo, A., & Boillat, P. (2014). Liquid water distribution patterns featuring back-diffusion transport in a PEM fuel cell with neutron imaging. *International journal of hydrogen energy*, 39(30), 17240-17245.

Iranzo, A., Muñoz, M., López, E., Pino, J., & Rosa, F. (2010). Experimental fuel cell performance analysis under different operating conditions and bipolar plate designs. *International Journal of Hydrogen Energy*, 35(20), 11437-11447.

Jaouen, F., Jones, D., Coutard, N., Artero, V., Strasser, P., & Kucernak, A. (2018). Toward platinum group metal-free catalysts for hydrogen/air proton-exchange membrane fuel cells. *Johnson Matthey Technology Review* 62:231-255.

Jeon, S., Lee, J., Rios, G. M., Kim, H. J., Lee, S. Y., Cho, E., ... & Jang, J. H. (2010). Effect of ionomer content and relative humidity on polymer electrolyte membrane fuel cell (PEMFC) performance of membrane-electrode assemblies (MEAs) prepared by decal transfer method. *International journal of hydrogen energy*, 35(18), 9678-9686.

Ji, M., & Wei, Z. (2009). A review of water management in polymer electrolyte membrane fuel cells. *Energies*, 2(4), 1057-1106.

Jiao, K., & Li, X. (2011). Water transport in polymer electrolyte membrane fuel cells. *Progress in energy and combustion Science*, 37(3), 221-291.

Jiao, K., Xuan, J., Du, Q., Bao, Z., Xie, B., Wang, B., ... & Guiver, M. D. (2021). Designing the next generation of proton-exchange membrane fuel cells. *Nature*, 595(7867), 361-369.

Kandlikar, S. G. (2008). Microscale and macroscale aspects of water management challenges in PEM fuel cells. *Heat Transfer Engineering* 29(7):575-587.

- Kang, D. G., Shin, D. K., Kim, S., & Kim, M. S. (2019). Experimental study on the performance improvement of polymer electrolyte membrane fuel cell with dual air supply. *Renewable Energy*, 141, 669-677.
- Kardjilov, N., Manke, I., Woracek, R., Hilger, A., & Banhart, J. (2018). Advances in neutron imaging. *Materials Today*, 21(6), 652-672.
- Kato, A., Kato, S., Yamaguchi, S., Suzuki, T., & Nagai, Y. (2022). Mechanistic insights into water transport in polymer electrolyte fuel cells with a variation of cell temperature and relative humidity of inlet gas elucidated by operando synchrotron X-ray radiography. *Journal of Power Sources*, 521, 230951.
- Kato, S., Yamaguchi, S., Yoshimune, W., Matsuoka, Y., Kato, A., Nagai, Y., & Suzuki, T. (2020). Ex-situ visualization of the wet domain in the microporous layer in a polymer electrolyte fuel cell by X-ray computed tomography under water vapor supply. *Electrochemistry Communications*, 111, 106644.
- Kawase, M., Sato, K., Mitsui, R., Asonuma, H., Kageyama, M., Yamaguchi, K., & Inoue, G. (2017). Electrochemical reaction engineering of polymer electrolyte fuel cell. *AIChE Journal*, 63(1), 249-256.
- Kim, B., Lee, Y., Woo, A., & Kim, Y. (2013). Effects of cathode channel size and operating conditions on the performance of air-blowing PEMFCs. *Applied energy*, 111, 441-448.
- Kim, J. M., Kim, J. H., Kim, J., Lim, Y., Kim, Y., Alam, A., ... & Kim, J. Y. (2020). Synergetic structural transformation of Pt electrocatalyst into advanced 3D architectures for hydrogen fuel cells. *Advanced Materials*, 32(51), 2002210.
- Kim, M., Jung, N., Eom, K., Yoo, S. J., Kim, J. Y., Jang, J. H., ... & Cho, E. (2014). Effects of anode flooding on the performance degradation of polymer electrolyte membrane fuel cells. *Journal of Power Sources*, 266, 332-340.
- Kim, S. G., & Lee, S. J. (2013). A review on experimental evaluation of water management in a polymer electrolyte fuel cell using X-ray imaging technique. *Journal of power sources*, 230, 101-108.

Kim, T., Jung, Y., Kim, M., Sim, C., Lee, S., & Jeon, J. (2006). Visualization of the internal water distribution at PEMFC using neutron imaging technology: Feasibility test at HANARO. *Nuclear Engineering and Technology*, 38(5), 449.

Klose, C. (2020). *Novel polymer electrolyte membrane compositions for electrolysis and fuel cell systems*. Doctoral Dissertation. University of Freiburg. Freiburg im Breisgau, Germany. 133 pp.

Kong, I. M., Jung, A., & Kim, M. S. (2016). Investigations on the double gas diffusion backing layer for performance improvement of self-humidified proton exchange membrane fuel cells. *Applied Energy*, 176, 149-156.

Kong, I. M., Jung, A., Kim, Y. S., & Kim, M. S. (2017). Numerical investigation on double gas diffusion backing layer functionalized on water removal in a proton exchange membrane fuel cell. *Energy*, 120, 478-487.

Kuhn, R., Scholta, J., Krüger, P., Hartnig, C., Lehnert, W., Arlt, T., & Manke, I. (2011). Measuring device for synchrotron X-ray imaging and first results of high temperature polymer electrolyte membrane fuel cells. *Journal of Power Sources*, 196(12), 5231-5239.

Lamb, W. F., Wiedmann, T., Pongratz, J., Andrew, R., Crippa, M., Olivier, J. G., ... & Minx, J. (2021). A review of trends and drivers of greenhouse gas emissions by sector from 1990 to 2018. *Environmental research letters*, 16(7), 073005.

Lee, D., & Bae, J. (2012). Visualization of flooding in a single cell and stacks by using a newly-designed transparent PEMFC. *International Journal of Hydrogen Energy*, 37(1), 422-435.

Lee, J., Yip, R., Antonacci, P., Ge, N., Kotaka, T., Tabuchi, Y., & Bazylak, A. (2015). Synchrotron investigation of microporous layer thickness on liquid water distribution in a PEM fuel cell. *Journal of The Electrochemical Society*, 162(7), F669.

Lee, S. J., Lim, N. Y., Kim, S., Park, G. G., & Kim, C. S. (2008). X-ray imaging of water distribution in a polymer electrolyte fuel cell. *Journal of Power Sources*, 185(2), 867-870.

Li, H., Tang, Y., Wang, Z., Shi, Z., Wu, S., Song, D., ... & Mazza, A. (2008). A review of water flooding issues in the proton exchange membrane fuel cell. *Journal of Power Sources*, 178(1), 103-117.

- Li, J., Yang, L., Wang, Z., Sun, H., & Sun, G. (2021). Degradation study of high temperature proton exchange membrane fuel cell under start/stop and load cycling conditions. *International Journal of Hydrogen Energy*, 46(47), 24353-24365.
- Li, Y., Yuan, F., Weng, R., Xi, F., & Liu, W. (2021). Variational-principle-optimized porosity distribution in gas diffusion layer of high-temperature PEM fuel cells. *Energy*, 235, 121350.
- Li, Y., Wang, L., Sharma, S., Zhang, G., Zhang, L., & Maréchal, F. (2022). Design and optimization of a solid oxide fuel cell-inverted gas turbine integrated system with zero carbon emission for distributed cogeneration. *Energy Conversion and Management*, 268, 116036.
- Litster, S., Buie, C.R., Fabian, T., Eaton, J.K., & Santiago, J.G. (2007). Active water management for PEM fuel cells. *Journal of the Electrochemical Society*, 154 (10): B1049-B1058. <http://doi.org/10.1149/1.2766650>.
- Litvinenko, V. S., Tsvetkov, P. S., Dvoynikov, M. V., & Buslaev, G. V. (2020). Barriers to implementation of hydrogen initiatives in the context of global energy sustainable development. *Journal of Mining Institute* 244:428-438.
- Liu, J., & Weber, A. Z. (2022). Ionomer Optimization for Hydroxide-Exchange-Membrane Water Electrolyzers Operated with Distilled Water: A Modeling Study. *Journal of The Electrochemical Society*, 169(5), 054506.
- Lochner, T., Kluge, R. M., Fichtner, J., El-Sayed, H. A., Garlyyev, B., & Bandarenka, A. S. (2020). Temperature effects in polymer electrolyte membrane fuel cells. *ChemElectroChem*, 7(17), 3545-3568.
- Lu, Z., Waldecker, J., Tam, M., & Cimenti, M. (2015). Influence of MPL structure modification on fuel cell oxygen transport resistance. *ECS Transactions*, 69(17), 1341.
- Manke, I., Hartnig, C., Grünerbel, M., Lehnert, W., Kardjilov, N., Haibel, A., ... & Rieseemeier, H. (2007). Investigation of water evolution and transport in fuel cells with high resolution synchrotron x-ray radiography. *Applied Physics Letters*, 90(17), 174105.

- Manohar, A. K., Bretschger, O., Neelson, K. H., & Mansfeld, F. (2008). The use of electrochemical impedance spectroscopy (EIS) in the evaluation of the electrochemical properties of a microbial fuel cell. *Bioelectrochemistry*, 72(2), 149-154.
- Manso, A. P., Marzo, F. F., Barranco, J., Garikano, X., & Mujika, M. G. (2012). Influence of geometric parameters of the flow fields on the performance of a PEM fuel cell. A review. *International journal of hydrogen energy*, 37(20), 15256-15287.
- Mansour, A., Faouzi, B., Jamel, G., & Ismahen, E. (2014). Design and analysis of a high frequency DC–DC converters for fuel cell and super-capacitor used in electrical vehicle. *International journal of hydrogen energy*, 39(3), 1580-1592.
- Mao, S., Zhang, Y., & Rodriguez, F. (2023). Zero-emission bus and truck market in China: A 2021 update.
- Marappan, M., Palaniswamy, K., Velumani, T., Chul, K. B., Velayutham, R., Shivakumar, P., & Sundaram, S. (2021). Performance studies of proton exchange membrane fuel cells with different flow field designs—review. *The Chemical Record*, 21(4), 663-714.
- Markötter, H., Manke, I., Haußmann, J., Arlt, T., Klages, M., Krüger, P., ... & Banhart, J. (2012). Combined synchrotron X-ray radiography and tomography study of water transport in gas diffusion layers. *Micro & nano letters*, 7(7), 689-692.
- McCain, B. A., Stefanopoulou, A. G., & Siegel, J. B. (2010). Controllability and observability analysis of the liquid water distribution inside the gas diffusion layer of a unit fuel cell model.
- Mench, M. M. (2008). *Fuel Cell Engines*. Wiley and Sons. Hoboken, New Jersey. ISBN 978-0-471-68958-4.
- Miansari, M., Sedighi, K., Amidpour, M., Alizadeh, E., & Miansari, M. O. (2009). Experimental and thermodynamic approach on proton exchange membrane fuel cell performance. *Journal of Power Sources*, 190(2), 356-361.
- Mirfarsi, S. H., Parnian, M. J., & Rowshanzamir, S. (2020). Self-humidifying proton exchange membranes for fuel cell applications: advances and challenges. *Processes*, 8(9), 1069.

Mortazavi, M., Santamaria, A.D., Benner, J.Z., & Chauhan, V. (2019). Enhanced water removal from PEM fuel cells using acoustic pressure waves. *Journal of the Electrochemical Society* 166(7):F3143-F3153. <http://doi.org/10.1149/2.0211917>.

Muirhead, D., (2017). Liquid water saturation and oxygen transport resistance in polymer electrolyte membrane fuel cell gas diffusion layers. Masters of Applied Science Thesis. University of Toronto. 136 pp.

Muirhead, D., Banerjee, R., George, M. G., Ge, N., Shrestha, P., Liu, H., Lee., and Bazylak, A. (2018). Liquid water saturation and oxygen transport resistance in polymer electrolyte membrane fuel cell gas diffusion layers. *Electrochimica Acta*, 274, 250-265.

Mukaide, T., Mogi, S., Yamamoto, J., Morita, A., Koji, S., Takada, K., ... & Noma, T. (2008). In situ observation of water distribution and behaviour in a polymer electrolyte fuel cell by synchrotron X-ray imaging. *Journal of synchrotron radiation*, 15(4), 329-334.

Mularczyk, A. (2021). *Liquid and vapour phase water transport mechanisms in fuel cell gas diffusion layers* (Doctoral dissertation, ETH Zurich).

Müller-Hülstede, J., Uhlig, L. M., Schmies, H., Schonvogel, D., Meyer, Q., Nie, Y., ... & Wagner, P. (2022a). Towards the Reduction of Pt Loading in High Temperature Proton Exchange Membrane Fuel Cells—Effect of Fe–N–C in Pt-Alloy Cathodes. *ChemSusChem*, e202202046.

Müller-Hülstede, J., Zierdt, T., Schmies, H., Schonvogel, D., Meyer, Q., Zhao, C., ... & Wark, M. (2022b). Implementation of different Fe–N–C catalysts in high temperature proton exchange membrane fuel cells—Effect of catalyst and catalyst layer on performance. *Journal of Power Sources*, 537, 231529.

National Academies of Sciences, Policy, Global Affairs, Board on Research Data, Information, Division on Engineering, ... & Replicability in Science. (2019). *Reproducibility and replicability in science*. National Academies Press.

Nazir, H., Muthuswamy, N., Louis, C., Jose, S., Prakash, J., Buan, M. E., ... & Kannan, A. M. (2020). Is the H<sub>2</sub> economy realizable in the foreseeable future? Part II: H<sub>2</sub> storage, transportation, and distribution. *International journal of hydrogen energy*, 45(41), 20693-20708.

Ogungbemi, E., Ijaodola, O., Khatib, F. N., Wilberforce, T., El Hassan, Z., Thompson, J., ... & Olabi, A. G. (2019). Fuel cell membranes—Pros and cons. *Energy*, *172*, 155-172.

O'Hayre, R., W. Colella, S-W. Cha, and F.B. Prinz. (2016). *Fuel Cell Fundamentals* (Third ed.). Hoboken, New Jersey: Wiley.

Okonkwo, P. C., & Otor, C. (2021). A review of gas diffusion layer properties and water management in proton exchange membrane fuel cell system. *International Journal of Energy Research*, *45*(3), 3780-3800.

Omasta, T. J., Peng, X., & Mustain, W. E. (2017, September). Approaching 2 W· cm<sup>-2</sup> AEMFCs through Electrode Engineering and Controlling the Cell Water Content and Balance. In *Electrochemical Society Meeting Abstracts 232* (No. 36, pp. 1609-1609). The Electrochemical Society, Inc..

Omasta, T. J., Park, A. M., LaManna, J. M., Zhang, Y., Peng, X., Wang, L., ... & Mustain, W. E. (2018). Beyond catalysis and membranes: visualizing and solving the challenge of electrode water accumulation and flooding in AEMFCs. *Energy & Environmental Science*, *11*(3), 551-558.

Omrani, R., & Shabani, B. (2017). Gas diffusion layer modifications and treatments for improving the performance of proton exchange membrane fuel cells and electrolyzers: a review. *International Journal of Hydrogen Energy*, *42*(47), 28515-28536.

O'Rourke, J., Ramani, M., & Arcak, M. (2009). In situ detection of anode flooding of a PEM fuel cell. *International Journal of Hydrogen Energy*, *34*(16), 6765-6770.

Osmieri, L., & Meyer, Q. (2022). Recent advances in integrating platinum group metal-free catalysts in proton exchange membrane fuel cells. *Current Opinion in Electrochemistry*, *31*, 100847.

Oukali, G., Salager, E., Ammar, M. R., Dutoit, C. E., Sarou-Kanian, V., Simon, P., ... & Deschamps, M. (2019). In situ magnetic resonance imaging of a complete supercapacitor giving additional insight on the role of nanopores. *ACS nano*, *13*(11), 12810-12815.

- Ous, T., & Arcoumanis, C. (2009). Visualisation of water accumulation in the flow channels of PEMFC under various operating conditions. *Journal of Power Sources*, 187(1), 182-189.
- Owejan, J. P., Trabold, T. A., Jacobson, D. L., Baker, D. R., Hussey, D. S., & Arif, M. (2006). In situ investigation of water transport in an operating PEM fuel cell using neutron radiography: Part 2—Transient water accumulation in an interdigitated cathode flow field. *International Journal of Heat and Mass Transfer*, 49(25-26), 4721-4731.
- Ozen, D. N., Timurkutluk, B., & Altinisik, K. (2016). Effects of operation temperature and reactant gas humidity levels on performance of PEM fuel cells. *Renewable and Sustainable Energy Reviews*, 59, 1298-1306.
- Palan, V., Shepard Jr, W. S., & Williams, K. A. (2006). Removal of excess product water in a PEM fuel cell stack by vibrational and acoustical methods. *Journal of Power Sources*, 161(2), 1116-1125.
- Pamplona Solis, B., Cruz Argüello, J. C., Gomez Barba, L., Gurrola, M. P., Zarhri, Z., & TrejoArroyo, D. L. (2019). Bibliometric analysis of the mass transport in a gas diffusion layer in PEM fuel cells. *Sustainability*, 11(23), 6682.
- Park, H. G., Piggott, W. T., Chung, J., Morse, J. D., Havstad, M., Grigoropoulos, C. P., ... & Upadhye, R. (2003). *A methanol steam reforming micro reactor for proton exchange membrane micro fuel cell system* (No. UCRL-JC-150223). Lawrence Livermore National Lab.(LLNL), Livermore, CA (United States).
- Park, J., & Li, X. (2006). Effect of flow and temperature distribution on the performance of a PEM fuel cell stack. *Journal of Power Sources*, 162(1), 444-459.
- Park, Y. H., & Caton, J. A. (2008). An experimental investigation of electro-osmotic drag coefficients in a polymer electrolyte membrane fuel cell. *International Journal of Hydrogen Energy*, 33(24), 7513-7520.
- Pasaogullari, U., & Wang, C. Y. (2004). Liquid water transport in gas diffusion layer of polymer electrolyte fuel cells. *Journal of the electrochemical society*, 151(3), A399.

Paul, D., Fraser, A., Pearce, J., & Karan, K. (2011). Understanding the ionomer structure and the proton conduction mechanism in PEFC catalyst layer: adsorbed nafion on model substrate. *ECS Transactions*, 41(1), 1393.

Peinador, R. I., Abba, O., & Calvo, J. I. (2022). Characterization of commercial gas diffusion layers (GDL) by liquid extrusion porometry (LEP) and gas liquid displacement porometry (GLDP). *Membranes*, 12(2), 212.

Prasanna, M., Ha, H. Y., Cho, E., Hong, S. A., & Oh, I. H. (2004). Investigation of oxygen gain in polymer electrolyte membrane fuel cells. *Journal of power sources*, 137(1), 1-8.

Qi, M., Hou, M., Zeng, Y., Gao, Y., Yang, Y., He, L., ... & Shao, Z. (2020). A robust esterified nanofibre electrode for proton exchange membrane fuel cells. *Journal of Materials Chemistry A* 8(10):5298-5307.

Qiao, J. N., Guo, H., Chen, H., & Ye, F. (2022). Improving round-trip energy efficiency of a unitized regenerative fuel cell by adopting staircase flow channel and counter flow configuration. *Energy Conversion and Management*, 271, 116345.

Qiao, Z. (2020). *Advanced Oxygen-reduction Cathode Electrocatalysts for Hydrogen Proton-exchange Membrane Fuel Cells* (Doctoral dissertation, State University of New York at Buffalo).

Rahimian, P., Anderson, R., & Zhang, L. (2017). Predictions of flow regimes in proton exchange membrane fuel cells: An analytical approach. *International Journal of Hydrogen Energy*, 42(7), 4679-4689.

Rahman, S. N. A., Masdar, M. S., Rosli, M. I., Majlan, E. H., Husaini, T., Daud, W. R. W., ... & Lye, C. C. (2016). Portable PEM fuel cell system: water and heat management. *J. Eng. Sci. Technol*, 11, 122-136.

Raman, S., Iyeswaria, K. B., Narasimhan, S., & Rengaswamy, R. (2017). Effects of water induced pore blockage and mitigation strategies in low temperature PEM fuel cells—A simulation study. *International Journal of Hydrogen Energy*, 42(37), 23799-23813.

Rapier, R. (2020, June 20). Fossil fuels still supply 84 percent of world energy - And other eye openers from BP's annual review. *Forbes Magazine*. Retrieved October 15, 2020 from: <https://www.forbes.com/sites/rrapier/2020/06/20/bp-review-new-highs-in-global-energy-consumption-and-carbon-emissions-in-2019/>

Rosli, M. I., Borman, D. J., Ingham, D. B., Ismail, M. S., Ma, L., & Pourkashanian, M. (2010). Transparent PEM fuel cells for direct visualization experiments. *Journal of Fuel Cell Science and Technology* 7(6).

Rosli, M. I., Pourkashanian, M., Ingham, D. B., Ma, L., Borman, D., & Ismail, M. S. (2009, January). Transparent PEM fuel cells for direct visualisation experiments. In *International Conference on Fuel Cell Science, Engineering and Technology* (Vol. 48814, pp. 329-337).

Salam, M. A., Habib, M., Ahmed, K., Uddin, M., Hossain, T., Papri, N., & Arefin, P. (2020). Effect of temperature on the performance factors and durability of proton exchange membrane of hydrogen fuel cell: A narrative review. *Material Science Research India (Online)*, 17(2), 179-191.

Santarelli, M. G., & Torchio, M. F. (2007). Experimental analysis of the effects of the operating variables on the performance of a single PEMFC. *Energy conversion and management*, 48(1), 40-51.

Sauermoser, M., Kizilova, N., Pollet, B., & Kjelstrup, S. (2020). Flow field patterns for proton exchange membrane (PEM) fuel cells. *Frontiers in Energy Research*:1-20.

Schmittinger, W., & Vahidi, A. (2008). A review of the main parameters influencing long-term performance and durability of PEM fuel cells. *Journal of power sources* 180(1):1-14.

Schwartz, F. A., & Brow, J. E. (1951). Diffusivity of water vapor in some common gases. *The Journal of Chemical Physics*, 19(5), 640-646.

Shabani, B., Hafttananian, M., Khamani, S., Ramiar, A., & Ranjbar, A. A. (2019). Poisoning of proton exchange membrane fuel cells by contaminants and impurities: Review of mechanisms, effects, and mitigation strategies. *Journal of Power Sources*, 427, 21-48.

- Shen, J., Xu, L., Chang, H., Tu, Z., & Chan, S. H. (2020). Partial flooding and its effect on the performance of a proton exchange membrane fuel cell. *Energy Conversion and Management*, 207, 112537.
- Shimpalee, S., & Van Zee, J. W. (2007). Numerical studies on rib & channel dimension of flow-field on PEMFC performance. *International Journal of Hydrogen Energy*, 32(7), 842-856.
- Singh, R., Oberoi, A. S., & Singh, T. (2022). Factors influencing the performance of PEM fuel cells: A review on performance parameters, water management, and cooling techniques. *International Journal of Energy Research*, 46(4), 3810-3842.
- Singh, Y., White, R. T., Najm, M., Haddow, T., Pan, V., Orfino, F. P., & Kjeang, E. (2019). Tracking the evolution of mechanical degradation in fuel cell membranes using 4D in situ visualization. *Journal of Power Sources* 412:224-237.
- Sinigaglia, T., Lewiski, F., Martins, M. E. S., & Siluk, J. C. M. (2017). Production, storage, fuel stations of hydrogen and its utilization in automotive applications-a review. *International journal of hydrogen energy*, 42(39), 24597-24611.
- Soler, J., Hontanon, E., & Daza, L. (2003). Electrode permeability and flow-field configuration: influence on the performance of a PEMFC. *Journal of Power Sources*, 118(1-2), 172-178.
- Song, D., Wang, Q., Liu, Z. S., & Huang, C. (2006). Transient analysis for the cathode gas diffusion layer of PEM fuel cells. *Journal of Power Sources*, 159(2), 928-942.
- Song, H. L., Zhu, Y., & Li, J. (2019). Electron transfer mechanisms, characteristics and applications of biological cathode microbial fuel cells—A mini review. *Arabian Journal of Chemistry*, 12(8), 2236-2243.
- Song, Y., Zhang, C., Ling, C. Y., Han, M., Yong, R. Y., Sun, D., & Chen, J. (2020). Review on current research of materials, fabrication and application for bipolar plate in proton exchange membrane fuel cell. *International Journal of Hydrogen Energy* 45(54):29832-29847.
- Song, Z., Cheng, N., Lushington, A., & Sun, X. (2016). Recent progress on MOF-derived nanomaterials as advanced electrocatalysts in fuel cells. *Catalysts* 6(8):116.

- Sorrentino, A., Sundmacher, K., & Vidakovic-Koch, T. (2020). Polymer electrolyte fuel cell degradation mechanisms and their diagnosis by frequency response analysis methods: a review. *Energies*, 13(21), 5825.
- Sovacool, B. K., Griffiths, S., Kim, J., & Bazilian, M. (2021). Climate change and industrial F-gases: A critical and systematic review of developments, sociotechnical systems and policy options for reducing synthetic greenhouse gas emissions. *Renewable and sustainable energy reviews*, 141, 110759.
- Spernjak, D., Prasad, A. K., & Advani, S. G. (2007). Experimental investigation of liquid water formation and transport in a transparent single-serpentine PEM fuel cell. *Journal of Power Sources*, 170(2), 334-344.
- Statista. 2022. Number of hydrogen fueling stations for road vehicles worldwide as of 2022, by country. Retrieved October 25, 2022, from <https://www.statista.com/statistics/1026719/number-of-hydrogen-fuel-stations-by-country/>
- Su, A., Weng, F. B., Hsu, C. Y., & Chen, Y. M. (2006). Studies on flooding in PEM fuel cell cathode channels. *International journal of hydrogen energy*, 31(8), 1031-1039.
- Su, A., Ferng, Y. M., & Shih, J. C. (2010). CFD investigating the effects of different operating conditions on the performance and the characteristics of a high-temperature PEMFC. *Energy*, 35(1), 16-27.
- Sun, H., Xie, C., Chen, H., & Almheiri, S. (2015). A numerical study on the effects of temperature and mass transfer in high temperature PEM fuel cells with ab-PBI membrane. *Applied Energy*, 160, 937-944.
- Tamayol, A., & Bahrami, M. (2011). Water permeation through gas diffusion layers of proton exchange membrane fuel cells. *Journal of power sources*, 196(15), 6356-6361.
- Taner, T. (2015). Alternative energy of the future: a technical note of PEM fuel cell water management. *Journal of Fundamentals of Renewable Energy and Applications*, 5(3), 1-4.

Tashie-Lewis, B. C., & Nnabuife, S. G. (2021). Hydrogen production, distribution, storage and power conversion in a hydrogen economy-a technology review. *Chemical Engineering Journal Advances*, 8, 100172.

Tongsh, C., Liang, Y., Xie, X., Li, L., Liu, Z., Du, Q., & Jiao, K. (2021). Experimental investigation of liquid water in flow field of proton exchange membrane fuel cell by combining X-ray with EIS technologies. *Science China Technological Sciences*, 64(10), 2153-2165

Trabold, T. A., Owejan, J. P., Jacobson, D. L., Arif, M., & Huffman, P. R. (2006). In situ investigation of water transport in an operating PEM fuel cell using neutron radiography: Part 1–Experimental method and serpentine flow field results. *International Journal of Heat and Mass Transfer*, 49(25-26), 4712-4720.

Trinh, N. V., Nguyen, X. L., Kim, Y., & Yu, S. (2022). Characteristics of Water Transport of Membrane Electrolyte over Selected Temperature for Proton Exchange Membrane Fuel Cell. *Polymers*, 14(15), 2972.

Tsushima, S., & Hirai, S. (2011). In situ diagnostics for water transport in proton exchange membrane fuel cells. *Progress in Energy and Combustion Science* 37(2):204-220.

United Nations Environment Programme (UNEP). 2022. The closing window: Climate crisis calls for rapid transformation of society – Emissions gap report 2022. Retrieved February 14, 2023, from [Emissions Gap Report 2022 \(unep.org\)](https://www.unep.org/emissions-gap-report-2022).

United States Environmental Protection Agency (USEPA). (2020). Global greenhouse gas emissions data. Retrieved October 15, 2020, from <https://www.epa.gov/ghgemissions/global-greenhouse-gas-emissions-data>

United States Environmental Protection Agency (USEPA). (2023). Sources of greenhouse gas emissions. Retrieved September 29, 2023, from [Sources of Greenhouse Gas Emissions | US EPA](https://www.epa.gov/ghgemissions/sources-of-greenhouse-gas-emissions)

United States Department of Energy (USDOE). 2020a. DOE Technical Targets for Fuel Cell Systems for Stationary (Combined Heating and Power) Applications. Hydrogen and Fuel Cell Technologies Office. Washington, D.C. Retrieved September 28, 2020, from

<https://www.energy.gov/eere/fuelcells/doe-technical-targets-fuel-cell-systems-stationary-combined-heat-and-power>

United States Department of Energy (USDOE). 2020b. DOE Technical Targets for Fuel Cell Systems and Stacks for Transportation Applications. Hydrogen and Fuel Cell Technologies Office. Washington, D.C. Retrieved September 28, 2020, from <https://www.energy.gov/eere/fuelcells/doe-technical-targets-fuel-cell-systems-and-stacks-transportation-applications>

United States Department of Energy (USDOE). 2023. Hydrogen production and distribution. Alternative Fuels Data Center. Energy Efficiency and Renewable Energy. Retrieved November 7, 2023, from [https://afdc.energy.gov/fuels/hydrogen\\_production.html](https://afdc.energy.gov/fuels/hydrogen_production.html)

Vahidi, A., Stefanopoulou, A., & Peng, H. (2004, June). Model predictive control for starvation prevention in a hybrid fuel cell system. In *Proceedings of the 2004 American control conference* (Vol. 1, pp. 834-839). IEEE.

velan Venkatesan, S., Lim, C., Rogers, E., Holdcroft, S., & Kjeang, E. (2015). Evolution of water sorption in catalyst coated membranes subjected to combined chemical and mechanical degradation. *Physical Chemistry Chemical Physics* 17(21):13872-13881.

Wahdame, B., Candusso, D., & Kauffmann, J. M. (2006). Study of gas pressure and flow rate influences on a 500 W PEM fuel cell, thanks to the experimental design methodology. *Journal of power sources*, 156(1), 92-99.

Wang, Y., Chen, K.S., Mishler, J., Cho, S.C., & Adroher, X.C. (2011). A review of polymer electrolyte membrane fuel cells: Technology, applications, and needs on fundamental research. *Applied Energy* 88(4):981-1007.  
<http://dx.doi.org/10.1016/j.apenergy.2010.09.030>

Wang, Y., Leung, D. Y., Xuan, J., & Wang, H. (2017). A review on unitized regenerative fuel cell technologies, part B: Unitized regenerative alkaline fuel cell, solid oxide fuel cell, and microfluidic fuel cell. *Renewable and Sustainable Energy Reviews*, 75, 775-795.

Wang, Y., Diaz, D.F.R., Chen, K.S., Wang, Z., & Adroher, X.C. (2020). Materials, technological status, and fundamentals of PEM fuel cells—a review. *Materials Today* 32:178-203. <http://dx.doi.org/10.1016/j.mattod.2019.06.005>.

Wei, T., Wu, J., & Chen, S. (2021). Keeping track of greenhouse gas emission reduction progress and targets in 167 cities worldwide. *Frontiers in Sustainable Cities*, 3, 696381.

Weng, F. B., Su, A., Hsu, C. Y., & Lee, C. Y. (2006). Study of water-flooding behaviour in cathode channel of a transparent proton-exchange membrane fuel cell. *Journal of power sources*, 157(2), 674-680.

Whiston, M. M., Azevedo, I. L., Litster, S., Whitefoot, K. S., Samaras, C., & Whitacre, J. F. (2019). Expert assessments of the cost and expected future performance of proton exchange membrane fuel cells for vehicles. *Proceedings of the National Academy of Sciences* 116(11):4899-4904.

White, R.T. (2019). Investigating cathode catalyst layer degradation in polymer electrolyte fuel cells by lab-based X-ray computed tomography. PhD Thesis. School of Mechatronic Systems Engineering. Faculty of Applied Sciences. Simon Fraser University. Surrey, B.C.

White, R. T., Orfino, F. P., El Hannach, M., Luo, O., Dutta, M., Young, A. P., & Kjeang, E. (2016). 3D printed flow field and fixture for visualization of water distribution in fuel cells by X-ray computed tomography. *Journal of The Electrochemical Society*, 163(13), F1337.

White, R. T., Eberhardt, S., Najm, M., Orfino, F. P., Dutta, M., & Kjeang, E. (2017). Quantification of Material Property Changes During Electrode Degradation in Polymer Electrolyte Fuel Cells Using X-ray Computed Tomography. *Microscopy and Microanalysis* 23(S1):2044-2045.

White, R. T., Eberhardt, S. H., Singh, Y., Haddow, T., Dutta, M., Orfino, F. P., & Kjeang, E. (2019). Four-dimensional joint visualization of electrode degradation and liquid water distribution inside operating polymer electrolyte fuel cells. *Scientific Reports* 9(1):1-12.

Xia, L., Ni, M., He, Q., Xu, Q., & Cheng, C. (2021). Optimization of gas diffusion layer in high temperature PEMFC with the focuses on thickness and porosity. *Applied Energy*, 300, 117357.

Xia, Z., Wang, B., Yang, Z., Wu, K., Du, Q., & Jiao, K. (2019). Effect of operating conditions on performance of proton exchange membrane fuel cell with anode recirculation. *Energy Procedia*, 158, 1829-1834.

Xing, L., Du, S., Chen, R., Mamlouk, M., & Scott, K. (2016). Anode partial flooding modelling of proton exchange membrane fuel cells: model development and validation. *Energy*, 96, 80-95.

Xu, F., Leclerc, S., Stemmelen, D., Perrin, J. C., Retournard, A., & Canet, D. (2017). Study of electro-osmotic drag coefficients in Nafion membrane in acid, sodium and potassium forms by electrophoresis NMR. *Journal of membrane science*, 536, 116-122.

Xu, H., Nagashima, S., Nguyen, H. P., Kishita, K., Marone, F., Büchi, F. N., & Eller, J. (2021). Temperature dependent water transport mechanism in gas diffusion layers revealed by subsecond operando X-ray tomographic microscopy. *Journal of Power Sources*, 490, 229492.

Xu, H., Bühner, M., Marone, F., Schmidt, T. J., Büchi, F. N., & Eller, J. (2022). Effects of gas diffusion layer substrates on PEFC water management: Part I. Operando liquid water saturation and diffusion properties. *Journal of The Electrochemical Society*, 168, 074505.

Xu, R., Yu, P., Abramson, M. J., Johnston, F. H., Samet, J. M., Bell, M. L., ... & Guo, Y. (2020). Wildfires, global climate change, and human health. *New England Journal of Medicine*, 383(22), 2173-2181.

Xu, Y., Xu, X., & Bi, L. (2022b). A high-entropy spinel ceramic oxide as the cathode for proton-conducting solid oxide fuel cells. *Journal of Advanced Ceramics*, 11(5), 794-804.

Yan, Q., Toghiani, H., & Causey, H. (2006a). Steady state and dynamic performance of proton exchange membrane fuel cells (PEMFCs) under various operating conditions and load changes. *Journal of Power Sources*, 161(1), 492-502.

- Yan, Q., Toghiani, H., & Wu, J. (2006b). Investigation of water transport through membrane in a PEM fuel cell by water balance experiments. *Journal of Power Sources*, 158(1), 316-325.
- Yang, X. G., Zhang, F. Y., Lubawy, A. L., & Wang, C. Y. (2004). Visualization of liquid water transport in a PEFC. *Electrochemical and Solid-State Letters*, 7(11), A408.
- Yang, X. Y., Xu, J. J., Bao, D., Chang, Z. W., Liu, D. P., Zhang, Y., & Zhang, X. B. (2017). High-Performance Integrated Self-Package Flexible Li–O<sub>2</sub> Battery Based on Stable Composite Anode and Flexible Gas Diffusion Layer. *Advanced Materials*, 29(26), 1700378.
- Yang, Y., Jia, H., Liu, Z., Bai, N., Zhang, X., Cao, T., ... & He, X. (2022). Overall and local effects of operating parameters on water management and performance of open-cathode PEM fuel cells. *Applied Energy*, 315, 118978.
- Yang, Z., Wang, B., & Jiao, K. (2020). Life cycle assessment of fuel cell, electric and internal combustion engine vehicles under different fuel scenarios and driving mileages in China. *Energy*, 198, 117365.
- Yuan, X. Z., Sun, J. C., Wang, H., & Li, H. (2012). Accelerated conditioning for a proton exchange membrane fuel cell. *Journal of Power Sources*, 205, 340-344.
- Zaffou, R., Jung, S. Y., Kunz, H. R., & Fenton, J. M. (2006). Temperature-driven water transport through membrane electrode assembly of proton exchange membrane fuel cells. *Electrochemical and Solid-State Letters*, 9(9), A418.
- Zawodzinski, T. A., Davey, J., Valerio, J., & Gottesfeld, S. (1995). The water content dependence of electro-osmotic drag in proton-conducting polymer electrolytes. *Electrochimica acta*, 40(3), 297-302.
- Zhang, J., Tang, Y., Song, C., Cheng, X., Zhang, J., & Wang, H. (2007). PEM fuel cells operated at 0% relative humidity in the temperature range of 23–120 C. *Electrochimica Acta*, 52(15), 5095-5101.
- Zhang, J., Tang, Y., Song, C., Xia, Z., Li, H., Wang, H., & Zhang, J. (2008). PEM fuel cell relative humidity (RH) and its effect on performance at high temperatures. *Electrochimica Acta*, 53(16), 5315-5321.

Zhang, J., Wu, J., Zhang, H., & Zhang, J. (2013). *PEM fuel cell testing and diagnosis*. Newnes.

Zhao, J., Huang, X., Chang, H., Chan, S. H., & Tu, Z. (2021). Effects of operating temperature on the carbon corrosion in a proton exchange membrane fuel cell under high current density. *Energy Conversion and Management: X*, 10, 100087.

Zhao, Q., Majsztrik, P., & Benziger, J. (2011). Diffusion and interfacial transport of water in Nafion. *The journal of physical chemistry B*, 115(12), 2717-2727.

Zhao, Q., Yu, P., Mahendran, R., Huang, W., Gao, Y., Yang, Z., ... & Guo, Y. (2022). Global climate change and human health: Pathways and possible solutions. *Eco-Environment & Health*, 1(2), 53-62.

Zhao, Y. M., Zhang, P. C., Xu, C., Zhou, X. Y., Liao, L. M., Wei, P. J., ... & Liu, J. G. (2020). Design and preparation of Fe–N5 catalytic sites in single-atom catalysts for enhancing the oxygen reduction reaction in fuel cells. *ACS applied materials & interfaces*, 12(15), 17334-17342.

Zhou, J., Tao, Y. L., Xu, C. J., Gong, X. N., & Hu, P. C. (2015). Electro-osmotic strengthening of silts based on selected electrode materials. *Soils and Foundations*, 55(5), 1171-1180.

Zhou, S., Lu, Y., Bao, D., Wang, K., Shan, J., & Hou, Z. (2022). Real-time data-driven fault diagnosis of proton exchange membrane fuel cell system based on binary encoding convolutional neural network. *International Journal of Hydrogen Energy*, 47(20), 10976-10989.